UC Berkeley
SEMM Reports Series

Title
Nonlinear Geometric, Material and Time Dependent Analysis of Reinforced Concrete Shells with Edge Beams

Permalink
https://escholarship.org/uc/item/3883z0br

Authors
Chan, Esmond
Scordelis, Alex

Publication Date
1982-12-01

eScholarship.org Powered by the California Digital Library
University of California

REPORT NO.
UCB/SESM-82/08

STRUCTURAL ENGINEERING AND
STRUCTURAL MECHANICS

NONLINEAR GEOMETRIC, MATERIAL AND TIME DEPENDENT ANALYSIS OF REINFORCED CONCRETE SHELLS WITH EDGE BEAMS

by
ESMOND C. CHAN

Prepared under the Sponsorship of
National Science Foundation
Grant CME 79 - 18057

DECEMBER 1982

DEPARTMENT OF CIVIL ENGINEERING
UNIVERSITY OF CALIFORNIA
BERKELEY, CALIFORNIA

BIBLIOGRAPHIC DATA SHEET	1. Report No.	2.	3. Recipient's Accession No.

4. Title and Subtitle

NONLINEAR GEOMETRIC, MATERIAL AND TIME DEPENDENT ANALYSIS OF REINFORCED CONCRETE SHELLS WITH EDGE BEAMS

5. Report Date December 1982

6.

7. Author(s)

Esmond Chi-Yiu Chan

8. Performing Organization Rept. No. UC-SESM 82-8

9. Performing Organization Name and Address

Department of Civil Engineering
University of California
Berkeley, California 94720

10. Project/Task/Work Unit No.

11. Contract/Grant No.

CME 79-18057

12. Sponsoring Organization Name and Address

National Science Foundation
Washington, D.C. 20550

13. Type of Report & Period Covered

Final Report

14.

15. Supplementary Notes

16. Abstracts

A numerical method of analysis has been developed for the analysis of 3D reinforced concrete frames, shells with or without edge beams through their elastic, inelastic and ultimate load ranges. Nonlinearities as a result of tensile cracking, nonlinear behavior of concrete in compression, yielding of the steel reinforcement, geometric nonlinearities as a result of finite displacement; and the time dependent effects of creep and shrinkage are included in the analysis.

A finite element displacement formulation coupled with a time step integration solution is used. The iterative scheme is based upon double step method with the constant imposed displacement constraint.

A series of numerical examples consisting of beams, columns, slabs and shells with or without edge members are analysed and compared with the available theoretical and experimental results to demonstrate the applicability and the validity of the present method of analysis.

17. Key Words and Document Analysis. 17a. Descriptors

Structural Engineering, Reinforced Concrete, Shell, Edge Beam, Nonlinear Material, Nonlinear Geometry, Cracking, Yielding, Creep, Shrinkage, Finite Element, Displacement Method, Elastic, Inelastic.

17b. Identifiers/Open-Ended Terms

17c. COSATI Field/Group

18. Availability Statement	19. Security Class (This Report)	21. No. of Pages
Release Unlimited	UNCLASSIFIED	372
	20. Security Class (This Page) UNCLASSIFIED	22. Price

FORM NTIS-35 (REV. 10-73) ENDORSED BY ANSI AND UNESCO. THIS FORM MAY BE REPRODUCED USCOMM-DC 8265-P74

Structures and Materials Research
Department of Civil Engineering
Division of Structural Engineering
and Structural Mechanics

UCB/SESM Report No. 82/8

NONLINEAR GEOMETRIC, MATERIAL AND TIME DEPENDENT ANALYSIS OF REINFORCED CONCRETE SHELLS WITH EDGE BEAMS

by

Esmond Chi-Yiu Chan

Faculty Investigator: A. C. Scordelis

Prepared under the Sponsorship of
National Science Foundation
Grant CME 79-18057

College of Engineering
Office of Research Services
University of California
Berkeley, California

December 1982

NONLINEAR GEOMETRIC, MATERIAL AND TIME DEPENDENT ANALYSIS OF REINFORCED CONCRETE SHELLS WITH EDGE BEAMS

Doctor of Philosophy | Esmond Chi-Yiu Chan | Civil Engineering

A. C. Scordelis
Chairman of Committee

ABSTRACT

A numerical method of analysis has been developed to study the nonlinear response of reinforced concrete structures with special emphasis on shells with edge members. Nonlinear material, nonlinear geometry and the time dependent effects of creep and shrinkage are included in the analysis. The structural response is traced through its elastic, inelastic and ultimate load ranges.

A finite element displacement formulation coupled with a time step integration solution is used. An incremental and iterative scheme based upon constant imposed displacement is used so that structures with local instabilities or strain softenings can also be analyzed.

An improved layered composite 9-node Lagrangian shell element with equivalent smeared steel layers is developed to represent the reinforced concrete shell in which the material properties can vary within an element.

A composite filamented 3D rectangular beam element with discrete reinforcement is used to model the edge beam. The material properties are assumed to be constant for each filament.

Material nonlinearities as a result of tension cracking, tension stiffening between cracks, the nonlinear response of concrete in

compression and the yielding of the reinforcement are considered. The concrete model used is based upon nonlinear elasticity by assuming concrete to be an orthotropic material. A biaxial and a uniaxial concrete model are assumed for the shell and the beam element, respectively. The steel reinforcement is assumed to be in a uniaxial stress state and is modelled as a bilinear material with strain hardening. The nonlinear torsional response in the edge beam is modelled by an effective torsional stiffness approach where the Saint-Venant torsion is assumed.

An updated Lagrangian formulation has been used to take into account the nonlinear geometry of the structure. The formulation is based upon small strains and small incremental rigid body rotations.

An efficient procedure for the evaluation of creep strain based upon an integral formulation, in which the creep strain increment at the current time step requires the knowledge of the hidden state variables of only the last time step, is incorporated. The stress is assumed to be constant within a time step, and creep under biaxial stress states is represented via the introduction of the creep Poisson's ratio.

Finally, a series of numerical examples consisting of beams, columns, slabs and shells with or without edge members are analyzed and compared with the available theoretical and experimental results to demonstrate the applicability and the validity of the proposed method of analysis.

ACKNOWLEDGEMENTS

The author wishes to express his sincere gratitude to his research advisor, Professor A. C. Scordelis, for his constant guidance, constructive suggestions, criticisms, encouragement and patience throughout the course of this work. Professors G. H. Powell and R. S. Lehman are also thanked for serving on the Dissertation Committee. Thanks are also extended to Linda Calvin for her fast and accurate typing of the manuscript.

The research was sponsored by the National Science Foundation, under Grant No. CME 79-18057. The computer centers at the University of California and the Lawrence Berkeley Laboratory are acknowledged for providing the facilities for the numerical work.

Finally, the love, support, patience, understanding and encouragement of family and friends, especially the author's parents and wife have played a very major role in the completion of this work.

TABLE OF CONTENTS

Table of Contents (cont'd) Page

Table of Contents (cont'd) Page

Table of Contents (cont'd) Page

Table of Contents (cont'd) Page

Table of Contents (cont'd) Page

1. INTRODUCTION

1.1 General

A reinforced concrete shell has the qualities of an ideal structure. From an economical viewpoint, it requires the minimum material to cover a given area. From an architectural viewpoint, it is aesthetically appealing. From an engineering viewpoint, the structure is very strong and has a tremendous load-carrying capacity. It is for these reasons that reinforced concrete shells have found wide application for the roofs of sports arenas, exhibition halls, and other long-span roof structures.

Their design is usually based upon membrane theory and, to some extent, classical shell theory, assuming a linear, homogeneous, uncracked material. Even then, only simple geometries and loading conditions can be analyzed. Model testing can give an insight into the structural behavior, but it is a very costly and time-consuming procedure. The advent of the modern digital computer has made it possible to analyze shell structures of arbitrary geometry and boundary conditions under general loading.

To assess the factor of safety against collapse and satisfy the continuous demand for longer spans and thinner shells, the ultimate load capacity and the serviceability of the structure throughout its useful life have to be ensured. In this case, a linear analysis may not be sufficient.

While model testing of a scaled prototype remains costly and time-consuming, analytical procedures that can predict the nonlinear response and the ultimate load capacity of the prototype must be developed to replace most of the experiments once verification of the analytical

method has been established from selective, well-controlled experimental results.

The correct simulation of the structural response requires that the geometry of the shell and the supporting members be modelled correctly. Then, realistic material laws have to be defined for the concrete and the steel. The inclusion of the nonlinear geometry in the analysis is essential because it increases the load-carrying capacity in a stiffening structural system and decreases the ultimate load in a softening system. Finally, the time dependent effects of creep and shrinkage and of stress history have to be considered in order to ensure the serviceability and the ultimate load capacity, even with possible stress redistribution. The nonlinear geometry and the time dependent effects are often particularly important in the analysis of thin concrete shell structures.

1.2 Review of Literature

The first published paper on the finite element analysis of reinforced concrete structures was by Ngo and Scordelis [1]. They modelled the concrete and the steel by constant strain triangular elements and with special linkage elements to simulate the bond between the concrete and the steel. Linear analysis of simply supported beams with predefined crack patterns were carried out. Since then, a tremendous amount of effort has been devoted to the development of the analytical procedures for the analysis of plane stress, axisymmetric solid and plate and shell systems. No attempt is made here to review each of these in the literature. Comprehensive reviews of the application of finite element analysis of reinforced concrete structures were made by Scordelis [2,3,4], Schnobrich [5], and Wegner [6]. Here, only pertinent references dealing with the subject of general thin shells will be discussed.

Bell and Elms [7] used a reduced flexural and membrane stiffness approach, where the stiffness is a function of the stress level.

Lin [8,9] used a layered, triangular finite element to represent the concrete and the steel. A biaxial state of stresses was assumed for both the concrete and the steel. Nonlinearities of the concrete and steel were included.

Hand et al [10] used a layered, shallow shell, rectangular element and adopted an approach similar to Lin [8,9] for the analysis of plates and shells.

Kabir [11,12] extended the work of Lin [8,9] to include the time dependent effects of creep and shrinkage and load history.

Mueller [13,14] used the procedure developed by Kabir [11] to analyze and study several types of reinforced concrete hyperbolic paraboloid shells.

Arnesen [15] employed a triangular shell element with numerical integration through the thickness. He used endochronic theory for the concrete and a trilinear stress-strain law for the steel. Nonlinear geometry was included using an updated Lagrangian approach. Cyclic loading was also considered.

Floegl [16,17,18] used curved triangular shell finite elements to analyze reinforced concrete shells in short time loading. Both nonlinear material and nonlinear geometry were included. Their tension stiffening model is based upon bond slip between the reinforcement and the surrounding concrete.

Most of the previous researchers on the subject were concerned with the shell itself. Modelling of other important components of the structure, such as the edge and the supporting members, was not considered.

In the past, the edge members have been modelled with shell elements. This approach is satisfactory when the beam is concentric with the shell [8,11,13,15]. However, when the beam is placed eccentrically with the shell, the important bending contribution due to the axial forces cannot be accounted for. Furthermore, the use of the layered shell element cannot adequately represent the torsional and the biaxial bending behavior of the edge beam.

The use of curved shell finite elements generally gives a better geometrical representation, and the solution converges much faster than that using simple flat shell elements [19,20]. The use of a curved shell element, therefore, allows a relatively coarse mesh to be used to achieve a desired degree of accuracy. At the same time this reduces the storage requirement for the solution.

1.3 Objective and Scope of the Present Work

A numerical procedure is developed to trace the structural response of a thin concrete shell, having arbitrary geometry, through its elastic, inelastic and the ultimate load ranges.

A curved shell finite element is developed using numerical integration through the thickness to represent a special case of a 3D continuum. The steel reinforcement is treated as a smeared layer, and it can be oriented in any direction. A filamented reinforced concrete beam element is used to model either concentric or eccentric edge beams. Perfect bond between the concrete and steel is assumed.

The nonlinearities included are the cracking of the concrete in tension and the nonlinear response of concrete in compression, yielding of the reinforcement, time dependent effects of creep and shrinkage of the concrete under biaxial stress states, and the nonlinear geometry due

to finite displacements and rotations.

A tangent stiffness formulation coupled with a time integration solution is used. The iterative procedure utilizes constant imposed displacements and allows the complete load-displacement response to be traced, including the unstable branch in the snap-through of the structure.

Several examples have been solved. They can be classified into three categories. The first category is limited to structures with linear materials and large displacements so that the procedure for the treatment of the nonlinear geometry can be checked out. The second category is limited to reinforced concrete beams and plates with nonlinear materials and geometry. The third category includes complete systems made up of reinforced concrete shells and beams. The examples are compared with available analytical and experimental results to verify the proposed method of analysis.

2. LARGE DISPLACEMENT ANALYSIS

2.1 General

The problem involving large strains and large displacements has been thoroughly treated in the literature. Depending on the way the motion of a material point is described, the kinematics of a deformable body can be generally described in three distinctive modes. They are the Total Lagrangian (T.L.), the Updated Lagrangian (U.L.), and the Convective Description (C.D.).

Both the T.L. and the U.L. use a referential description in which the state variables are referred to a known configuration. Both formulations include all the geometric nonlinear effects through the coordinate transformation and the complete strain displacement relationships including the nonlinear terms. The two formulations are mathematically equivalent [21].

The Convective Description is also a referential description in the sense that the kinematic variables are referred to a set of convected axes while the displacements are referred to sets of material points. This formulation has often been used in solving small strain, large displacement problems [22,23,24,25,26], where the convected axes can be assumed to be orthogonal before and after deformation. In this case, the major geometric nonlinearities are embodied in the establishment of the convected axes, while retaining only linear terms in the strain expressions. For lower order elements, this formulation is very efficient because the displacements relative to some points can be easily established and also large rotations do not exist within an element. However, this is not true for higher order elements. In addition, the

transformation into and out of the convected coordinates is very time consuming [22] and thus cannot be justified from a computational standpoint. Therefore, the convected descriptive formulation will not be pursued further.

Before the equations of equilibrium are formulated, it would be worthwhile to present some of the necessary preliminaries in continuum mechanics. For this reason, the definition of stresses and strains will be reviewed briefly. More detailed description can be found in Malvern [27] and Fung [28].

2.2 Fundamentals of Continuum Mehcanics

2.2.1 Definition of Strains

Considering a body undergoing a deformation path (Fig. 2.1), the undeformed body is identified as B_0 with coordinates ${}^0x_i$, ${}^0z_i$ and base vector ${}^0g_i$. The current deformed body is B_1 with coordinates ${}^1x_i$, ${}^1z_i$ and base vector ${}^1g_i$. The next configuration close to B_1 is B_2 with coordinates ${}^2x_i$, ${}^2z_i$ and base vector ${}^2g_i$.

The deformation of a body can now be described. A generic point P undergoes translations and rotations and is finally deformed into configuration B_2.

In order to characterize the deformation, the Green strain tensor, E_{ij}, is introduced which is defined as $\frac{d\underset{\sim}{s} - d\underset{\sim}{s}_0}{d\underset{\sim}{s}_0}$, where $d\underset{\sim}{s}$ is the infinitesimal line element after deformation and $d\underset{\sim}{s}_0$ is the same line element before deformation. For small strains, the tensor E_{ij} is equivalent to the engineering strains [29].

The strain at configuration 1 is:

$$ {}^1E_{ij} = {}^1g_i \cdot {}^1g_j - {}^0g_i \cdot {}^0g_j $$

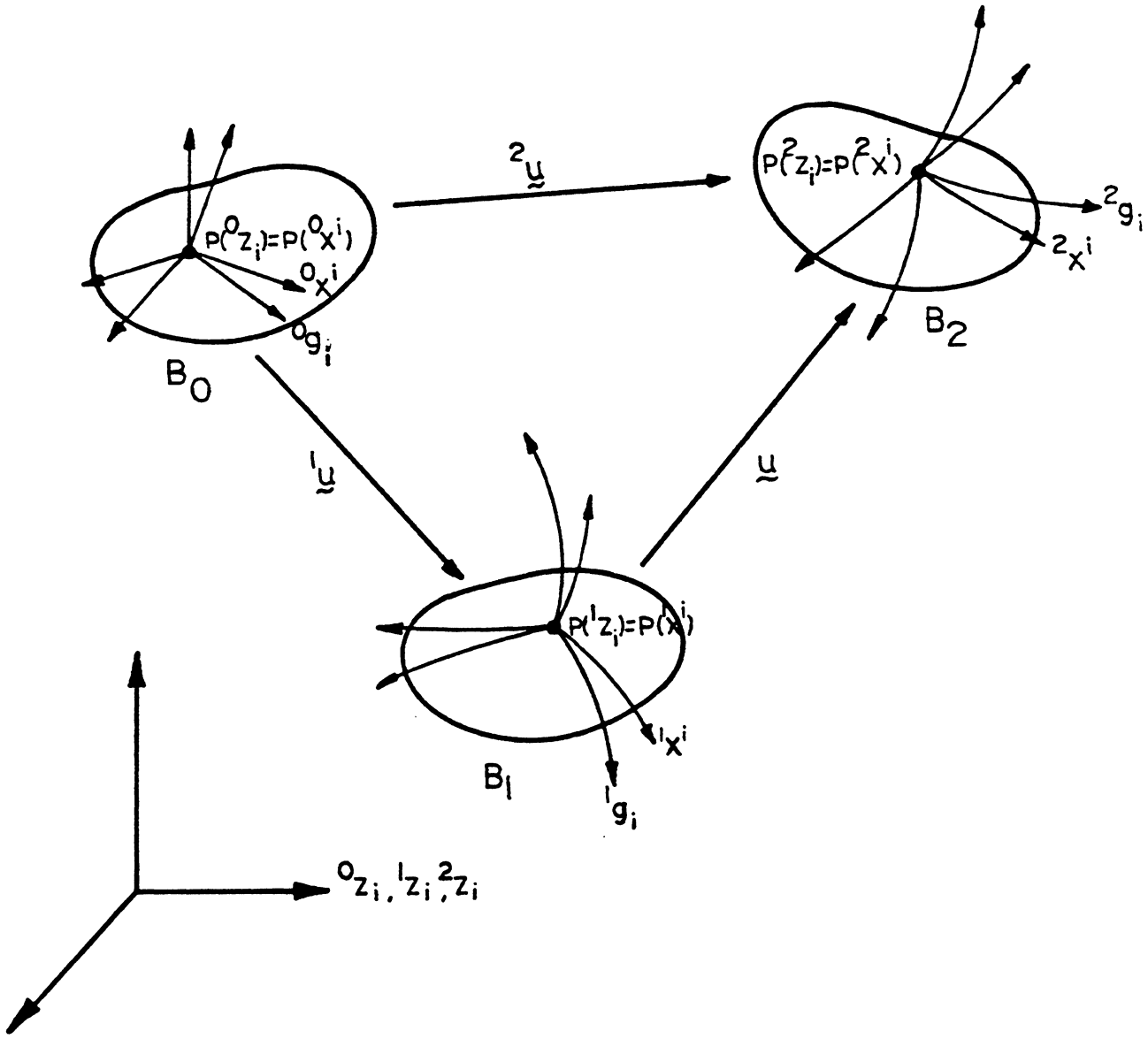

FIG. 2.1 DESCRIPTION OF THE KINEMATICS OF A DEFORMABLE BODY

where ${}^0g_i$ is chosen to be orthogonal. Therefore,

$$ {}^1E_{ij} = {}^1g_{ij} - \delta_{ij} \tag{2.1} $$

where ${}^1g_{ij}$ is the metric tensor defined as ${}^1g_i \cdot {}^1g_j$ and δ_{ij} is the Kronecker delta.

The base vector ${}^1g_i$ can be related to ${}^0g_i$ through the deformation gradient ${}^1F_{ij}$, where ${}^1F_{ij}$ maps ${}^0g_i$ into ${}^1g_i$. Mathematically, this is a linear transformation such that:

$$ {}^1g_i = {}^1F_{ij}\, {}^0g_j \tag{2.2} $$

Similarly, the strain at state 2 can be written down immediately following the definition of E_{ij}, Eq. 2.1.

$$ {}^2E_{ij} = {}^2g_i \cdot {}^2g_j - {}^0g_i \cdot {}^0g_j $$

$$ = {}^2g_{ij} - \delta_{ij} \tag{2.3} $$

$$ {}^2g_i = {}^2F_{ij}\, {}^0g_j \tag{2.4} $$

Now a functional dependence of the coordinates of the material points ${}^0z_i$, ${}^1z_i$ and ${}^2z_i$ has to be established.

$$ {}^1z_i = {}^0z_i + {}^1u_i $$

Together with the definition of the covariant base vector ${}^1g_i$:

$$ {}^1g_i = \frac{\partial}{\partial {}^0z_m}\, {}^0z_i\, {}^0g_m + \frac{\partial {}^1u_i}{\partial {}^0z_m}\, {}^0g_m $$

which can be simplified to:

$$ {}^1g_i = (\delta_{im} + {}^1u_{i,m})\, {}^0g_m $$

Therefore, the deformation gradient can now be defined as:

$$ {}^{1}F_{ij} = \delta_{ij} + {}^{1}u_{i,j} \tag{2.5} $$

and

$$ {}^{2}F_{ij} = \delta_{ij} + {}^{2}u_{i,j} \tag{2.6} $$

where ,j is understood to be the derivative with respect to the undeformed coordinates.

The strain increment E_{ij} can be obtained by subtracting the total strain at state 1 from the total strain at state 2,

$$ E_{ij} = {}^{2}E_{ij} - {}^{1}E_{ij} $$

or by introducing the deformation gradient:

$$ 2E_{ij} = {}^{2}F_{mi}\, i_m \cdot {}^{2}F_{nj}\, i_n - {}^{1}F_{mi}\, i_m \cdot {}^{1}F_{nj}\, i_n \tag{2.7} $$

However,

$$ {}^{2}u_i = {}^{1}u_i + u_i $$

Therefore,

$$ {}^{2}F_{ij} = \delta_{ij} + {}^{1}u_{i,j} + u_{i,j} \tag{2.8} $$

Introducing Eq. 2.8 into Eq. 2.7 and simplifying, one obtains the Lagrange strain increment referred to B_0 and expressed in terms of the displacement increments u_i.

$$ 2E_{ij} = u_{i,j} + u_{j,i} + {}^{1}u_{n,j}\, u_{n,i} + {}^{1}u_{n,i}\, u_{n,j} + u_{n,i}\, u_{n,j} \tag{2.9} $$

A similar expression for the increments of Lagrange strain ε_{ij} but referred to B_1 can be derived in a similar manner.

where $$2\varepsilon_{ij} = \overline{F}_{mi}\, i_m\, \overline{F}_{nj}\, i_n - \delta_{ij} \tag{2.10}$$

$$\overline{F}_{mi} = \delta_{mi} + u_{m,i} \tag{2.11}$$

and ,i denotes differentiation with respect to ${}^1z_i$. Upon substituting Eq. 2.11 into Eq. 2.10, one obtains:

$$2\varepsilon_{ij} = u_{i,j} + u_{j,i} + u_{n,i}\, u_{n,j} \tag{2.12}$$

It should be noticed that the Lagrange strain referred to B_1, Eq. 2.12, is not equal to the Lagrange strain referred to B_0 in Eq. 2.9. However, they are related through a geometrical transformation [30].

$$E_{ij} = \frac{\partial {}^1z_m}{\partial {}^0z_i}\, \frac{\partial {}^1z_n}{\partial {}^0z_j}\, \varepsilon_{mn} \tag{2.13}$$

The strains E_{ij} and ε_{ij} are used to derive the virtual work equation in the subsequent sections.

Equivalently, when the curvilinear coordinate x^i is used, the deformation gradient and the two Lagrange strains are related as follows:

$${}^1F^i_{.j} = \delta^i_{.j} + {}^1u^i|_j = \delta_{ij} + {}^1u_{i,j} \tag{2.14}$$

where ${}^0x^i$ is rectangular and $\delta^i_{.j} = \delta_{ij}$, ${}^1u^i|_j = {}^1u_{i,j}$.

$$\overline{F}^i_{.j} = \delta^i_{.j} + u^i|_j \tag{2.15}$$

where u^i is the displacement with reference to ${}^1x^i$.

$$2\varepsilon_{ij} = u^i|_j + u^j|_i + u^n|_i\, u^n|_j \tag{2.16}$$

$$E_{ij} = {}^1x^m|_i\, {}^1x^n|_j\, \varepsilon_{mn} \tag{2.17}$$

where $|_j$ denotes covariant derivatives.

2.2.2 Definition of Stresses

The stresses at a point P can be described in several ways depending on the basis of their reference. Generally, three different kinds of stresses can be distinguished. They are the 1st and the 2nd Piola-Kirchhoff stress and the Cauchy stress tensor.

Considering a typical deformation path, an undeformed body B_0, with base vector ${}^0g_i$, and a deformed body B_1, with base vector ${}^1g_i$ (Fig. 2.2), the equilibrium condition ignoring the body forces in the deformed configuration is:

$$\tau_{ij,j} = 0$$

where ,j is the derivative with respect to ${}^1z_i$ and τ_{ij} is the Cauchy stress defined as force per unit deformed area.

Defining a pseudo-force vector $\hat{\underset{\sim}{T}}$ in the undeformed body B_0 such that:

$$\hat{\underset{\sim}{T}}\, dA = \hat{\underset{\sim}{t}}\, da \qquad (2.18)$$

Using the Cauchy principle, Eq. 2.18 can be recast into:

$$T_{ij}\, N_i\, dA = \tau_{ij}\, n_i\, da$$

Introducing the Piola transformation of area [27,28],

$$n_i\, da = J\, f_{ji}\, N_j\, dA$$

where $J = \left(\det\left(\frac{\partial {}^0z_i}{\partial {}^1z_i}\right)\right)^{-1} = \frac{\rho_0}{\rho} = \frac{dv}{dV}$.

$$f_{ij} = \frac{\partial {}^0z_i}{\partial {}^1z_j}$$

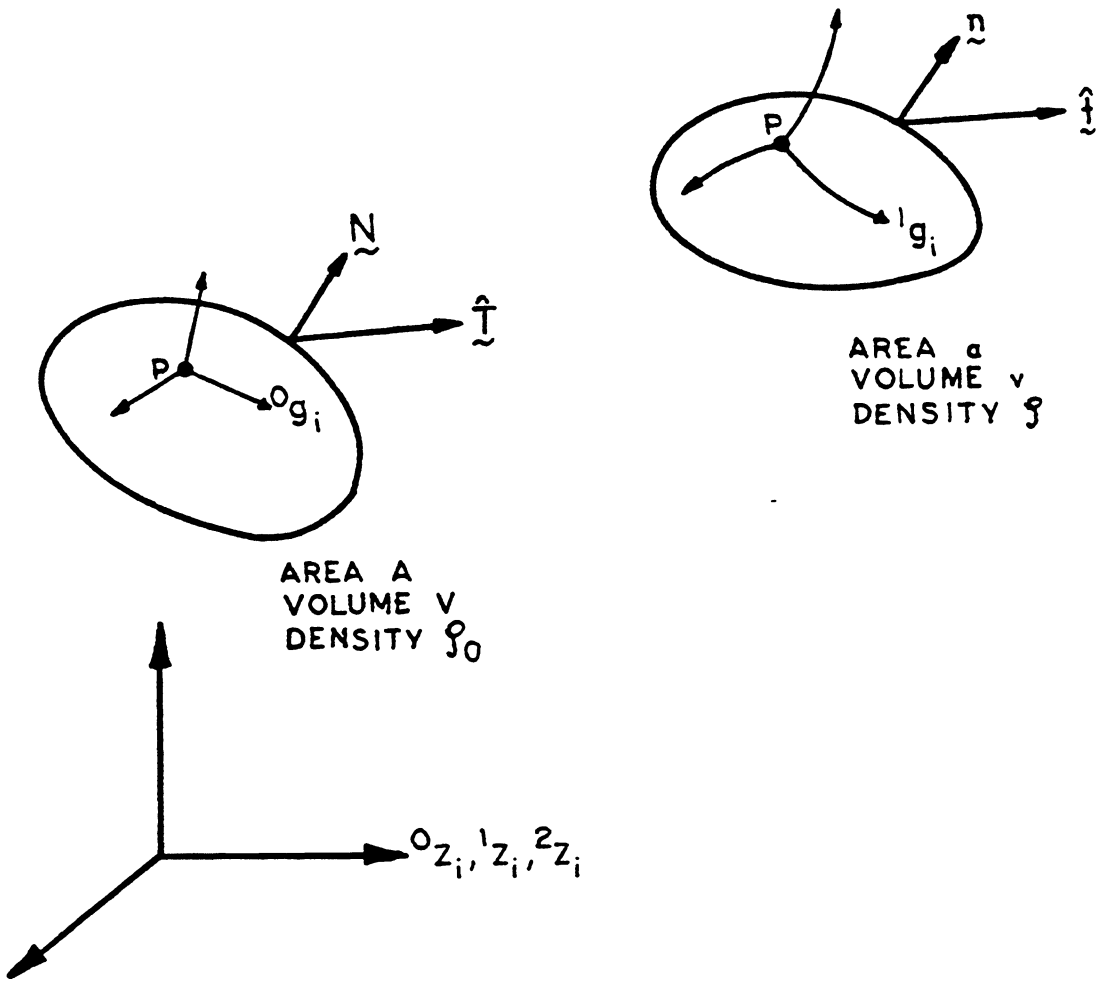

FIG. 2.2 DEFORMED AND UNDEFORMED BODY SHOWING TRUE STRESS VECTOR $\hat{t}$ AND PSEUDO STRESS VECTOR $\hat{T}$

Therefore,

$$T_{ij} = J f_{im} \tau_{mj} = J \frac{\partial^0 z_i}{\partial^1 z_m} \tau_{mj} \tag{2.19}$$

The tensor T_{ij} is associated with the name 1st Piola-Kirchhoff stress tensor. It can be interpreted as force per unit undeformed area acting in the direction of the deformed axes. Geometrically, it is illustrated in Fig. 2.3 together with the physical meaning of the Cauchy stresses. The tensor T_{ij} is therefore a tensor in two different spaces, namely the deformed axes and undeformed area and is, therefore, unsymmetric.

Because of the lack of symmetry of the 1st Piola-Kirchhoff stresses, a transformation of T_{ij} is performed to restore the symmetry condition. The resulting tensor denoted as S_{ij} is called the 2nd Piola-Kirchhoff stress tensor. Mathematically,

$$S_{ij} = T_{im} f_{mj}$$

or, in component form,

$$S_{ij} = J \frac{\partial^0 z_i}{\partial^1 z_m} \frac{\partial^0 z_j}{\partial^1 z_n} \tau_{mn} \tag{2.20}$$

Unlike T_{ij}, the tensor S_{ij} generally does not have a direct physical meaning and thus it is purely a mathematical definition, such that S_{ij} is conjugate to E_{ij} in the energy sense. That is, their products represent work [28].

2.3 Derivation of the Incremental Virtual Work Equation

With the preceding preliminaries, the virtual work equation can now be stated. The virtual work equation is based upon the minimum potential energy principle and represents a statement of equilibrium of a deformable

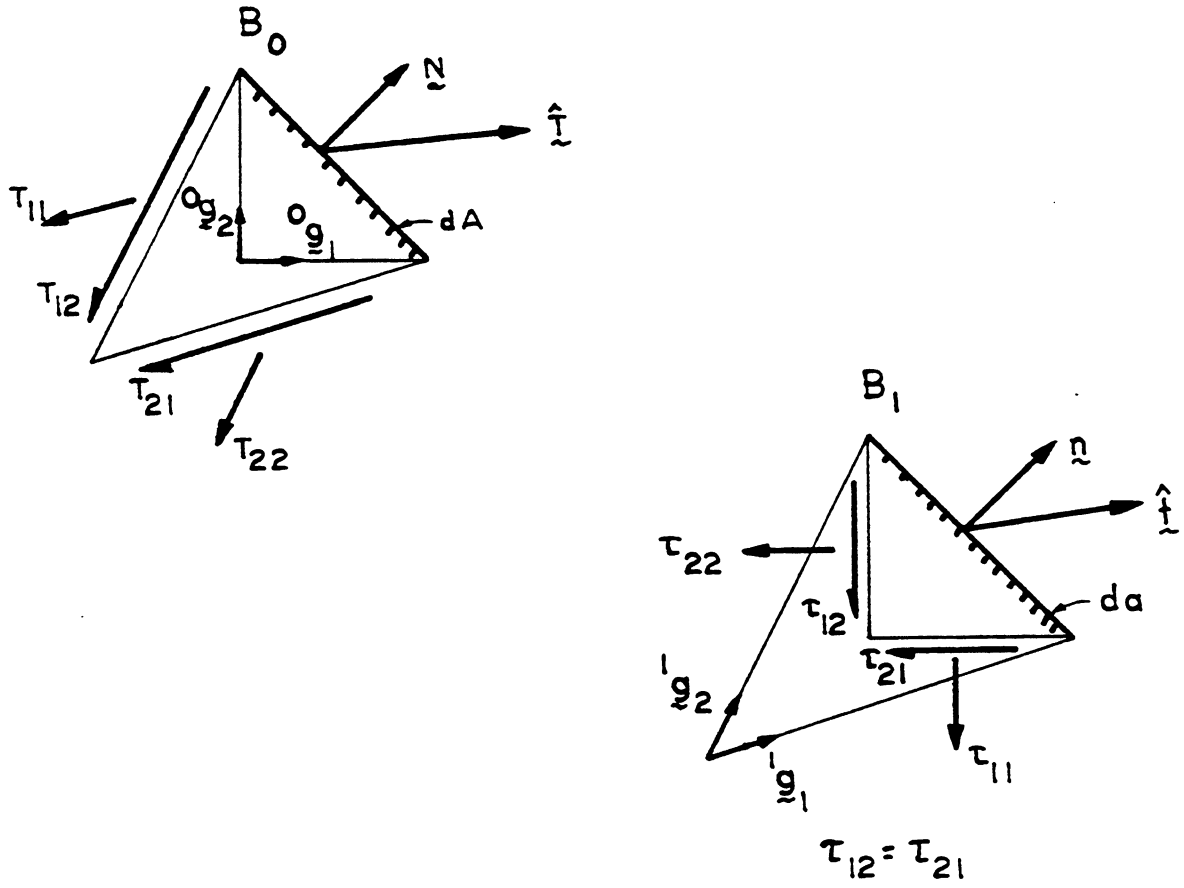

FIG. 2.3 GEOMETRICAL INTERPRETATION OF STRESSES

body. This equilibrium condition is valid in the current deformed configuration. Depending on which configuration the state variables are referred to, different forms of the equation can be obtained. However, they can be shown to be equivalent to each other [21,31]. In this section, the virtual work equation is written with reference to the undeformed configuration B_0 and the deformed configuration B_1, resulting in what is known as T.L. and U.L. formulations, respectively. The notation ${}^{\alpha}_{\beta}X$ used in the following derivation means the variable X at state α refers to state β.

2.3.1 Virtual Work Equation in T.L. Formulation

The internal work done in B_2 close to B_1 due to the deformation is:

$$W_I = \int_{B_0} {}^{2}_{0}S_{ij} \, {}^{2}_{0}E_{ij} \, dV$$

where the integral is performed over the undeformed body B_0.

The external work done by the surface traction ${}^{2}_{0}\underset{\sim}{t}$ is:

$$W_E = \int_{\partial B_0} {}^{2}_{0}\underset{\sim}{t} \; {}^{2}_{0}\underset{\sim}{u} \, dA$$

The potential energy Π of the system is:

$$\Pi = \int_{B_0} {}^{2}_{0}S_{ij} \, {}^{2}_{0}E_{ij} \, dV - \int_{\partial B_0} {}^{2}_{0}t_i \, {}^{2}_{0}u_i \, dA \qquad (2.21)$$

The equilibrium condition requires that the total potential energy of the system be stationary, i.e., $\delta\Pi = 0$.

$$\delta\Pi = \int_{B_0} {}^{2}_{0}S_{ij} \, \delta {}^{2}_{0}E_{ij} \, dV - \int_{\partial B_0} {}^{2}_{0}t_i \, \delta {}^{2}_{0}u_i \, dA = 0 \qquad (2.22)$$

where the traction ${}^{2}_{0}t_i$ is assumed to be a conservative load, for which its direction and magnitude remain constant throughout the deformation.

Alternatively, Eq. 2.22 can be derived by considering the equilibrium equation written in the deformed configuration with reference to the undeformed state and thus obtain the weak form of the equation [32]. However, this derivation will not be elaborated upon here.

Equation 2.22 is a total rather than an incremental formulation. In general, materials do exhibit path dependency to a certain extent. Therefore, an incremental form of the Eq. 2.22 will be more useful.

The decomposition of the stresses ${}^{2}_{0}S_{ij}$ and strains ${}^{2}_{0}E_{ij}$ are trivial and can be written as:

$$ {}^{2}_{0}S_{ij} = {}^{1}_{0}S_{ij} + \Delta_0 S_{ij} \tag{2.23} $$

$$ {}^{2}_{0}E_{ij} = {}^{1}_{0}E_{ij} + \Delta_0 E_{ij} \tag{2.24} $$

where ${}^{1}_{0}S_{ij}$ and ${}^{1}_{0}E_{ij}$ are the values at state 1 with reference to the undeformed state and $\Delta_0 S_{ij}$ and $\Delta_0 E_{ij}$ are increments from state 1 to state 2.

Equation 2.22 can now be written as:

$$ \int_{B_0} \left({}^{1}_{0}S_{ij} + \Delta_0 S_{ij} \right) \delta \left({}^{1}_{0}E_{ij} + \Delta_0 E_{ij} \right) dV = \int_{\partial B_0} {}^{2}_{0}t_i \; \delta \; {}^{2}_{0}u_i \; dA \tag{2.25} $$

Expanding and collecting terms and noting that ${}^{1}_{0}E_{ij}$ is not subjected to variation, Eq. 2.25 now becomes:

$$ \int_{B_0} {}^{1}_{0}S_{ij} \; \delta\Delta_0 E_{ij} + \Delta_0 S_{ij} \; \delta\Delta_0 E_{ij} \; dV = \int_{\partial B_0} {}^{2}_{0}t_i \; \delta \; {}^{2}_{0}u_i \; dA \tag{2.26} $$

Equation 2.26 is nonlinear in the displacement increments. A linearized form can be obtained by assuming a constitutive relationship of the form:

$$\Delta_0 S_{ij} = {}_0C_{ijkl}\, \Delta_0 e_{kl} \tag{2.27}$$

where $\Delta_0 e_{kl}$ is the linear part of the Lagrange strain increment.

$$\Delta_0 E_{ij} = \Delta_0 e_{ij} + \Delta_0 \eta_{ij}$$

and, in component form,

$$2\Delta_0 e_{ij} = \Delta u_{i,j} + \Delta u_{j,i} + {}^1u_{n,j}\, \Delta u_{n,i} + {}^1u_{n,i}\, \Delta u_{n,j} \tag{2.28}$$

$$2\Delta_0 \eta_{ij} = \Delta u_{n,i}\, \Delta u_{n,j} \tag{2.29}$$

By substituting Eq. 2.27, Eq. 2.28, and Eq. 2.29 into Eq. 2.26 and neglecting higher order terms, the linearized form of the equilibrium equation becomes:

$$\int_{B_0} \left({}^1_0S_{ij}\delta\Delta_0\eta_{ij} + {}_0C_{ijkl}\, \Delta_0 e_{kl}\, \delta\Delta_0 e_{ij} \right) dV = \int_{\partial B_0} {}^2_0t_i\, \delta {}^2_0u_i\, dA - \int_{B_0} {}^1_0S_{ij}\, \delta\Delta_0 e_{ij}\, dV \tag{2.30}$$

Equation 2.26 can now be satisfied by an iterative procedure where the piecewise linear solution of Eq. 2.30 is solved successively.

2.3.2 Virtual Work Equation in U.L. Formulation

The equilibrium equation governing the deformed state B_2 with reference to B_1 can be obtained from Eq. 2.22 by suitable transformations.

The equilibrium equation written with reference to the undeformed state B_0 is:

$$\int_{B_0} {}^2_0S_{ij}\, \delta {}^2_0E_{ij}\, dV - \int_{\partial B_0} {}^2_0t_i\, \delta {}^2_0u_i\, dA = 0 \tag{2.31}$$

The transformations are as follows:

$$ {}^{2}_{0}S_{ij} = \frac{\rho_0}{\rho_1} \frac{\partial {}^{0}z_i}{\partial {}^{1}z_m} \frac{\partial {}^{0}z_j}{\partial {}^{1}z_n} {}^{2}_{1}S_{mn} \tag{2.32} $$

$$ {}^{2}_{0}E_{ij} = \frac{\partial {}^{1}z_m}{\partial {}^{0}z_i} \frac{\partial {}^{1}z_n}{\partial {}^{0}z_j} {}^{2}_{1}E_{mn} \tag{2.33} $$

$$ dV = \frac{\rho_1}{\rho_0} dv \tag{2.34} $$

$$ {}^{2}_{0}t_i \, dA = {}^{2}_{1}t_i \, da \tag{2.35} $$

$$ \delta {}^{2}_{0}u_i = \delta {}^{2}_{1}u_i \tag{2.36} $$

Substituting Eq. 2.32 through Eq. 2.36 into Eq. 2.31, the equilibrium equation then becomes:

$$ \int_{\partial B_1} \frac{\rho_0}{\rho_1} \frac{\partial {}^{0}z_i}{\partial {}^{1}z_m} \frac{\partial {}^{0}z_j}{\partial {}^{1}z_n} {}^{2}_{1}S_{mn} \cdot \frac{\partial {}^{1}z_k}{\partial {}^{0}z_i} \frac{\partial {}^{1}z_l}{\partial {}^{0}z_j} \delta {}^{2}_{1}E_{kl} \cdot \frac{\rho_1}{\rho_0} dv = \int_{\partial B_1} {}^{2}_{1}t_i \, \delta {}^{2}_{1}u_i \, da $$

Noting that $\frac{\partial {}^{0}z_i}{\partial {}^{1}z_m} \cdot \frac{\partial {}^{1}z_k}{\partial {}^{0}z_i} = \delta_{mk}$ and $\delta_{mk} \, \delta_{nl} \, E_{kl} = E_{mn}$. The equation can now be simplified to:

$$ \int_{B_1} {}^{2}_{1}S_{mn} \, \delta {}^{2}_{1}E_{mn} \, dv = \int_{\partial B_1} {}^{2}_{1}t_i \, \delta {}^{2}_{1}u_i \, da \tag{2.37} $$

The incremental form of Eq. 2.37 can be obtained by a decomposition of the form:

$$ {}^{2}_{1}S_{ij} = {}^{1}_{1}\tau_{ij} + \Delta_1 S_{ij} \tag{2.38} $$

$$ {}^{2}_{1}E_{ij} = {}^{1}_{1}E_{ij} + \Delta_1 E_{ij} \tag{2.39} $$

where ${}^{1}_{1}\tau_{ij}$ and ${}^{1}_{1}E_{ij}$ are the stresses and strains at state 1 and $\Delta_1 S_{ij}$ and $\Delta_1 E_{ij}$ are the increments referred to state 1.

The equilibrium equation in the incremental form is:

$$ \int_{\partial B_1} \left({}^{1}_{1}\tau_{ij} + \Delta_1 S_{ij} \right) \delta \left({}^{1}_{1}E_{ij} + \Delta_1 E_{ij} \right) dv = \int_{\partial B_1} {}^{2}_{1}t_i \; \delta {}^{2}_{1}u_i \; da \tag{2.40} $$

and upon introducing the constitutive relationship:

$$ \Delta_1 S_{ij} = {}_1C_{ijkl} \, \Delta_1 e_{kl} \tag{2.41} $$

where

$$ \Delta_1 E_{kl} = \Delta_1 e_{kl} + \Delta_1 \eta_{kl} \tag{2.42} $$

$$ 2\Delta_1 e_{kl} = \frac{\partial u_k}{\partial {}^{1}z_l} + \frac{\partial u_l}{\partial {}^{1}z_k} $$

$$ 2\Delta_1 \eta_{kl} = \frac{\partial u_n}{\partial {}^{1}z_k} \cdot \frac{\partial u_n}{\partial {}^{1}z_l} $$

and upon expanding, the equation of equilibrium in the U.L. formulation after neglecting higher order terms is:

$$ \int_{B_1} {}^{1}_{1}\tau_{ij} \delta \Delta_1 \eta_{ij} + {}_1C_{ijkl} \Delta_1 e_{kl} \delta \Delta_1 e_{ij} \, dv = \int_{\partial B_1} {}^{2}_{1}t_i \; \delta {}^{2}_{1}u_i \; da - \int_{B_1} {}^{1}_{1}\tau_{ij} \delta \Delta_1 e_{ij} \, dv \tag{2.43} $$

Equations 2.43 and 2.30 are mathematically equivalent since they both represent the equilibrium of a body in the deformed state. The

choice between the U.L. and T.L. descriptions depends upon their relative numerical efficiency. This point will be discussed in more detail later in the chapter.

2.4 Large Displacements and Small Strains Problem

The definition of the stresses and strains in the case of large strains and large displacements problems have been stated in Section 2.2. Here some simplification will be made in the case where displacements are large while the strains remain small. This is a typical problem found in the stability of plates and shells and is particularly true for reinforced concrete structures whose crushing strain is of the order of 3.7×10^{-3}.

For the purpose of presentation, it would be useful to introduce the polar decomposition theorem [33] which asserts that a nonsingular matrix $\underset{\sim}{A}$ can be decomposed into an orthogonal matrix $\underset{\sim}{R}$ and a matrix $\underset{\sim}{\theta}$, such that:

$$\underset{\sim}{A} = \underset{\sim}{R}\,\underset{\sim}{\theta}$$

and

$$\underset{\sim}{\theta} = (\underset{\sim\sim}{A}\underset{\sim\sim}{A}^{T})^{\frac{1}{2}}$$

The deformation gradient F_{ij} defined in Eq. 2.5 can be similarly decomposed into:

$$F_{ij} = R_{ik}\,\theta_{kj} \tag{2.44}$$

where

$$\theta_{kj} = (F_{kn}\,F_{jn})^{\frac{1}{2}} = (C_{kj})^{\frac{1}{2}} \tag{2.45}$$

and C_{kj} is the deformation tensor such that:

$$2E_{ij} = C_{ij} - \delta_{ij}$$

If the strains are small, the tensor θ_{kj} can be expanded in the Taylor's series:

$$\theta_{kj} = (\delta_{ij} + 2E_{ij})^{\frac{1}{2}} \approx (\delta_{ij} + E_{ij} + 0E_{ij}^2) \tag{2.46}$$

It follows that if the rotations are large and the deformation is small, the latter can be ignored and:

$$F_{ij} \cong R_{ij} \tag{2.47}$$

In this case, no distinction has to be made between the derivative with respect to the deformed and the undeformed coordinates:

$$\frac{\partial {}^1z_i}{\partial {}^0z_j} = \frac{\partial {}^0z_j}{\partial {}^1z_i} \cong R_{ij} \tag{2.48}$$

or, in terms of curvilinear coordinates:

$$\frac{\partial {}^1x^i}{\partial {}^0x^j} = \frac{\partial {}^0x^j}{\partial {}^1x^i} \cong R^i_{\cdot j} \cong R_{ij} \tag{2.49}$$

The direct consequence of Eq. 2.48 and Eq. 2.49 is that under the assumption of small strains, the local coordinate axes ${}^1x^i$ remain essentially orthogonal and can be considered as ${}^0x^i$ being rigidly rotated as described by the rotation tensor R_{ij}. That is,

$${}^1x_i = R_{ij}\, {}^0x_i$$

In this case, the covariant derivative is identical to the ordinary derivative and no distinction needs to be made between the covariant base vector g_i or the contravariant base vector g^i. All the relationships as stated in the previous sections are valid in z_i as well as in x_i, except

that x_i now replaces z_i and the displacements are measured with respect to x_i.

Therefore, the relationship between E_{ij} and ε_{ij} as defined in Eq. 2.13 and Eq. 2.17 in Section 2.2.1 now reads:

$$E_{ij} = R_{mi} R_{nj} \varepsilon_{mn} \tag{2.50}$$

and the relationship between the 2nd Piola-Kirchhoff stress and the Cauchy stress tensor now becomes:

$$S_{ij} = J R_{mi} R_{nj} \tau_{mn} \tag{2.51}$$

where $J = \left|\frac{\partial {}^1x}{\partial {}^0x}\right| \cong 1$ for small strains.

Equations 2.50 and 2.51 simply imply that the E_{ij} and S_{ij}, when measured in the coordinate ${}^0x_i$, are identical numerically to the ε_{ij} and τ_{ij} with reference to ${}^1x_i$.

Under this assumption, the incremental values of ε_{ij} and τ_{ij} can be added from increment to increment without any geometrical transformation, provided that the local ${}^1x_i$ is computed consistently.

The virtual work equation in the T.L. and the U.L. formulations are mathematically equivalent. Any difference in the results can be attributed to the inconsistency in the use of the material tensor C_{ijkl} [21]. However, in the case of small strains the tensors ${}_0C_{ijkl}$ and ${}_1C_{ijkl}$, as defined in Eq. 2.27 and Eq. 2.41, are equal [31,34].

Under this assumption, Eq. 2.30 and Eq. 2.43 yield identical stiffness matrices and unbalanced nodal forces. A detailed discussion of these matters can be found in [31] and will not be elaborated upon here.

2.5 Choice of the Formulation

As has been stated in Section 2.3.2, the T.L. and U.L. are fundamentally equivalent. However, it is usually concluded that the U.L. is more efficient computationally [21,31]. This is due to the fact that in the U.L. formulation all the essential transformations are done at the element level and through the updating of the nodal point coordinates and the local axes. Thus the computation of the stiffness due to initial displacements can be avoided.

Also, by using the U.L. formulation, the problem of artificial straining which occurs with large rigid body rotations will be avoided. This problem has been thoroughly investigated by Søriede [35]. Essentially, the problem can be circumvented by splitting the large rigid body rotation into a series of smaller increments and the final solution is obtained by summation.

In the case of reinforced concrete structures where cracking is the predominant nonlinearity, the use of the local axes in the deformed state allows the modification of the material modulus easily. The cracks direction need not be transformed back to the undeformed configuration.

It is because of the numerical efficiency, the ease of implementation, and the accuracy that the U.L. formulation is chosen in the present study over the T.L. formulation.

3. MATERIAL MODELLING FOR THE REINFORCED CONCRETE

3.1 General

Reinforced concrete is a composite material made up of concrete and steel. The stress-strain relationship for steel is very well defined. Concrete, however, is heterogeneous and has completely different properties in tension and in compression. The properties of concrete are further complicated by its time dependent behavior, such as aging, creep, and shrinkage.

To model a reinforced concrete specimen, it is not only necessary to model the concrete and the steel correctly but their interaction as well. This involves the tension stiffening effect in concrete due to bond slip between the concrete and steel and the effect of dowel action and shear due to the reinforcement.

For reinforced concrete thin shell structures, the stress normal to the shell surface and the transverse shear is usually small; and it is therefore reasonable to assume a biaxial stress state exists in the concrete and the steel.

In this chapter, the short-time behavior of concrete under a biaxial stress state is discussed. The long-time behavior is presented in a separate chapter.

3.2 Concrete

3.2.1 Concrete in a Biaxial Stress State

Concrete is an anisotropic material, and its properties are significantly influenced by the presence of confinement. Figure 3.1 shows the results of a typical concrete specimen subjected to biaxial compression. It is observed that both an increase in strength and ductility

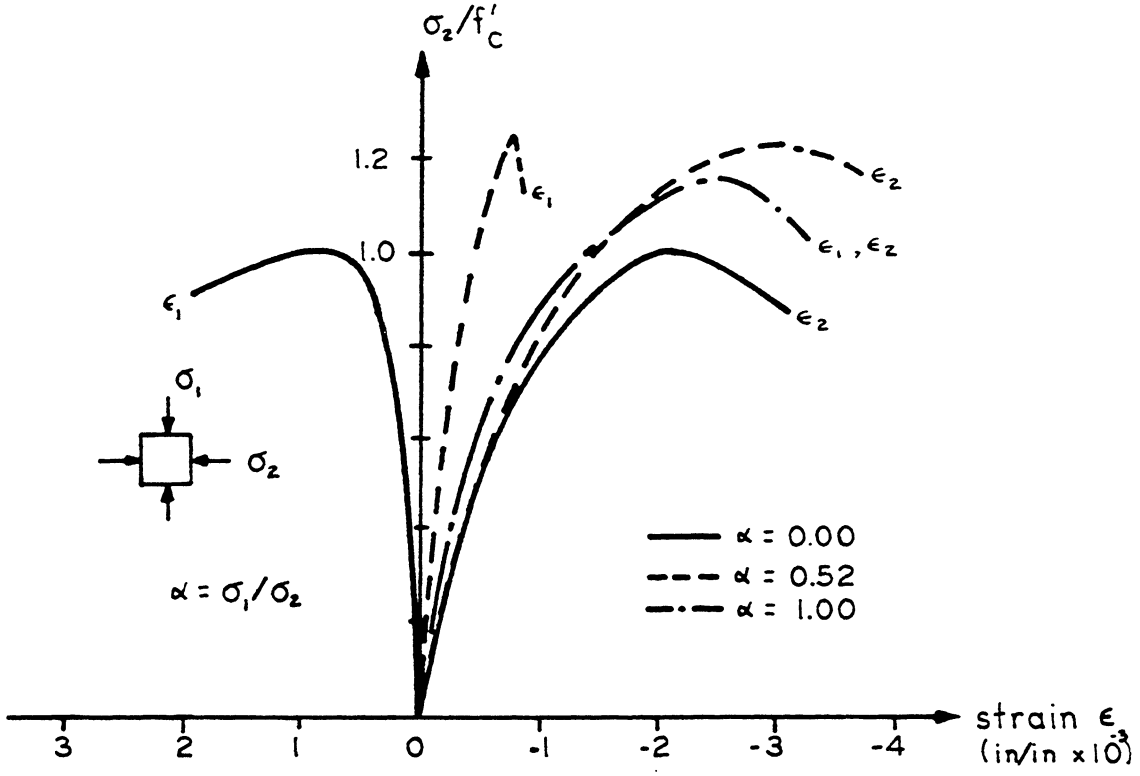

FIG. 3.1 EXPERIMENTAL STRESS-STRAIN CURVE FOR BIAXIAL COMPRESSION [36]

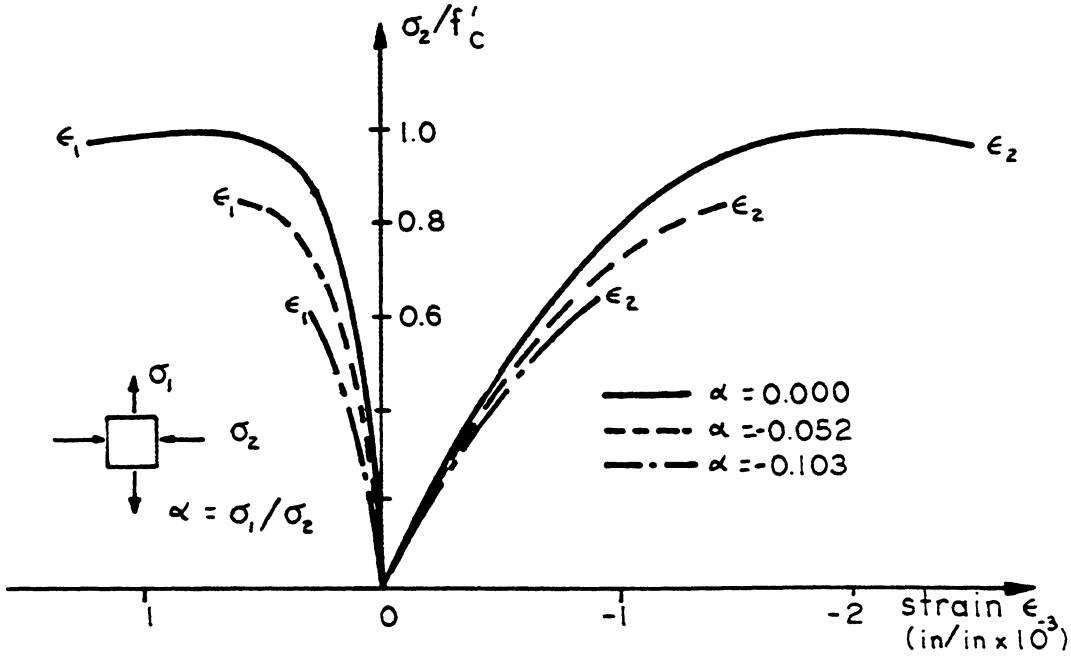

FIG. 3.2 EXPERIMENTAL STRESS-STRAIN CURVE FOR TENSION-COMPRESSION [36]

results due to the confinement of the orthogonal stress. For the case of tension-compression (Fig. 3.2), a substantial reduction in tensile strength results in the presence of the compressive stresses. Under biaxial tension, the tensile strength is independent of the stress ratio (Fig. 3.3).

Experimental investigations of the failure envelope of concrete under biaxial stress states have been reported by Kupfer et al [36]. They have used a special brush bearing which effectively eliminated the edge restraints. Their results cover the full range of biaxial stress states and are considered to be the most reliable test data available.

Figure 3.4 shows the biaxial strength envelope obtained by Kupfer et al [36]. A maximum increase in strength of 27% over the uniaxial compressive strength is observed and, for equal biaxial compression $\sigma_1 = \sigma_2$, a 16% strength increase is found.

Poisson's ratio for concrete also shows some dependency on the stress and the stress ratios. It increases towards the ultimate load. Kupfer et al [36] obtained a value of 0.2 for biaxial compression, 0.18 for biaxial tension, and a range from 0.18 to 0.2 for tension-compression. In general, a constant value of Poisson's ratio is usually assigned, ranging from 0.15 to 0.20.

3.2.2 Modelling of Concrete

Unlike most metals, concrete is not an isotropic or a homogeneous material. It is made up of cement, aggregate, and sand. Its properties are very much dependent on the proportion of each of its components; and furthermore, environmental factors and the method of loading play a very important role in its behavior. Therefore, it is only meaningful to model the macroscopic behavior of concrete rather than the microscopic

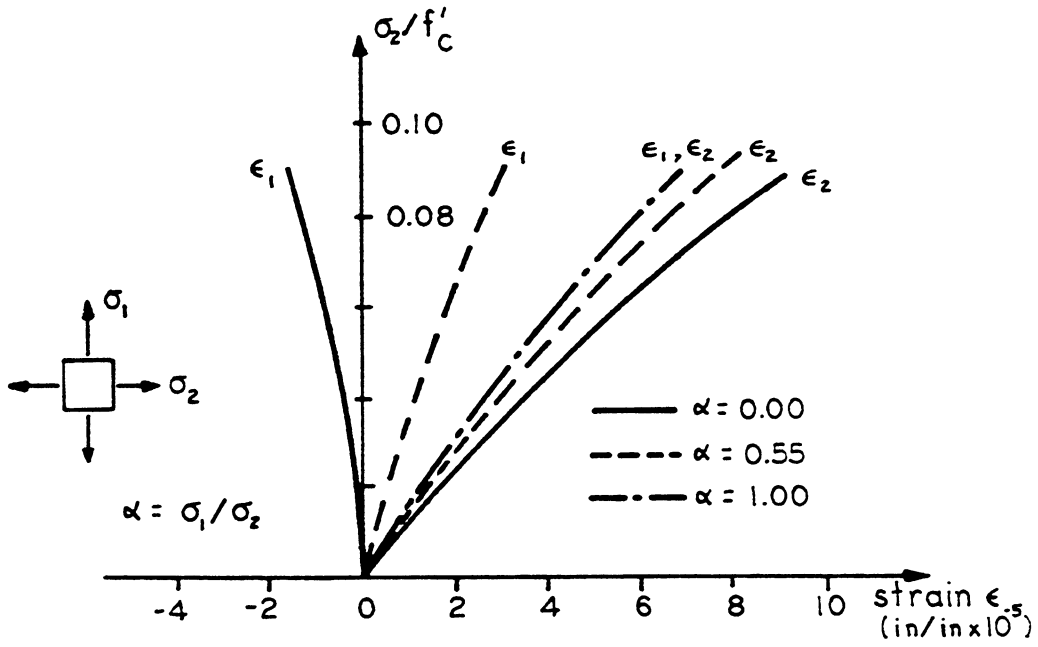

FIG. 3.3 EXPERIMENTAL STRESS-STRAIN CURVE FOR BIAXIAL TENSION [36]

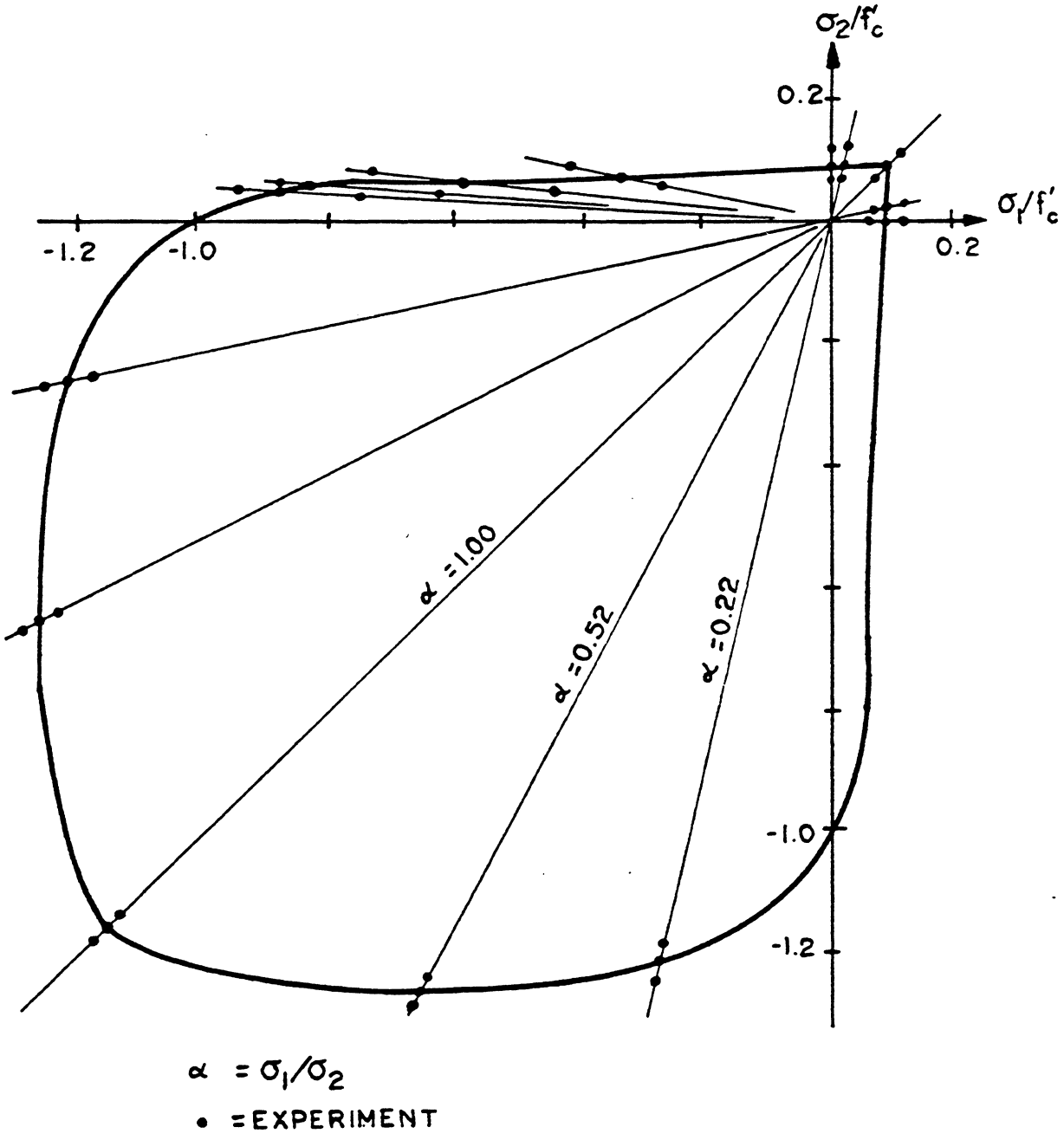

FIG. 3.4 EXPERIMENTAL BIAXIAL STRENGTH ENVELOPE OF PLAIN CONCRETE [36]

behavior of each individual component making up the concrete. Moreover, tests on concrete specimens show substantial scattering, and the correlation between the experimental and the analytical results always require some form of statistical averaging.

With the advent of modern computers and sophisticated analytical techniques for concrete structures, an intense research effort has been used recently to model the concrete under short-time loading for one, two or three-dimensional stress states. However, no general agreement has yet been obtained on the best approach to use. Excellent reviews on modelling the concrete material have been presented by Aoyama et al [37], Argyris et al [38], and in the book by Chen [39].

Most of the material models developed define the concrete using a single reference parameter, namely the uniaxial ultimate compressive strength f'_c. Other parameters that reflect the macroscopic behavior of concrete have also been used, such as the uniaxial tensile strength f'_t.

The majority of the formulations of concrete material models fall into one of the following three categories: (1) plasticity theory, (2) endochronic theory, and (3) nonlinear elasticity.

1. Plasticity Model

The plasticity model, originally developed for metals, has been extended to include concrete. The formulation involves the assumption of a flow rule, a yield surface, and in the case of hardening plasticity, an appropriate hardening rule. Due to the assumption of isotropy in the plasticity model, stress induced anisotropy and the effect of coupling at high stress levels cannot be included. Strain softening is generally not considered.

Chen and Chen [40] developed a 3D concrete model using a combination of kinematic and isotropic hardening. The failure of concrete is assumed

to depend on the hydrostatic and deviatoric stresses as expressed in terms of the first and second stress invariants, I_1 and J_2 respectively, where I_1 is the first stress invariant and J_2 is the second stress invariant of the stress deviator. The model is very dependent on the choice of the initial yield surface.

Epstein et al [41] developed a two parameter model for concrete under a biaxial stress state. The two parameters reflect the different properties of concrete in compression and in tension. Isotropic hardening is assumed and strain softening in compression and in tension are included.

Murray et al [42] extended the work of Epstein et al [41] and developed a three parameter model for concrete under a biaxial stress state. The model is primarily adopted to trace the post-cracking behavior in tension, with the two parameters describing the two principal tensile directions.

Buyukozturk [43] developed an elastic-plastic strain hardening model for concrete under a biaxial stress state. The Mohr-Coulomb failure criteria has been used for concrete in biaxial compression and tension-compression.

Lin [8] and Cervenka et al [44] assumed an elasto-plastic material with Von Mises yield criteria for concrete under biaxial compression. This represents the simplest model for concrete under a biaxial stress state.

2. Endochronic Theory

The endochronic theory developed for metals by Valanis [45] has been extended to concrete by Bazant [46,47]. The modifications include the hydrostatic pressure sensitivity, strain softening, and inelastic dilatancy due to shear.

The plastic strain increment is assumed to depend on a scalar parameter called "intrinsic time", which is a measure of the cumulative damage of the concrete. The intrinsic time is assumed to be a function of the increment of the second deviatoric stress invariant J_2.

The formulation utilizes the variable bulk and shear moduli. Stress induced anisotropy is included. Cyclic loading is also considered. The only input to the material model is the uniaxial compressive strength f'_c, and yet good agreement between experimental and analytical results is found.

3. Nonlinear Elasticity

This class of model either considers concrete to be an orthotropic material or an isotropic material with variable bulk and shear moduli. The orthotropic model generally assumes concrete to be hypoelastic, which characterizes concrete to be a path dependent and a reversible material.

It should be mentioned that the majority of the formulations in this class cannot be justified on a rigorous theoretical ground. For example, the invariant requirement is violated in some orthotropic models. The violation of the invariance is of little consequence when large rotations of the principal stress directions do not exist. This has happened for proportional loading on a structure. Nevertheless, this class of semi-empirical models is useful in reproducing the concrete macroscopic behavior once limited test results are available.

No attempt will be made here to review all the available models in this class. A comprehensive state-of-the-art report on orthotropic models has been presented in a committee report [48].

Liu et al [49] developed an orthotropic model which takes into account the Poisson's ratio effect and the effect of microcrack confinement.

The biaxial stress-strain relationship is described by a family of 1D stress-strain curves. The formulation relates the total stress and the total strain in the concrete.

Darwin et al [50] employed a different approach than Liu et al [49] and related the incremental stresses to the incremental strains. The use of an equivalent uniaxial strain allows the separation of confinement effect and the Poisson's effect and represents a convenient measure of the damage to the concrete. The concrete stresses and the moduli are then related to the equivalent uniaxial strains through the use of Saenz's equation [51]. The incremental formulation has made it possible to include the effect of stress history on the current material properites and characterizes concrete as a truly path dependent material.

Bashur et al [52] adopted the model of Darwin et al [50] and developed a moment-curvature relationship for reinforced concrete plates.

Elwi et al [53] extended the work of Darwin et al [50] and developed a 3D hypoelastic concrete model for the analysis of axisymmetric solids.

Ottosen [54] developed a triaxial concrete model for short-time loading. The model utilizes variable secant Young's moduli and variable Poisson's ratio governing the strain softening. The damage to the concrete is measured by the nonlinearity index defined as the ratio of the algebraic minimum principal stress to the minimum stress at failure. Unlike other orthotropic models, the dilation due to compression is included, and the failure is defined in terms of the three deviatoric stress invariants, J_1, J_2, and J_3. The uniaxial stress-strain curve proposed by Sargin [55] is also used.

Kupfer et al [56] proposed variable secant bulk and shear moduli as well as tangent bulk and shear moduli approaches for the modelling of

concrete. A more rigorous formulation for the tangent bulk and shear moduli was recently proposed by Murray [57].

Cedolin et al [58], by analyzing a large amount of experimental data, obtained a set of empirical equations governing failure and the variation of the tangent bulk and shear moduli with the octahedral normal and shear strains.

By defining the ultimate strength as the state at which the volume of the concrete is minimum, Kotsovos et al [59] obtained a lower bound solution for the strength of concrete. The stress-strain relationship is also expressed in terms of variable bulk and shear moduli.

Romstad et al [60] adopted a different approach involving weighting and averaging of the material moduli and Poisson's ratio. The cumulative damage to the concrete is replaced by four damaged regions in which constant parameters are assumed. The formulation is of the incremental form.

Noguchi [61] compared the model based upon classicial plasticity theory using Drucker-Prager's yield criterion and four other biaxial models with the tests of Kupfer [36] and Nelissen [62] and concluded that the plasticity model cannot represent the nonlinear behavior of concrete adequately, especially in biaxial compression with a large value of the stress ratio and at high stress levels. He also concluded that the orthotropic material model of Darwin et al [50] gives the best results in both principal directions among the concrete models he considered.

It is believed that for a lightly reinforced concrete, the majority of the material nonlinearity arises from cracking of the concrete at low tensile stresses. Therefore, it is questionable whether a more sophisticated concrete model than Darwin's would yield a much better result. Consequently, in this study, the model of Darwin et al [50] will be used

with some modifications. The same model has been used by Kabir [11] and Van Gruenen [26], and the results they obtained without significant increase in the computational effort are improvements to those obtained by Lin [8] using a simpler model.

3.2.3 Concrete Model for the Present Study

(a) Stress-Strain Relationship

Under a biaxial stress state, the incremental constitutive relationship in the orthotropic directions 1 and 2 for an orthotropic material can be written as:

$$\begin{bmatrix} d\varepsilon_1 \\ d\varepsilon_2 \\ d\varepsilon_{12} \end{bmatrix} = \begin{bmatrix} E_1^{-1} & -\nu_{12}E_2^{-1} & 0 \\ -\nu_{21}E_1^{-1} & E_2^{-1} & 0 \\ 0 & 0 & G_{12}^{-1} \end{bmatrix} \begin{bmatrix} d\sigma_1 \\ d\sigma_2 \\ d\sigma_{12} \end{bmatrix} \qquad (3.1)$$

Using the symmetry condition of $\nu_{12}E_1 = \nu_{21}E_2$, Eq. 3.1 can be rewritten as:

$$\begin{bmatrix} d\varepsilon_1 \\ d\varepsilon_2 \\ d\varepsilon_{12} \end{bmatrix} = \begin{bmatrix} E_1^{-1} & -\sqrt{\nu_{12}\nu_{21}}E_1^{-1}E_2^{-1} & 0 \\ & E_2^{-1} & 0 \\ \text{SYMM.} & & G_{12}^{-1} \end{bmatrix} \begin{bmatrix} d\sigma_1 \\ d\sigma_2 \\ d\sigma_{12} \end{bmatrix} \qquad (3.2)$$

Inverting Eq. 3.2, the result is:

$$\begin{bmatrix} d\sigma_1 \\ d\sigma_2 \\ d\sigma_{12} \end{bmatrix} = \frac{1}{1-\nu_{12}\nu_{21}} \begin{bmatrix} E_1 & \sqrt{\nu_{12}\nu_{21}}\sqrt{E_1E_2} & 0 \\ & E_2 & 0 \\ \text{SYMM.} & & (1-\nu_{12}\nu_{21})G_{12} \end{bmatrix} \begin{bmatrix} d\varepsilon_1 \\ d\varepsilon_2 \\ d\varepsilon_{12} \end{bmatrix} \qquad (3.3a)$$

Upon transforming to arbitrary coordinate axes x,y:

$$\begin{bmatrix} d\sigma_{xx} \\ d\sigma_{yy} \\ d\sigma_{xy} \end{bmatrix} = \frac{1}{1-\nu_{12}\nu_{21}} \begin{bmatrix} E_1C^2+E_2S^2 & \sqrt{\nu_{12}\nu_{21}}\sqrt{E_1E_2} & \frac{1}{2}(E_1-E_2)CS \\ & E_1S^2+E_2C^2 & \frac{1}{2}(E_1-E_2)CS \\ \text{SYMM.} & & G' \end{bmatrix} \begin{bmatrix} d\varepsilon_{xx} \\ d\varepsilon_{yy} \\ d\varepsilon_{xy} \end{bmatrix} \quad (3.3b)$$

where $C = \cos\theta$ and $S = \sin\theta$, with θ the angle between the x axis and the orthotropic 1-direction.

$$G' = \frac{1}{4(1-\nu_{12}\nu_{21})} (E_1 + E_2 - 2\sqrt{\nu_{12}\nu_{21}}\sqrt{E_1E_2})$$

is the shear modulus which is invariant under the transformation of axes [50,53].

Equation 3.3 can be rearranged to:

$$\begin{bmatrix} d\sigma_1 \\ d\sigma_2 \\ d\sigma_{12} \end{bmatrix} = \begin{bmatrix} E_1 & 0 & 0 \\ 0 & E_2 & 0 \\ 0 & 0 & (1-\nu_{12}\nu_{21})G'_{12} \end{bmatrix} \begin{bmatrix} d\varepsilon_{1u} \\ d\varepsilon_{2u} \\ d\varepsilon_{12} \end{bmatrix} \quad (3.4)$$

where the increment of equivalent uniaxial strain $d\varepsilon_{1u}$ and $d\varepsilon_{2u}$ are defined:

$$d\varepsilon_{1u} = \frac{1}{1-\nu_{12}\nu_{21}} d\varepsilon_1 + \frac{\sqrt{\nu_{12}\nu_{21}}\sqrt{E_2}}{(1-\nu_{12}\nu_{21})\sqrt{E_1}} d\varepsilon_2 \quad (3.4a)$$

$$d\varepsilon_{2u} = \frac{\sqrt{\nu_{12}\nu_{21}}\sqrt{E_1}}{(1-\nu_{12}\nu_{21})\sqrt{E_2}} d\varepsilon_1 + \frac{1}{1-\nu_{12}\nu_{21}} d\varepsilon_2 \quad (3.4b)$$

Substituting $d\varepsilon_1 = \frac{d\sigma_1}{E_1} - \nu_{12}\frac{d\sigma_2}{E_2}$ and $d\varepsilon_2 = \frac{d\sigma_2}{E_2} - \nu_{21}\frac{d\sigma_1}{E_1}$ with $\nu_{12}E_1 = \nu_{21}E_2$, Eq. 3.4a and Eq. 3.4b can be rewritten as:

$$d\varepsilon_{1u} = \frac{d\varepsilon_1}{1-\nu_{12}\,\alpha n} \tag{3.5a}$$

$$d\varepsilon_{2u} = \frac{d\varepsilon_2}{1-\nu_{21}\,\alpha n} \tag{3.5b}$$

where $\alpha = d\sigma_1/d\sigma_2$ and $n = E_2/E_1$.

Equation 3.4 suggests a set of uniaxial stress-strain relationships in which the stress is related to the equivalent uniaxial strains $d\varepsilon_{1u}$ and $d\varepsilon_{2u}$. E_1 and E_2 include the effects of confinement but not of Poisson's ratio, which is removed through the use of the equivalent uniaxial strain. A family of such curves can then be constructed from biaxial test data.

Computationally, the increment of the equivalent uniaxial strain $d\varepsilon_{iu}$ is:

$$d\varepsilon_{iu} = \frac{d\sigma_i}{E_i} \qquad i = 1,2 \tag{3.6}$$

and the total equivalent uniaxial strain is then obtained by summation along the deformation path:

$$\varepsilon_{iu} = \sum \frac{\Delta\sigma_i}{E_i} \qquad i = 1,2 \tag{3.7}$$

Equation 3.7 characterizes concrete as a path dependent material.

Darwin et al [50] proposed the use of an equivalent uniaxial stress-strain curve for the biaxial stress state. A typical curve is shown in Fig. 3.5.

In the compressive portion, the curve is described by the Saenz's equation [51]:

$$\sigma_i = \frac{E_o\varepsilon_{iu}}{1 + \left(\frac{E_o}{E_S} - 2\right)\left(\frac{\varepsilon_{iu}}{\varepsilon_{ic}}\right) + \left(\frac{\varepsilon_{iu}}{\varepsilon_{ic}}\right)^2} \tag{3.8}$$

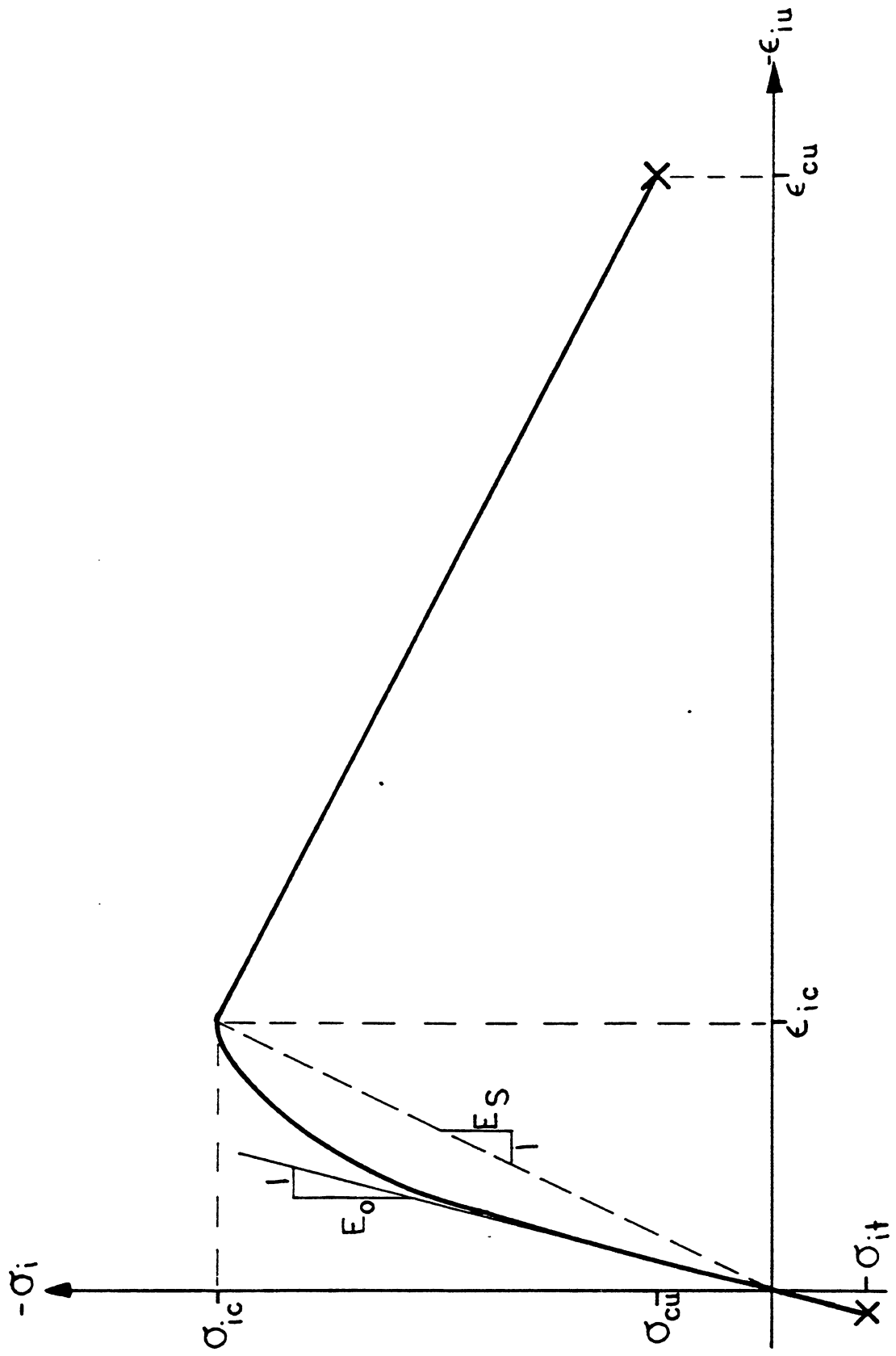

FIG. 3.5 EQUIVALENT UNIAXIAL STRESS-STRAIN CURVE

where $E_S = \frac{\sigma_{ic}}{\varepsilon_{ic}}$;

$\sigma_{ic}, \varepsilon_{ic}$ are maximum compressive stress and the corresponding strain in the direction i; and

ε_{iu} is the equivalent uniaxial strain in the direction i.

In tension, the relationship is linear:

$$\sigma_i = E_o \varepsilon_{iu} \quad \text{for} \quad \sigma_i \leq \sigma_{it}$$

where σ_{it} is the tensile strength in the direction i.

The value of σ_{ic}, σ_{it}, ε_{ic} can be determined from tests.

Beyond the maximum compressive strength, strain softening occurs, and the concrete is finally crushed at a stress of σ_{cu} and a corresponding strain of ε_{cu}.

The modulus of elasticity E_i in the compressive portion can be obtained by differentiating Eq. 3.8 with respect to ε_{iu} and:

$$E_i = \frac{\partial \sigma_i}{\partial \varepsilon_{iu}} = \frac{E_o(1 - q^2)}{\left[1 + \left(\frac{E_o}{E_S} - 2\right) q + q^2\right]} \tag{3.9}$$

$$q = \frac{\varepsilon_{iu}}{\varepsilon_{ic}}$$

For tension with $\sigma_i \leq \sigma_{it}$, $E_i = E_o$.

In the present study, the biaxial strength envelope of Kupfer et al [36] is used to find the maximum stresses σ_{ic} and the corresponding strain ε_{ic}. The biaxial strength envelope is divided into four different regions (Fig. 3.6), depending on the biaxial stress ratio α, where $\alpha = \sigma_1/\sigma_2$ and σ_1 is algebraically greater than σ_2.

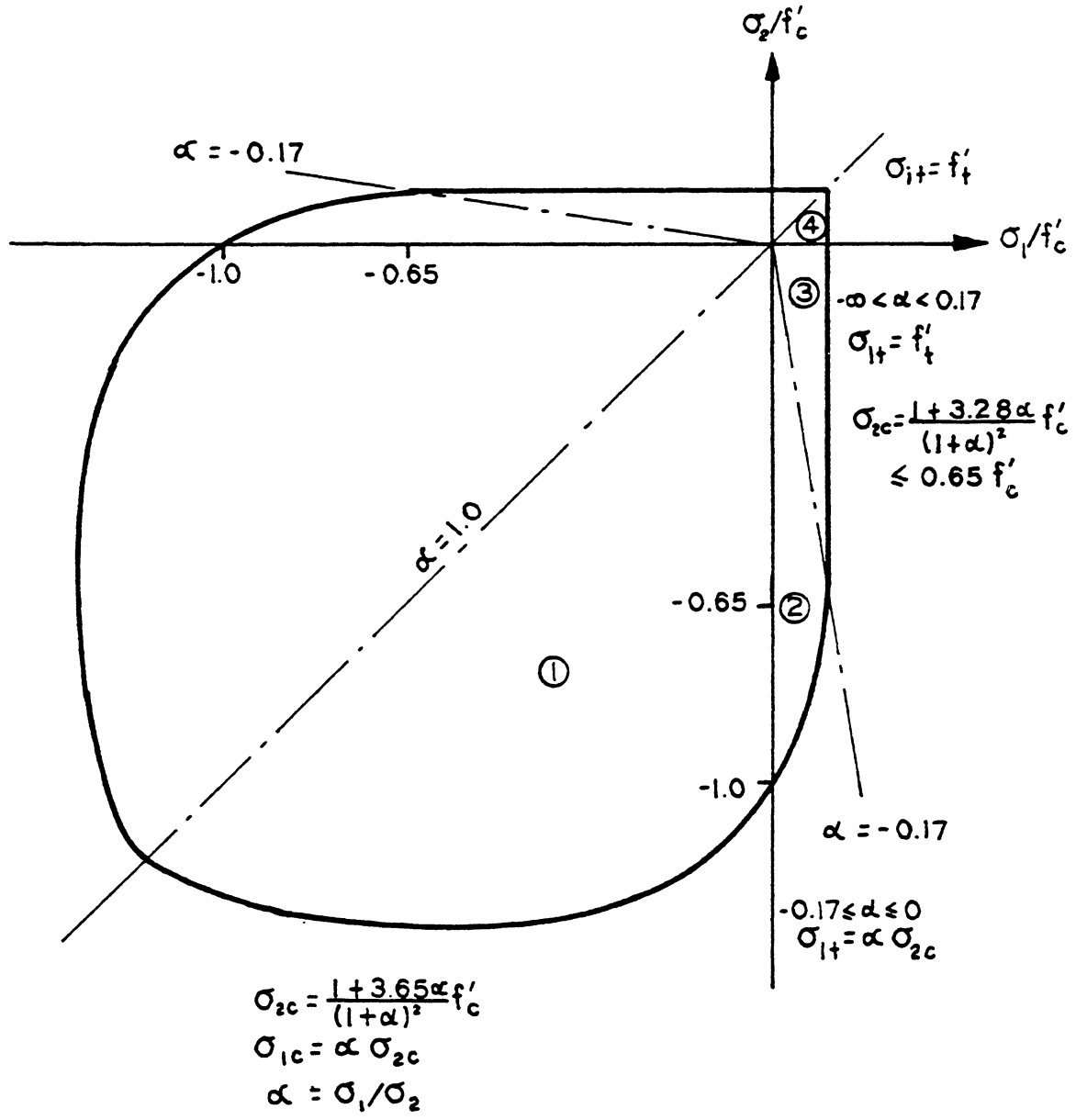

FIG. 3.6 BIAXIAL STRENGTH ENVELOPE USED IN THE PRESENT STUDY

The different regions are:

1. Biaxial compression, σ_1 = compression, σ_2 = compression, $0 \leq \alpha \leq 1$.

$$\sigma_{2c} = \frac{1 + 3.65\alpha}{(1 + \alpha)^2} f'_c \tag{3.10a}$$

$$\sigma_{1c} = \alpha\sigma_{2c} \tag{3.10b}$$

$$\varepsilon_{2c} = \varepsilon_c [3p_2 - 2] \tag{3.11a}$$

$$\varepsilon_{1c} = \varepsilon_c [-1.6\, p_1^3 + 2.25\, p_1^2 + 0.35\, p_1] \tag{3.11b}$$

$$p_1 = \sigma_{1c}/f'_c \quad \text{and} \quad p_2 = \sigma_{2c}/f'_c$$

Equation 3.10 is based upon the biaxial strength envelope of Kupfer et al [36], while Eq. 3.11 was proposed by Darwin et al [50]. Concrete in this region is assumed to yield beyond maximum compressive strength and finally fail by crushing of the concrete.

2. Tension-compression, σ_1 = tension, σ_2 = compression, $-0.17 \leq \alpha \leq 0$.

$$\sigma_{2c} = \frac{1 + 3.28\alpha}{(1 + \alpha)^2} f'_c \tag{3.12a}$$

$$\sigma_{1t} = \alpha\sigma_{2c} \tag{3.12b}$$

$$\varepsilon_{2c} = \varepsilon_c [4.42 - 8.38\, p_2 + 7.54\, p_2^2 - 2.58\, p_2^3] \tag{3.13a}$$

$$\varepsilon_{1t} = \sigma_{1t}/E_o \tag{3.13b}$$

and

$$p_2 = \sigma_{2c}/f'_c \,.$$

Darwin suggested Eq. 3.12 while Eq. 3.13 was proposed by Rajagopal [63]. Failure in this region is by yielding and crushing of the concrete.

3. Tension-compression, σ_1 = tension, σ_2 = compression, $-\infty < \alpha < -0.17$.

$$\sigma_{2c} = 0.65\, f'_c \tag{3.14a}$$

$$\sigma_{1t} = f'_t \tag{3.14b}$$

$$\varepsilon_{2c} = \varepsilon_c \left[4.42 - 8.38\, p_2 + 7.54\, p_2^2 - 2.58\, p_2^3\right] \tag{3.15a}$$

$$p_2 = \sigma_{2c}/f'_c \leq 0.65$$

$$\varepsilon_{1t} = \sigma_{1t}/E_o \tag{3.15b}$$

Failure is assumed to be caused by cracking of the concrete in the 1-direction and yielding in the 2-direction.

4. Biaxial tension, σ_1 = tension, σ_2 = tension, $1 < \alpha < \infty$.

$$\sigma_{1t} = \sigma_{2t} = f'_t \tag{3.16a}$$

$$\varepsilon_{1t} = \varepsilon_{2t} = f'_t/E_o \tag{3.16b}$$

Failure occurs in the i direction once the maximum tensile strength σ_{it} is exceeded.

The necessary input data to describe the model completely are the (1) uniaxial compressive strength f'_c; (2) uniaxial tensile strength; (3) initial uniaxial modulus of elasticity; (4) the strain at uniaxial compressive strength; (5) the strain at crushing; (6) the stress at crushing; and (7) Poisson's ratio. These values can be obtained from

tests. However, in the absence of test data, ACI Committee 209 [64] recommends the following values at time t:

$$E_o(t) = 33.0\ w^{1.5}\sqrt{f'_c(t)}$$

$$f'_c(t) = \frac{t}{4 + 0.85t}\ f'_c(28)$$

$$f'_t(t) = 1/3\ \sqrt{wf'_c(t)}$$

where

w = weight per unit volume in pcf

t = days after casting

$f'_c(28)$ = uniaxial compressive strength in psi at 28 days

$f'_t(28)$ = tensile strength in psi

Hognestad [65] suggested that strain $\varepsilon_c(t)$ at maximum uniaxial compressive strength at time t:

$$\varepsilon_c(t) = 2f'_c(t)/E_o(t)$$

The strain and the corresponding stress at crushing show substantial scattering in the test results depending on the method of loading. In the present study, the crushing strain ε_{cu} and the corresponding stress are assumed to be:

$$\varepsilon_{cu} = 4\ \varepsilon_{ic}(t)$$

$$\sigma_{cu} = 0.2\ f'_c(t)$$

A Poisson's ratio of 0.15 is generally assumed in the present study.

(b) Strain Softening in Compression

Beyond the maximum compressive stress σ_{ic}, the stress in the concrete decreases with an increase in strain causing yielding. This will result in unloading in the concrete until it crushes at the strain ε_{cu}.

In the present study, a linear unloading curve based on the envelope curve obtained from uniaxial cyclic load tests of Karsan and Jirsa [66] is used. Figure 3.7 shows a typical strain softening curve beyond the maximum stress σ_{ic}. At a strain $\varepsilon_{iu} < \varepsilon_{ic}$, the stress in the concrete is $\sigma_{ic} + \frac{\sigma_{cu} - \sigma_{ic}}{\varepsilon_{cu} - \varepsilon_{ic}} (\varepsilon_{iu} - \varepsilon_{ic})$. The modulus of elasticity is assumed to be zero to avoid numerical difficulty in using a negative stiffness.

It should be noted that the unconstrained flow rule is used once the concrete yields.

$$d\underset{\sim}{\sigma} = \underset{\sim}{Q}\, d\underset{\sim}{\varepsilon} \tag{3.17}$$

Lin [8] used both the unconstrained flow rule and the associated flow rule with Von Mises yield criterion and found little difference in the results. Therefore, the same unconstrained flow rule is adopted in this study.

(c) Stress Reversal and Concrete States

To account for the unloading due to creep and shrinkage and the load history, a simple stress reversal model is adopted. It is assumed that unloading and reloading take place with the initial stiffness of concrete E_o. Cyclic loading is not considered.

Figure 3.8 illustrates the different possible states of the concrete.

(1) Tension in the primary path.

(2) Compression in the primary path.

(3) Unloading or reloading in compression before yield.

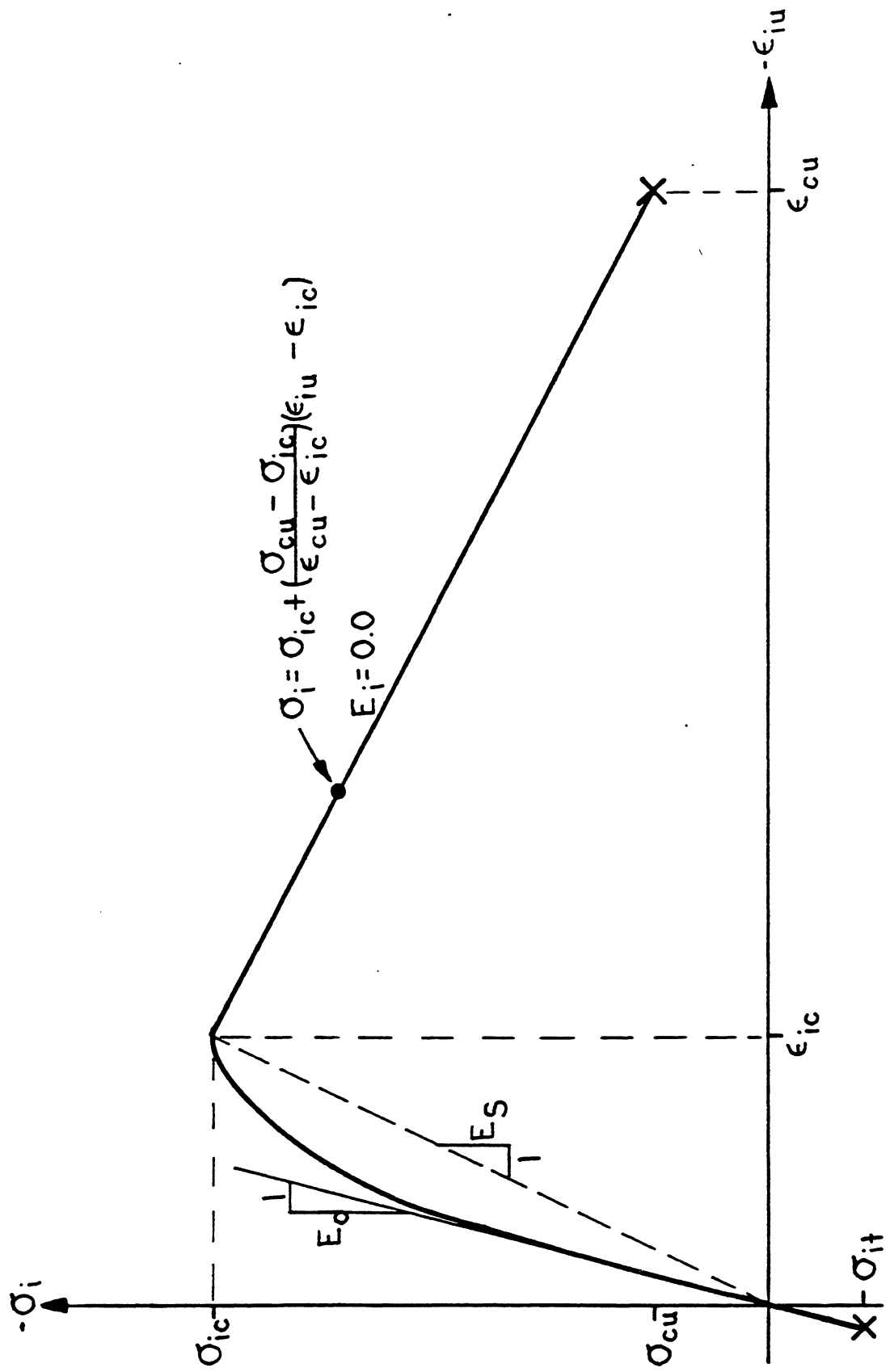

FIG. 3.7 STRAIN SOFTENING BEYOND MAXIMUM COMPRESSIVE STRESS σ_{ic}

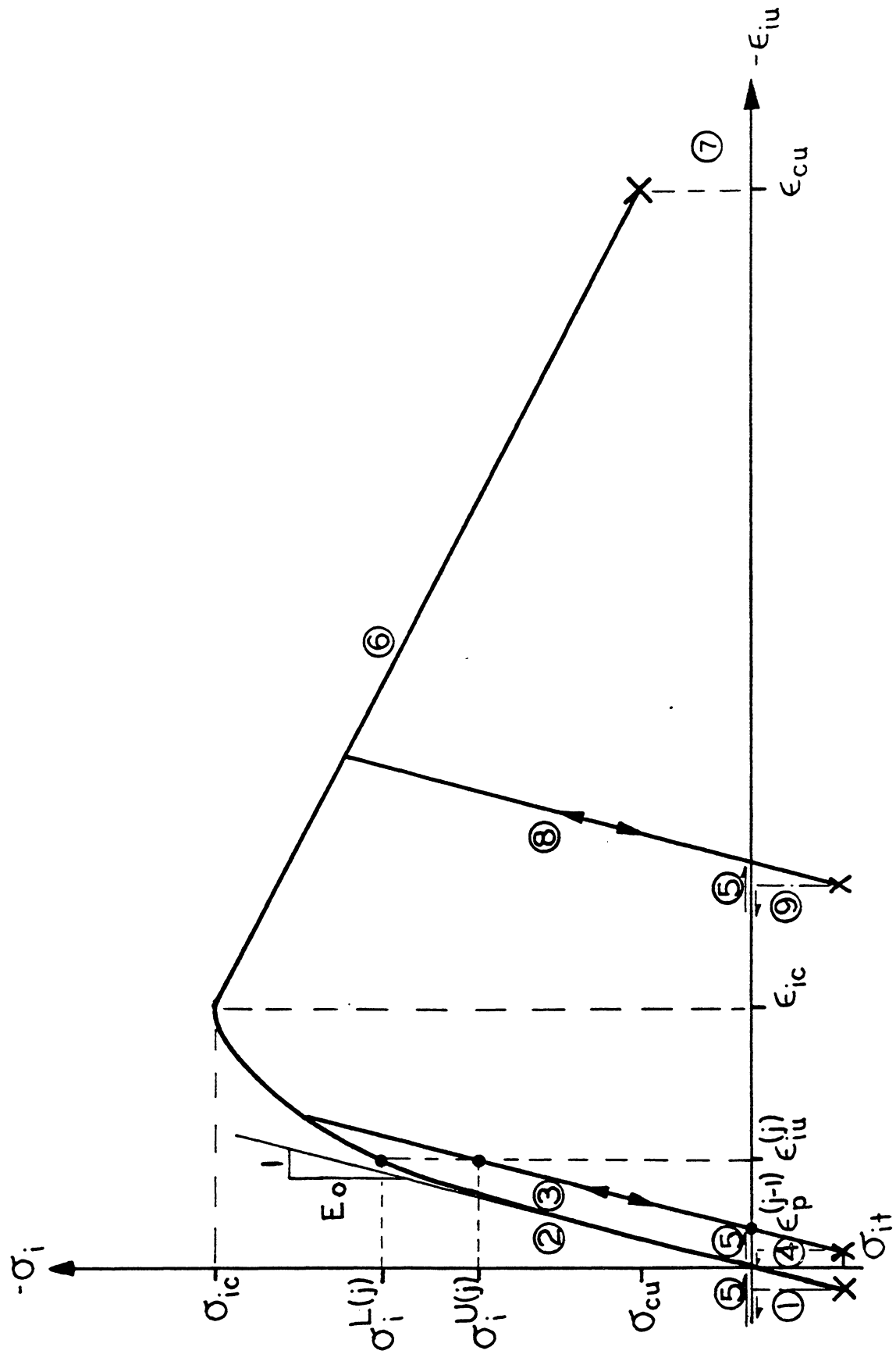

FIG. 3.8 LOAD REVERSAL AND DIFFERENT STATES IN THE CONCRETE

(4) Unloading or reloading in tension before yield.

(5) Crack open.

(6) Yield in the primary path.

(7) Crush in compression.

(8) Unloading or reloading in compression after yield.

(9) Unloading or reloading in tension after yield.

It is assumed that concrete cracks with stiffness dropping to zero when σ_{it} is exceeded and thereafter the concrete cannot take any tension. However, the concrete can carry compressive stress once the crack is closed.

The criteria for unloading or reloading with initial tangent E_o is:

$$\sigma_i^{U(j)} > \sigma_i^{L(j)} \tag{3.18}$$

where $\sigma_i^{U(j)} = E_o(\varepsilon_{iu}^{(j)} - \varepsilon_p^{(j-1)})$

$\sigma_i^{L(j)}$ = stress in concrete along primary path, i.e. state 2 or state 6 in step j

$\varepsilon_p^{(j-1)}$ = plastic strain at the j-1 step

$$= \varepsilon_{iu}^{(j-1)} - \frac{\sigma_i^{L(j-1)}}{E_o}$$

$\varepsilon_{iu}^{(j)}$ = equivalent uniaxial strain at step j.

3.3 Reinforcing Steel

The majority of the steel reinforcement is mild steel having a stress-strain diagram as shown in Fig. 3.9. Mathematical formulation of this stress-strain relationship is difficult due to the nonconvexity of the stress-strain diagram. This is therefore usually modelled as a multilinear material. For example, the actual stress-strain can be

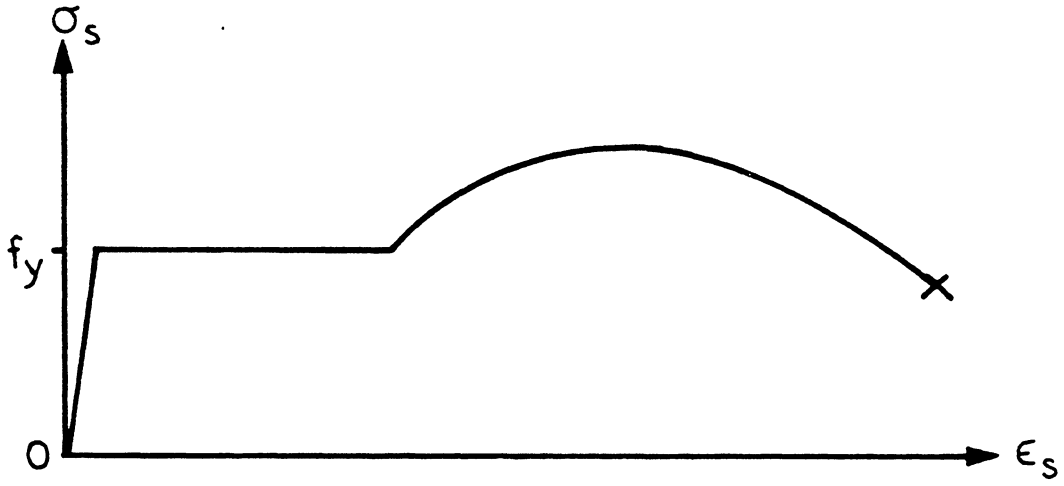

FIG. 3.9 EXPERIMENTAL STRESS-STRAIN CURVE FOR MILD STEEL

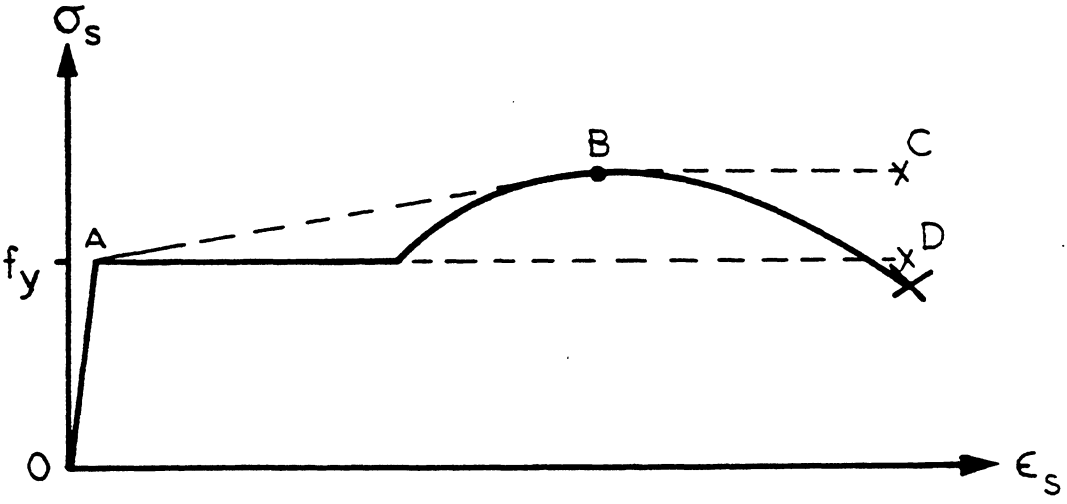

FIG. 3.10 MULTILINEAR STRESS-STRAIN CURVE FOR MILD STEEL

replaced by a trilinear model, path OABC or a bilinear model having path OAB or OAD (Fig. 3.10).

In this study, a bilinear steel model is used and stress reversal with Bauschinger effect is included (Fig. 3.11), meaning that the yield strength is decreased upon inelastic unloading. Loading along AB will cause yielding at B and subsequent loading will follow path BC. Unloading or reloading after yield will follow path CD; further unloading will follow path DE and reloading along path EF. The steel will fail when the total strain exceeds $|\varepsilon_{su}|$.

Four parameters are necessary as input data into the model, the initial modulus E_s, the strain hardening modulus E_{sh}, the yield stress f_y, and the ultimate strain at failure ε_{su}.

The steel is modelled as a one-dimensional material in the reinforcing direction and the stiffness relative to other coordinate axes can be obtained by a simple transformation.

3.4 Cracking and Tension Stiffening Effect

Concrete is assumed to crack once the maximum tensile strength σ_{it} is reached, the principal stress directions are fixed against rotations, and the concrete is assumed to be a uniaxial material in the two principal stress directions. In the present study, a smeared crack model is assumed. The use of discrete cracking [67] necessitates a complex redefinition of the topology of the structure and is therefore not pursued any further.

Cracking is further complicated by the presence of the reinforcement. Due to the bond stress developed between the steel and the surrounding concrete, the concrete is capable of carrying tension between adjacent primary cracks, a phenomenon termed "tension stiffening".

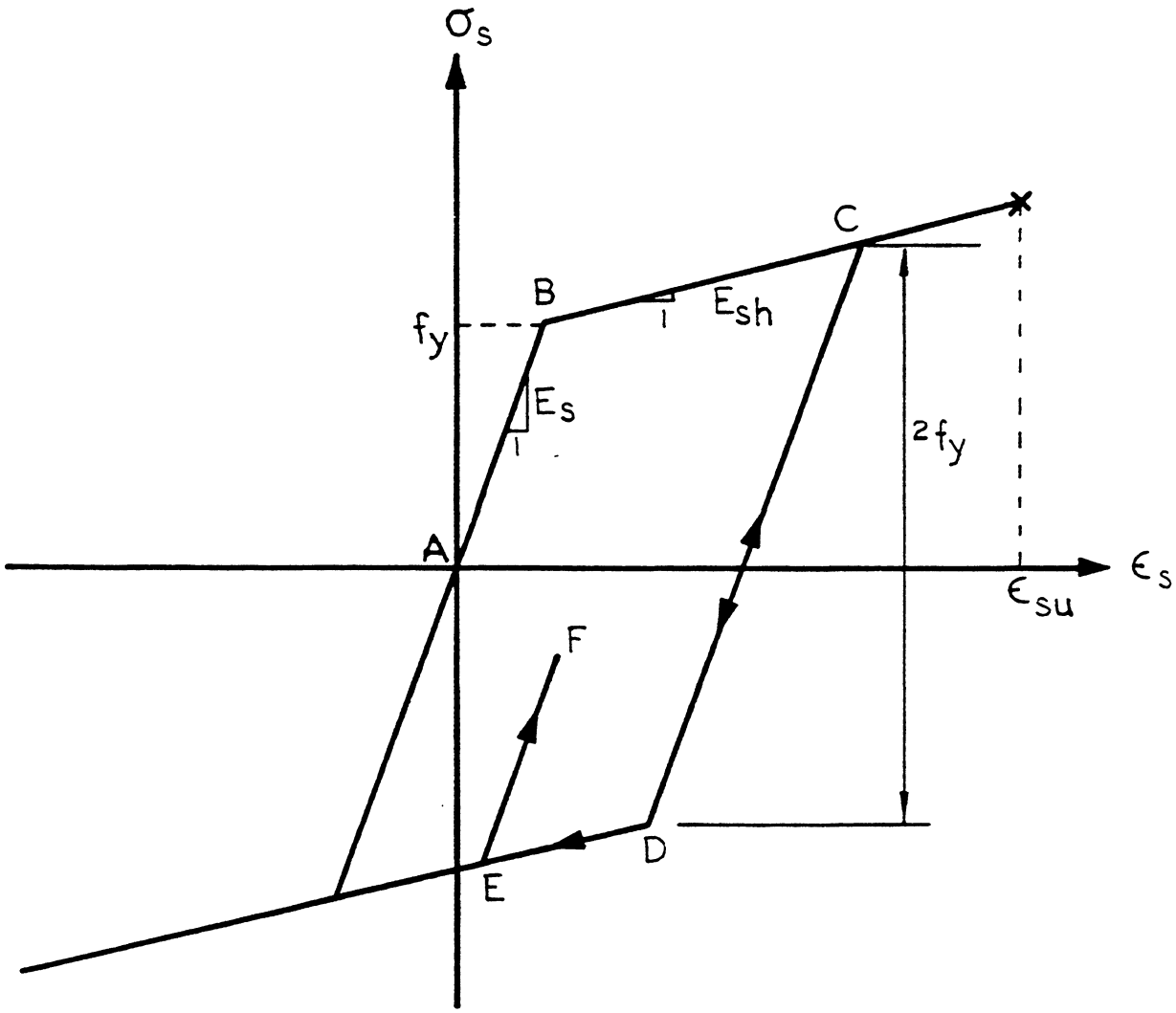

FIG. 3.11 STRESS-STRAIN DIAGRAM FOR THE BILINEAR STEEL MODEL

Figure 3.12 shows a typical stress distribution in the concrete and steel in a tension specimen.

To account for the tension carried by the concrete, Scanlon [68] used a stepped response for concrete in tension (Fig. 3.13a). Lin [8] modified Scanlon's approach and used a gradual unloading model for concrete in tension (Fig. 3.13b).

Scanlon's [68] and Lin's [8] approaches are generally termed the concrete referred method because the tension is taken care of by lumping the tension stiffening into the concrete. This approach has the disadvantage that neither the concrete stress nor the steel stress is exact. Furthermore, it does not take into account the direction and the location of the reinforcement in the thickness direction relative to the cracks.

Another approach used by Gilbert [69] is generally termed the steel referred method (Fig. 3.13c). The additional tension carried by the concrete is lumped at the steel level resulting in an added stiffness of the steel. The stress in the concrete is exact at the crack. However, the steel stress is magnified to include the tension in the concrete. Unlike the concrete referred method, this model takes into account the direction of the steel reinforcement and the location of the steel reinforcement in the thickness direction approximately.

Recently, Mang and Floegl [16,17,18] proposed a tension stiffening model for short-time loading. Their model is based upon bond slip, where the actual bond stress, steel stress, and the concrete stress between the cracks are replaced by the assumed distribution. From the assumed stress distribution, the bond slip between the cracks can be found. Using a shear-slip relationship together with an experimental expression for the bond shear, the additional work done by this bond force can be found.

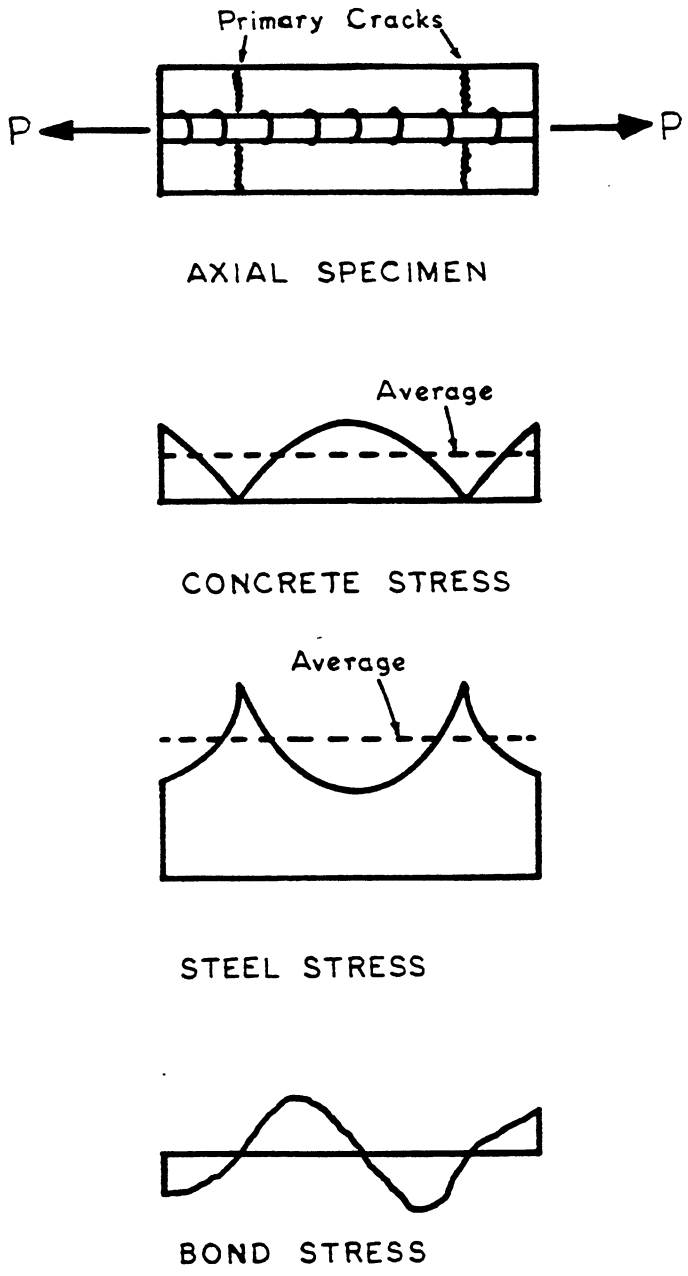

FIG. 3.12 STRESS DISTRIBUTION IN A CRACKED CONCRETE AXIAL SPECIMEN

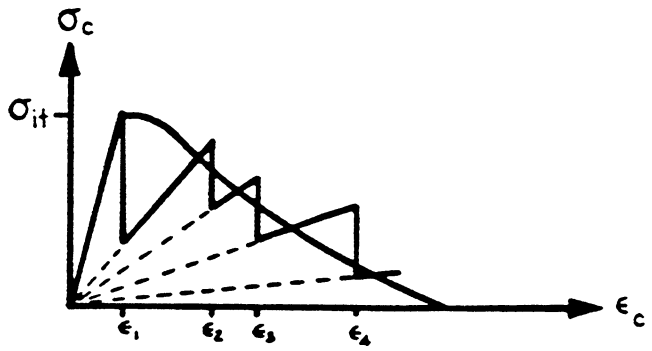

(a) SCANLON'S APPROACH

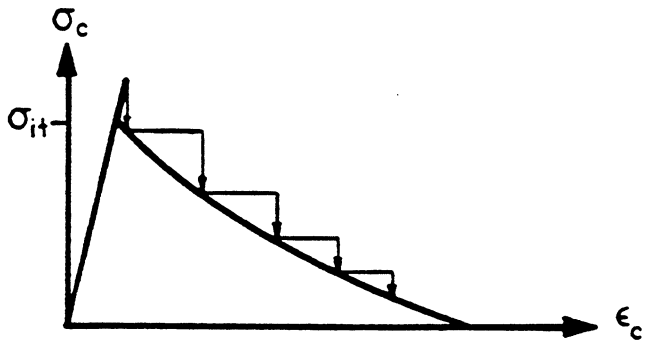

(b) LIN'S GRADUAL UNLOADING

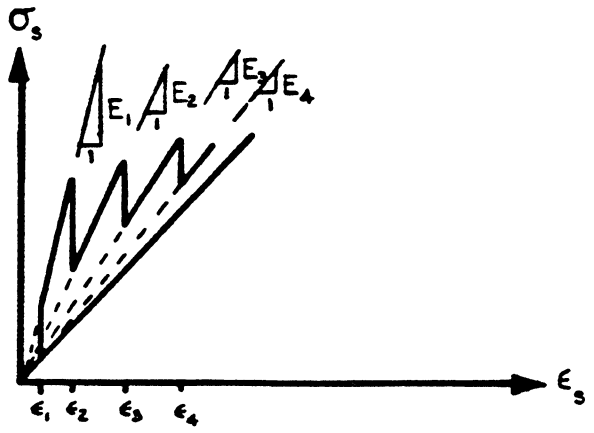

(c) GILBERT ET AL MODIFIED STRESS-STRAIN FOR STEEL

FIG. 3.13 DIFFERENT TENSION STIFFENING MODELS

Their model is a steel referred method. However, it takes into account the crack spacing, direction of reinforcement and its location relative to the depth, and the effect of the secondary cracks in a more vigorous manner.

Aldstdt [24] also treats the tension stiffening effect using bond slip, but the bond slip is treated as an added internal degree of freedom.

In the present study, the steel referred method of Gilbert et al [69] will be adopted. However, modification must be made to account for the cracking due to load reversal.

Figure 3.14 illustrates the sequence of events due to unloading in a reinforced concrete axial specimen. For simplicity, it is assumed that all the strains are mechanical strains and that perfect bond between concrete and steel exists.

The specimen is first loaded in compression and then unloaded in tension. Concrete and steel are in compression for loading to point A. Upon unloading, the concrete and the steel both unload elastically. Concrete will crack at point B; however, the strain in the steel is still compressive. To account for the tension stiffening effect, it is therefore necessary to shift the origin of the steel stress-strain diagram from point D to point C so that the tension stiffening factor is computed based upon $(\varepsilon_s - \varepsilon_p)/\varepsilon_t$ instead of $\varepsilon_s/\varepsilon_t$.

Upon closing of the cracks, the stiffness associated with the largest attainable value of $(\varepsilon_s - \varepsilon_p)/\varepsilon_t$ in the load history is used. Geometrically, this is illustrated in Fig. 3.15. Opening of cracks corresponds to path AB, CD, etc.; closing of cracks corresponds to path DCO.

For a biaxial stress state, the plastic strain in the concrete is transformed to the direction of the reinforcement and the tension

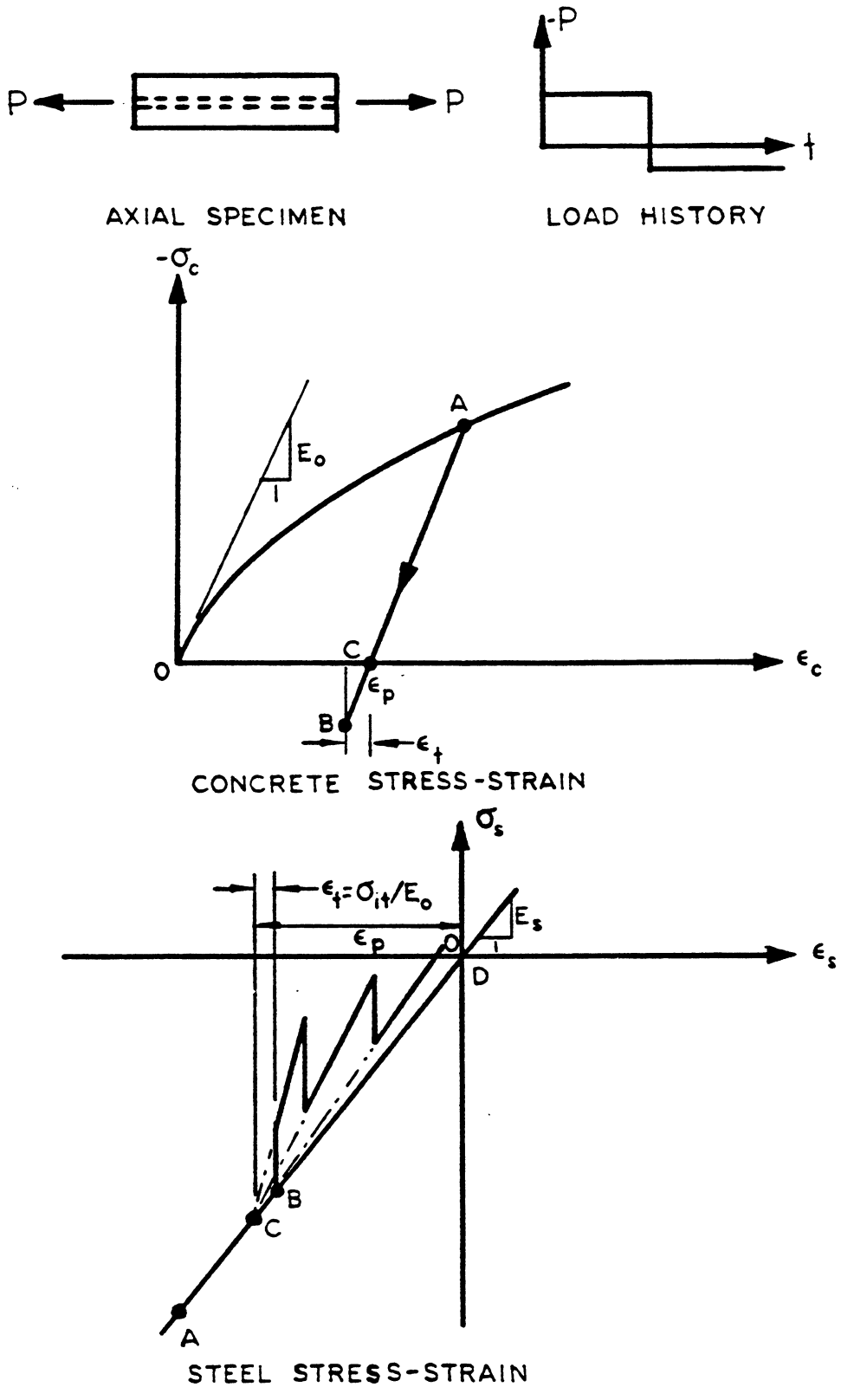

FIG. 3.14 STRESSES IN THE CONCRETE AND STEEL DUE TO UNLOADING

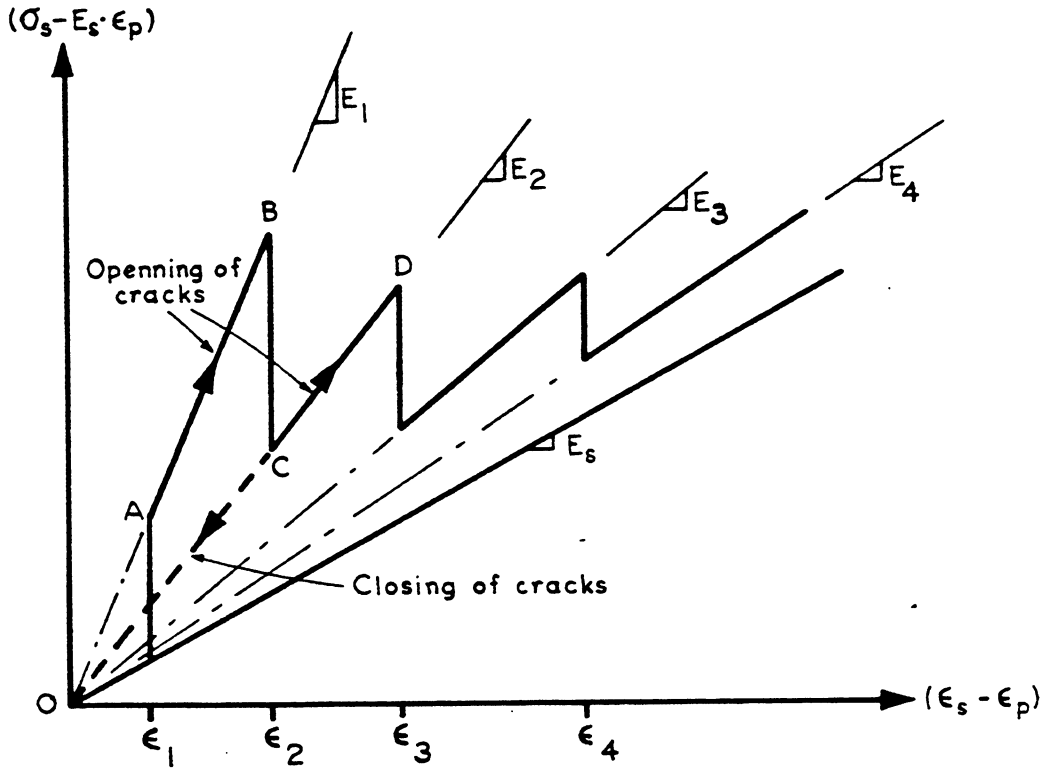

FIG. 3.15 MODIFIED STRESS-STRAIN CURVE FOR STEEL INCLUDING TENSION STIFFENING EFFECT WITH LOAD REVERSAL

stiffening factor is again computed.

In the present study, the following tension stiffening factors are used unless specified otherwise.

$\frac{\varepsilon_s - \varepsilon_p}{\varepsilon_t}$	Tension Stiffening Factor (TSF)
1.0	1.0
1.5	4.0
3.0	2.7
5.0	2.0
8.0	1.6
12.0	1.15
18.0	1.05

Gilbert [69] has found that the above values are good for lightly reinforced concrete. For a heavily reinforced concrete specimen such as an edge beam, the use of the above values will result in a cracked stiffness larger than the uncracked stiffness. Therefore, the value must be scaled down accordingly, but TSF must not be less than 1.0.

Furthermore, it is assumed that once the steel has yielded, the effect of the tension stiffening is ignored.

3.5 Cracked Shear Stiffness

Once the concrete has cracked, the shear stiffness is reduced. However, the aggregate interlock in the crack and the dowel action of the steel reinforcement will permit the concrete to carry additional shear stresses. To estimate such an effect, the shear stiffness G' in

Eq. 3.3b is replaced by the cracked stiffness αG, where $G = \frac{E_o}{2(1+\nu)}$ and α is the shear retention factor, having a value ranges from 0.0 to 1.0. Lin [8] has found that the result of the analysis is insensitive to the value of α; however, a small value is required to avoid numerical problems.

4. TIME DEPENDENT EFFECTS OF CONCRETE

4.1 General

The time dependent behavior of concrete can be of two different origins, producing stress originated and the non-stress originated strains. Creep strain is an example of a stress originated time dependent effect, while thermal and shrinkage induced strains are examples of non-stress originated time dependent effects.

Creep and shrinkage are not independent of each other. Even under the simple case of an isothermal condition, the presence of shrinkage increases the creep. This means that creep and shrinkage effects are coupled. However, from a practical point of view, it is almost always assumed that the creep strains and the shrinkage strains are independent and additive.

Creep is defined as the increase in strain under a sustained stress. The increase in strain is asymptotic, approaching an ultimate value (Fig. 4.1). Upon unloading, there is an instantaneous recovery and a delayed creep recovery. In the presence of creep, full recovery of strain cannot be achieved, thus resulting in a permanent deformation.

In studying creep phenomenon, it is useful to introduce the specific compliance $\overline{C}(\tau,t-\tau)$, defined as the strain at time t due to a unit stress applied at concrete age τ (Fig. 4.2). Note that the specific compliance includes both the instantaneous elastic strain and the creep strain. The instantaneous elastic deformation is also decreased when the stress is applied at a later age τ because of the aging of the concrete.

The factors that influence the creep of concrete are the stress intensity, the compressive strength of the concrete, the age of the

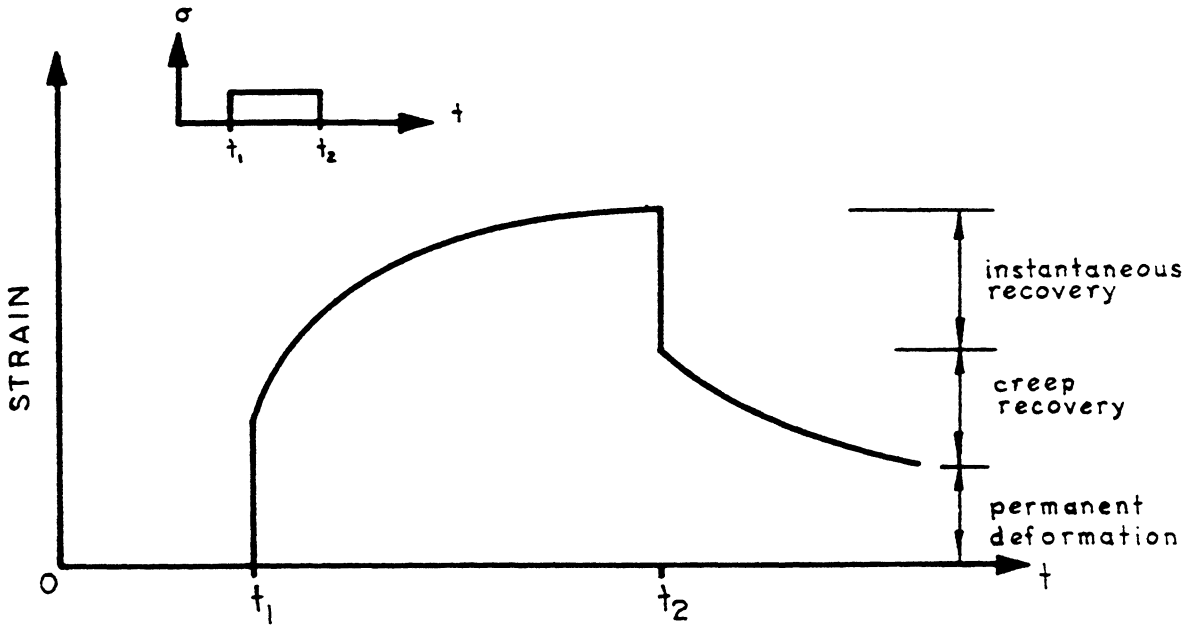

FIG. 4.1 CREEP RESPONSE OF A UNIAXIAL SPECIMEN

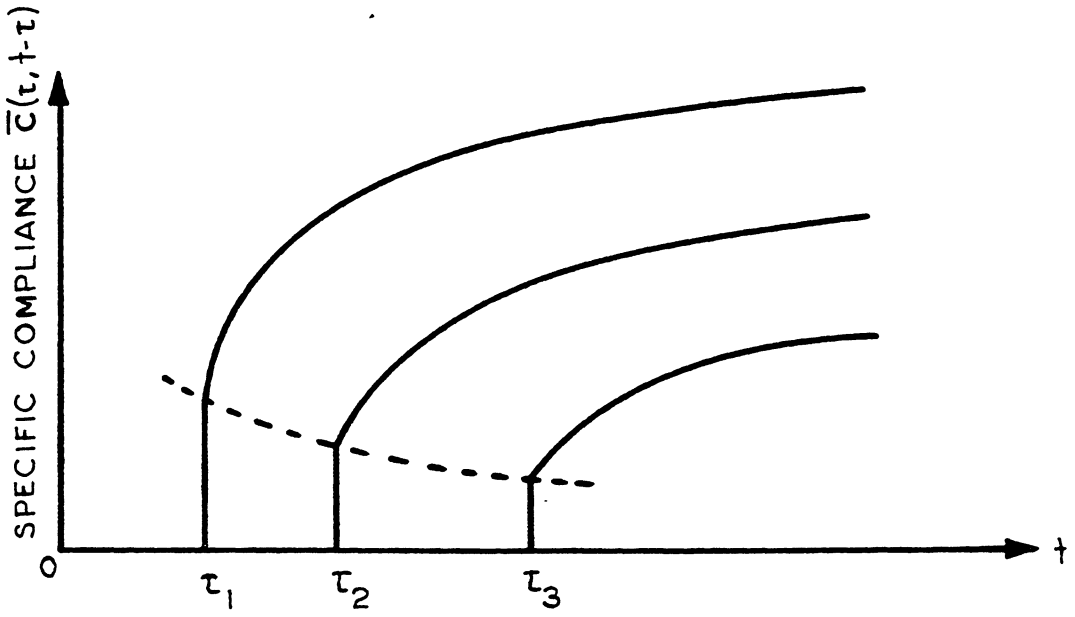

FIG. 4.2 SPECIFIC COMPLIANCE $\bar{C}(\tau,t-\tau)$ FOR AGE τ_i

concrete, the size of the members, temperature, ambient relative humidity, and the aggregate content. Except for the stress intensity and the temperature, creep is an inverse function of the above variables.

Shrinkage is defined as non-stress and non-thermal produced volume change. It arises from the loss of water on drying and volume changes on carbonation. The influential factors are the water-cement ratio, size of the member, relative humidity, and the aggregate content.

The mechanism of creep and shrinkage are still not completely understood, and the correlations between laboratory and field conditions are still lacking. These present some additional uncertainties and further complicate the modelling of the time-dependent response of creep and shrinkage.

4.2 Mathematical Formulation of Creep

Creep is a very complex phenomenon involving a lot of influential factors. The modelling of creep is therefore a statistical problem involving curve fitting.

Creep may be formulated in integral form as follows:

$$\varepsilon(t) = \int_0^t \bar{C}(\tau, t-\tau) \frac{\partial \sigma(\tau)}{\partial \tau} d\tau \qquad (4.1)$$

where $\varepsilon(t)$ is the strain at time t and $\bar{C}(\tau, t-\tau)$ is the specific compliance. Equation 4.1 is a convolution integral where the principle of superposition is assumed.

When the specific compliance is separated into the instantaneous part and the creep part:

$$\bar{C}(\tau, t-\tau) = \frac{1}{E(\tau)} + C(\tau, t-\tau) \qquad (4.2)$$

where $E(\tau)$ is the modulus of elasticity at age τ and $C(\tau,t-\tau)$ is the creep compliance at time $t-\tau$ after load application. The creep strain $\varepsilon^c(t)$ can then be calculated as:

$$\varepsilon^c(t) = \int_0^t C(\tau,t-\tau) \frac{\partial\sigma(\tau)}{\partial\tau} d\tau \qquad (4.3)$$

However, when the creep is formulated in differential form, the general form of the differential equation for an aging concrete is:

$$\left[p_n(t) \frac{d^n}{dt^n} + p_{n-1}(t) \frac{d^{n-1}}{dt^{n-1}} + \ldots\ldots p_o(t) \right] \varepsilon(t) =$$

$$\left[q_n(t) \frac{d^n}{dt^n} + q_{n-1}(t) \frac{d^{n-1}}{dt^{n-1}} + \ldots\ldots q_o(t) \right] \sigma(t) \qquad (4.4)$$

where $p_n(t)$ and $q_n(t)$ are time-dependent variables representing the properties of concrete.

Equations 4.1 and 4.4 are mathematically equivalent. However, the identification of the coefficients may be difficult in the differential formulation. Consequently, the integral formulation is often used.

Argyris et al [70] present a theoretical framework for thermo-mechanical creep of aging concrete using an internal variable approach. A good summary of the available creep models is presented by Kabir [11].

Using the integral formulation (Eq. 4.1), it can be seen that the strain $\varepsilon(t)$ at time t involves the integration of all the previous stress histories. This will overtax the computational effort and the computer storage requirements in the solution process. For this reason, the notion of finite material memory, where the current strain $\varepsilon(t)$ is based upon finite past stress histories [71] or a degenerate

model where the stress histories are stored as hidden state variables [72], is often used.

4.3 Creep Model for the Present Study

In the present study, an efficient numerical procedure developed by Kabir [11] for the evaluation of creep strain, taking into account both the effects of temperature and age of the concrete, is used. The method is an extension of the creep model developed by Zienkiewicz and Watson [72] to include the temperature shift function.

The inherent assumptions are the linearity in creep strain and the applied stress, both in tension and in compression; linear superposition; additivity of different strain components; and a thermorheologically simple concrete material obeying a time shift principle for a temperature variation [73].

The creep compliance function $C(\tau,t-\tau,T)$ was given by Kabir [11] in the form of a Dirichlet series.

$$C(\tau,t-\tau,T) = \sum_{i=1}^{m} a_i(\tau)\left[1 - e^{-\lambda_i \phi(T)(t-\tau)}\right] \qquad (4.5)$$

where $a_i(\tau)$ are the aging parameters depending on the age at loading τ, λ_i are the retardation times governing the shape of the logarithmically decaying creep curve and $\phi(T)$ is the temperature shift function dependent on the temperature T.

A step-by-step method together with the Dirichlet series (Eq. 4.5) is used to solve for the creep strain (Eq. 4.3). The stress histories are stored in a set of hidden state variables. Kabir [11], Kang [74], Van Zyl [75], and Van Gruenen [26] have used the same algorithm which has been found to be numerically stable.

Following Kabir [11], the increment of creep strain $\Delta\underset{\sim}{\varepsilon}^c(t)$ and the increment of stress $\Delta\underset{\sim}{\sigma}(t)$ in the orthotropic directions 1 and 2 are related:

$$\Delta\underset{\sim}{\varepsilon}^c(t) = \underset{\sim}{D}_o^{-1}\ \underset{\sim}{C}(\tau,t-\tau,T)\ \Delta\underset{\sim}{\sigma}(t) \tag{4.5}$$

where

$$\Delta\underset{\sim}{\varepsilon}^c(t) = \begin{bmatrix} \Delta\varepsilon_{11}^c(t) \\ \Delta\varepsilon_{22}^c(t) \\ \Delta\varepsilon_{12}^c(t) \end{bmatrix} \qquad \Delta\underset{\sim}{\sigma}(t) = \begin{bmatrix} \Delta\sigma_{11}(t) \\ \Delta\sigma_{22}(t) \\ \Delta\sigma_{12}(t) \end{bmatrix}$$

$$\underset{\sim}{D}_o^{-1} = \begin{bmatrix} 1 & -\nu_c & 0 \\ -\nu_c & 1 & 0 \\ 0 & 0 & 2(1+\nu_c) \end{bmatrix}$$

and ν_c is the creep Poisson's ratio, assumed to be equal to the elastic Poisson's ratio.

The total creep strain $\underset{\sim}{\varepsilon}^c(t)$ from the initial age of loading t_1 to the observation time t_n is then obtained by summation:

$$\underset{\sim}{\varepsilon}^c(t_n) = \sum_{i=1}^{n-1} \underset{\sim}{D}_o^{-1}\ C(t_i,t_n-t_i,T_i)\ \Delta\underset{\sim}{\sigma}(t_i) \tag{4.6}$$

Equation 4.6 is represented graphically in Fig. 4.3 for a one-dimensional stress state. Here, linear superposition is used.

Substituting the creep compliance function of Eq. 4.5 into the expression for creep strain of Eq. 4.6, and simplifying:

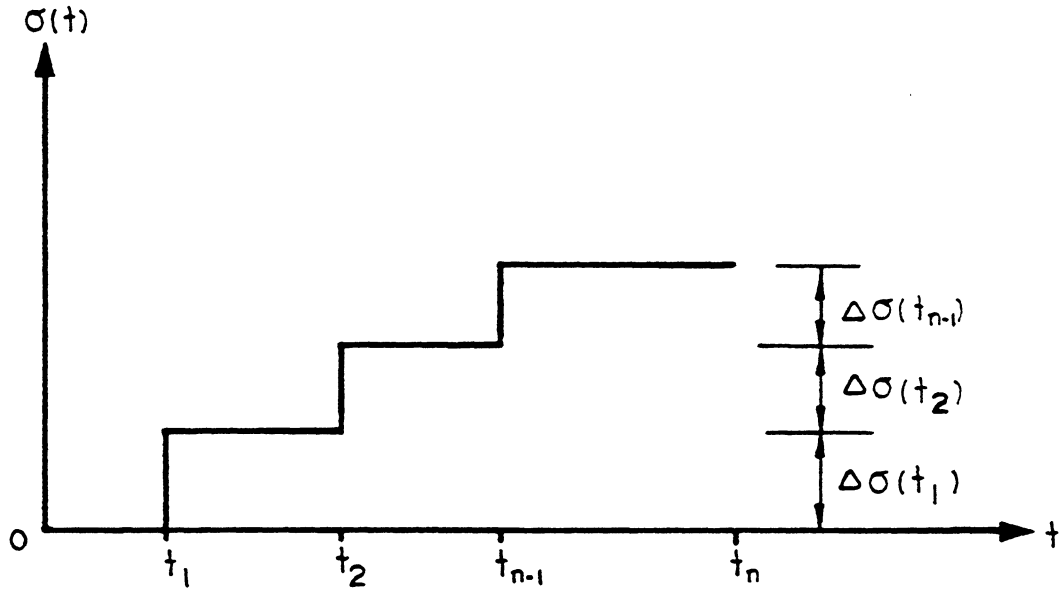

STRESS HISTORY

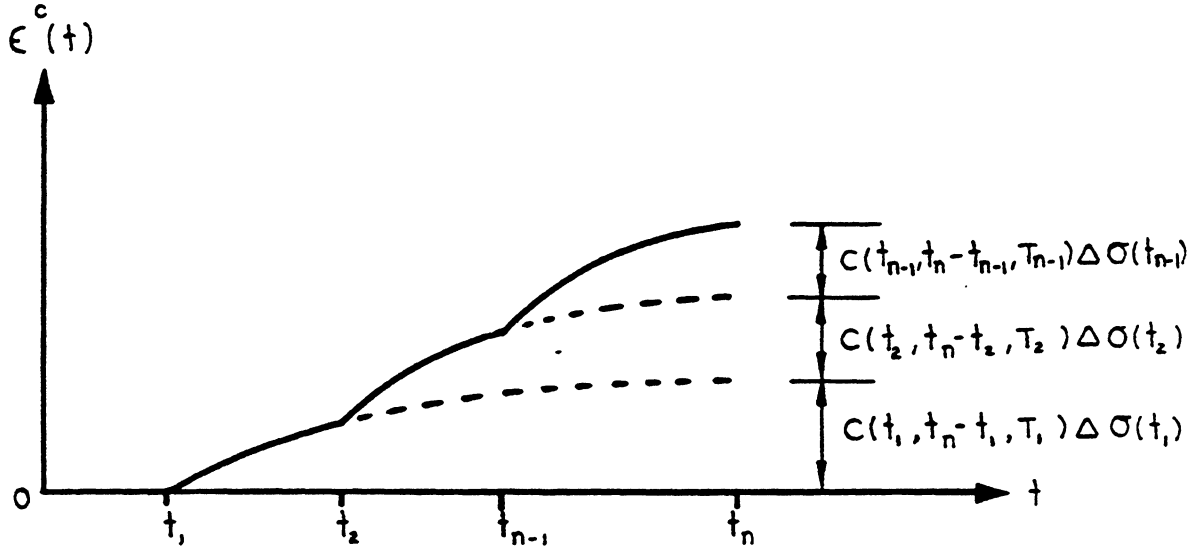

TOTAL CREEP STRAIN

FIG. 4.3 GEOMETRICAL REPRESENTATION OF THE LINEAR SUPERPOSITION OF CREEP STRAINS

$$\underset{\sim}{D}_o \underset{\sim}{\varepsilon}^c(t_n) = \Delta\underset{\sim}{\sigma}(t_1) \sum_{i=1}^{m} a_i(t_1) \left[1 - e^{-\lambda_i\phi_1\Delta t_1 - \ldots - \lambda_i\phi_{n-1}\Delta t_{n-1}}\right]$$

$$+ \Delta\underset{\sim}{\sigma}(t_2) \sum_{i=1}^{m} a_i(t_2) \left[1 - e^{-\lambda_i\phi_2\Delta t_2 - \ldots - \lambda_i\phi_{n-1}\Delta t_{n-1}}\right]$$

$$+ \ldots\ldots\ldots\ldots\ldots\ldots\ldots$$

$$+ \Delta\underset{\sim}{\sigma}(t_{n-1}) \sum_{i=1}^{m} a_i(t_{n-1}) \left[1 - e^{-\lambda_i\phi_{n-1}\Delta t_{n-1}}\right] \qquad (4.7)$$

where $\Delta t_i = t_{i+1} - t_i$ and $\phi_i = \phi(T_i)$.

Similarly, the creep strain at time t_{n+1} is:

$$\underset{\sim}{D}_o \underset{\sim}{\varepsilon}^c(t_{n+1}) = \Delta\underset{\sim}{\sigma}(t_1) \sum_{i=1}^{m} a_i(t_1) \left[1 - e^{-\lambda_i\phi_1\Delta t_1 - \ldots - \lambda_i\phi_n\Delta t_n}\right]$$

$$+ \Delta\underset{\sim}{\sigma}(t_2) \sum_{i=1}^{m} a_i(t_2) \left[1 - e^{-\lambda_i\phi_2\Delta t_2 - \ldots - \lambda_i\phi_n\Delta t_n}\right]$$

$$+ \ldots\ldots\ldots\ldots\ldots\ldots\ldots$$

$$+ \Delta\underset{\sim}{\sigma}(t_n) \sum_{i=1}^{m} a_i(t_n) \left[1 - e^{-\lambda_i\phi_n\Delta t_n}\right] \qquad (4.8)$$

The increment of creep strain can then be obtained by subtracting the values of Eq. 4.7 from Eq. 4.8.

$$\underset{\sim}{D}_o \, \Delta\underset{\sim}{\varepsilon}^c(t_n) = \underset{\sim}{D}_o \, \underset{\sim}{\varepsilon}^c(t_{n+1}) - \underset{\sim}{D}_o \, \underset{\sim}{\varepsilon}^c(t_n)$$

$$= \Delta\underset{\sim}{\sigma}(t_1) \sum_{i=1}^{m} a_i(t_1) \, e^{-\lambda_i \phi_1 \Delta t_1 - \cdots - \lambda_i \phi_{n-1} \Delta t_{n-1}} \left[1 - e^{-\lambda_i \phi_n \Delta t_n}\right]$$

$$+ \Delta\underset{\sim}{\sigma}(t_2) \sum_{i=1}^{m} a_i(t_2) \, e^{-\lambda_i \phi_2 \Delta t_2 - \cdots - \lambda_i \phi_{n-1} \Delta t_{n-1}} \left[1 - e^{-\lambda_i \phi_n \Delta t_n}\right]$$

$$+ \cdots\cdots\cdots\cdots\cdots\cdots$$

$$+ \Delta\underset{\sim}{\sigma}(t_n) \sum_{i=1}^{m} a_i(t_n) \left[1 - e^{-\lambda_i \phi_n \Delta t_n}\right] \qquad (4.9)$$

The recursion relationships necessary to calculate the increment of creep strains are:

$$D_o \, \Delta\underset{\sim}{\varepsilon}^c(t_n) = \sum_{i=1}^{m} \underset{\sim}{A}_i(t_n) \left[1 - e^{-\lambda_i \phi_n \Delta t_n}\right] \qquad (4.10)$$

and

$$\underset{\sim}{A}_i(t_n) = \underset{\sim}{A}_i(t_{n-1}) \, e^{-\lambda_i \phi_{n-1} \Delta t_{n-1}} + \Delta\underset{\sim}{\sigma}(t_n) a_i(t_n) \qquad (4.11)$$

$$\underset{\sim}{A}_i(t_1) = \Delta\underset{\sim}{\sigma}(t_1) \, a_i(t_1) \qquad (4.12)$$

This formulation does not require the storage of all the stress histories in order to calculate the creep strain increment, rather the stress history is stored in a vector $\underset{\sim}{A}_i(t_n)$ which can be calculated recursively by Eq. 4.11 and Eq. 4.12 knowing the stress changes $\Delta\underset{\sim}{\sigma}(t_n)$ within a time increment $t_n - t_{n-1}$.

The assumption of constant stress within an increment is necessary in order to arrive at Eq. 4.10. This means that any changes in stress can only occur at the beginning of a time step. For a proper choice

of time step, this assumption is justifiable.

Experimental results on creep [77] indicated that creep is linearly proportional to stress up to approximately 0.35 f'_c, beyond that it is nonlinear. To take into account creep at high stress levels, the notion of effective stress proposed by Becker and Bresler [76] is used to calculate the creep strain. The effective stress σ_{eff_i} in the i orthotropic direction is:

$$\sigma_{eff_i} = \sigma_i \quad \text{for} \quad \sigma_i/f'_c \leq 0.35 \tag{4.13a}$$

$$\sigma_{eff_i} = 2.33\,\sigma_i - 0.465\,f'_c \quad \text{for} \quad 0.35 \leq \sigma_i/f'_c \leq 1.0 \tag{4.13b}$$

Equation 4.13 is an empirical equation based on experimental data, particularly that of Roll [77]. However, when calculating creep recovery, the actual stress should always be used [77].

4.4 Determination of the Creep Compliance Function

The key to the success of the creep model is the proper choice of the creep function. The Dirichlet series representation of the creep function in Eq. 4.5 is:

$$C(\tau,t-\tau,T) = \sum_{i=1}^{m} a_i(\tau)\,[1 - e^{-\lambda_i \phi(T)(t-\tau)}]$$

The unknown parameters m, $a_i(\tau)$, λ_i, and $\phi(T)$ have to be determined.

1. Experiment

In the case where experimental creep curves are available, a least squares fit, as discussed in the following section, can be used.

At a particular age τ_o and temperature T_o, the following steps are followed.

(i) m and λ_i, i=1,...m are chosen on a trial basis

(ii) Various time t_j, j=1,...n are chosen such that $t_j \geq \tau$

(iii) Values of $C(\tau_o, t_j-\tau_o, T_o)$ are found at the time t_j, j=1,...n

(iv) The simultaneous equations are set up:

$$\begin{bmatrix} 1-e^{-\lambda_1(t_1-\tau_o)} & \cdots\cdots & 1-e^{-\lambda_m(t_1-\tau_o)} \\ \vdots & & \vdots \\ 1-e^{-\lambda_1(t_n-\tau_o)} & \cdots\cdots & 1-e^{-\lambda_m(t_n-\tau_o)} \end{bmatrix} \begin{bmatrix} a_1(\tau_o) \\ \vdots \\ a_m(\tau_o) \end{bmatrix} = \begin{bmatrix} C(\tau_o, t_1-\tau_o, T_o) \\ \vdots \\ C(\tau_o, t_n-\tau_o, T_o) \end{bmatrix} \tag{4.14}$$

The overdetermined system of equations (Eq. 4.14) is solved for $a_i(\tau_o)$ by the least squares method.

(v) A different value of m and λ_i are again chosen and steps (ii) through (iv) are followed.

(vi) Optimum m and λ_i are chosen such that:

(a) The least squares error is minimized.

(b) The ultimate creep strain $a_i(\tau_o)$ is about 4/3 of the one-year creep strain.

(c) The contributions of all $a_i(\tau_o)[1-e^{-\lambda_i(t-\tau_o)}]$ are nearly equal.

(vii) A different age τ is then chosen and steps (i) through (vi) are followed to find the $a_i(\tau)$. The $a_i(\tau)$ of the inbetween ages can be found by interpolation.

(viii) The temperature shift function $\phi(T)$ can be calculated from the experimental data following the procedure outlined by Mukaddam [73].

2. ACI Committee 209 Method

In the absence of experimental data, the following empirical expression for the prediction of creep deformation recommended by ACI Committee 209 [64] and based on the studies of Branson et al [78, 79] may be used.

$$C_t = K_s K_H K_h K_\tau \frac{t-\tau}{10+(t-\tau)^{0.6}} C_u \qquad (4.15)$$

where

C_t = creep coefficient = $\frac{\text{creep strain at any time t}}{\text{initial instantaneous strain}}$

C_u = ultimate creep coefficient to be determined from experimental data

= $\frac{\text{creep strain at infinite time after loading}}{\text{initial strain at time of loading}}$

= 2.35 for standard condition

K_s = slump correction factor

= 0.81 + 0.07 s

K_H = humidity correction factor

= 1.27 - 0.0067 H, H $\geq$ 40

K_h = size correction factor

= 1.0 - 0.0167 (sz - 6.0), sz $\geq$ 6.0
sz $\leq$ 6.0

= 1.0

K_τ = age at loading correction factor

= 1.25 τ - 0.118 for moist cured concrete for 7 days

s = slump in inches, 2.7 inches for standard conditions

H = relative humidity, 40% or less for standard conditions

sz = minimum thickness or size of member in inches, 6 inches or less for standard conditions

τ = age at loading in days, standard condition is 7 days for moist cured concrete

t = observation time in days

For the standard condition, all the correction factors are 1.0.

Kabir [11], using the standard condition, generated the creep curves for 15 loading ages - 7, 10, 14, 21, 28, 40, 60, 80, 91, 100, 120, 180, 270, 365, 400 days. Using $m = 3$, $\lambda_1 = 0.1$, $\lambda_2 = 0.01$, and $\lambda_3 = 0.001$, the coefficients $a_i(\tau)$ for each loading age are generated using the procedure outlined previously. The values of $a_i(\tau)$ are then stored in the computer subroutine. The $a_i(\tau)$ for intermediate ages are found by interpolation. For any condition other than the standard, the values of $a_i(\tau)$ are corrected by the correction factors, K_s, K_H, K_h, and K_τ.

The comparisons between the analytical creep curve and the experimental results [80] are satisfactory within a range of discrepancy of ±5%.

4.5 Analytical Formulation of Shrinkage

The shrinkage strains can be found from either experimental shrinkage curves or making use of ACI Committee 209 recommendations [64] based on the studies of Branson et al [78,79].

The ACI Committee recommends:

$$\varepsilon^s(t) = K_s K_h K_H \frac{(t-\tau_o)^e}{f+(t-\tau_o)^e} \varepsilon_u^s \qquad (4.16)$$

where

$\varepsilon^s(t)$ = shrinkage strain at observation time t

ε_u^s = ultimate shrinkage strain to be determined from experiment

τ_o = age of curing

f,e = constants to be determined from experiments

K_s = slump correction factor

K_h = size correction factor

K_H = relative humidity correction factor

Normally, the range of values for e,f and ε_u^s for normal or light weight concrete, moist-cured, or steam-cured, are found to be:

e = 0.90 to 1.10

f = 20 to 130

ε_u^s = 415×10^{-6} to 1070×10^{6} in/in.

ACI Committee 209 [64] also recommends the following standard equations for shrinkage prediction.

For concrete moist cured for 7 days:

$$\varepsilon^s(t) = K_s K_h K_H \frac{t-7}{35 + (t-7)} 800 \times 10^{-6}$$

For concrete steam cured for 3 days:

$$\varepsilon^s(t) = K_s K_h K_H \frac{t-3}{55 + (t-3)} 730 \times 10^{-6}$$

The correction factors are:

K_s = 0.89 + 0.041 s, s = slump in inches

K_H = 1.40 - 0.010 H $40 \leq H \leq 80$

K_H = 3.00 - 0.030 H $80 \leq H \leq 100$

where H is the percent relative ambient humidity.

The correction factor K_h for the size of the member is as shown in Fig. 4.4c. The linearized correction factors for size are:

K_h = 1.14 - 0.023 h for $\leq$ 1 year drying

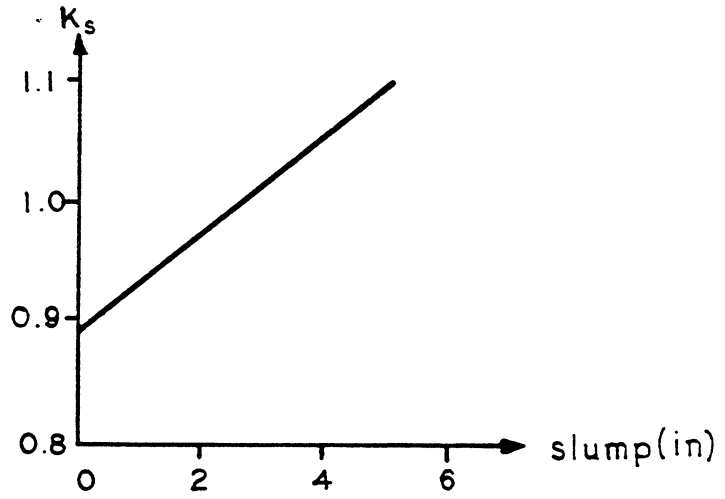

(a) SLUMP CORRECTION

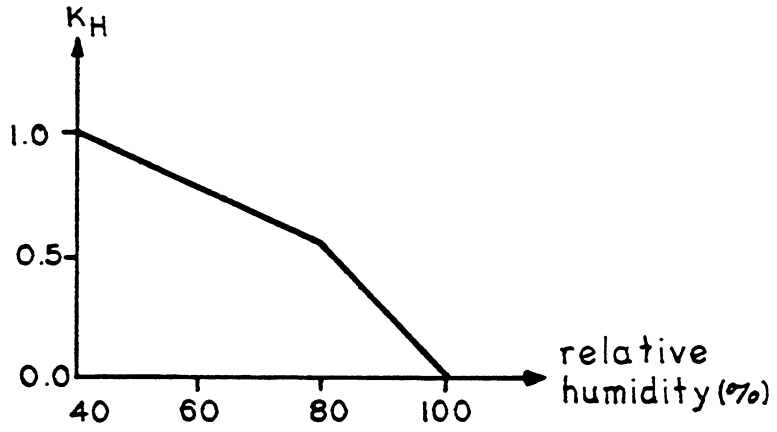

(b) HUMIDITY CORRECTION

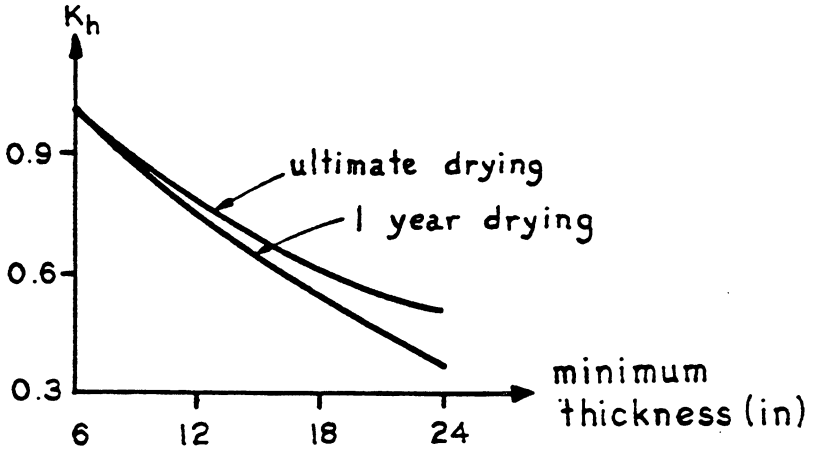

(c) THICKNESS CORRECTION

FIG. 4.4 SHRINKAGE CORRECTION FACTORS

$$K_h = 1.10 - 0.017\ h \quad \text{for ultimate drying}$$

where h is the minimum thickness in inches.

The shrinkage strains are assumed to consist of axial components only and are uniform in all directions.

5. FINITE ELEMENT FOR NONLINEAR SHELL ANALYSIS

5.1 Introduction

The analysis of a shell structure by the finite element method involves the following approximations:

(1) Discretization errors: This form of error stems from the approximation of the true shell surface by a series of flat elements or curved elements. Depending on the geometry of the shell, this form of error can be more severe than the degree of approximation used in the displacement fields.

(2) Polynomial expansion of the displacement fields: The choice of the polynomial representations of the displacement fields should adequately satisfy:

   (a) Constant strain states - This condition is necessary for convergence with mesh refinement because, as the size of the element decreases, the stresses within an element approach a constant value in the limit.

   (b) Include all rigid body modes - This ensures that no strain will be induced when an element is subjected to a rigid body motion.

   (c) Interelement continuity - This will ensure that no displacement gaps are formed between adjacent elements during deformation.

   (d) Invariance requirement - The invariance of energy requires that the element stiffness be invariant with respect to the frame of reference. Mathematically, this can be expressed as [81]:

$$\underset{\sim}{T}^T f(\underset{\sim}{K})\ \underset{\sim}{T} = f(\underset{\sim}{T}^T\ \underset{\sim}{K}\ \underset{\sim}{T})$$

where $\underset{\sim}{T}$ is a transformation matrix between local and global coordinate axes, $\underset{\sim}{K}$ is the stiffness matrix in the local coordinate system, and f are some isotropic functions.

The invariance requirement is satisfied automatically when an isotropic polynomial is used in representing the displacement fields. The simplest choice is a complete polynomial.

The satisfaction of (a), (b), (c), and (d) as described previously is by no means an easy problem, if not impossible in some cases. The satisfaction of both the rigid body modes and the interelement continuity requirement always represent a contradiction to each other, especially in the case of a curved element. Fonder [82], for example, used trigonometric functions to represent the displacement fields so that the rigid body modes could be reproduced at the expense of violating the interelement continuity requirement. The invariance requirement, however, can be relaxed as long as the invariance of energy can be restored in the limit. The invariance will therefore be satisfied in the limit if constant strain states are included in the field expansions [81].

The necessary conditions for the solution to converge with mesh refinement are therefore the inclusion of both the constant strain states and all the rigid body modes in the displacement expansions. The same conclusion was reached by Cantin [83] and Allman [84].

In the case of nonlinear analysis, including both the effects of nonlinear geometry and material, the frequent updating of the

element stiffnesses necessitates that the element must be computationally efficient with respect to the number of elements required to achieve a solution of given accuracy. The large amount of storage required for the state variables necessitates that the mesh be as coarse as possible.

The type of shell element to be used falls into one of the following categories:

(1) Flat element

(2) Curved shell element

(3) 3D isoparametric solid

(4) Degenerated isoparametric element

In the following sections, each category will be reviewed to form the basis for comparisons and, ultimately, a suitable choice of element for the present study.

5.2 Flat Elements

There are basically two types of flat element geometry, the triangle and the quadrilateral. The elements are obtained by superimposing a plate bending element on a membrane element. Coupling between the in-plane membrane and bending actions is ignored in the element local coordinate systems. Moreover, the flat element cannot represent the shell geometry completely.

In cases where the normal in-plane rotation is undefined, numerical problems will exist when the adjacent shell elements meeting at a nodal point are coplanar or near coplanar, unless that degree of freedom is constrained against rotation.

The flat element, however, has the advantages that it is relatively economical computationally in the formation of its

element stiffness, and its stiffness matrix has a relatively small bandwidth compared to other higher order elements.

The triangular element has the advantage over the quadrilateral element in that it is simple to use, causing no problem with mesh refinement in regions of high stress gradient and in modelling a warped shell surface. The triangle, however, will show bias with respect to the orientation of the element, and for some nonconforming elements, the refinement of an irregular mesh fails to reproduce the constant strain states exactly [85].

(1) Triangular Flat Element

One of the earliest and yet still very successful conforming flat elements is the LCCT9 triangular plate bending element developed by Clough and Tocher [86] and later reformulated by Felippa [87].

The LCCT12 (Fig. 5.1a) employs a complete cubic expansion in the displacement fields. The displacement degrees of freedom are w, θ_x, θ_y at each node and a normal slope, θ_n, along each side of a triangle plus three internal degrees of freedom w_o, θ_{x_o} and θ_{y_o}. The LCCT12 is assembled from three subtriangles and the internal degrees of freedom are eliminated by enforcing compatibility of normal slope between subtriangles. The LCCT9 can be obtained from LCCT12 by enforcing a linear variation of normal slope along the sides of a triangle.

A shell element can be obtained by combining a LCCT9 with a constant strain triangular membrane element (CST) with u and v as nodal degrees of freedom, Fig. 5.1b. However, the constant strain approximation is incapable of representing the stresses in regions of high stress gradients. Therefore, a highly refined mesh has to

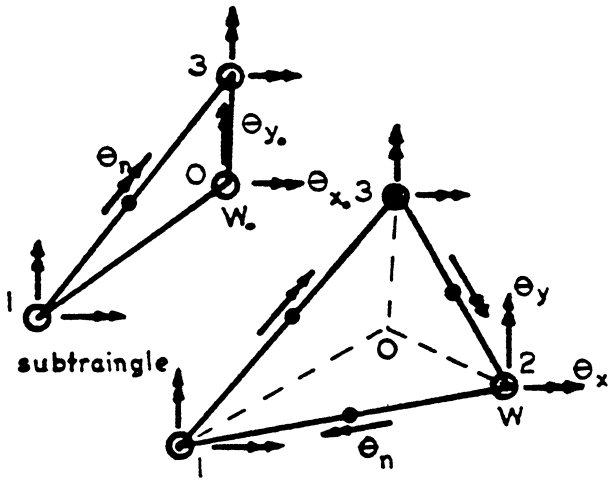

(a) LCCT12 PLATE BENDING ELEMENT

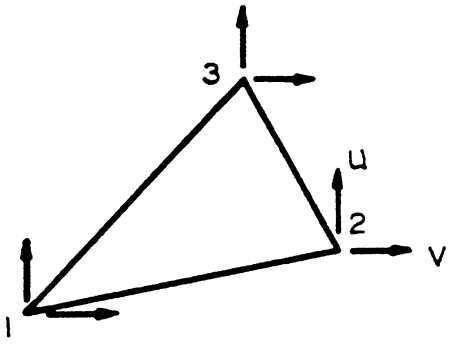

(b) CST PLANE STRESS ELEMENT

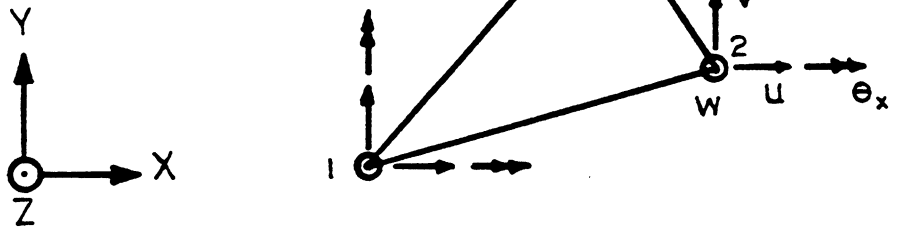

(c) LCCT9+CST SHELL ELEMENT

FIG. 5.1 LCCT9+CST TRIANGULAR FLAT SHELL ELEMENT

be used in problems where the membrane action is predominant.

Carr [88] developed a quadratic strain triangular membrane element (QST, Fig. 5.2) to represent the membrane action of the shell element. He used a complete cubic polynomial expansion for the displacement fields. The degrees of freedom are u, v, w, θ_x, θ_y, θ_z, ε_x, ε_y, and ε_{xy} at each corner node and two internal degrees of freedom u_o and v_o, which are eliminated by static condensation.

Using the QST, Carr [88] obtained significant improvements over the LCCT9+CST. However, the use of strains as nodal quantities not only present some problems in the assembly process but local perturbations may also result. Carr [88] claimed that this perturbation is small.

Other nonconforming plate bending elements can also be used. Olson et al [89] combines the nonconforming plate bending element of Zienkiewicz (NCT) with their plane stress membrane triangular element (OBT) to form a shell element. The OBT membrane element has 6 nodal degrees of freedom (Fig. 5.3), a total of 18 for the triangle. Nine kinematic constraints are applied to reduce the total degrees of freedom to 9, 3 at each node, namely u, v, and θ_z.

The OBT gives considerably better results than the CST. However, the use of incomplete polynomial expansions in the displacement fields precludes a complete convergence to the exact solution.

Irons et al [85,90] developed two synthetic plate bending elements, the A9 and the A12. They employed complete cubic polynomials for the displacement expansions and three synthetic rational functions ε_1^*, ε_2^*, and ε_3^*. The ε_i^* when expressed in area coordinates, L_i, has the form:

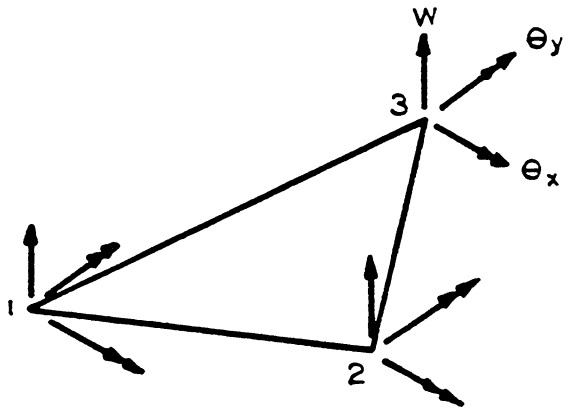

LCCT9 PLATE BENDING ELEMENT

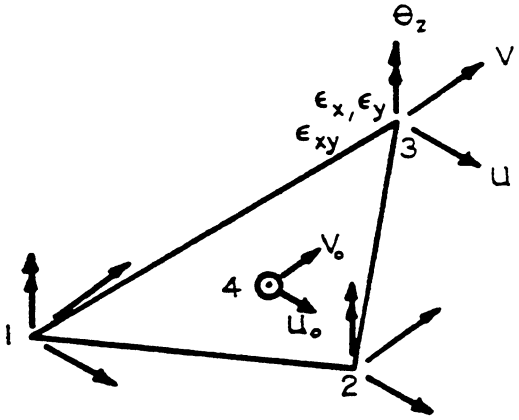

QST PLANE STRESS ELEMENT

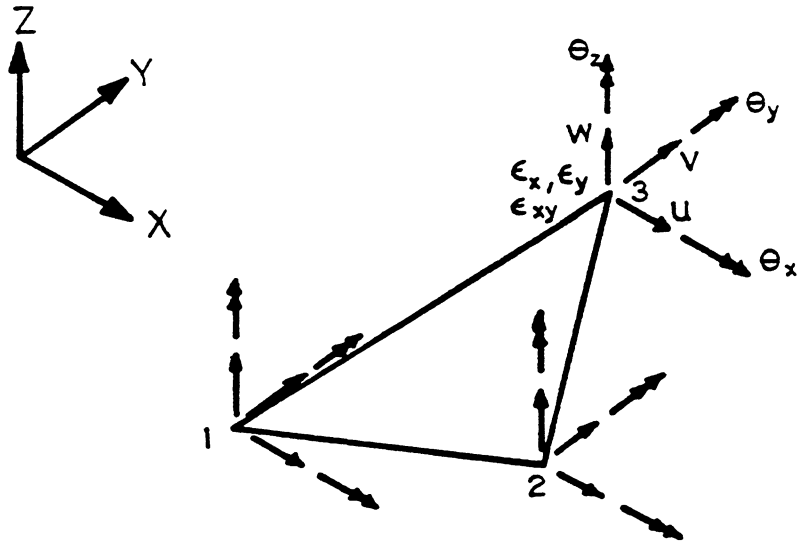

uo & vo are removed by static condensation

LCCT9+QST SHELL ELEMENT

FIG. 5.2 LCCT9+QST TRIANGULAR FLAT SHELL ELEMENT

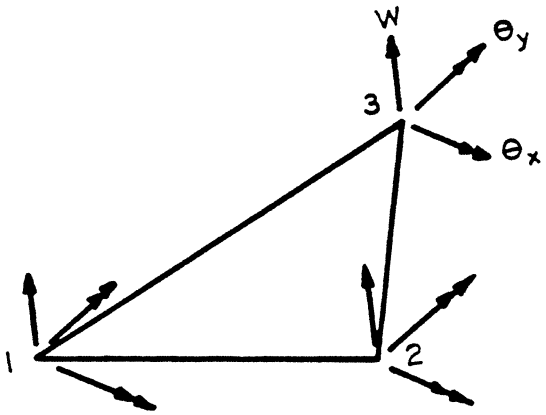

NCT PLATE BENDING ELEMENT

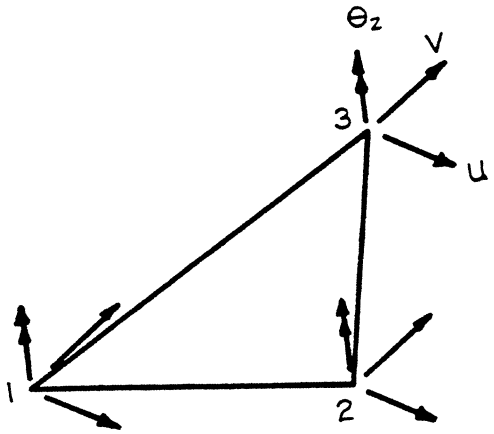

OBT PLANE STRESS ELEMENT

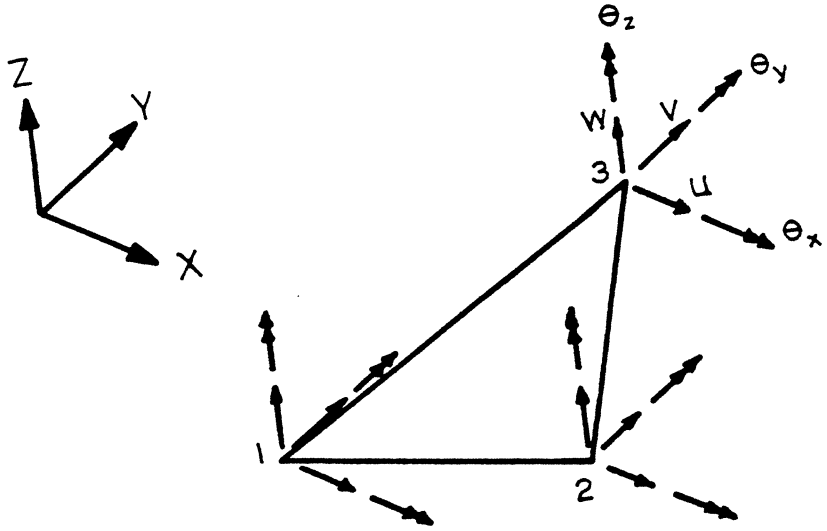

NCT+OBT SHELL ELEMENT

FIG. 5.3 NCT+OBT TRIANGULAR FLAT SHELL ELEMENT

$$\varepsilon_i^* = \frac{1}{6}(2L_i^3 - 3L_i^2 + L_i)$$

which gives correct nodal displacements but incorrect slopes along the sides of a triangle. The element is therefore nonconforming. The use of ε_i^* gives relatively smooth second derivatives and allows the element stiffness to be integrated exactly using a 3-point rule.

The A9 is obtained from A12 by constraining the normal slope along the sides to vary linearly. The degrees of freedom are the same as the LCCT9, namely w, θ_x, and θ_y at each corner node. The element when used in the context of a plate is very well behaved. However, the author has found that the convergence is very slow when it is combined with a CST membrane element to form a shell element.

(2) Quadrilateral Flat Element

Due to the inherent difficulties in representing a warped surface by a plane, the use of a quadrilateral flat element presents some problems in defining the stiffness and the subsequent assembly. Johnson [91], by defining the stiffness in an imaginary plane, overcomes these problems.

The one that is commonly used is the Q19 (Fig. 5.4a) fully compatible quadrilateral element developed by Felippa [87]. A shell element can be obtained by superimposing on Q19 four constrained linear strain triangular membrane elements (CLST, Fig. 5.4b). The resulting element has 37 DOF, the 17 internal DOF are to be eliminated by static condensation, leaving only 20 DOF as nodal DOF (Fig. 5.4c).

The Q19 is obtained by assembling four LCCT11 triangular plate bending elements, which are again formed from LCCT12 by constraining the normal slope along one side of the triangle to vary linearly.

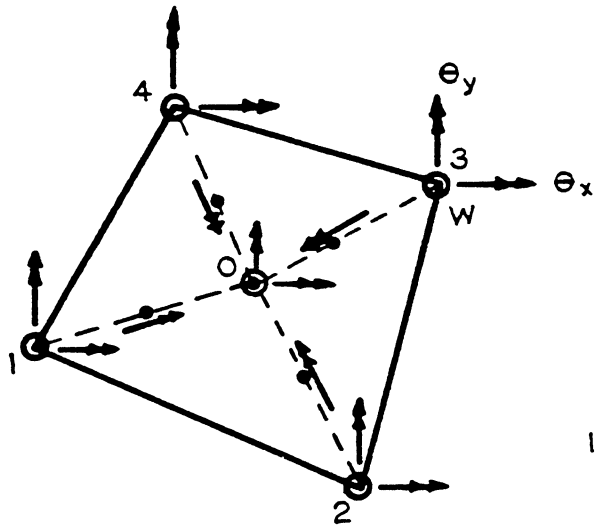

(a) Q19 PLATE BENDING ELEMENT

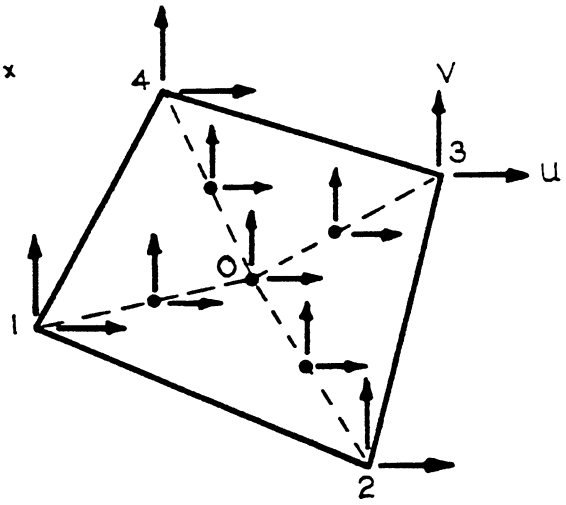

(b) 4CLST PLANE STRESS ELEMENT

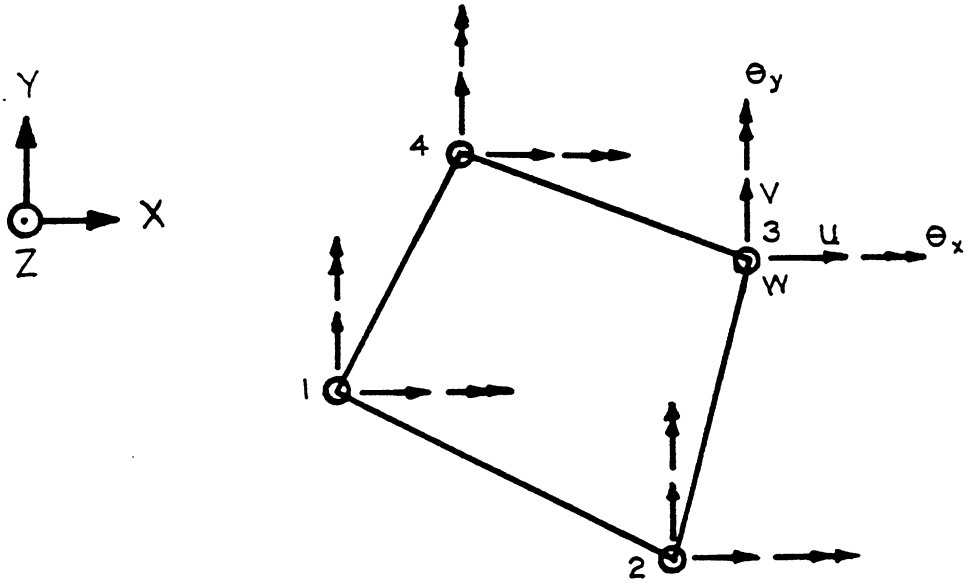

(c) Q19 + 4CLST SHELL ELEMENT

FIG. 5.4 Q19+4CLST QUADRILATERAL FLAT SHELL ELEMENT

The CLST membrane element is obtained from a linear strain triangular element by constraining the axial strains normal to and along one side of a triangle to be constant.

The Q19 + 4 CLST shell element gives considerably better results than the LCCT9 + CST. However, Lin [8] has found that the computational time required in forming the element stiffness of a Q19 is about 9 times that of a LCCT9. The use of the Q19 is therefore not easily justifiable from a computational standpoint, especially for nonlinear analyses.

(3) Other Flat Elements

All of the previous discussions have been focused on displacement formulations. Other formulations are possible, such as the hybrid elements of Pian [92] and Allman [93] who use the generalized complementary energy principle. Another possibility is to make use of the duality principle, such as the mixed-Mongrel planar shell element developed by Hung et al [94]. However, the details of those mentioned formulations will not be reviewed here.

5.3 Curved Shell Elements

This form of shell element usually gives a better geometrical representation of the shell surface. However, the use of cubic or quintic expansion in the displacement fields results in a large number of nodal unknowns which usually contain some first and higher order derivatives as field variables. This makes the imposition of the boundary conditions more difficult. The curved geometry also has a detrimental effect in that the rigid body modes are more difficult to reproduce. The use of curvatures to define the geometry

also makes them impossible to use to model a shell with sharp corners and discontinuities.

The shell element may be formulated in either deep, shallow, or inconsistent shell theory. Two of the commonly used shell theories are those of Koiter and Sanders, and of Donnell-Mashtari-Vlassov (DMV). The shell element thus derived is good within the validity of the chosen shell theory. It has been found by Batoz [95] in his buckling of arches analysis that the critical load is very dependent on the choice of the strain-displacement relationships, especially in the deep shell range.

Thomas et al [96] developed a doubly curved triangular shell element (TGT, Fig. 5.5) using a consistent deep shell theory for the strain-displacement relationships. Complete cubic polynomials are used and the continuity in the normal slope between adjacent shell elements is ensured through the use of Lagrange multipliers.

The geometry of the shell element is described by the curvilinear coordinate systems α and β, and the curvatures at a point. There are 9 DOF (u, v, w, $u_{,\alpha}$, $u_{,\beta}$, $v_{,\alpha}$, $v_{,\beta}$, $w_{,\alpha}$, $w_{,\beta}$) at each corner node and 3 internal DOF (u_o, v_o, w_o) which are eliminated by static condensation. Together with the unknown moment m_o to enforce slope compatibility, a total of 30 DOF exists within an element.

The zero diagonals encountered in the stiffness matrix because of the use of Lagrange multipliers also require special treatment in equation solving.

Using Koiter's shallow shell theory, Dawe [97] developed a curved shell element (DAT, Fig. 5.6) with incomplete quintic polynomials.

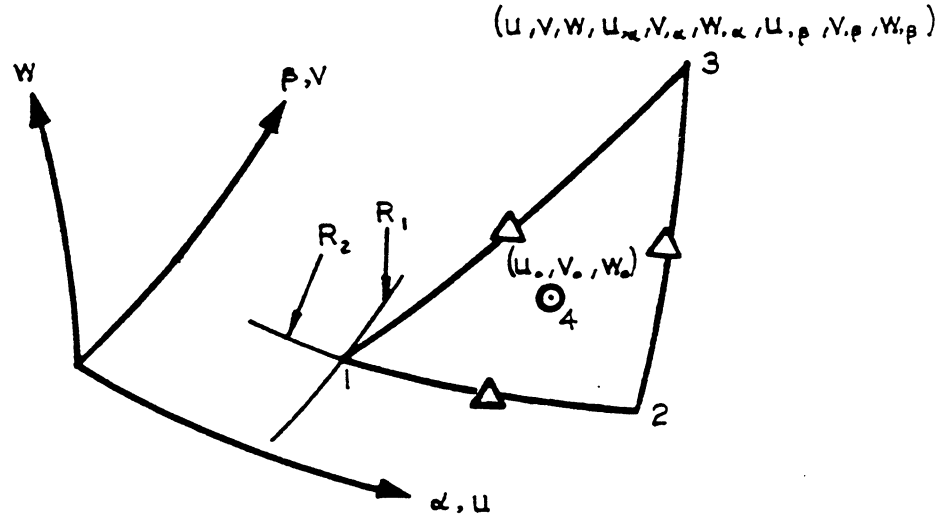

VIRGIN TGT SHELL ELEMENT

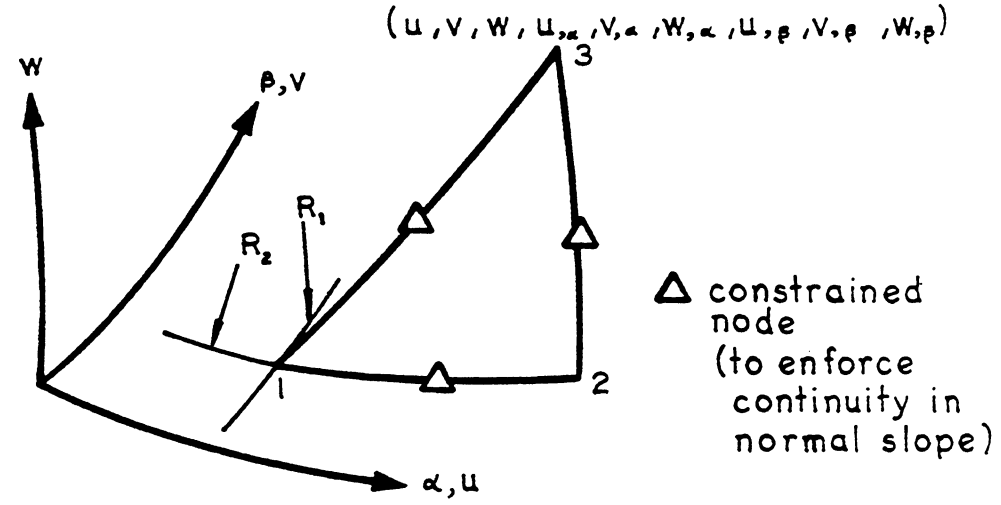

FINAL TGT SHELL ELEMENT

FIG. 5.5 TGT CURVED TRIANGULAR SHELL ELEMENT

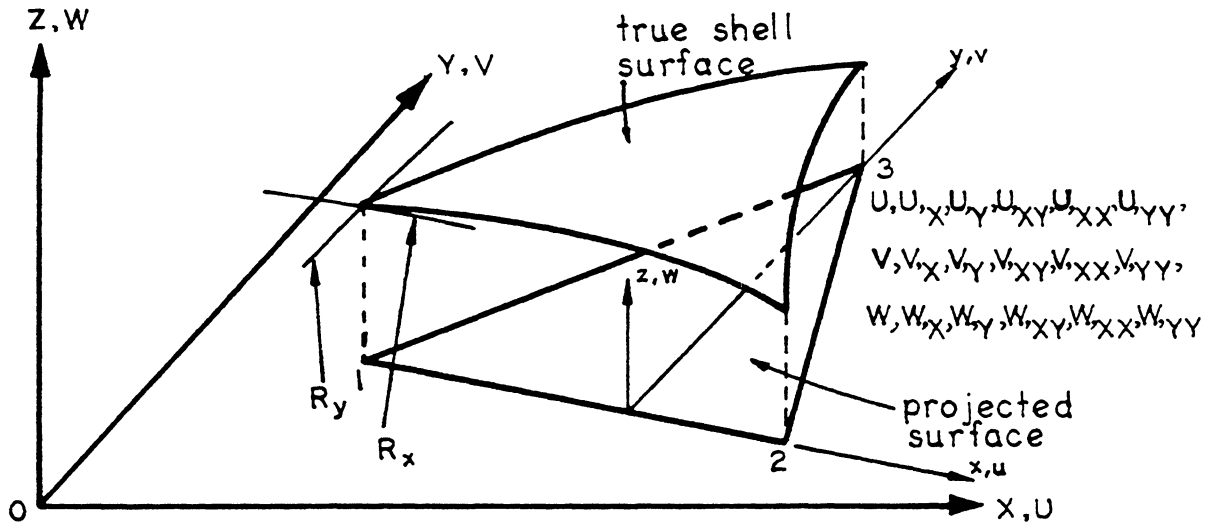

FIG. 5.6 DAT CURVED TRIANGULAR SHELL ELEMENT

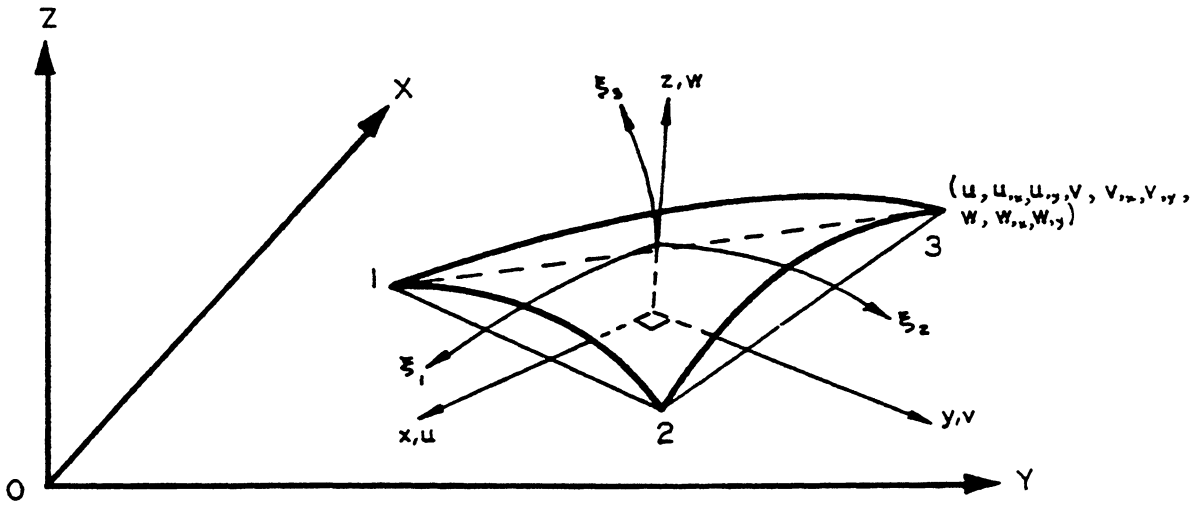

FIG. 5.7 DHT TRIANGULAR SHALLOW SHELL ELEMENT

There are 18 DOF (u, $u_{,x}$, $u_{,y}$, $u_{,xx}$, $u_{,yy}$, $u_{,xy}$, v, $v_{,x}$..... $v_{,xy}$, w, $w_{,x}$..... $w_{,xy}$) at each node, a total of 54 for the element. The large amount of nodal unknowns is a serious handicap in solving non-linear shell problems.

Dhatt [98] by utilizing a combination of discrete Kirchhoff shear constraint and the Sander's shallow shell theory, developed a curved triangular shell element (DHT, Fig. 5.7). He uses a 9-term incomplete cubic polynomial for the u, v, and w displacements and a complete quadratic polynomial for the rotations, θ_x and θ_y.

The shallow quadratic surface is approximated by the procedure of Bonnes et al [99]. There are 9 DOF (u, $u_{,x}$, $u_{,y}$, v, $v_{,x}$, $v_{,y}$, w, $w_{,x}$, $w_{,y}$) at each node, a total of 27 for the element.

5.4 3D Isoparametric Solid

By treating a shell as a 3D continuum, the stiffness can be obtained by using 3D theory of elasticity for the strain-displacement relationships. Here, little attention has to be paid to the uncertainties of the classical thin shell theories.

The isoparametric elements satisfy the constant strain states, including all the rigid body modes and maintaining C° continuity.

The element, when used in thin shell situations, may tend to be overstiff due to the existence of the extraneous shear strain energy. As a result, the bending mode cannot be represented correctly. Doherty [100] suggests the use of reduced integration and Wilson [101] introduces the use of incompatible modes in order to correct this deficiency. The two techniques have been applied to the thin shell situation by Dovey [102].

The commonly used shell type can belong to either a serendipity

or a Lagrange family. The two are only different in the polynomial expansion in the displacements. Figure 5.8 illustrates the terms in the Pascal triangle included in the serendipity and the Lagrange element for a polynomial expansion of order n. The difference between the serendipity and the Lagrange element is the missing higher order terms in the serendipity element (Fig. 5.8).

The elements that are commonly used are the 8-node element (Fig. 5.9a), 16-node element (Fig. 5.9b), and to some extent the 27-node element (Fig. 5.9c). Higher order elements are possible but they are not easily justified from a computational standpoint.

The geometry is completely described by the nodal point coordinates, and the coordinates at any other locations can be obtained by interpolation by making use of the same shape functions that describe the displacement fields.

There are 3 DOF (u,v,w) at each node. The usual problem associated with the missing normal in-plane rotation does not exist in this case.

5.5 Degenerate Isoparametric Elements

The use of the degeneration concept is credited to Ahmad [103]. The idea involves the coupling of the top and bottom in-plane displacements to form a rotation by assuming a linear variation in displacements across the depth of an element. This avoids the numerical sensitivities that may exist in the case of a thin shell [102].

Like the 3D isoparametric solid, the isoparametric nature of the element satisfies the constant strain states, including all rigid body modes, and maintains a C° continuity in displacements [107].

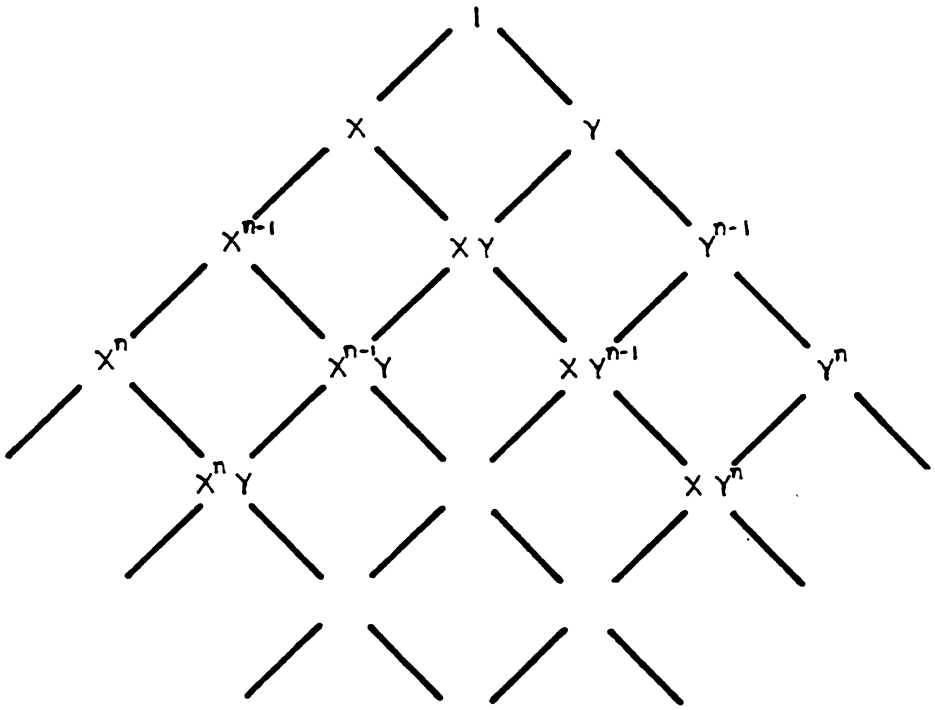

SERENDIPITY

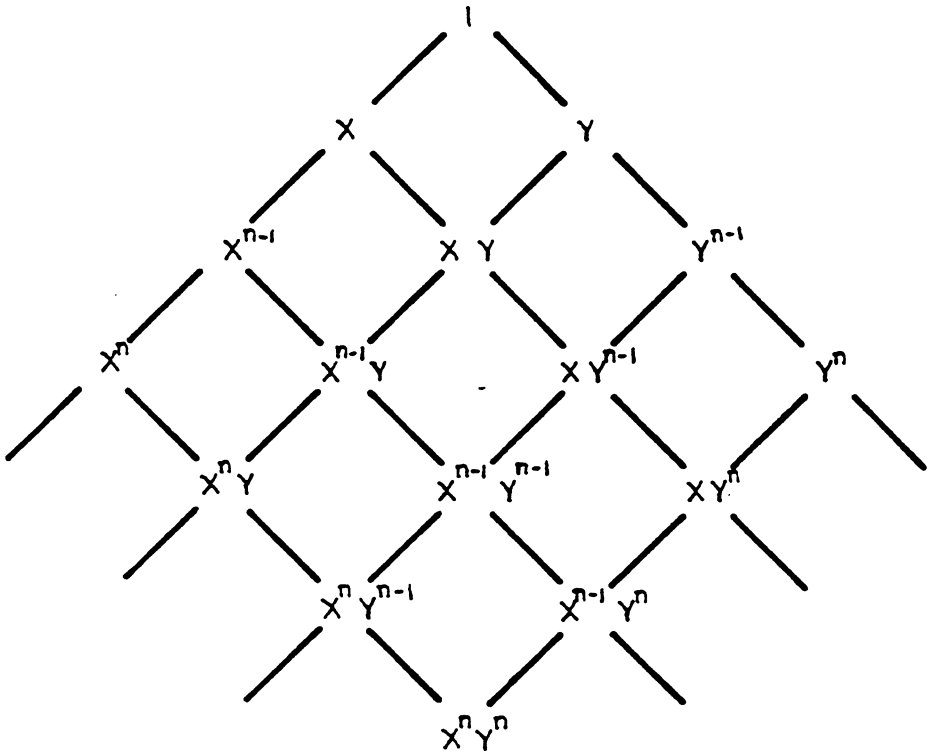

LAGRANGE

FIG. 5.8 TERMS INCLUDED IN THE SERENDIPITY AND LAGRANGE ELEMENTS OF ORDER n

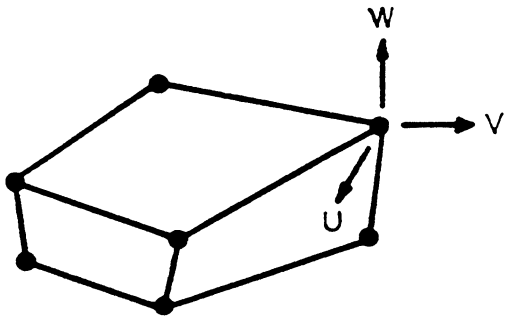

(a) 8 NODE ELEMENT

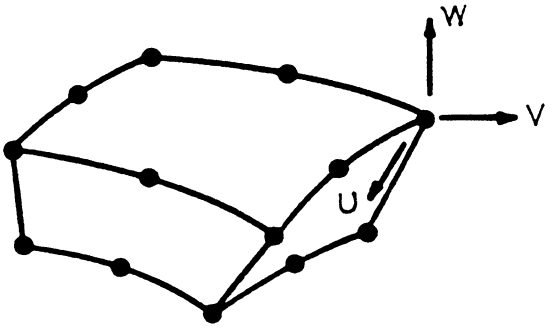

(b) 16 NODE ELEMENT

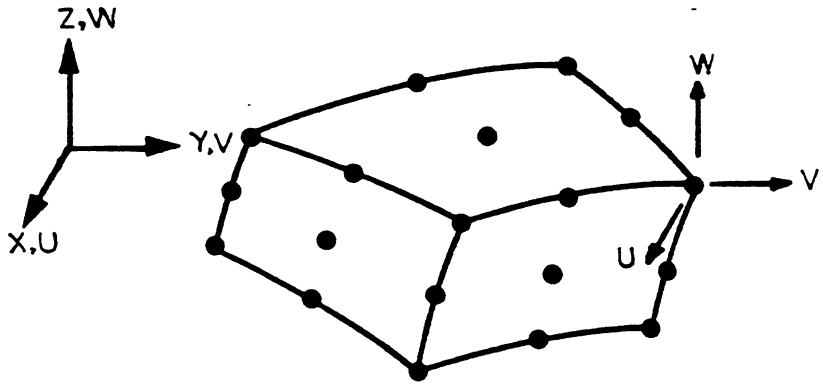

(c) 27 NODE ELEMENT

FIG. 5.9 TYPICAL ISOPARAMETRIC SOLID ELEMENT

The degenerate elements, however, are computationally more efficient than the corresponding 3D solid because of the fewer DOF and the smaller bandwidth.

This class of element ranges from a simple bilinear element with selective integration involving different orders of integration for membrane and shear terms [104] to a very sophisticated element employing the discrete Kirchhoff shear constraint [105].

The bilinear degenerate shell (BDS, Fig. 5.10) developed by Kanoknukulchai and Taylor [104] employs a selective integration scheme where the transverse shear stiffness is under-integrated using a 1-point rule. Normal in-plane rotational stiffness is obtained by constraining the normal rotation to be an averaged value.

The element is simple and is highly competitive with some higher order elements. However, Van Gruenen [26] has found that the element is rank deficient and the zero energy mode propagates in a weakly constrained system. This will place some restrictions on its usefulness.

Better elements belong to the quadratic element of the Ahmad shell family. These elements, when used in connection with reduced, selective integrations, and with internal bubble functions, are very efficient.

The 8-node serendipity (Fig. 5.11a) [19] uses a 2×2 Gaussian integration scheme to obtain its stiffness.

Onate [20] (Fig. 5.11b) demonstrates how the 8-node serendipity element can be improved by using a selective integration and an internal bubble function at the center node. The DOF (u_0, v_0, w_0, α_0 , β_0) at the center node are weakly constrained and are later

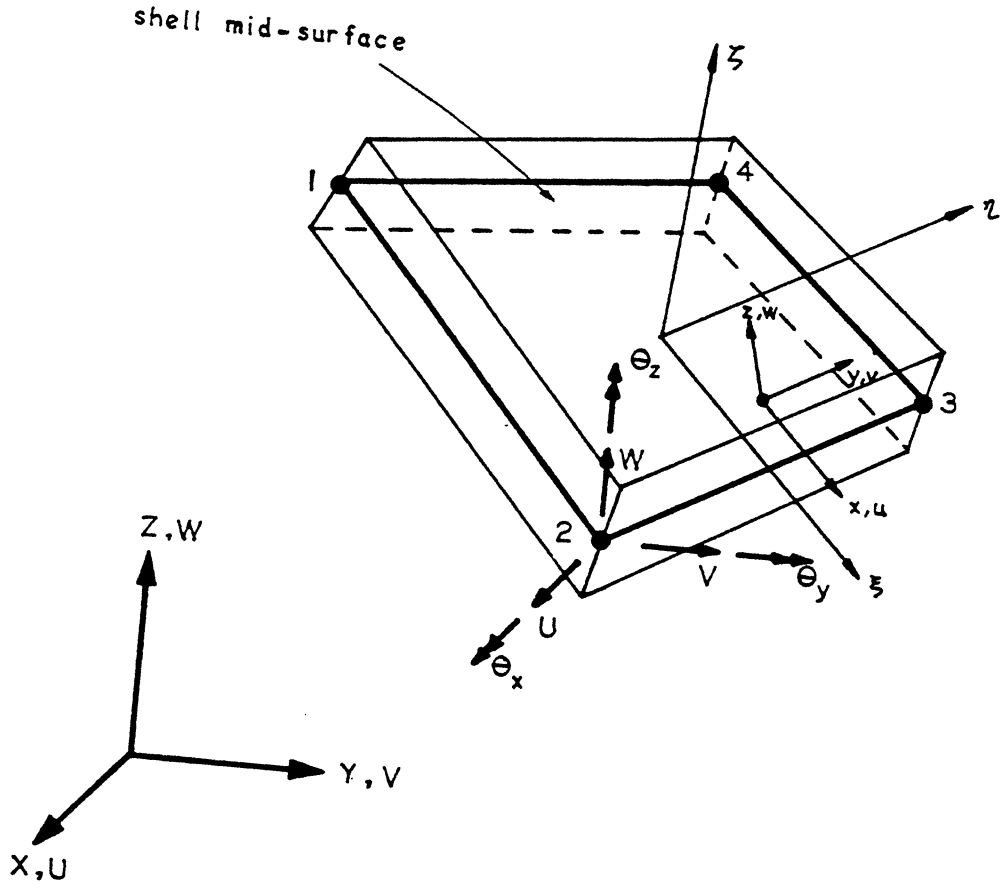

FIG. 5.10 BDS DEGENERATE SHELL ELEMENT

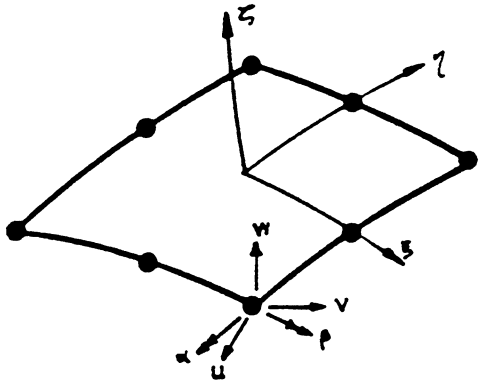

(a) 8 NODE SERENDIPITY

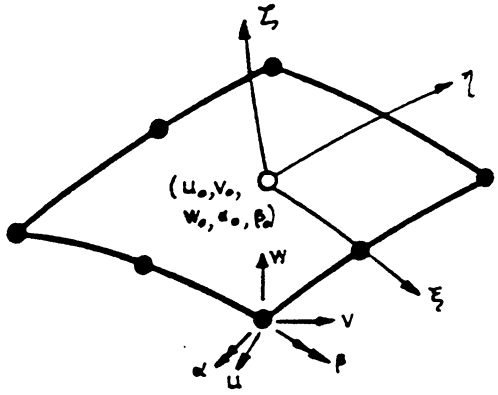

(b) ONATE'S QUADRATIC ELEMENT

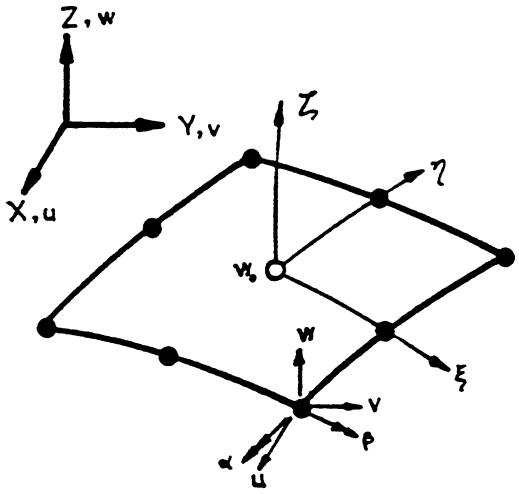

o internal bubble function

(c) TALHA'S QUADRATIC ELEMENT

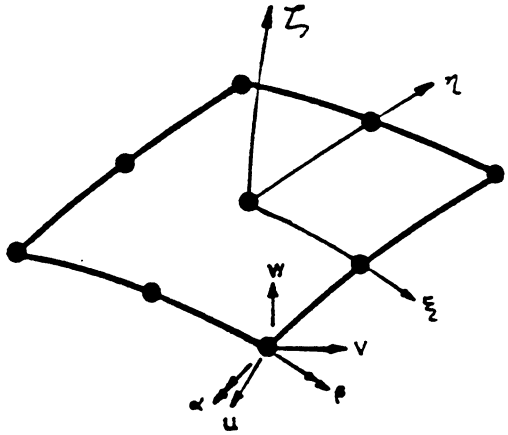

(d) 9 NODE LAGRANGE ELEMENT

FIG. 5.11 TYPICAL SHELL ELEMENT OF THE AHMAD FAMILY

eliminated by static condensation.

Talha [106] (Fig. 5.11c) developed an 8-node serendipity with one internal DOF (w_o) which is constrained at the center node and eliminated by static condensation. He uses a fully reduced integration for the evaluation of the element stiffness.

Pawsey [107] (Fig. 5.11d) developed a Lagrange element with different order of integration for different strain energy components. His element only involves the eight boundary nodes for a suitable choice of location of the center node.

Irons [105] (Fig. 5.12) developed the most complicated isoparametric element at present. The virgin element has 45 DOF, 3 translational DOF for each node and 2 rotational DOF at each loof node along the element sides and at the center of the element. The 11 shear constraints are then applied to reduce the total number of DOF to 34. The element thus obtained is of C^1 continuity.

The main drawback is the complex inversions and calculations involved at the element level, which are necessary to enforce the shear constraints, an undesirable situation from a computational viewpoint.

5.6 Comparison of Elements

The criteria for the selection of an element for use in the nonlinear analysis of shell structures can be explicitly defined following the arguments described in Section 5.1. The criteria are:

(a) Minimize the discretization errors.

(b) Include all the constant strain states.

(c) Include all the rigid body modes.

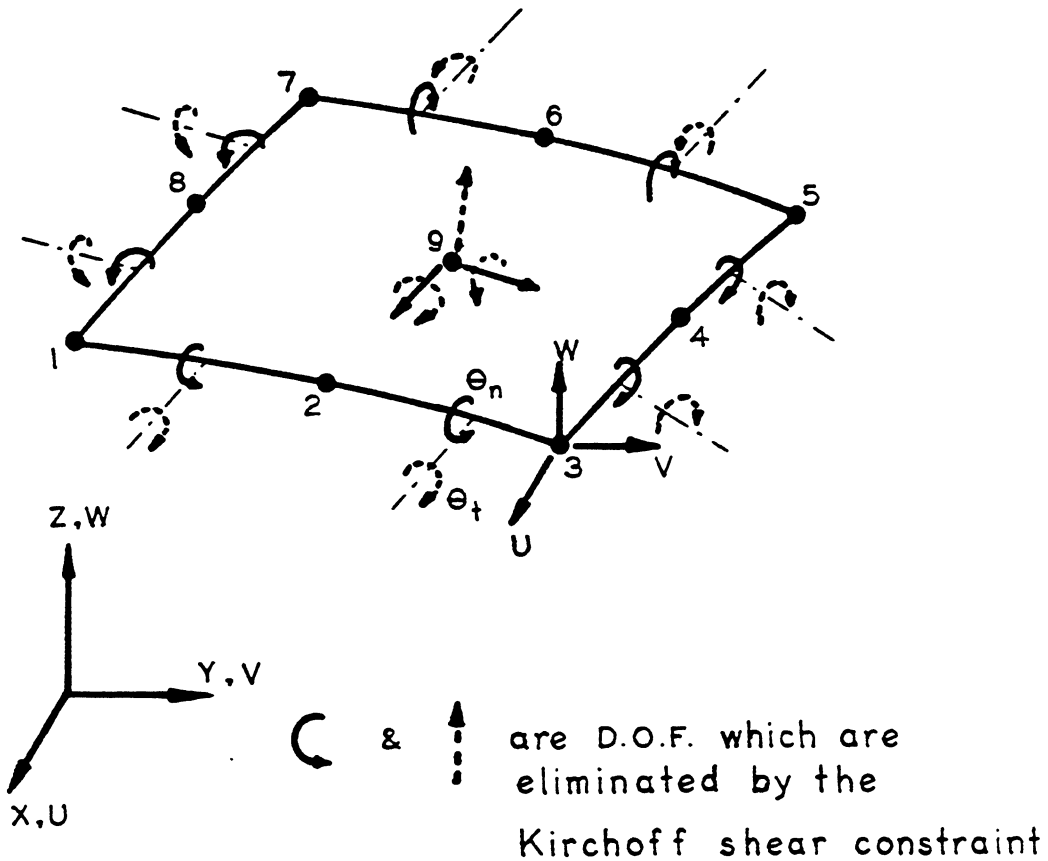

FIG. 5.12 SEMILOOF SHELL ELEMENT

(d) Minimize the computational time required for forming the element stiffnesses for a given degree of accuracy desired.

(1) Discretization Errors

In general, the flat element is a poor competitor in representing the shell geometry, while curved shell and isoparametric elements can adequately represent the smooth shell surface. However, when the shell encountered has sharp corners or discontinuities, the use of curved shell elements is undesirable.

(2) Constant Strain

The constant strain states requirement is the easiest to satisfy. It requires that the displacement expansions be one order higher than the highest derivatives. Consequently, all the elements described satisfy this condition.

(3) Rigid Body Modes

The rigid body modes requirement is the most difficult to satisfy and is very difficult to generalize. Detailed investigation involves an eigenvalue analysis on the shell element. In general, the flat elements with complete polynomial expansions and the isoparametric elements include all the required rigid body modes.

(4) Numerical Efficiency

To assess the numerical efficiency of a given element, one should compare the required total number of DOF of different elements in order to achieve the same degree of accuracy in the solution. The total number of DOF is not the only controlling parameter, but it usually reflects the required mesh sizes and the solution effort used in solving the equilibrium equations and should represent the required overall solution effort adequately.

5.7 Selection of Elements

To demonstrate the accuracy and efficiency of different elements, a cylindrical shell example has been chosen as a basis for comparing the elements.

5.7.1 Example 5.1 - Cylindrical Shell

The cylindrical shell roof analyzed by Scordelis and Lo [108], using classical shell theory, has been used by many investigators as a basis for the comparisons of their finite element results. Here, the same shell is used in the present study to study the relative numerical efficiency and the accuracy of different elements described previously together with the results obtained from the proposed 9-node degenerate element with Lagrangian shape functions, which is to be described later.

The geometry and the material properties of the shell are shown in Fig. 5.13. It spans 50 feet longitudinally with a thickness of 3 inches. The radius is 25 feet and it subtends a central angle of 80°. The shell has free longitudinal edges and is simply supported at its two ends. One-quarter of the shell is analyzed for a uniform gravity load of 90 psf of surface.

The results for the mid-span vertical edge deflection (V_A) of the shell obtained using different elements are summarized in Table 5.1 and plotted in Fig. 5.14. The "exact" value of V_A obtained by Scordelis and Lo [108] is 3.70 inches and the percentage error given in Table 5.1 is with reference to this value.

The results of the analyses indicate that the flat element with a constant strain membrane element, such as the LCCT9 + CST element and the A9 + CST element, converges very slowly. Significant

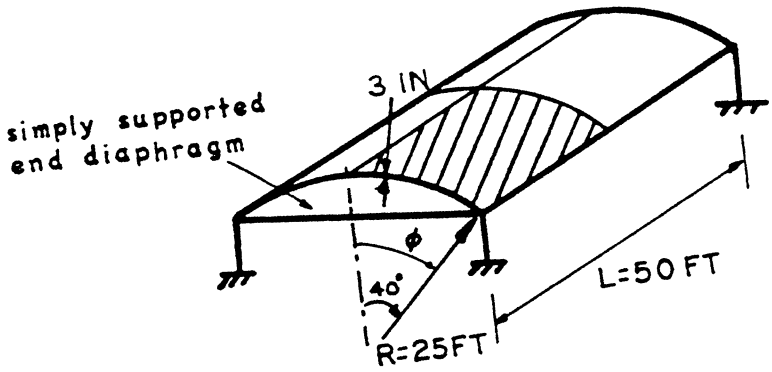

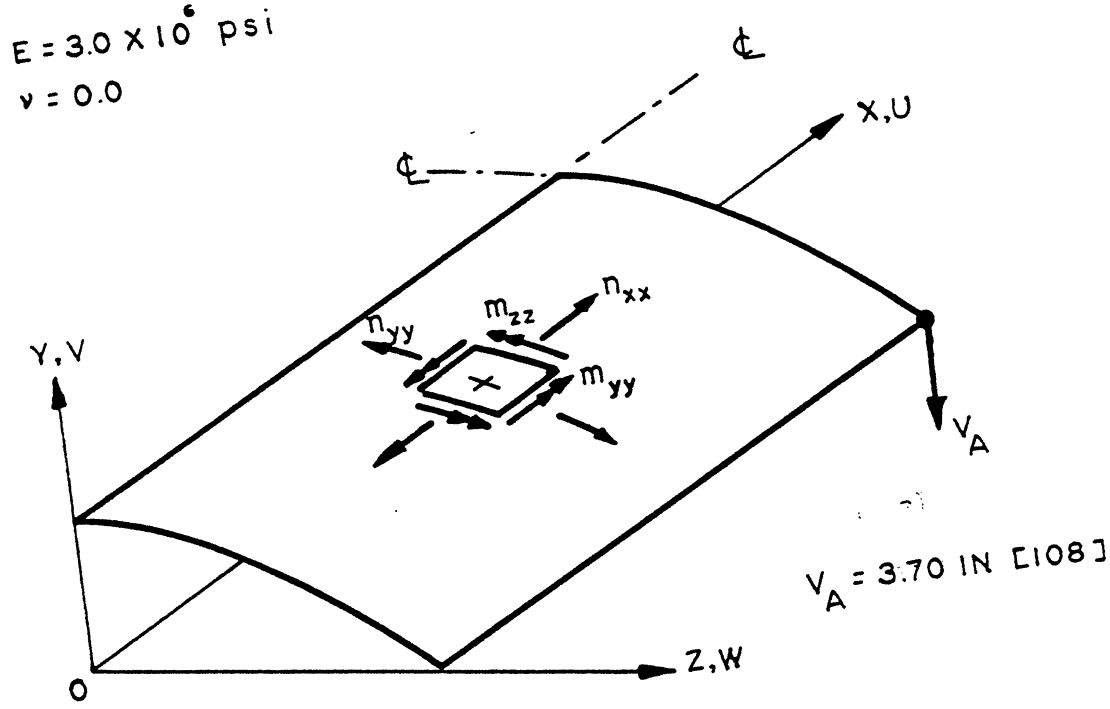

FIG. 5.13 CYLINDRICAL SHELL ROOF [108] (EX. 5.1) - GEOMETRY AND MATERIAL PROPERTIES

TABLE 5.1 EXAMPLE 5.1 - COMPARISON OF V_A FOR DIFFERENT SHELL ELEMENTS WITH VALUE OBTAINED BY SCORDELIS AND LO [108]

Type	Element	DOF/ Element	Mesh Sizes	Total DOF	% Error in V_A
Flat Planar Shell Element	Clough et al [86] (LCCT9 + CST)	15	4x5 8x12 12x18 16x22	180 546 1482 2346	-26.4 -13.3 - 7.7 - 5.8
	Carr [88] (LCCT9 + QST)	27	4x5 8x12	270 1053	- 2.2 - 1.0
	Olson et al [89] (NCT + OBT)	18	2x2 3x3 4x4 5x5 10x10	30 63 108 165 630	+23.5 - 1.9 - 4.6 - 4.7 - 3.7
	Irons et al [85] (A9 + CST)	15	4x4 8x4	121 433	-31.3 -16.0
	Felippa [87] (Q19 + 4CLST)	20	4x5 8x12	180 702	- 4.6 - 2.7
Curved Shell Element	Thomas et al [96] (TGT)*	30	- - - -	100 180 260 370	- 3.0 - 2.2 - 1.8 - 2.2
	Dawe [97] (DAT)*	54	1x1 2x2 3x3	72 162 288	- 4.8 - 1.6 ≈ 0.0
	Dhatt [98] (DHT)	27	2x3 4x5 8x12	108 270 1053	- 5.2 + 1.3 + 0.9
Isoparametric Solid	Dovey [102] (S18R)	48	2x2 3x3	126 240	- 1.4 - 0.16

Table 5.1 (cont'd)

Type	Element	DOF/ Element	Mesh Sizes	Total DOF	% Error in V_A
Degenerated Isoparametric Element	Kanoknukulchai [104] (BDS)	24	2x2 4x4 8x8 -	24 120 350 530	+23.0 - 6.5 - 4.6 - 3.8
	Zienkiewicz et al [19] (S8)	40	1x1 2x2 3x3 4x4	23 76 159 272	+ 5.4 - 2.7 - 0.2 ≈ 0.0
	Proposed Element (L9)	45	1x1 2x2	28 96	26.2 1.6

*The total number of D.O.F. are scaled values from the available figures.

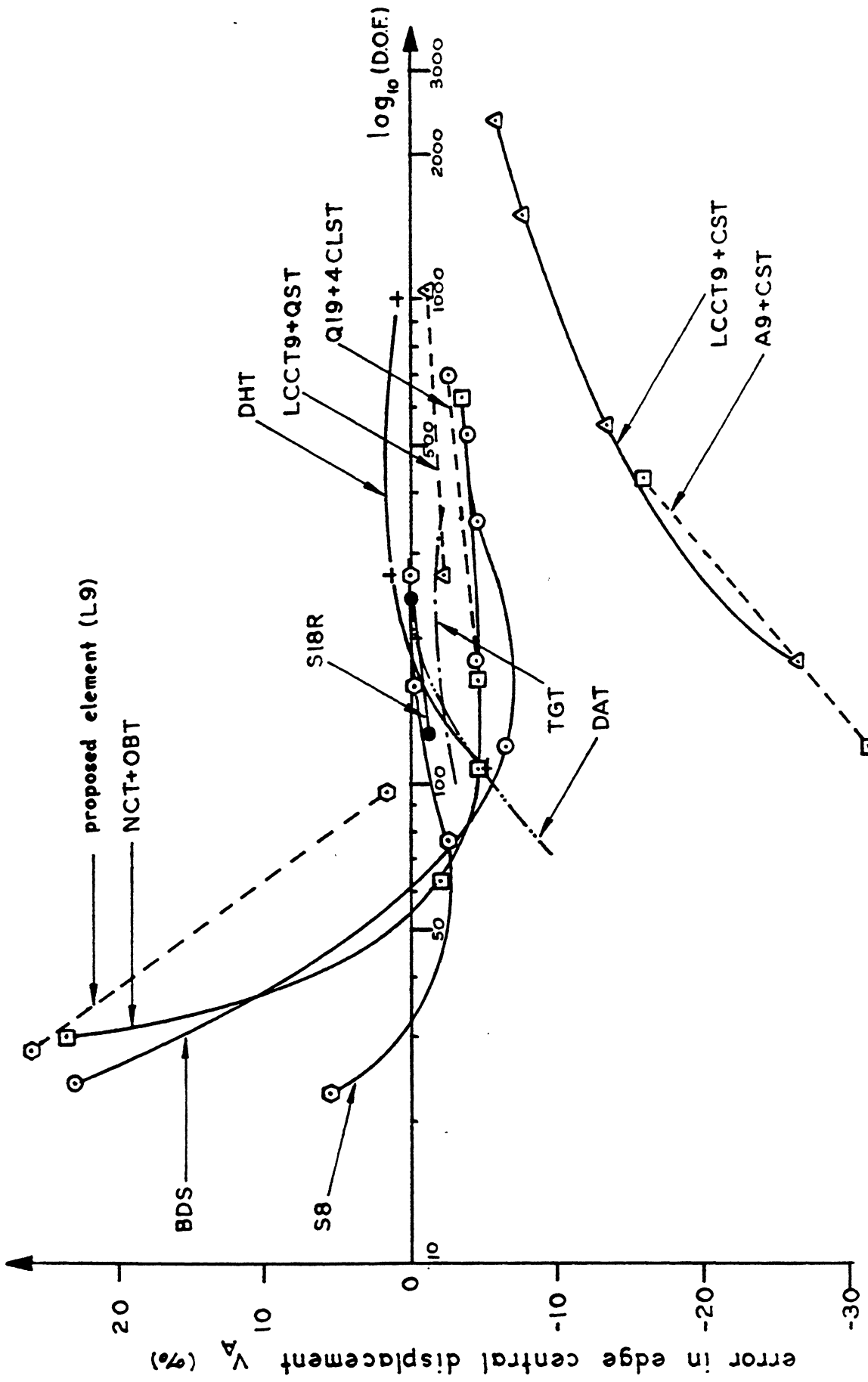

FIG. 5.14 CYLINDRICAL SHELL ROOF [108] (EX. 5.1) - CONVERGENCE STUDY OF MID-SPAN EDGE VERTICAL DEFLECTION, V_A, FOR VARIOUS SHELL ELEMENTS

improvement is obtained by using a refined membrane element; examples are the Q19 + 4CLST element and the LCCT9 + QST element.

The curved shell elements derived from curved shell theory converge to the true solution for a relatively coarse mesh.

The good convergence characteristics of the quadratic isoparametric element are especially noted. For a very coarse mesh of 2 x 2, Dovey's [102] S18R 16-node element attains an error of only 1.4% in the displacement V_A; Taylor's S8 [19] has an error of 2.7%; and for the proposed element, an error of 1.6% is found.

It is then tentatively concluded that the S18R solid element and the degenerate quadratic isoparametric elements seem to be the most promising. However, the larger bandwidth within an S18R element makes it less efficient to use. Consequently, the degenerate elements seem to be the best of all the elements studied and, in particular, the proposed element is proven to be more reliable, as discussed later.

To further illustrate the accuracy of the proposed element, the results obtained from a computer program developed by Van Greunen [26], who uses the A9 + CST flat shell element, are compared with that of the proposed element. The results are shown in Fig. 5.15.

It can be seen that the proposed element represents the membrane and the bending behavior adequately and gives good agreement for both the displacements and the internal forces. The A9, which is considered to be the best triangular plate bending element [15,26], when it combines with CST to form a shell element, still gives significant errors in the longitudinal bending moment m_{zz} (Fig. 5.15) for a fine mesh of 8 x 8. The longitudinal moment, however, is small compared to the overall total midspan statical moment.

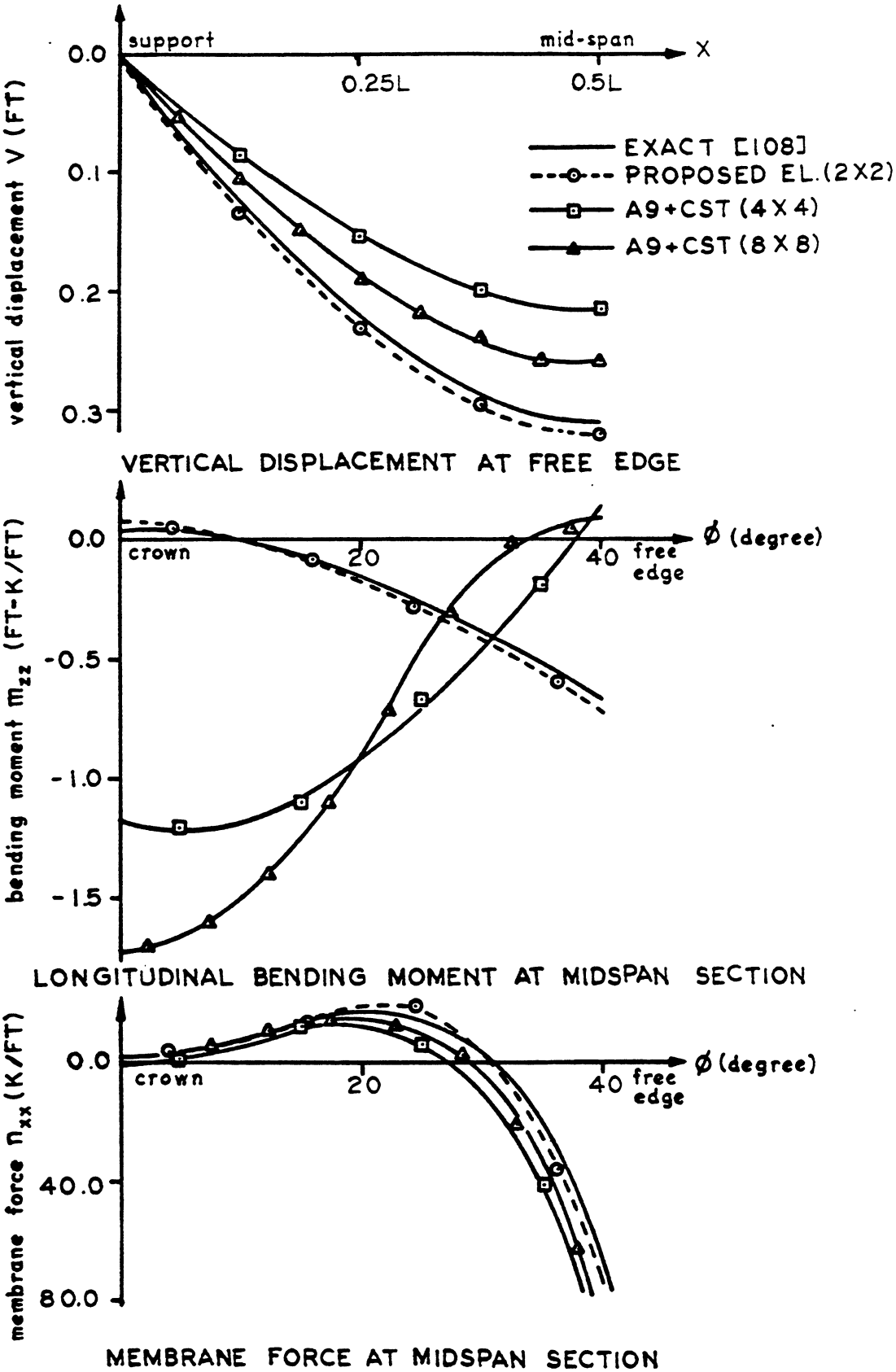

FIG. 5.15 CYLINDRICAL SHELL ROOF (EX. 5.1) - COMPARISON OF DISPLACEMENTS AND INTERNAL FORCES FOR THE PROPOSED ELEMENT AND A9+CST

Similarly, a large discrepancy in the vertical displacement V_A remains for a fine mesh of 8 x 8 using the A9 + CST shell element.

To demonstrate its efficiency, the solution time for the proposed element and for the A9 + CST element are again compared. The solution times required for the cylindrical shell example to be solved on the CDC6400 computer for the two elements are summarized in Table 5.2.

It can be seen that the time required to form each element stiffness is longer for the proposed element as compared to each A9 + CST element. However, considering the accuracy attained for a coarse mesh of 2 x 2 using the proposed element (Fig. 5.15), with a total solution time of about 1/4 of that of a more refined mesh of 8 x 8 using the A9 + CST element, the efficiency of the proposed element is clearly proven.

5.7.2 Conclusion

The efficiency and the accuracy of the proposed element (degenerate isoparametric 9-node element) are well demonstrated in Example 5.1. The inclusion of the constant strain states and the required rigid body modes guarantee the convergence of the element. The curved geometry of the element also minimizes the discretization error in the geometry.

The capability of representing high stress gradients within an element allows the use of fewer elements for the whole structure. The computer storage required in the solution process is then reduced and makes the nonlinear analysis possible.

The use of fewer elements will also necessitate that the proposed element can represent the varying material properties within an

TABLE 5.2 - EXAMPLE 5.1 - COMPARISON OF THE EFFICIENCY OF THE PROPOSED ELEMENT AND THE A9 + CST SHELL ELEMENT

Element Type	Proposed Element		A9 + CST Shell Element	
Mesh Sizes	1 x 1	2 x 2	4 x 4	8 x 8
Number of Equations	28	96	121	433
Number of Elements	1	4	32	128
Time in Forming the Element Stiffnesses (sec)	2.75	10.84	6.63	25.65
Time in Solving Equations (sec)	0.21	2.26	1.72	19.59
Total Solution Time (sec)	3.81	16.29	12.60	66.12

element in a nonlinear analysis considering geometric and material nonlinearities. This should cause no problem when the proposed higher order element is used, because the material properties can always be evaluated and varied at the several integration points within the element.

The degenerate concept also allows an extension to include the nonlinear geometric effects very easily by adopting a 3D general theory of elasticity, as discussed in Chapter 2, without any regard to the uncertainties in the classical shell theory.

It is because of these simplicities, as well as the efficiency and the accuracy of the proposed element, that it is adopted in the present study. A detailed description of the proposed shell element can be found in Chapter 6.

6. FINITE ELEMENT FORMULATION FOR THE REINFORCED CONCRETE SHELL ELEMENT FOR NONLINEAR ANALYSIS

6.1 Discretization of the Equations of Motion

The equilibrium condition of a deformable body in the current state with reference to the last known configuration is mathematically represented by Eq. 2.43.

$$\int_{B_1} ({}_1\tau_{ij}\delta\Delta_1\eta_{ij} + {}_1C_{ijkl}\Delta_1e_{kl}\delta\Delta_1e_{ij})\, dv = \int_{\partial B_1} {}^2_1t_i\delta^2_1u_i\, da - \int_{B_1} {}_1\tau_{ij}\delta\Delta_1e_{ij}\, dv$$

In the present study, a finite element displacement formulation is used in which the displacement fields are assumed for each subdomain which is called an element. The equilibrium equation for each element at the element level can then be written as:

$$\underset{\sim}{K}^e_E\, \underset{\sim}{r} + \underset{\sim}{K}^e_G\, \underset{\sim}{r} = \underset{\sim}{R}^e_E - \underset{\sim}{R}^e_I \qquad (6.1)$$

where

$\underset{\sim}{K}^e_E = \int_{B_1} {}_1C_{ijkl}\Delta_1e_{kl}\delta\Delta_1e_{ij}\, dv$ = Element elastic stiffness

$\underset{\sim}{K}^e_G = \int_{B_1} {}_1\tau_{ij}\delta\Delta_1\eta_{ij}\, dv$ = Element geometric stiffness

$\underset{\sim}{R}^e_E = \int_{\partial B_1} {}^2_1t_i\delta^2_1u_i\, da$ = Element external load

$\underset{\sim}{R}^e_I = \int_{B_1} {}_1\tau_{ij}\delta\Delta_1e_{ij}\, dv$ = Element internal resisting load

The equilibrium equation for the entire structure can then be obtained by a standard direct stiffness assembly process. The assembled equations of equilibrium are:

$$\Sigma \underset{\sim}{K}^e_E \underset{\sim}{r} + \Sigma \underset{\sim}{K}^e_G \underset{\sim}{r} = \Sigma \underset{\sim}{R}^e_E - \Sigma \underset{\sim}{R}^e_I \qquad (6.2)$$

where the summation Σ is applied to all the subdomains of the structure.

6.2 Description of the Shell Element used in the Present Study

As discussed in Chapter 5, the Ahmad shell element with Lagrangian interpolation functions for the displacement fields is adopted. The elastic stiffness, the geometric stiffness, the load vector due to initial stresses, and the external load can be derived once the geometry, the displacement field, and the constitutive relationship are described over the element.

6.2.1 Geometry of the Shell Element

Figure 6.1 shows a typical shell element. The geometry of the nodal points is described by the Cartesian X,Y,Z coordinates of the mid-surface of the shell and a set of surface orthogonal vectors $\underset{\sim}{V}_1$, $\underset{\sim}{V}_2$, and $\underset{\sim}{V}_3$, in which $\underset{\sim}{V}_3$ is perpendicular to the shell mid-surface and $\underset{\sim}{V}_1$ and $\underset{\sim}{V}_2$ are tangent to it.

The shape functions N_i associated with node i are:

$$N_1 = \tfrac{1}{4}\xi\eta(1+\xi)(1+\eta)$$
$$N_2 = -\tfrac{1}{4}\xi\eta(1-\xi)(1+\eta)$$
$$N_3 = \tfrac{1}{4}\xi\eta(1-\xi)(1-\eta)$$
$$N_4 = -\tfrac{1}{4}\xi\eta(1+\xi)(1-\eta)$$
$$N_5 = \tfrac{1}{2}\eta\,(1-\xi^2)(1+\eta)$$
$$N_6 = -\tfrac{1}{2}\xi\,(1-\xi)(1-\eta^2)$$
$$N_7 = -\tfrac{1}{2}\eta\,(1-\xi^2)(1-\eta)$$
$$N_8 = \tfrac{1}{2}\xi\,(1+\xi)(1-\eta^2)$$
$$N_9 = (1-\xi^2)(1-\eta^2)$$

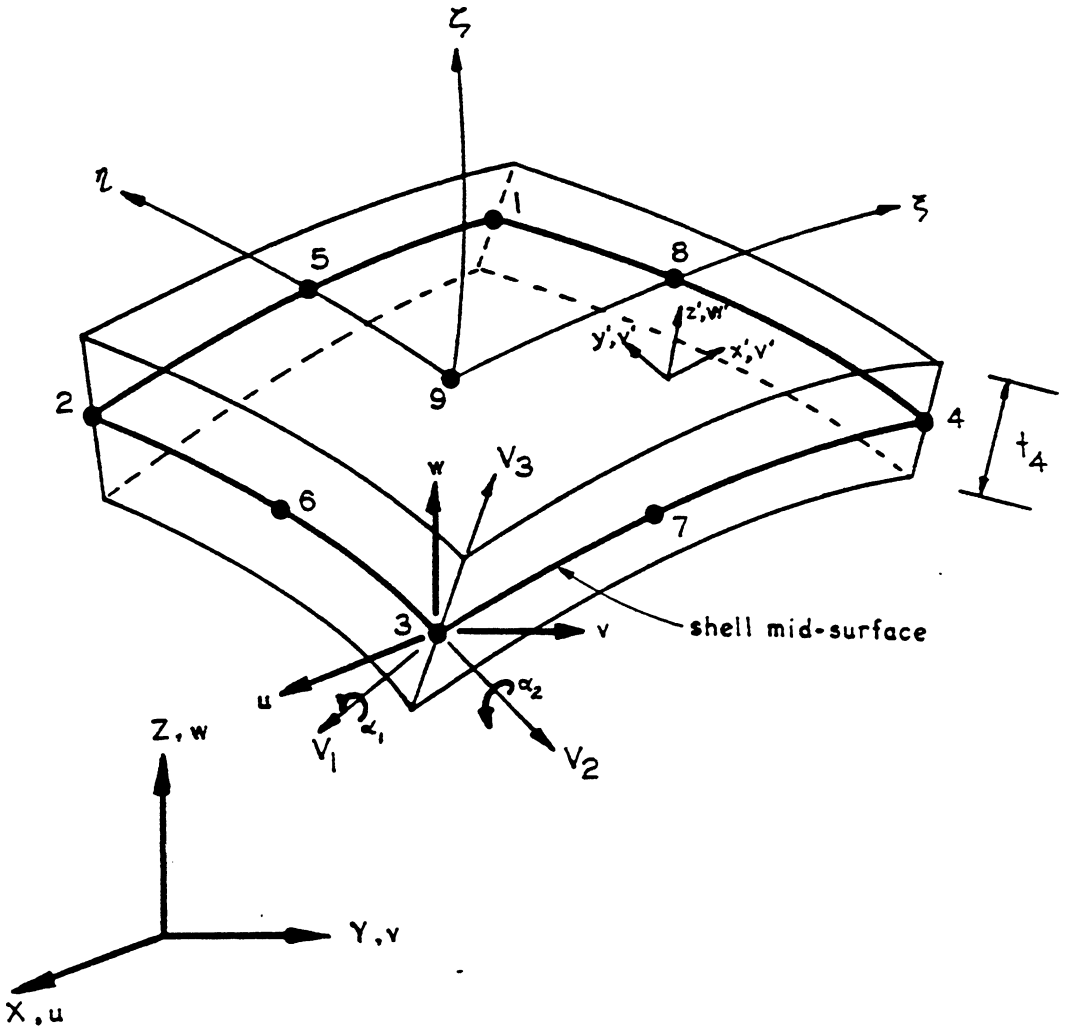

FIG. 6.1 GEOMETRY AND DEGREES OF FREEDOM OF THE SHELL ELEMENT

in which ξ and η are natural coordinates in the plane of the shell and ζ is normal to it.

The coordinates of a point within the shell element can be obtained by interpolation.

$$\begin{bmatrix} X \\ Y \\ Z \end{bmatrix} = \underset{\sim}{N}^a \underset{\sim}{X}^a + \frac{\zeta}{2} t^a \underset{\sim}{N}^a \underset{\sim}{V}_3^a \tag{6.3}$$

where

$$\underset{\sim}{X}^a = \begin{bmatrix} X \\ Y \\ Z \end{bmatrix}_i , \quad \underset{\sim}{N}^a = \begin{bmatrix} N \\ N \\ N \end{bmatrix}_i , \quad t^a = t_i$$

Here, summation is implied on a.

The surface vector $\underset{\sim}{V}_1$ is along the ξ isoparametric line:

$$\underset{\sim}{V}_1 = \underset{\sim}{N}^a_{,\xi} \underset{\sim}{X}^a / |\underset{\sim}{N}^a_{,\xi} \underset{\sim}{X}^a| \tag{6.4a}$$

and $\underset{\sim}{V}_3$ is normal to the shell surface:

$$\underset{\sim}{V}_3 = \underset{\sim}{V}_1 \times \underset{\sim}{V}_2^* \tag{6.4b}$$

$$\underset{\sim}{V}_2^* = \underset{\sim}{N}^a_{,\eta} \underset{\sim}{X}^a / |\underset{\sim}{N}^a_{,\eta} \underset{\sim}{X}^a| \tag{6.4c}$$

$\underset{\sim}{V}_2$ is normal to both $\underset{\sim}{V}_1$ and $\underset{\sim}{V}_3$.

$$\underset{\sim}{V}_2 = \underset{\sim}{V}_3 \times \underset{\sim}{V}_1 \tag{6.4d}$$

The local orthogonal x', y', and z' axes are obtained similarly, where z' is perpendicular to the shell mid-surface, x' is in the ξ

direction, and y' is perpendicular to both x' and z' axes.

However, to ensure a unique definition of the system of surface vectors, some modifications have to be made when several elements are joining at a node. Here the normal vector $\underset{\sim}{V}_3$ is computed as the averaged normal and $\underset{\sim}{V}_1$ is chosen to be the $\underset{\sim}{V}_1$ vector of the element with the highest element number joining at a node. Here, $\underset{\sim}{V}_1$ is not necessarily perpendicular to the averaged $\underset{\sim}{V}_3$. The set of orthogonal vectors can now be uniquely computed.

$$\underset{\sim}{V}_2 = \underset{\sim}{V}_3 \times \underset{\sim}{V}_1 \tag{6.5a}$$

$$\underset{\sim}{V}_1 = \underset{\sim}{V}_2 \times \underset{\sim}{V}_3 \tag{6.5b}$$

6.2.2 Displacement Fields

The displacement fields are described by the 5 nodal point displacement degrees of freedom, the three translations, u, v, w, in the global X,Y,Z direction and the two rotations, α_1 and α_2, about the surface vectors $\underset{\sim}{V}_1$ and $\underset{\sim}{V}_2$, respectively. The rotation about the $\underset{\sim}{V}_3$ axis is ignored in order to avoid numerical difficulties when dealing with flat plates or shell structures with nearly coplanar elements at a node.

The assumption of plane sections remain plane in the thickness direction allows the displacements of a point within the shell to be found by interpolation.

$$\begin{bmatrix} u \\ v \\ w \end{bmatrix} = \underset{\sim}{N}^a \underset{\sim}{u}^a + \frac{r}{2} t^a \underset{\sim}{N}^a \underset{\sim}{\phi}^a \begin{bmatrix} \alpha_1 \\ \alpha_2 \end{bmatrix}^a \tag{6.6}$$

where

$$\underset{\sim}{u}^a = \begin{bmatrix} u \\ v \\ w \end{bmatrix}_i \quad \text{and} \quad \underset{\sim}{\phi}^a = [-\underset{\sim}{V}_2, \underset{\sim}{V}_1]_i$$

The first term of Eq. 6.6 represents the membrane action and the second term represents the bending action.

6.2.3 Strain-Displacement Relationships

In the case of finite displacement, the strain-displacement relationships given by Eq. 2.42 are:

$$\Delta_1 E'_{kl} = \Delta_1 e'_{kl} + \Delta_1 \eta'_{kl} = \frac{\partial \Delta u'_k}{\partial \Delta x'_l} + \frac{1}{2} \frac{\partial \Delta u'_i}{\partial x'_k} \frac{\partial \Delta u'_i}{\partial x'_l} \qquad (6.7)$$

Replacing ${}_1E'_{kl}$ by ε'_{kl} and dropping the Δ in Eq. 6.7, and with the understanding that the equation represents the incremental relationships, Eq. 6.7 then becomes:

$$\varepsilon'_{kl} = e'_{kl} + \eta'_{kl} = \frac{\partial u'_k}{\partial x'_l} + \frac{1}{2} \frac{\partial u'_i}{\partial x'_k} \frac{\partial u'_i}{\partial x'_l} \qquad (6.8)$$

or in component form, Eq. 6.8 can be written as:

$$\varepsilon_{x'x'} = \frac{\partial u'}{\partial x'} + \frac{1}{2}\left(\frac{\partial u'}{\partial x'}\right)^2 + \frac{1}{2}\left(\frac{\partial u'}{\partial y'}\right)^2 + \frac{1}{2}\left(\frac{\partial u'}{\partial z'}\right)^2 \qquad (6.9a)$$

$$\varepsilon_{y'y'} = \frac{\partial v'}{\partial y'} + \frac{1}{2}\left(\frac{\partial v'}{\partial x'}\right)^2 + \frac{1}{2}\left(\frac{\partial v'}{\partial y'}\right)^2 + \frac{1}{2}\left(\frac{\partial v'}{\partial z'}\right)^2 \qquad (6.9b)$$

$$\varepsilon_{x'y'} = \frac{1}{2}\left(\frac{\partial u'}{\partial y'} + \frac{\partial v'}{\partial x'}\right) + \frac{1}{2}\frac{\partial u'}{\partial y'}\frac{\partial u'}{\partial x'} + \frac{1}{2}\frac{\partial v'}{\partial y'}\frac{\partial v'}{\partial x'} + \frac{1}{2}\frac{\partial w'}{\partial y'}\frac{\partial w'}{\partial x'} \qquad (6.9c)$$

$$\varepsilon_{x'z'} = \frac{1}{2}\left(\frac{\partial u'}{\partial z'} + \frac{\partial w'}{\partial x'}\right) + \underline{\frac{1}{2}\frac{\partial u'}{\partial x'}\frac{\partial u'}{\partial z'} + \frac{1}{2}\frac{\partial v'}{\partial x'}\frac{\partial v'}{\partial z'} + \frac{1}{2}\frac{\partial w'}{\partial x'}\frac{\partial w'}{\partial z'}} \qquad (6.9d)$$

$$\varepsilon_{y'z'} = \frac{1}{2}\left(\frac{\partial v'}{\partial z'} + \frac{\partial w'}{\partial y'}\right) + \underline{\frac{1}{2}\frac{\partial u'}{\partial y'}\frac{\partial u'}{\partial z'} + \frac{1}{2}\frac{\partial v'}{\partial y'}\frac{\partial v'}{\partial z'} + \frac{1}{2}\frac{\partial w'}{\partial y'}\frac{\partial w'}{\partial z'}} \qquad (6.9e)$$

In the case of small strains with small displacements, the underlined terms vanish and $\varepsilon'_{ij} \cong e'_{ij}$.

6.2.4 Element Elastic Stiffness

The element elastic stiffness is obtained by evaluating the expression $\int_{B_1} {}_1C_{ijkl}\, e_{kl}\, \delta e_{ij}\, dv$. This is the same as the elastic stiffness used in small displacement analysis but modified for the current material properties ${}_1C_{ijkl}$ and also for the integration being performed over the current deformed configuration.

Following Ahmad et al [103] and Zienkiewicz et al [19], the strain-displacement relationship can be most easily established by considering the displacement gradients in the global coordinate directions.

$$\begin{bmatrix} \frac{\partial u}{\partial X} & \frac{\partial v}{\partial X} & \frac{\partial w}{\partial X} \\ \frac{\partial u}{\partial Y} & \frac{\partial v}{\partial Y} & \frac{\partial w}{\partial Y} \\ \frac{\partial u}{\partial Z} & \frac{\partial v}{\partial Z} & \frac{\partial w}{\partial Z} \end{bmatrix} = \underset{\sim}{J}^{-1} \begin{bmatrix} \frac{\partial u}{\partial \xi} & \frac{\partial v}{\partial \xi} & \frac{\partial w}{\partial \xi} \\ \frac{\partial u}{\partial \eta} & \frac{\partial v}{\partial \eta} & \frac{\partial w}{\partial \eta} \\ \frac{\partial u}{\partial \zeta} & \frac{\partial v}{\partial \zeta} & \frac{\partial w}{\partial \zeta} \end{bmatrix} \qquad (6.10)$$

where $\underset{\sim}{J}$ is the Jacobian matrix such that:

$$\begin{bmatrix} \frac{\partial}{\partial \xi} \\ \frac{\partial}{\partial \eta} \\ \frac{\partial}{\partial \zeta} \end{bmatrix} = \underset{\sim}{J} \begin{bmatrix} \frac{\partial}{\partial X} \\ \frac{\partial}{\partial Y} \\ \frac{\partial}{\partial Z} \end{bmatrix} \tag{6.11a}$$

and

$$\underset{\sim}{J} = \begin{bmatrix} \frac{\partial X}{\partial \xi} & \frac{\partial Y}{\partial \xi} & \frac{\partial Z}{\partial \xi} \\ \frac{\partial X}{\partial \eta} & \frac{\partial Y}{\partial \eta} & \frac{\partial Z}{\partial \eta} \\ \frac{\partial X}{\partial \zeta} & \frac{\partial Y}{\partial \zeta} & \frac{\partial Z}{\partial \zeta} \end{bmatrix} \tag{6.11b}$$

The displacement gradients in the local axes x', y', and z' can then be obtained by a transformation.

$$\begin{bmatrix} \frac{\partial u'}{\partial x'} & \frac{\partial v'}{\partial x'} & \frac{\partial w'}{\partial x'} \\ \frac{\partial u'}{\partial y'} & \frac{\partial v'}{\partial y'} & \frac{\partial w'}{\partial y'} \\ \frac{\partial u'}{\partial z'} & \frac{\partial v'}{\partial z'} & \frac{\partial w'}{\partial z'} \end{bmatrix} = \underset{\sim}{\Theta}^T \begin{bmatrix} \frac{\partial u}{\partial X} & \frac{\partial v}{\partial X} & \frac{\partial w}{\partial X} \\ \frac{\partial u}{\partial Y} & \frac{\partial v}{\partial Y} & \frac{\partial w}{\partial Y} \\ \frac{\partial u}{\partial Z} & \frac{\partial v}{\partial Z} & \frac{\partial w}{\partial Z} \end{bmatrix} \underset{\sim}{\Theta} \tag{6.12}$$

in which Θ relates the local x', y', z' to the global X,Y,Z coordinate axes.

$$\underset{\sim}{\Theta} = \begin{bmatrix} (\underset{\sim}{x}' \cdot \underset{\sim}{X}) & (\underset{\sim}{y}' \cdot \underset{\sim}{X}) & (\underset{\sim}{z}' \cdot \underset{\sim}{X}) \\ (\underset{\sim}{x}' \cdot \underset{\sim}{Y}) & (\underset{\sim}{y}' \cdot \underset{\sim}{Y}) & (\underset{\sim}{z}' \cdot \underset{\sim}{Y}) \\ (\underset{\sim}{x}' \cdot \underset{\sim}{Z}) & (\underset{\sim}{y}' \cdot \underset{\sim}{Z}) & (\underset{\sim}{z}' \cdot \underset{\sim}{Z}) \end{bmatrix}$$

Substituting Eq. 6.10 into Eq. 6.12, the displacement gradients in the x', y', and z' axes are:

$$\begin{bmatrix} \frac{\partial u'}{\partial x'} & \frac{\partial v'}{\partial x'} & \frac{\partial w'}{\partial x'} \\ \frac{\partial u'}{\partial y'} & \frac{\partial v'}{\partial y'} & \frac{\partial w'}{\partial y'} \\ \frac{\partial u'}{\partial z'} & \frac{\partial v'}{\partial z'} & \frac{\partial w'}{\partial z'} \end{bmatrix} = \underset{\sim}{\Theta}^T \underset{\sim}{J}^{-1} \begin{bmatrix} \frac{\partial u}{\partial \xi} & \frac{\partial v}{\partial \xi} & \frac{\partial w}{\partial \xi} \\ \frac{\partial u}{\partial \eta} & \frac{\partial v}{\partial \eta} & \frac{\partial w}{\partial \eta} \\ \frac{\partial u}{\partial \zeta} & \frac{\partial v}{\partial \zeta} & \frac{\partial w}{\partial \zeta} \end{bmatrix} \underset{\sim}{\Theta} \qquad (6.13)$$

The linear strain-displacement relationship in the local axes x', y', and z' can be written in matrix form as:

$$\begin{bmatrix} e_{x'x'} \\ e_{y'y'} \\ e_{x'y'} \\ e_{x'z'} \\ e_{y'z'} \end{bmatrix} = \begin{bmatrix} \frac{\partial}{\partial x'} & 0 & 0 \\ 0 & \frac{\partial}{\partial y'} & 0 \\ \frac{\partial}{\partial y'} & \frac{\partial}{\partial x'} & 0 \\ \frac{\partial}{\partial z'} & 0 & \frac{\partial}{\partial x'} \\ 0 & \frac{\partial}{\partial z'} & \frac{\partial}{\partial y'} \end{bmatrix} \begin{bmatrix} u' \\ v' \\ w' \end{bmatrix} \qquad (6.14)$$

where

$$\begin{bmatrix} u' \\ v' \\ w' \end{bmatrix} = \underset{\sim}{\Theta}^T \begin{bmatrix} u \\ v \\ w \end{bmatrix}$$

Substituting Eq. 6.6 into Eq. 6.14 and noting that $\underset{\sim}{\Theta}^T \underset{\sim}{J}^{-1}$ has the following form [19]:

$$\underset{\sim}{\Theta}^T \underset{\sim}{J}^{-1} = \underset{\sim}{A} = \begin{bmatrix} A_{11} & A_{12} & 0 \\ A_{21} & A_{22} & 0 \\ 0 & 0 & A_{33} \end{bmatrix} \qquad (6.15)$$

The strain-displacement relationship now becomes:

$$\underset{\sim}{e}' = \underset{\sim}{B}_i \, \underset{\sim}{\Theta}^T \begin{bmatrix} u_i \\ v_i \\ w_i \end{bmatrix} + \frac{t_i}{2} (\zeta \, \underset{\sim}{B}_i + \underset{\sim}{C}_i) \, \underset{\sim}{\Theta}^T \, \underset{\sim}{\phi}_i \begin{bmatrix} \alpha_{1_i} \\ \alpha_{2_i} \end{bmatrix} \quad (6.16)$$

where

$$\underset{\sim}{e}' = \begin{bmatrix} e_{x'x'} \\ e_{y'y'} \\ e_{x'y'} \\ e_{x'z'} \\ e_{y'z'} \end{bmatrix}$$

$$\underset{\sim}{B}_i = \begin{bmatrix} B_1 & 0 & 0 \\ 0 & B_2 & 0 \\ B_2 & B_1 & 0 \\ 0 & 0 & B_1 \\ 0 & 0 & B_2 \end{bmatrix}_i \qquad \underset{\sim}{C}_i = \begin{bmatrix} 0 & 0 & 0 \\ 0 & 0 & 0 \\ 0 & 0 & 0 \\ C_1 & 0 & 0 \\ 0 & C_1 & 0 \end{bmatrix}_i$$

and

$$B_1 = A_{11} \, N_{i,\xi} + A_{12} \, N_{i,\eta}$$

$$B_2 = A_{21} \, N_{i,\xi} + A_{22} \, N_{i,\eta}$$

$$C_1 = A_{33} \, N_i$$

Eq. 6.16 can also be partitioned as:

$$\underset{\sim}{e}' = \left[\begin{array}{c|c} \underset{\sim}{B}_i & \zeta\underset{\sim}{B}_i + \underset{\sim}{C}_i \end{array}\right] \left[\begin{array}{c|c} \underset{\sim}{\Theta}^T & 0 \\ \hline 0 & \frac{t_i}{2}\underset{\sim}{\Theta}^T\underset{\sim}{\phi}_i \end{array}\right] \left[\begin{array}{c} u_i \\ v_i \\ w_i \\ \hline \alpha_{1_i} \\ \alpha_{2_i} \end{array}\right] \tag{6.17}$$

The linearized stress-strain relationship as given in Chapter 2 including the initial strains $\Delta\underset{\sim}{e}^{o'}$ is:

$$\Delta\underset{\sim}{\sigma}' = \underset{\sim}{D}\,(\Delta\underset{\sim}{e}' - \Delta\underset{\sim}{e}^{o'}) \tag{6.18}$$

where

$$\Delta\underset{\sim}{\sigma}'^{T} = [\,\Delta\sigma_{x'x'} \quad \Delta\sigma_{y'y'} \quad \Delta\sigma_{x'y'} \quad \Delta\sigma_{x'z'} \quad \Delta\sigma_{y'z'}]$$

$$\Delta\underset{\sim}{e}^{o'^{T}} = [\,\Delta e^{o}_{x'x'} \quad \Delta e^{o}_{y'y'} \quad \Delta e^{o}_{x'y'} \quad \Delta e^{o}_{x'z'} \quad \Delta e^{o}_{y'z'}\,]$$

The $\underset{\sim}{D}$ matrix for an isotropic material modified for zero normal stress $\sigma_{z'z'}$ in the thickness direction is:

$$\underset{\sim}{D} = \frac{1}{1-\nu^2}\begin{bmatrix} E & \nu & 0 & 0 & 0 \\ & E & 0 & 0 & 0 \\ & & \frac{1-\nu^2}{2(1+\nu)}E & 0 & 0 \\ & & & \kappa\frac{1-\nu^2}{2(1+\nu)}E & 0 \\ \text{SYMM.} & & & & \kappa\frac{1-\nu^2}{2(1+\nu)}E \end{bmatrix} \tag{6.19}$$

where κ = shape factor = 5/6 for rectangular section, and for an orthotropic material as described in Chapter 3 ,

$$D = \frac{1}{1-\nu^2}\begin{bmatrix} E_1C^2 + E_2S^2 & \nu\sqrt{E_1E_2} & \tfrac{1}{2}(E_1 - E_2)CS & 0 & 0 \\ & E_1S^2 + E_2C^2 & \tfrac{1}{2}(E_1 - E_2)CS & 0 & 0 \\ & & \tfrac{1}{4}(E_1 + E_2 - 2\nu\sqrt{E_1E_2}) & 0 & 0 \\ \text{SYMM.} & & & \kappa G_{x'z'} & 0 \\ & & & & \kappa G_{y'z'} \end{bmatrix} \tag{6.20}$$

The element elastic stiffness can then be computed.

$$\underset{\sim}{K}_E^{ij} = \int_{V_1} \left[\begin{array}{c|c} \underset{\sim}{\Theta}^T & 0 \\ \hline 0 & \frac{t_i}{2}\,\underset{\sim}{\Theta}^T\underset{\sim}{\phi}_i \end{array}\right]^T \left[\underset{\sim}{B}_i \,\middle|\, \zeta\underset{\sim}{B}_i + \underset{\sim}{C}_i\right]^T \underset{\sim}{D} \left[\underset{\sim}{B}_j \,\middle|\, \zeta\underset{\sim}{B}_j + \underset{\sim}{C}_j\right] \left[\begin{array}{c|c} \underset{\sim}{\Theta}^T & 0 \\ \hline 0 & \frac{t_j}{2}\,\underset{\sim}{\Theta}^T\underset{\sim}{\phi}_j \end{array}\right] dv \tag{6.21}$$

where $\underset{\sim}{K}_E^{ij}$ is a 5×5 submatrix of the 45×45 element elastic stiffness and represents the clamping forces for the degrees of freedom at node i due to a unit displacement of the degrees of freedom at node j.

6.2.5 Element Geometric Stiffness

The geometric stiffness comes from the evaluation of $\int_{B_1} 1^{\tau}{}_{ij}\, \delta\eta_{ij}\, dv$ and represents the work done by the system due to a finite change in displacements. In the case where nonlinear geometry is not included in the analysis, this matrix should not be included.

The nonlinear strain increment η'_{ij} in component form is:

$$\eta_{x'x'} = \tfrac{1}{2}\left(\frac{\partial u'}{\partial x'}\frac{\partial u'}{\partial x'} + \frac{\partial v'}{\partial x'}\frac{\partial v'}{\partial x'} + \frac{\partial w'}{\partial x'}\frac{\partial w'}{\partial x'}\right) \tag{6.22a}$$

$$\eta_{y'y'} = \tfrac{1}{2}\left(\frac{\partial u'}{\partial y'}\frac{\partial u'}{\partial y'} + \frac{\partial v'}{\partial y'}\frac{\partial v'}{\partial y'} + \frac{\partial w'}{\partial y'}\frac{\partial w'}{\partial y'}\right) \tag{6.22b}$$

$$\eta_{x'y'} = \tfrac{1}{2}\left(\frac{\partial u'}{\partial x'}\frac{\partial u'}{\partial y'} + \frac{\partial v'}{\partial x'}\frac{\partial v'}{\partial y'} + \frac{\partial w'}{\partial x'}\frac{\partial w'}{\partial y'}\right) \tag{6.22c}$$

$$\eta_{x'z'} = \tfrac{1}{2}\left(\frac{\partial u'}{\partial x'}\frac{\partial u'}{\partial z'} + \frac{\partial v'}{\partial x'}\frac{\partial v'}{\partial z'} + \frac{\partial w'}{\partial x'}\frac{\partial w'}{\partial z'}\right) \tag{6.22d}$$

$$\eta_{y'z'} = \tfrac{1}{2}\left(\frac{\partial u'}{\partial y'}\frac{\partial u'}{\partial z'} + \frac{\partial v'}{\partial y'}\frac{\partial v'}{\partial z'} + \frac{\partial w'}{\partial y'}\frac{\partial w'}{\partial z'}\right) \tag{6.22e}$$

$$\eta_{z'z'} = \tfrac{1}{2}\left(\frac{\partial u'}{\partial z'}\frac{\partial u'}{\partial z'} + \frac{\partial v'}{\partial z'}\frac{\partial v'}{\partial z'} + \frac{\partial w'}{\partial z'}\frac{\partial w'}{\partial z'}\right) \tag{6.22f}$$

Following Zienkiewicz [109], the nonlinear strain increments can be rearranged and written in matrix form:

$$\begin{bmatrix} \eta_{x'x'} \\ \eta_{y'y'} \\ \eta_{z'z'} \\ 2\eta_{y'z'} \\ 2\eta_{x'z'} \\ 2\eta_{x'y'} \end{bmatrix} = \begin{bmatrix} \frac{\partial u'}{\partial x'} & \frac{\partial v'}{\partial x'} & \frac{\partial w'}{\partial x'} & 0 & 0 \\ 0 & \frac{\partial u'}{\partial y'} & \frac{\partial v'}{\partial y'} & \frac{\partial w'}{\partial y'} & 0 \\ 0 & 0 & \frac{\partial u'}{\partial z'} & \frac{\partial v'}{\partial z'} & \frac{\partial w'}{\partial z'} \\ 0 & \frac{\partial u'}{\partial z'} & \frac{\partial v'}{\partial z'} & \frac{\partial w'}{\partial z'} & \frac{\partial u'}{\partial y'} & \frac{\partial v'}{\partial y'} & \frac{\partial w'}{\partial y'} \\ \frac{\partial u'}{\partial z'} & \frac{\partial v'}{\partial z'} & \frac{\partial w'}{\partial z'} & 0 & \frac{\partial u'}{\partial x'} & \frac{\partial v'}{\partial x'} & \frac{\partial w'}{\partial x'} \\ \frac{\partial u'}{\partial y'} & \frac{\partial v'}{\partial y'} & \frac{\partial w'}{\partial y'} & \frac{\partial u'}{\partial x'} & \frac{\partial v'}{\partial x'} & \frac{\partial w'}{\partial x'} & 0 \end{bmatrix} \begin{bmatrix} \frac{\partial u'}{\partial x'} \\ \frac{\partial v'}{\partial x'} \\ \frac{\partial w'}{\partial x'} \\ \frac{\partial u'}{\partial y'} \\ \frac{\partial v'}{\partial y'} \\ \frac{\partial w'}{\partial y'} \\ \frac{\partial u'}{\partial z'} \\ \frac{\partial v'}{\partial z'} \\ \frac{\partial w'}{\partial z'} \end{bmatrix} \tag{6.23}$$

Substituting Eq. 6.6 and Eq. 6.15 into Eq. 6.13 and simplifying, the displacement gradients $\underset{\sim}{\partial}$ are:

$$\begin{bmatrix} \frac{\partial u'}{\partial x'} \\ \frac{\partial v'}{\partial x'} \\ \frac{\partial w'}{\partial x'} \\ \frac{\partial u'}{\partial y'} \\ \frac{\partial v'}{\partial y'} \\ \frac{\partial w'}{\partial y'} \\ \frac{\partial u'}{\partial z'} \\ \frac{\partial v'}{\partial z'} \\ \frac{\partial w'}{\partial z'} \end{bmatrix} = \left[\begin{array}{ccc|ccc} B_1 & 0 & 0 & \zeta B_1 & 0 & 0 \\ B_2 & 0 & 0 & \zeta B_2 & 0 & 0 \\ 0 & 0 & 0 & C_1 & 0 & 0 \\ 0 & B_1 & 0 & 0 & \zeta B_1 & 0 \\ 0 & B_2 & 0 & 0 & \zeta B_2 & 0 \\ 0 & 0 & 0 & 0 & C_1 & 0 \\ 0 & 0 & B_1 & 0 & 0 & \zeta B_1 \\ 0 & 0 & B_2 & 0 & 0 & \zeta B_2 \\ 0 & 0 & 0 & 0 & 0 & C_1 \end{array}\right]_i \left[\begin{array}{c|c} \underset{\sim}{\Theta}^T & 0 \\ \hline 0 & \frac{1}{2} t_i \underset{\sim}{\Theta}^T \underset{\sim}{\Phi}_i \end{array}\right] \begin{bmatrix} u_i \\ v_i \\ w_i \\ \alpha 1_i \\ \alpha 2_i \end{bmatrix} \tag{6.24}$$

or symbolically,

$$\underset{\sim}{\partial} = \underset{\sim i}{G} \; \underset{\sim i}{T} \; \underset{\sim i}{r} \tag{6.25}$$

and

$$\underset{\sim i}{r}^T = [\, u_i \, v_i \, w_i \, \alpha 1_i \, \alpha 2_i \,]$$

Again, B_1, B_2, and C_1 have the same meaning as in Eq. 6.16.

The geometric stiffness is then:

$$\underset{\sim G}{K}^{ij} = \int_{V_1} \underset{\sim i}{T}^T \; \underset{\sim i}{G}^T \; \underset{\sim}{M} \; \underset{\sim j}{G} \; \underset{\sim j}{T} \, dv \tag{6.26}$$

where $\underset{\sim}{M}$ is a 9×9 matrix:

$$\underset{\sim}{M} = \begin{bmatrix} \overline{\underset{\sim}{\sigma}} & 0 & 0 \\ 0 & \overline{\underset{\sim}{\sigma}} & 0 \\ 0 & 0 & \overline{\underset{\sim}{\sigma}} \end{bmatrix}$$

and

$$\overline{\underset{\sim}{\sigma}} = \begin{bmatrix} {}_1\sigma_{x'x'} & {}_1\sigma_{x'y'} & {}_1\sigma_{x'z'} \\ & {}_1\sigma_{y'y'} & {}_1\sigma_{y'z'} \\ \text{SYMM.} & & 0 \end{bmatrix}$$

is the matrix of total stresses at the last known configuration.

6.2.6 Load Vector due to Initial Stresses

The internal resisting load vector $\underset{\sim}{R}^I$ obtained by evaluating $\int_{v_1} {}_1\tau_{ij}\, \delta e_{ij}\, dv$ can be written in matrix form as:

$$\underset{\sim}{R}^I = \int_{v_1} \underset{\sim}{b}^T\, {}_1\underset{\sim}{\sigma}\, dv \qquad (6.27)$$

$${}_1\underset{\sim}{\sigma}^T = [\, {}_1\sigma_{x'x'} \;\; {}_1\sigma_{y'y'} \;\; {}_1\sigma_{x'y'} \;\; {}_1\sigma_{x'z'} \;\; {}_1\sigma_{y'z'} \,]$$

where ${}_1\underset{\sim}{\sigma}$ is the initial stress at the current known configuration and $\underset{\sim}{b}$ is the strain displacement transformation matrix, such that $\underset{\sim}{e}' = \underset{\sim}{b}^a \underset{\sim}{r}^a$. Here, summation is implied on a.

The internal resisting force $\underset{\sim}{R}^I_i$ at node i is then:

$$\begin{bmatrix} R_X^I \\ R_Y^I \\ R_Z^I \\ M_1^I \\ M_2^I \end{bmatrix}_i = \int_{V_1} \left[\begin{array}{c|c} \underset{\sim}{\Theta}^T & 0 \\ \hline 0 & \frac{t_i}{2}\underset{\sim}{\Theta}^T\underset{\sim}{\phi}_i \end{array}\right]^T \left[\begin{array}{c|c} \underset{\sim}{B}_i & \zeta\underset{\sim}{B}_i + \underset{\sim}{C}_i \end{array}\right]^T \begin{bmatrix} 1\sigma_{x'x'} \\ 1\sigma_{y'y'} \\ 1\sigma_{x'y'} \\ 1\sigma_{x'z'} \\ 1\sigma_{y'z'} \end{bmatrix} dv \quad (6.28)$$

where R_X^I, R_Y^I, and R_Z^I are the resisting loads in the global X, Y, Z directions and M_1^I,M_2^I are the resisting moments about the surface vectors $\underset{\sim}{V}_1$ and $\underset{\sim}{V}_2$.

6.2.7 Load Vector due to Initial Strains

The clamping forces $\underset{\sim}{R}^o$ due to the initial strains can be computed analogous to $\underset{\sim}{R}^I$

$$\underset{\sim}{R}^o = \int_{V_1} \underset{\sim}{b}^T \underset{\sim}{D}\, \underset{\sim}{\varepsilon}^{o'} dv$$

where D is the material matrix at the last known configuration and $\underset{\sim}{\varepsilon}^o$ is the initial strains vector. In matrix form, the clamping forces $\underset{\sim}{R}_i^o$ at node i are

$$\begin{bmatrix} R_X^o \\ R_Y^o \\ R_Z^o \\ M_1^o \\ M_2^o \end{bmatrix}_i = \int_{V_1} \left[\begin{array}{c|c} \underset{\sim}{\Theta}^T & 0 \\ \hline 0 & \frac{t_i}{2}\underset{\sim}{\Theta}^T\underset{\sim}{\phi}_i \end{array}\right]^T \left[\begin{array}{c|c} \underset{\sim}{B}_i & \zeta\underset{\sim}{B}_i + \underset{\sim}{C}_i \end{array}\right]^T \underset{\sim}{D} \begin{bmatrix} \varepsilon^o_{x'x'} \\ \varepsilon^o_{y'y'} \\ \varepsilon^o_{x'y'} \\ \varepsilon^o_{x'z'} \\ \varepsilon^o_{y'z'} \end{bmatrix} dv \quad (6.29)$$

6.2.8 Load Vectors due to Element Distributed Load

The most commonly encountered distributed loads on the shell are the gravity loads and the pressure loads. The gravity loads are conservative because their direction and magnitude remain unchanged during deformation. Pressure loads, on the other hand, are non-conservative in the sense that their direction and magnitude change during deformation. The unsymmetrical pressure stiffness matrix which arises due to the non-conservative nature of the pressure loads has been discussed extensively in the literature [110,111]. Generally, when the direction of the pressure is updated and an equilibrium correction is carried out, this unsymmetrical pressure stiffness is ignored. The same technique is used in the present study in solving nonlinear problems involving nonlinear geometry with pressure loading.

Gravity Load

The gravity load is assumed to act in the -ve Z direction.

For a weight density of ρ for the shell element, the nodal force $R^g_{Z_i}$ at node i is:

$$\underset{\sim}{R}^g_{Z_i} = -\int_V \rho N_i \, dv \tag{6.30}$$

or

$$\underset{\sim}{R}^g_{Z_i} = -\int_A \rho N_i \, t^a \, N^a \, dA \quad \text{(sum on a)} \tag{6.31}$$

Normal Pressure

The normal pressure load p_n is positive in the z' direction.

The normal displacement w' can be expressed as:

$$w' = \begin{bmatrix} V_{3X} & V_{3Y} & V_{3Z} \end{bmatrix} \begin{bmatrix} N_i & & \\ & N_i & \\ & & N_i \end{bmatrix} \begin{bmatrix} u_i \\ v_i \\ w_i \end{bmatrix} \tag{6.32}$$

where $\underset{\sim}{V}_3$ is normal to the shell surface at the point in question.

The nodal forces at node i due to the pressure load p_n is:

$$\begin{bmatrix} R_X^{p_n} \\ R_Y^{p_n} \\ R_Z^{p_n} \end{bmatrix}_i = \int_{A_1} p_n \, N_i \, \underset{\sim}{V}_3 \, dA \tag{6.33}$$

where A_1 is the area of the deformed surface.

X Pressure

The pressure p_x in the positive X direction produces a nodal force $R_{X_i}^{p_x}$ at node i, where:

$$R_{X_i}^{p_x} = \int_{A_1} p_X \, N_i \, \Theta_{31} \, dA \tag{6.34}$$

$$\Theta_{31} = (\underset{\sim}{z}' \cdot \underset{\sim}{X})$$

Y Pressure

The pressure p_y in the positive Y direction produces a nodal force $R_{Y_i}^{p_y}$ at node i:

$$R_{Y_i}^{p_y} = \int_{A_1} p_Y \, N_i \, \Theta_{32} \, dA \tag{6.35}$$

$$\Theta_{32} = (\underset{\sim}{z}' \cdot \underset{\sim}{Y})$$

Z Pressure

Similarly, the nodal force $R_{Z_i}^{p_Z}$ due to the positive Z pressure is:

$$R_{Z_i}^{p_Z} = \int_{A_1} p_Z \, N_i \, \Theta_{33} \, dA \tag{6.36}$$

$$\Theta_{33} = (\underset{\sim}{z}' \cdot \underset{\sim}{Z})$$

6.3 Numerical Integration Scheme

6.3.1 Introduction

The use of reduced integration as a means to improve the element performance has been first proposed by Doherty et al [100]. The topic has been discussed by Zienkiewicz et al [19], Pawsey [107], Dovey [102], Onate et al [20] and Kanoknukulchai [104].

It has been found that the use of independent interpolations for slopes and rotations will induce extraneous shear strains which will slow down the convergence of the solution. The use of reduced integration will serve as a means to optimize the sampling points where the extraneous strain energy is small or vanishes. For example, Pawsey [107] has demonstrated that the use of the two-point integration scheme for a quadratic straight beam element enables the beam element to represent the bending mode for a linear moment with shear deformation.

The problem of shear locking effects can be understood if one considers the strain energy of the system and makes use of the energy splitting

$$\Pi = \Pi_1 + \Pi_2 \tag{6.37}$$

where

Π = total strain energy of the system

Π_1 = strain energy associated with bending deformations

Π_2 = strain energy associated with the shear deformations

For simplicity, a beam type element with bending stiffness EI and shear stiffness GA, having independent rotation Θ and slope $\frac{dw}{dx}$, is chosen as an illustration. The strain energy expressions are:

$$\Pi_1 = \tfrac{1}{2}\int_L EI\left(\frac{d\Theta}{dx}\right)^2 dx \qquad (6.38a)$$

$$\Pi_2 = \tfrac{1}{2}\int_L \kappa GA\left(\Theta - \frac{dw}{dx}\right)^2 dx \qquad (6.38b)$$

where the transverse shear strain γ is:

$$\gamma = \Theta - \frac{dw}{dx} \qquad (6.38c)$$

and κ = shape factor = 5/6 in this case.

For a linear beam element, Fig. 6.2, the beam element stiffness, excluding the rigid body displacements, can be evaluated using Eq. 6.38a and Eq. 6.38b together with the assumed displacement fields. The resulting force-displacement relationship is:

$$\begin{bmatrix} M_1 \\ M_2 \end{bmatrix} = \left[EI\int_0^L \begin{bmatrix} \frac{1}{L^2} & -\frac{1}{L^2} \\ \frac{1}{L^2} & \frac{1}{L^2} \end{bmatrix} dx + \kappa AG\int_0^L \begin{bmatrix} (1-\frac{x}{L})^2 & (1-\frac{x}{L})(\frac{x}{L}) \\ (1-\frac{x}{L})(\frac{x}{L}) & \frac{x^2}{L^2} \end{bmatrix} dx \right] \begin{bmatrix} \Theta_1 \\ \Theta_2 \end{bmatrix} \qquad (6.39)$$

Using the two-point integration scheme, the resulting stiffness is:

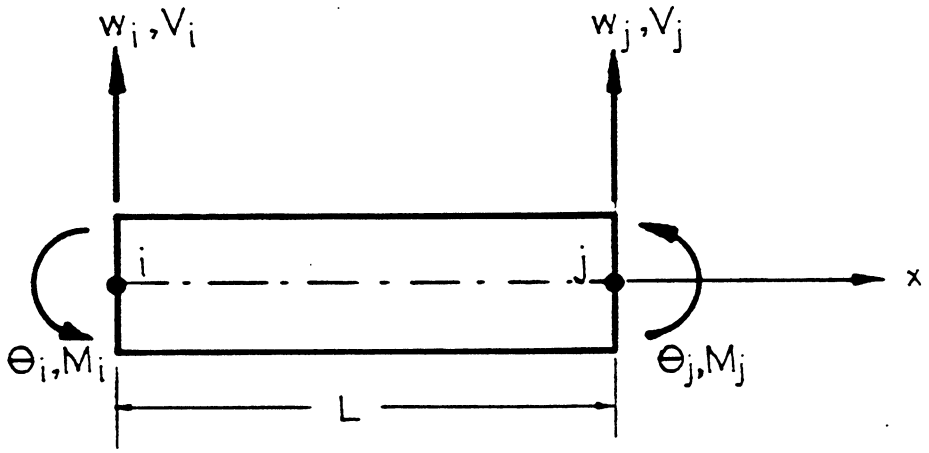

$$\Theta = \begin{bmatrix} 1 - \frac{x}{L} & \frac{x}{L} \end{bmatrix} \begin{bmatrix} \Theta_1 \\ \Theta_2 \end{bmatrix}$$

$$w = \begin{bmatrix} 1 - \frac{x}{L} & \frac{x}{L} \end{bmatrix} \begin{bmatrix} w_1 \\ w_2 \end{bmatrix}$$

FIG. 6.2 GEOMETRY AND DISPLACEMENT FIELDS OF A LINEAR BEAM ELEMENT

$$\underset{\sim}{K}_2 = \frac{EI}{L}\begin{bmatrix} 1 & -1 \\ -1 & 1 \end{bmatrix} + \frac{\kappa AGL}{6}\begin{bmatrix} 2 & 1 \\ 1 & 2 \end{bmatrix} \tag{6.40}$$

However, when one-point integration scheme is applied for the shear stiffness, the stiffness of the beam element is:

$$\underset{\sim}{K}_1 = \frac{EI}{L}\begin{bmatrix} 1 & -1 \\ -1 & 1 \end{bmatrix} + \frac{\kappa AGL}{4}\begin{bmatrix} 1 & 1 \\ 1 & 1 \end{bmatrix} \tag{6.41}$$

The exact solution from elementary beam theory for a constant moment with $\Theta_1 = -\Theta_2 = \Theta$ is

$$M_1^* = -M_2^* = \frac{2EI}{L}\Theta \tag{6.42}$$

The two-point integration scheme gives a resulting moment M_1'':

$$M_1'' = \frac{2EI}{L}\Theta + \frac{\kappa AGL}{6}\Theta \tag{6.43}$$

while the one-point integration scheme for the shear stiffness gives the moment M_1':

$$M_1' = M_1^* = \frac{2EI}{L}\Theta \tag{6.44}$$

which is exact.

In Eq. 6.43, the error in the moment is a function of the relative magnitude of the EI and the AG. For a beam with rectangular section, $EI = \frac{Ebt^3}{12}$ and $AG = \frac{Ebt}{2(1+\nu)}$, it is obvious that EI term decreases more rapidly than the AG term as t decreases. This means that the error in the moment increases as t decreases. This effect, on the other hand, does not exist when the reduced integration is used for

the shear strain energy, Eq. 6.44. Note that for the linear beam element with constant moment, the ordinate of the zero of the first order polynomial in shear strain is exactly at the center of the element.

It turns out that the necessary condition to avoid the problem of shear locking is to ensure that the stiffness matrix obtained from the evaluation of the troubled strain energy, which in this case is the transverse shear strain energy, is singular [104,112]. It is not difficult to verify that this is indeed the case for the component of shear stiffnesses in $\underset{\sim}{K}_2$ (Eq. 6.40) and $\underset{\sim}{K}_1$ (Eq. 6.41). Similar conclusions can be drawn for plate and shell elements with independent slopes and rotations.

Unfortunately, the use of reduced integration on the shear strain energy, while ensuring the singularity of its stiffness, does not necessarily guarantee the positive definiteness of the complete element stiffness. If this is the case, the complete stiffness matrix is rank deficient and it has more zero energy modes other than the rigid body modes allow. These spurious zero energy modes may or may not propagate depending on the imposed boundary conditions. This is perhaps the only shortcoming associated with the reduced integration.

6.3.2 Spurious Zero Energy Modes for the 9-Node Element

It is generally agreed that the Lagrange elements with appropriate reduced integration on the shear term are better than the serendipity elements [20,113,114,115]. It is the higher order terms in the Lagrange elements that makes the difference.

However, for a quadratic 9-node plate element (a shell tends geometrically to a plate in the limit), it has four spurious zero

energy modes when 2×2 Gaussian quadrature is used. These spurious zero energy modes are [114]:

(1) w hourglass mode

$$w = x^2y^2 - \frac{1}{3}(x^2+y^2), \quad \alpha_1 = \alpha_2 = 0 \tag{6.45}$$

(2) α_1 hourglass mode

$$w = 0, \quad \alpha_1 = (x^2-\tfrac{1}{3})(y^2-\tfrac{1}{3}), \quad \alpha_2 = 0 \tag{6.46}$$

(3) α_2 hourglass mode

$$w = 0, \quad \alpha_1 = 0, \quad \alpha_2 = (x^2 - \tfrac{1}{3})(y^2 - \tfrac{1}{3}) \tag{6.47}$$

(4) In-plane twist mode due to rotation α_i

$$w = 0, \quad \alpha_1 = x(y^2 - \tfrac{1}{3}), \quad \alpha_2 = -y(x^2 - \tfrac{1}{3}) \tag{6.48}$$

When selective integration is used involving 3×3 for bending energy and 2×2 for shear energy, only the w hourglass mode (Eq. 6.45) exists.

In an attempt to remedy these deficiencies, Hughes et al [115] developed a Heterosis element where the serendipity shape functions are used for the transverse displacement w and Lagrange shape functions are used for the rotations α_1 and α_2. Using a 2×2 integration scheme, the element is found to possess sufficient rank. However, the element is only nearly optimal in accommodating the zero shear strain constraint which is developed in the thin plate limit and the Lagrange element is considered to be the most optimum [115].

When the in-plane displacements u and v are included in the Lagrange element, the 2×2 integration scheme gives an additional three spurious zero energy modes. They are:

(5) u hourglass

$$u = (x^2 - \tfrac{1}{3})(y^2 - \tfrac{1}{3}), \; v = 0 \tag{6.49}$$

(6) v hourglass

$$u = 0,\ v = (x^2 - \tfrac{1}{3})(y^2 - \tfrac{1}{3}) \tag{6.50}$$

(7) In-plane twist due to in-plane displacements

$$u = x(y^2 - \tfrac{1}{3}),\quad v = -y(x^2 - \tfrac{1}{3}) \tag{6.51}$$

The problem now is to select an integration scheme that will suppress the above-mentioned spurious energy modes and maintain the flexibility of the Lagrange element.

6.3.3 Integration Scheme Used in the Present 9-Node Element

For a parabolic variation in the shear strain due to a linear moment, the ordinates of the zeros of this second order Legendre polynomial correspond exactly to $\pm 1/\sqrt{3}$. These are at the locations of the integration points for a two-point Gauss quadrature rule. This in effect is enforcing the Kirchhoff shear constraint at the $\pm 1/\sqrt{3}$ ordinates. These ordinates are therefore the best locations for the evaluation of the element stiffnesses and stresses. In this study, an attempt has been made to retain the ordaintes of $\pm 1/\sqrt{3}$.

This is made possible by Dovey [102], who developed an 8-point integration scheme. The evaluation of the function:

$$I = \int_{-1}^{+1}\int_{-1}^{+1} F(\xi,\eta)\, d\xi\, d\eta \tag{6.52}$$

with $F(\xi,\eta)$ represented by a polynomial:

$$F(\xi,\eta) = \sum_j \sum_i A_{ij}\xi^i \eta^j \tag{6.53}$$

gives the result:

$$\begin{aligned} I &= \frac{2^2 A_{ij}}{(i+1)(j+1)} \qquad i,j \text{ even} \\ I &= 0 \qquad\qquad\quad 0 \quad \text{otherwise} \end{aligned} \tag{6.54}$$

The quadrature rule for N integration points can be written as:

$$I' = \sum_{n=1}^{N} w_n F(\xi_n,\eta_n) \tag{6.55}$$

Substituting Eq. 6.53 into Eq. 6.55:

$$I' = \sum_{n=1}^{N} (A_{00} w_n + A_{10} w_n \xi_n + A_{01} w_n \eta_n + \ldots. A_{40} w_n \xi_n^4 + A_{04} w_n \eta_n^4 \ldots) \tag{6.56}$$

For an eight-point rule:

$$I' = w_\alpha F(\pm\alpha,\pm\alpha) + w_\beta [F(\pm\beta,0) + F(0,\pm\beta)] \tag{6.57}$$

Substituting Eq. 6.57 into Eq. 6.56 and equating the coefficients A_{ij} in Eq. 6.54.

The results are:

$$\begin{aligned} A_{00} &: \quad 4w_\alpha + 4w_\beta = 4 \\ A_{20} &: \quad 4w_\alpha \alpha^2 + 2w_\beta \beta^2 = 4/3 \\ A_{22} &: \quad 4w_\alpha \alpha^4 = 4/9 \\ A_{40} &: \quad 4w_\alpha \alpha^4 + 2w_\beta \beta^4 = 4/5 \end{aligned} \tag{6.58}$$

Solving the simultaneous equations in Eq. 6.58 gives:

$$\begin{aligned} w_\alpha &= 9/49 , \quad \alpha = \sqrt{7/9} \\ w_\beta &= 40/49, \quad \beta = \sqrt{7/15} \end{aligned} \tag{6.59}$$

Note that the leading error term in A_{40} is identically zero for the values given by Eq. 6.59. This is the same order of accuracy in the 3×3 Gaussian quadrature.

If the first three equations in Eq. 6.58 are satisfied, leaving an error term in A_{40} and choosing w_β as arbitrary,

$$(I' - I) = 4w_\alpha \alpha^4 + 2w_\beta \beta^4 - 4/5$$

and

$$\begin{aligned} 0.0 \le w_\beta &\le 40/49 \\ w_\alpha &= 1.0 - w_\beta \\ \alpha &= 1/(9w_\alpha)^{\frac{1}{4}} \\ \beta &= (2/3 - 2w_\alpha \alpha^2)^{\frac{1}{2}}/(w_\beta)^{\frac{1}{2}} \end{aligned} \qquad (6.60)$$

For $w_\beta = 0$ in Eq. 6.60,

$w_\alpha = 1.0$, $\alpha = 1/\sqrt{3}$,

which corresponds exactly to the 2×2 Gaussian quadrature.

Now the evaluation of the function $F(\xi,\eta)$ can be continuously varied from an accuracy attained by using 2×2 Gaussian quadrature to the 3×3 Gaussian quadrature by continuously changing the parameter w_β in Eq. 6.60. This can be interpreted as an interpolating scheme in obtaining solution accuracy between the 2×2 and the 3×3 Gaussian rule.

The variations in the α coordinates with respect to w_β where w_β is small are summarized in the following table. It can be seen that for $w_\beta << 1.0$, the integration coordinates are not drastically different from that of the 2×2 Gaussian rule. Therefore, the resulting integrated function I' can be interpreted as the integrated function, $I_{2\times 2}$, with the 2×2 rule plus an augmented integrated function, I_A, at the β coordinate with a weight of w_β.

w_β	α
0.0	0.5773502692
0.00001	0.5773517126
0.0001	0.5773647038
0.001	0.5774946970
0.01	0.5788027342
0.1	0.5927598033

$$
\begin{aligned}
I' &\cong I_{2\times 2} + I_A \\
I_{2\times 2} &= w_\alpha\, F(\pm\alpha,\pm\alpha) \\
I_A &= w_\beta\, [F(\pm\beta,0) + F(0,\pm\beta)] \qquad (6.61) \\
w_\beta &<< 1.0 \\
\alpha &\cong 1/\sqrt{3}
\end{aligned}
$$

The scheme proposed in Eq. 6.61 retains the advantage of the $1/\sqrt{3}$ coordinate and the use of the β coordinate will tend to eliminate the spurious zero energy modes described in the previous section. It is not difficult to verify that the strain energy of the deformation modes (Eq. 6.45 through Eq. 6.51) are nonzero at the β coordinates. The I_A term then has the same effect of constraining the spurious zero energy modes by assigning to them a fictitious strain energy at the β coordinate.

The integration grid for the 8-point rule is shown schematically in Fig. 6.3.

6.4 The Proposed Element

A Lagrange shell element with the 8-point integration rule is proposed. The w_β value in Eq. 6.61 is chosen to be 0.0001. This same value has been used by Dovey [102]. It has been found that for $w_\beta = 0.0001$, the stiffness matrix is nonsingular for a weakly constrained system.

6.4.1 Example 6.1 - Constant Twist of a Square Plate

A square plate simply supported at the three corners A, B, and D and loaded at the fourth corner C with a vertical load of 5 lb. is analyzed. The plate is discretized by one shell element and the geometry and the material properties are shown in Fig. 6.4.

The exact solution [85] is:

$$\begin{aligned} M_{xx} &= M_{yy} = 0 \\ M_{xy} &= 2.5 \text{ in-lb/in} \end{aligned} \tag{6.62}$$

The deformed shape for constant twist is:

$$w = kxy \tag{6.63}$$

where k is yet to be determined.

The relationship between the twisting moment M_{xy} and the transverse deflection w is:

$$M_{xy} = D(1-\nu) \frac{\partial^2 w}{\partial x \partial y} \tag{6.64}$$

where D is the plate stiffness:

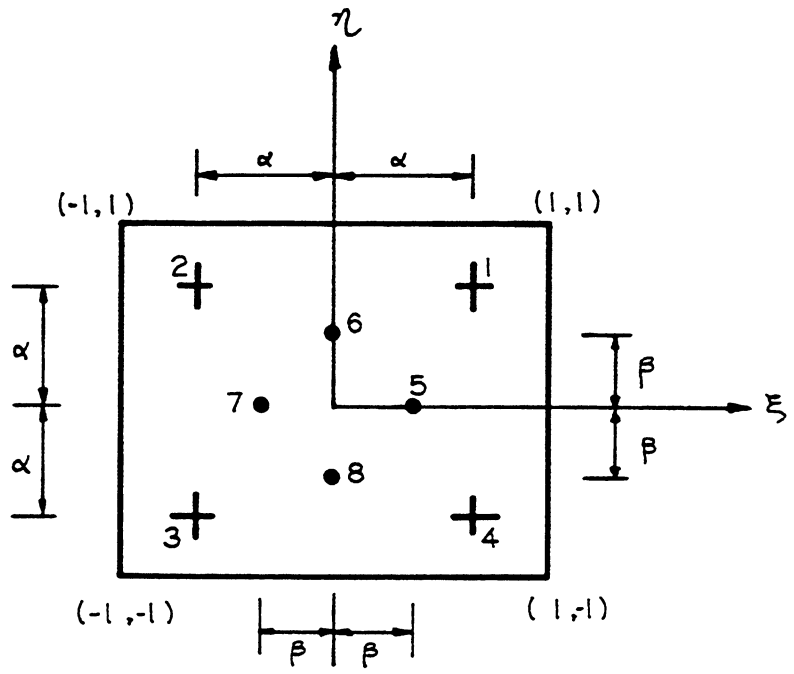

$$0 \leq W_\beta \leq 40/49$$

$$W_\alpha = 1 - W_\beta$$

$$\alpha = 1 / (9 W_\alpha)^{1/4}$$

$$\beta = \sqrt{\frac{2/3 - 2 W_\alpha \alpha^2}{W_\beta}}$$

FIG. 6.3 LOCATION OF INTEGRATION POINTS FOR THE 8-POINT RULE

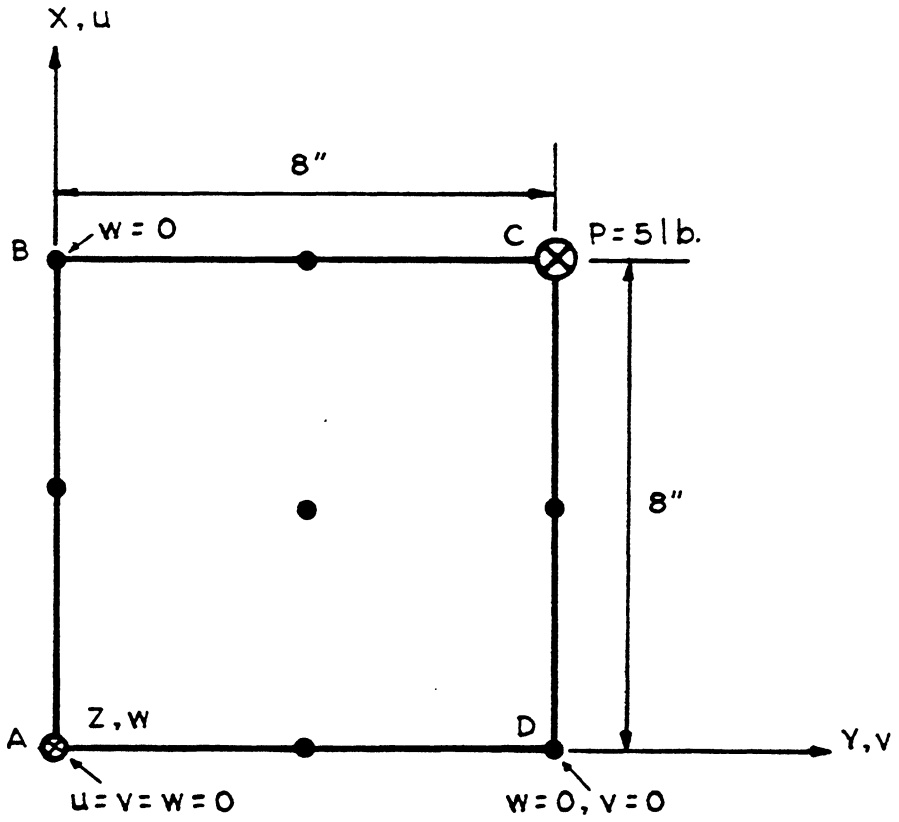

E = 10000 psi
t = 1 in.
ν = 0.3

FIG. 6.4 CONSTANT TWIST OF A SQUARE PLATE (EX. 6.1)
- GEOMETRY AND MATERIAL PROPERTIES

$$D = \frac{Et^3}{12(1-\nu^2)}$$

Using Eq. 6.62, Eq. 6.63 and Eq. 6.64, the coefficient k in Eq. 6.63 is found to be

$$k = 0.0039$$

The vertical deflection at point C is therefore 0.2496 in.

The 9-node shell element with a 2×2 integration rule gives a singular stiffness and a mechanism is formed. The w hourglass mode, the α_1 hourglass and the α_2 hourglass modes pollute the solution in this case.

However, when $w_\beta = 0.0001$ is used, the spurious zero energy modes disappear and the deflection at point C is found to be 0.25896 in. and the internal moments are:

$$M_{xx} = M_{yy} = 0.0$$

$$M_{xy} = 2.5 \text{ in-lb/in}$$

It is noted that the present element gives a deflection at point C larger than the theoretical solution, namely 3.75% higher. This is due to the transverse shear deformation included in the present analysis.

This example demonstrates that the present integration scheme is a significant improvement over the 2×2 integration and gives the correct solution in this weakly constrained system.

It is later found that the use of this 8-point rule with $w_\beta = 0.0001$ is not always necessary. The imposed boundary conditions and the curved shell geometry always tend to prevent the formation of

mechanisms. A conservative criterion to be used in determining if the stiffness is nonsingular when a 2×2 integration is used is:

$$\text{Available D.O.F.} < R \cdot 4 \cdot \text{Numel} \tag{6.65}$$

where

R = 6 = Rank of the material matrix $\underset{\sim}{D}$.

Numel = Number of elements.

6.5 Modelling of the Reinforcement

The major nonlinearities in the reinforced concrete structure are from the effects of cracking. Cracks are initiated even at a low service load and the redistribution of the stresses in the concrete to the surrounding reinforcement necessitates that the reinforcement be modelled correctly. Two of the most commonly used methods to represent the reinforcements are the embedded and the distributed models.

6.5.1 Embedded Reinforcement

In this case, discrete reinforcing bars are assumed to be embedded within the element. Perfect bond is assumed to exist between the reinforcement and the concrete. For straight reinforcement, the coordinates of the two ends of the reinforcement have to be specified. As the reinforcement is curved in space, more coordinate points along the reinforcement have to be defined.

Referring to Fig. 6.5, the added stiffness from the reinforcement is computed as:

$$\int_L \underset{\sim}{b}^T E \, \underset{\sim}{b} \, A \, dx$$

where $\underset{\sim}{b}$ relates the strains along the reinforcing direction x and the

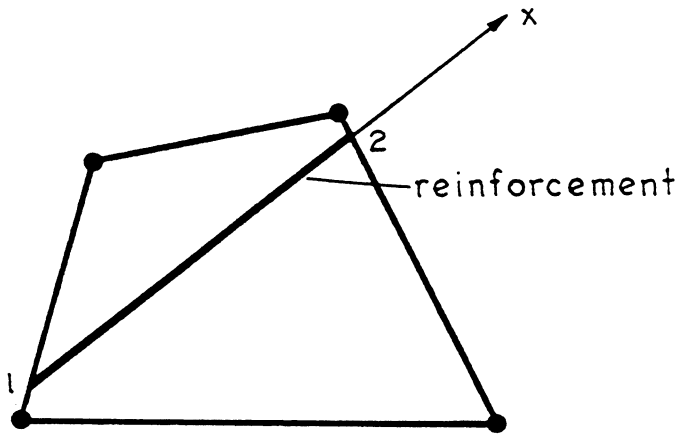

FIG. 6.5 EMBEDDED REINFORCEMENT

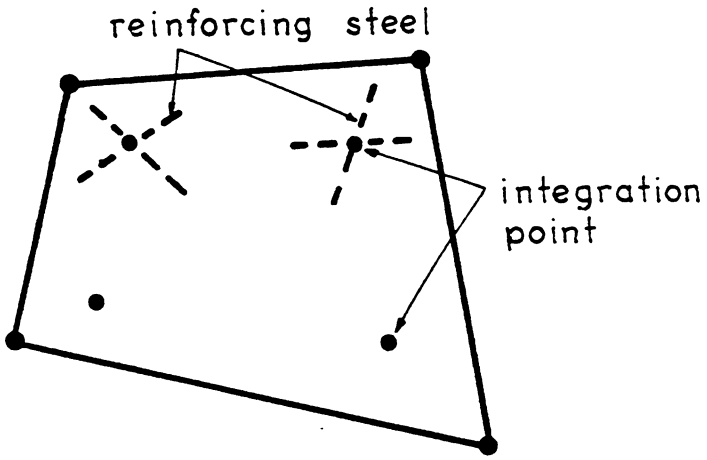

FIG. 6.6 DISTRIBUTED REINFORCEMENT

nodal degrees of freedom of the element, E is the uniaxial modulus of elasticity, A is the area of the reinforcement, and L is the length of the reinforcement. It can be seen that the computation of the added stiffness of a single reinforcement is about the same as the computation of the element stiffness itself. As the number of reinforcing bars within an element is increased, the computational effort increases rapidly until the solution is computationally prohibitive.

Sørensen [116] and Elwi [117] use this approach.

6.5.2 Distributed Reinforcement

In this case, the amount of reinforcement and their directions are lumped at the integration points, Fig. 6.6. Perfect bond between the concrete and the steel is assumed.

This approach is computationally efficient and is best in modelling closely spaced reinforcing bars, a typical case found in shell type structures. It does not model the discrete reinforcement exactly, however. On the other hand, when the distributed crack method is used to represent cracking in the structure, this method in the author's view is a more consistent approach.

6.5.3 Modelling of the Reinforcement in the Present Study

The distributed method of modelling reinforcement is used in this study where the integration points are chosen to be the controlling points. Uniaxial stress state is assumed in each reinforced direction.

Fig. 6.7 shows a typical shell element. At the integration point O, the shell element is reinforced in both $\underset{\sim}{A}$ and $\underset{\sim}{B}$ directions. The projection of vector $\underset{\sim}{A}$ on the XY plane, vector $\underset{\sim}{C}$, is identified by the angle Θ. Then the two orthogonal directions $\underset{\sim}{A}$ and $\underset{\sim}{B}$ on the shell

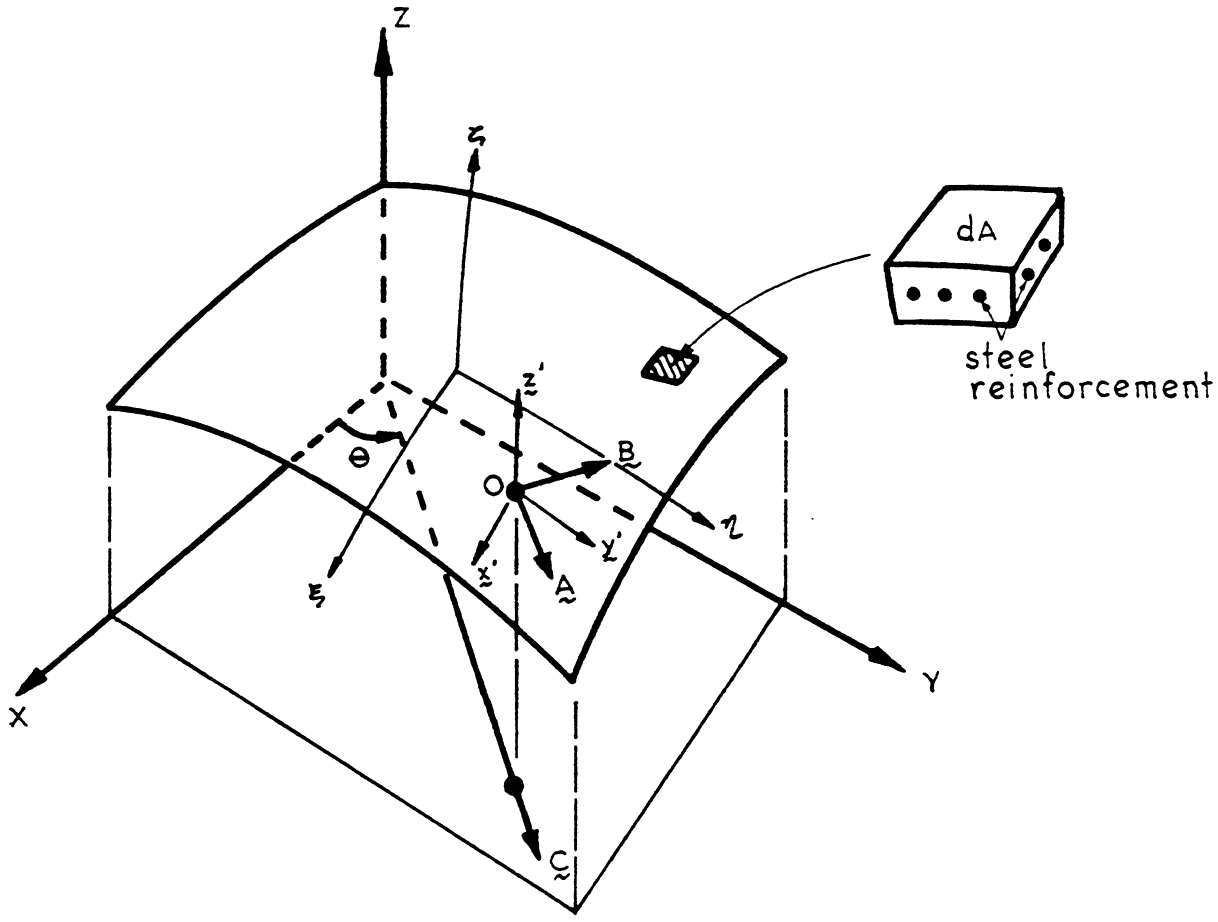

FIG. 6.7 REPRESENTATION OF THE REINFORCEMENT SHOWING THE REINFORCING DIRECTIONS A AND B

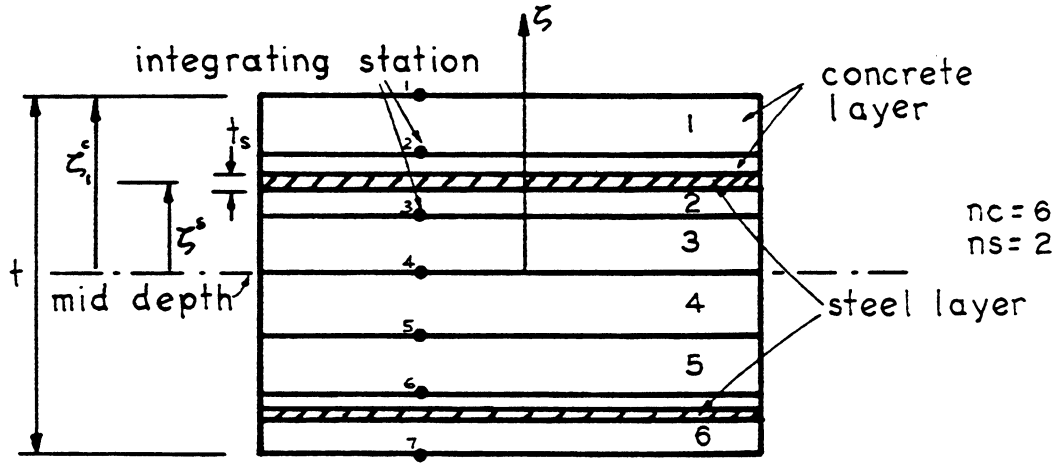

FIG. 6.8 TYPICAL REINFORCED CONCRETE LAYER SYSTEM

surface can be computed with $\underset{\sim}{A}$ tangent to the shell in the ZC plane.

$$\underset{\sim}{B} = \underset{\sim}{C} \times \underset{\sim}{z}'$$

$$\underset{\sim}{A} = \underset{\sim}{B} \times \underset{\sim}{z}'$$

The defaults for the reinforcing directions $\underset{\sim}{A}$ and $\underset{\sim}{B}$ coincide with the local axes x' and y'.

The material matrix $\underset{\sim}{D}_s'$ for the reinforcement in both the $\underset{\sim}{A}$ and $\underset{\sim}{B}$ directions is:

$$\underset{\sim}{D}_s' = \begin{bmatrix} E_s & & & 0 \\ & E_s & & \\ & & 0 & \\ & & & 0 \\ 0 & & & \\ & & & 0 \end{bmatrix} \tag{6.65}$$

For reinforcement in the $\underset{\sim}{A}$ direction only:

$$\underset{\sim}{D}_s' = \begin{bmatrix} E_s & & & 0 \\ & 0 & & \\ & & 0 & \\ 0 & & & 0 \\ & & & 0 \end{bmatrix} \tag{6.66}$$

and for reinforcement in the $\underset{\sim}{B}$ direction only:

$$\underset{\sim}{D}_s' = \begin{bmatrix} 0 & & & \\ & E_s & & 0 \\ & & 0 & \\ & & & 0 \\ 0 & & & \\ & & & 0 \end{bmatrix} \tag{6.67}$$

The material matrix in the local x', y' directions are then obtained by a coordinate transformation:

$$\underset{\sim}{D}^{s} = \underset{\sim}{T}^{T} \underset{\sim}{D}_{s}' \underset{\sim}{T} \tag{6.68}$$

where

$$\underset{\sim}{T} = \begin{bmatrix} a_{11}^2 & a_{12}^2 & 2a_{12}a_{11} & 0 & 0 \\ a_{21}^2 & a_{22}^2 & 2a_{21}a_{22} & 0 & 0 \\ a_{11}a_{21} & a_{12}a_{22} & a_{22}^2 + a_{12}^2 & 0 & 0 \\ 0 & 0 & 0 & 0 & 0 \\ 0 & 0 & 0 & 0 & 0 \end{bmatrix}$$

and

$$\underset{\sim}{A} = \begin{bmatrix} a_{11} & a_{12} \\ a_{21} & a_{22} \end{bmatrix} = \begin{bmatrix} (\underset{\sim}{A} \cdot \underset{\sim}{x}') & (\underset{\sim}{A} \cdot \underset{\sim}{y}') \\ (\underset{\sim}{B} \cdot \underset{\sim}{x}') & (\underset{\sim}{B} \cdot \underset{\sim}{y}') \end{bmatrix}$$

The amount of reinforcement is specified by the equivalent smeared thickness t_s, such that:

$$t_s = \frac{A_s}{s} \tag{6.69}$$

A_s = area of one reinforcing bar

s = spacing of the reinforcing bars

6.6 Reinforced Concrete Shell Element

The previous derivation of the element stiffnesses and load vectors are also valid for the case of reinforced concrete. An 8-point, and occasionally a 4-point rule is used to integrate across the surface

of the shell, Simpson's rule is used through the thickness of the concrete, and the contribution of the steel reinforcement is accounted for by the use of rectangular rule.

6.6.1 Elastic Stiffness

The element elastic stiffness is:

$$\underset{\sim}{K}_E^{ij} = \int_{-1}^{+1}\int_{-1}^{+1}\int_{-1}^{+1} \begin{bmatrix} \underset{\sim}{\Theta}^T & 0 \\ 0 & \frac{t_i}{2}\,\underset{\sim}{\Theta}^T \underset{\sim}{\phi}_i \end{bmatrix}^T \left[\underset{\sim}{B}_i \mid \zeta \underset{\sim}{B}_i + \underset{\sim}{C}_i\right]^T \underset{\sim}{D} \left[\underset{\sim}{B}_j \mid \zeta \underset{\sim}{B}_j + \underset{\sim}{C}_j\right]$$

$$\cdot \begin{bmatrix} \underset{\sim}{\Theta}^T & 0 \\ 0 & \frac{t_j}{2}\,\underset{\sim}{\Theta}^T \underset{\sim}{\phi}_j \end{bmatrix} \cdot \det \underset{\sim}{J}\, d\xi\, d\eta\, d\zeta \qquad (6.70)$$

and, for reinforced concrete, it can be written as:

$$\underset{\sim}{K}_E^{ij} = \left(\underset{\sim}{K}_E^{ij}\right)_c + \left(\underset{\sim}{K}_E^{ij}\right)_s \qquad (6.71)$$

where $\left(\underset{\sim}{K}_E^{ij}\right)_c$ and $\left(\underset{\sim}{K}_E^{ij}\right)_s$ are due to concrete and steel, respectively.

$$\left(\underset{\sim}{K}_E^{ij}\right)_c = \sum_{m=1}^{N}\sum_{n=1}^{nc+1} w_m \cdot w_n^c \cdot \begin{bmatrix} \underset{\sim}{\Theta}^T & 0 \\ 0 & \frac{t_i}{2}\,\underset{\sim}{\Theta}^T \underset{\sim}{\phi}_i \end{bmatrix}_m^T \left[\underset{\sim}{B}_i \mid \zeta_n^c \underset{\sim}{B}_i + \underset{\sim}{C}_i\right]_m$$

$$\cdot \underset{\sim}{D}_{mn}^c \left[\underset{\sim}{B}_j \mid \zeta_n^c \underset{\sim}{B}_j + \underset{\sim}{C}_j\right]_m \begin{bmatrix} \underset{\sim}{\Theta}^T & 0 \\ 0 & \frac{t_j}{2}\,\underset{\sim}{\Theta}^T \underset{\sim}{\phi}_j \end{bmatrix}_m \det \underset{\sim}{J}_m \qquad (6.72)$$

$$\left(\underset{\sim}{K}_E^{ij}\right)_s = \sum_{m=1}^{N} \sum_{n=1}^{ns} w_m w_n^s \left[\begin{array}{c|c} \underset{\sim}{\Theta}^T & 0 \\ \hline 0 & \frac{t_i}{2} \underset{\sim}{\Theta}^T \underset{\sim}{\phi}_i \end{array}\right]_m^T \left[\underset{\sim}{B}_i \mid \zeta_n^s \underset{\sim}{B}_i + \underset{\sim}{C}_i^T\right] \underset{\sim}{D}_{mn}^s$$

$$\cdot \left[\underset{\sim}{B}_j \mid \zeta_n^s \underset{\sim}{B}_j + \underset{\sim}{C}_j\right]_m \left[\begin{array}{c|c} \underset{\sim}{\Theta}^T & 0 \\ \hline 0 & \frac{t_i}{2} \underset{\sim}{\Theta}^T \underset{\sim}{\phi}_j \end{array}\right]_m \det \underset{\sim}{J}_m \qquad (6.73)$$

where the subscripts m and n refer to the integration point m on the surface and at station n in the thickness direction.

N = number of integration points across the surface of the shell

nc = number of concrete layers which must be an even number

w_m = weight as given in Eq. 6.61

w_n^c = $2/nc \cdot g_i$

$g_i = (1/3)t_m$ i=1, nc+1

$g_i = (4/3)t_m$ i=even

$g_i = (2/3)t_m$ i=odd

ζ_n^c = coordinate of the concrete layer n measured in the natural ζ direction

$\underset{\sim}{D}_{mn}^c$ = material matrix for concrete

ns = number of steel layers

ζ_n^s = coordinate of the steel layer n in the natural ζ direction

$\underset{\sim}{D}_{mn}^s$ = material matrix for steel

w_n^s = $[(t_s)_n/t_m] \cdot 2$

t_m = thickness of the shell at the integration point m

A typical reinforced concrete element is shown in Fig. 6.8.

6.6.2 Geometric Stiffness

The geometric stiffness can be similarly computed from Eq. 6.26 and

$$\underset{\sim}{K}_G^{ij} = \left(\underset{\sim}{K}_G^{ij}\right)_c + \left(\underset{\sim}{K}_G^{ij}\right)_s \tag{6.74}$$

$$\left(\underset{\sim}{K}_G^{ij}\right)_c = \int_{-1}^{+1}\int_{-1}^{+1}\int_{-1}^{+1} \underset{\sim}{T}_i^T \underset{\sim}{G}_i^T \underset{\sim}{M}^c \underset{\sim}{G}_j \underset{\sim}{T}_j \det \underset{\sim}{J}\; d\xi\, d\eta\, d\zeta$$

$$= \sum_{m=1}^{N} \sum_{n=1}^{nc+1} w_m w_n^c \left(\underset{\sim}{T}_m^T \underset{\sim}{G}_{mn}^T\right)_i \underset{\sim}{M}_{mn}^c \left(\underset{\sim}{G}_{mn} \underset{\sim}{T}_m\right)_j \det \underset{\sim}{J}_m \tag{6.75}$$

$$\left(\underset{\sim}{K}_G^{ij}\right)_s = \int_{-1}^{+1}\int_{-1}^{+1}\int_{-1}^{+1} \underset{\sim}{T}_i^T \underset{\sim}{G}_i^T \underset{\sim}{M}^s \underset{\sim}{G}_j \underset{\sim}{T}_j \det \underset{\sim}{J}\; d\xi\, d\eta\, d\zeta$$

$$= \sum_{m=1}^{N} \sum_{n=1}^{ns} w_m w_n^s \left(\underset{\sim}{T}_m^T \underset{\sim}{G}_{mn}^T\right)_i \underset{\sim}{M}_{mn}^s \left(\underset{\sim}{G}_{mn} \underset{\sim}{T}_m\right)_j \det \underset{\sim}{J}_m \tag{6.76}$$

where

$$\underset{\sim}{M}_{mn}^c = \begin{bmatrix} \underset{\sim}{\bar{\sigma}}^c & & \\ & \underset{\sim}{\bar{\sigma}}^c & \\ & & \underset{\sim}{\bar{\sigma}}^c \end{bmatrix}$$

$$\underset{\sim}{\bar{\sigma}}^c = \begin{bmatrix} {}^1\sigma^c_{x'x'} & {}^1\sigma^c_{x'y'} & {}^1\sigma^c_{x'z'} \\ & {}^1\sigma^c_{y'y'} & {}^1\sigma^c_{y'z'} \\ \text{SYMM.} & & 0 \end{bmatrix}_{mn}$$

$$\underset{\sim}{M}_{mn}^s = \begin{bmatrix} \underset{\sim}{\bar{\sigma}}^s & & \\ & \underset{\sim}{\bar{\sigma}}^s & \\ & & \underset{\sim}{\bar{\sigma}}^s \end{bmatrix}$$

$$\underset{\sim}{\bar{\sigma}}^{s} = \begin{bmatrix} {}^{1}\sigma^{s}_{x'x'} & {}^{1}\sigma^{s}_{x'y'} & 0 \\ & {}^{1}\sigma^{s}_{y'y'} & 0 \\ \text{SYMM.} & & 0 \end{bmatrix}_{mn}$$

$$(\underset{\sim}{T}_{m})_{i} = \left[\begin{array}{c|c} \underset{\sim}{\Theta}^{T} & 0 \\ \hline 0 & \frac{1}{2}t_{i}\,\underset{\sim}{\Theta}^{T}\,\underset{\sim}{\phi}_{i} \end{array}\right]_{m}$$

$$(\underset{\sim}{G}_{mn})_{i} = \left[\begin{array}{ccc|ccc} B_1 & 0 & 0 & \zeta_n B_1 & 0 & 0 \\ B_2 & 0 & 0 & \zeta_n B_2 & 0 & 0 \\ 0 & 0 & 0 & C_1 & 0 & 0 \\ 0 & B_1 & 0 & 0 & \zeta_n B_1 & 0 \\ 0 & B_2 & 0 & 0 & \zeta_n B_2 & 0 \\ 0 & 0 & 0 & 0 & C_1 & 0 \\ 0 & 0 & B_1 & 0 & 0 & \zeta_n B_1 \\ 0 & 0 & B_2 & 0 & 0 & \zeta_n B_2 \\ 0 & 0 & 0 & 0 & 0 & C_1 \end{array}\right]_{m}$$

All other variables have the same meaning as defined previously in Section 6.6.1.

6.6.3 Load Vector due to Initial Stresses

This can be computed by a direct application of the numerical procedure to Eq. 6.27.

$$\underset{\sim}{R}^{I}_{i} = (\underset{\sim}{R}^{I})^{c}_{i} + (\underset{\sim}{R}^{I})^{s}_{i} \qquad (6.77)$$

$$(\underset{\sim}{R}_i^I)^c = \sum_{m=1}^{N} \sum_{n=1}^{nc+1} w_m w_n^c \left[\begin{array}{c|c} \underset{\sim}{\Theta}^T & 0 \\ \hline 0 & \frac{t_i}{2} \underset{\sim}{\Theta}^T \underset{\sim}{\phi}_i \end{array}\right]_m^T \left[\underset{\sim}{B}_i \mid \zeta_n^c \underset{\sim}{B}_i + \underset{\sim}{C}_i\right]_m^T \cdot \begin{bmatrix} \sigma_{x'x'} \\ \sigma_{y'y'} \\ \sigma_{x'y'} \\ \sigma_{x'z'} \\ \sigma_{y'z'} \end{bmatrix}_{mn} \det \underset{\sim}{J}_m \qquad (6.78)$$

$$(\underset{\sim}{R}_i^I)^s = \sum_{m=1}^{N} \sum_{n=1}^{ns} w_m w_n^s \left[\begin{array}{c|c} \underset{\sim}{\Theta}^T & 0 \\ \hline 0 & \frac{t_i}{2} \underset{\sim}{\Theta}^T \underset{\sim}{\phi}_i \end{array}\right]_m^T \left[\underset{\sim}{B}_i \mid \zeta_n^s \underset{\sim}{B}_i + \underset{\sim}{C}_i\right]_m^T \cdot \begin{bmatrix} \sigma_{x'x'} \\ \sigma_{y'y'} \\ \sigma_{x'y'} \\ 0 \\ 0 \end{bmatrix}_{mn} \det \underset{\sim}{J}_m \qquad (6.79)$$

6.6.4 Load Vector due to Initial Strains

Here the initial strains for both the concrete and the steel are considered. For initial strains produced by creep and shrinkage of

concrete, the initial strains on the steel should be neglected.

$$\underset{\sim}{R}_i^o = (\underset{\sim}{R}_i^o)^c + (\underset{\sim}{R}_i^o)^s \tag{6.80}$$

$$(\underset{\sim}{R}_i^o)^c = \sum_{m=1}^{N} \sum_{n=1}^{nc+1} w_m w_n^c \left[\begin{array}{c|c} \underset{\sim}{\Theta}^T & 0 \\ \hline 0 & \frac{t_i}{2} \underset{\sim}{\Theta}^T \underset{\sim}{\phi}_i \end{array}\right]_m^T \left[\underset{\sim}{B}_i \mid \zeta_n \underset{\sim}{B}_i + \underset{\sim}{C}_i\right]_m^T$$

$$\cdot \underset{\sim}{D}_{mn}^c \begin{bmatrix} \varepsilon^o_{x'x'} \\ \varepsilon^o_{y'y'} \\ \varepsilon^o_{x'y'} \\ 0 \\ 0 \end{bmatrix} \det \underset{\sim}{J}_m \tag{6.81}$$

$$(\underset{\sim}{R}_i^o)^s = \sum_{m=1}^{N} \sum_{n=1}^{ns} w_m w_n^s \left[\begin{array}{c|c} \underset{\sim}{\Theta}^T & 0 \\ \hline 0 & \frac{t_i}{2} \underset{\sim}{\Theta}^T \underset{\sim}{\phi}_i \end{array}\right]_m^T \left[\underset{\sim}{B}_i \mid \zeta_n \underset{\sim}{B}_i + \underset{\sim}{C}_i\right]_m^T$$

$$\cdot \underset{\sim}{D}_{mn}^s \begin{bmatrix} \varepsilon^o_{x'x'} \\ \varepsilon^o_{y'y'} \\ \varepsilon^o_{x'y'} \\ 0 \\ 0 \end{bmatrix} \det \underset{\sim}{J}_m \tag{6.82}$$

6.7 Treatment of the Large Displacements and Finite Rotations

One of the most important steps in handling the large displacement problem is the updating of the geometry of the structure based on which equilibrium is checked.

The coordinates of the nodal point at current step i can be readily updated as:

$$\underset{\sim}{X}^{i} = \underset{\sim}{X}^{i-1} + \Delta\underset{\sim}{u}^{i} \tag{6.83}$$

$$\underset{\sim}{X}^{i} = \begin{bmatrix} X^{i} \\ Y^{i} \\ Z^{i} \end{bmatrix}_j \qquad \Delta\underset{\sim}{u}^{i} = \begin{bmatrix} \Delta u \\ \Delta v \\ \Delta w \end{bmatrix}_j$$

The surface vector can be updated by considering a series of orthogonal transformations due to the rotations α_1 and α_2. Referring to Fig. 6.9, the rotations α_1 and α_2 will move the original surface vector $\underset{\sim}{V}_1^{i-1}$, $\underset{\sim}{V}_2^{i-1}$, and $\underset{\sim}{V}_3^{i-1}$ to a new position $\underset{\sim}{V}_1^{i}$, $\underset{\sim}{V}_2^{i}$, and $\underset{\sim}{V}_3^{i}$. It can be conceived as two consecutive rotations. Rotation due to α_1 about the $\underset{\sim}{V}_1^{i-1}$ axes transform $\underset{\sim}{V}_1^{i-1}$, $\underset{\sim}{V}_2^{i-1}$, and $\underset{\sim}{V}_3^{i-1}$ to $\underset{\sim}{V}_1^{i-1}$, $\underset{\sim}{V}_2^{i}$, and $\underset{\sim}{t}$. The rotation α_2 about $\underset{\sim}{V}_2^{i}$ then brings the vectors to the final position $\underset{\sim}{V}_1^{i}$, $\underset{\sim}{V}_2^{i}$, and $\underset{\sim}{V}_3^{i}$.

The transformation for the two motions are:

$$\begin{bmatrix} \underset{\sim}{V}_1^{i-1^T} \\ \underset{\sim}{V}_2^{i^T} \\ \underset{\sim}{t}^{T} \end{bmatrix}_j = \begin{bmatrix} 1 & 0 & 0 \\ 0 & \cos\alpha_1 & \sin\alpha_1 \\ 0 & -\sin\alpha_1 & \cos\alpha_1 \end{bmatrix}_j \begin{bmatrix} \underset{\sim}{V}_1^{i-1^T} \\ \underset{\sim}{V}_2^{i-1^T} \\ \underset{\sim}{V}_3^{i-1^T} \end{bmatrix}_j \tag{6.84}$$

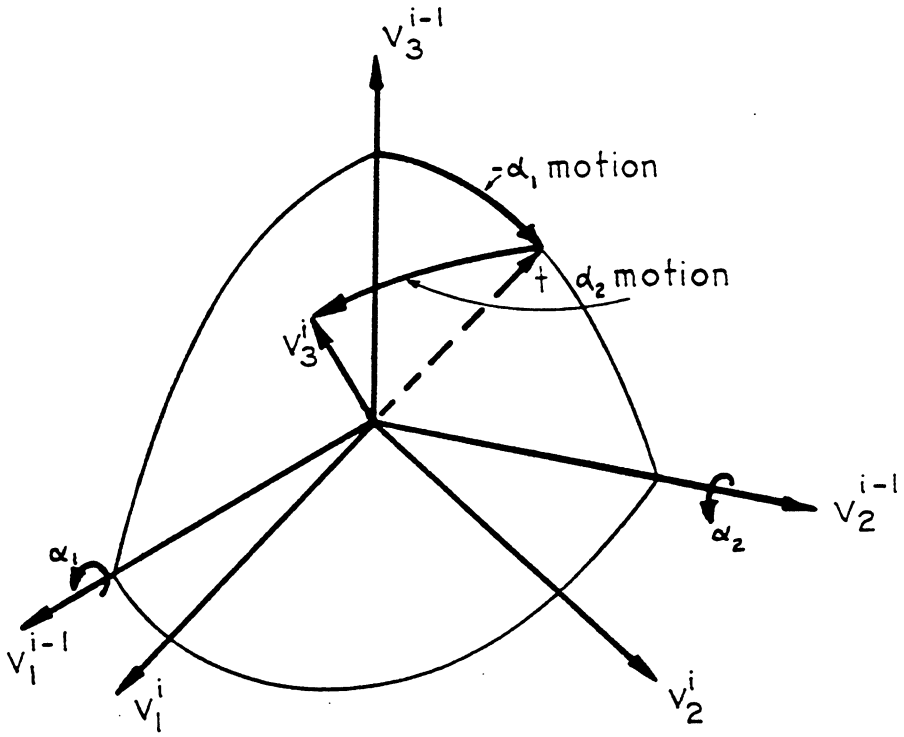

FIG. 6.9 TRANSFORMATION OF THE SHELL SURFACE VECTORS IN A LARGE DISPLACEMENT ANALYSIS

$$\begin{bmatrix} \underset{\sim}{v}_1^{i\,T} \\ \underset{\sim}{v}_2^{i\,T} \\ \underset{\sim}{v}_3^{i\,T} \end{bmatrix}_j = \begin{bmatrix} \cos\alpha_2 & 0 & -\sin\alpha_2 \\ 0 & 1 & 0 \\ \sin\alpha_2 & 0 & \cos\alpha_2 \end{bmatrix}_j \begin{bmatrix} \underset{\sim}{v}_1^{i-1\,T} \\ \underset{\sim}{v}_2^{i\,T} \\ \underset{\sim}{t}^{T} \end{bmatrix}_j \tag{6.85}$$

and the required transformation is:

$$\begin{bmatrix} \underset{\sim}{v}_1^{i\,T} \\ \underset{\sim}{v}_2^{i\,T} \\ \underset{\sim}{v}_3^{i\,T} \end{bmatrix}_j = \begin{bmatrix} \cos\alpha_2 & 0 & -\sin\alpha_2 \\ 0 & 1 & 0 \\ \sin\alpha_2 & 0 & \cos\alpha_2 \end{bmatrix}_j \begin{bmatrix} 1 & 0 & 0 \\ 0 & \cos\alpha_1 & \sin\alpha_1 \\ 0 & -\sin\alpha_1 & \cos\alpha_2 \end{bmatrix}_j \begin{bmatrix} \underset{\sim}{v}_1^{i-1\,T} \\ \underset{\sim}{v}_2^{i-1\,T} \\ \underset{\sim}{v}_3^{i-1\,T} \end{bmatrix}_j$$

$$= \begin{bmatrix} \cos\alpha_2 & \sin\alpha_1\sin\alpha_2 & -\sin\alpha_2\cos\alpha_1 \\ 0 & \cos\alpha_1 & \sin\alpha_1 \\ \sin\alpha_2 & -\sin\alpha_1\cos\alpha_2 & \cos\alpha_1\cos\alpha_2 \end{bmatrix}_j \begin{bmatrix} \underset{\sim}{v}_1^{i-1\,T} \\ \underset{\sim}{v}_2^{i-1\,T} \\ \underset{\sim}{v}_3^{i-1\,T} \end{bmatrix}_j \tag{6.86}$$

The above procedure assumes that the incremental rotations are small. For large rotation problems, the rotations have to be divided into smaller increments. The upper limit should be set at 0.1 radians.

It should also be noted that the sequence of motions due to α_1 and α_2 are order dependent. However, when the incremental rotations are small, the dependency on the order is diminished.

7. EDGE AND SUPPORTING MEMBERS

7.1 Introduction

The incorporation of the edge and supporting members is of utmost importance in the analysis of shell structures, because a free form shell is rarely built without edge members. Fig. 7.1 shows some of the typical shell structures with edge members. The edge members may or may not be prestressed to carry the forces delivered from the shell proper. Furthermore, they may be placed eccentrically to the shell. In the present study, both concentric and eccentric edge members are included, but prestressing is not considered.

In the analysis of reinforced concrete structures with edge or supporting members, the edge members may be modelled in some cases by shell elements. This approach is generally satisfactory as long as the beam is placed concentrically with the shell. However, in this approach, the torsional and the biaxial bending behavior of the actual edge member cannot be modelled adequately.

Arnesen [15] in his reinforced cylindrical shell analysis has demonstrated that the modelling of the geometry of the shell-beam system by shell elements, which forces the edge beam to behave as a plane stress system, does not necessarily yield better results.

Schnobrich [118] in his linear analyses of HP shells uses a high order beam element to model the edge beams and the crown beams.

Jackson [119], in his nonlinear plate analyses, uses a three-dimensional filamented reinforced concrete beam element to model the eccentric edge beam. Only nonlinear material is considered in his analyses.

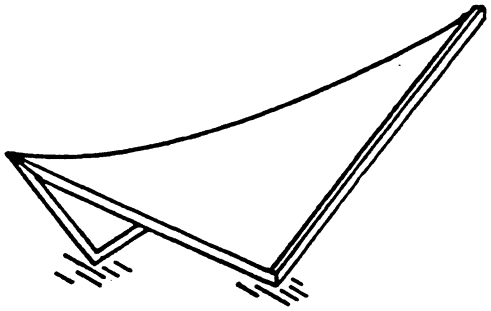

HP SADDLE SHELL

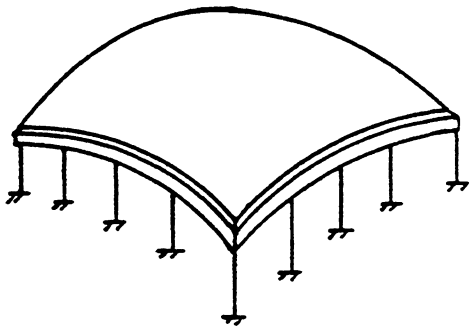

TRANSLATIONAL DOME

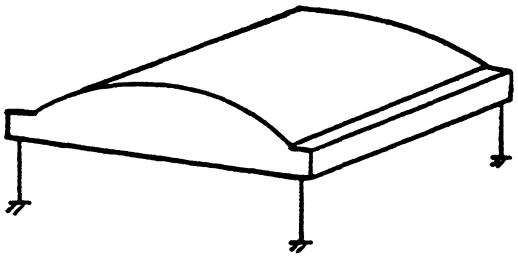

CYLINDRICAL SHELL

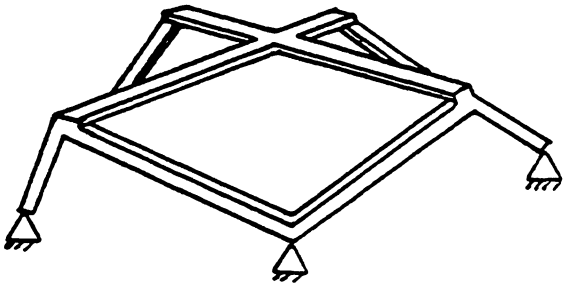

HP GABLED SHELL

FIG. 7.1 TYPICAL SHELL STRUCTURE WITH EDGE MEMBERS

In this study, a three-dimensional reinforced concrete edge beam element is adapted to the analysis, which includes the effects of nonlinear material, nonlinear geometry, and the time-dependent effects of creep and shrinkage.

7.2 Modelling of Edge Beam

In the modelling of edge beam, it is important to recognize that the beam and the shell act as a composite. The strains at the shell-beam junction are equal.

In the present study, a curved shell element is used. This means that a curved beam element should be used in order to accurately model the full composite action. In this case, not only is the computational effort high, but also the coupling between the bending and the torsional behavior of the beam requires special treatment involving a theory of warping torsion.

As a first approximation and to simplify the problem in the present study, the usual Saint-Venant torsion is assumed, where free warping of the cross section is permitted. In this case, the bending and the torsional behavior are uncoupled, and equilibrium conditions limit the beam's geometry to be longitudinally straight.

Once a longitudinal straight beam geometry is assumed, the notion of equal strains at the shell-beam junction becomes meaningless when it is curved. However, following the arguments of Chapter 5, which stipulate that the necessary conditions for a converged system are the inclusion of the constant strain states and all the required rigid body modes; the shell-beam system, although it cannot represent the composite action completely, will tend to converge to the true solution with mesh refinements. The effect is to enforce compatibility only

at nodal displacements and to lump the interactive forces at the nodes.

In this study, two straight beam elements are used along one side of each shell element (Fig. 7.2a). The use of only one linear strain beam element (Fig. 7.2b) connected to each curved shell element boundary poses a number of problems which preclude its use and it is therefore not further pursued here.

The beam elements are assumed to be connected to the shell by rigid links.

7.3 Reinforced Concrete Beam Element for the Present Study

7.3.1 General

In the present study, a filamented reinforced concrete beam element is adopted. Each filament is assumed to be in a uniaxial stress state and perfect bond between adjacent filaments is assumed. At any cross section, the material properties in each filament can vary to accommodate material nonlinearities. The beam stiffness at some reference axes can be obtained by summing the contributions from all the filaments.

It should be emphasized that while the location of the reference axis is arbitrary, the use of different orders of strain fields for the in-plane and the bending actions results in a beam stiffness which will be different for each different location of the reference axis.

As an illustration, two different planar beam elements are studied. The CCB beam element (Fig. 7.3a) assumes linear and cubic displacement fields at the reference axis for the axial and the bending deformations, respectively. The CLB beam element (Fig. 7.3b) has the same displacement fields as the CCB and an additional axial displacement degree of freedom u_n, which is eliminated by static condensation. With the Euler-Bernoulli's assumptions for the beam's kinematics, it can be seen

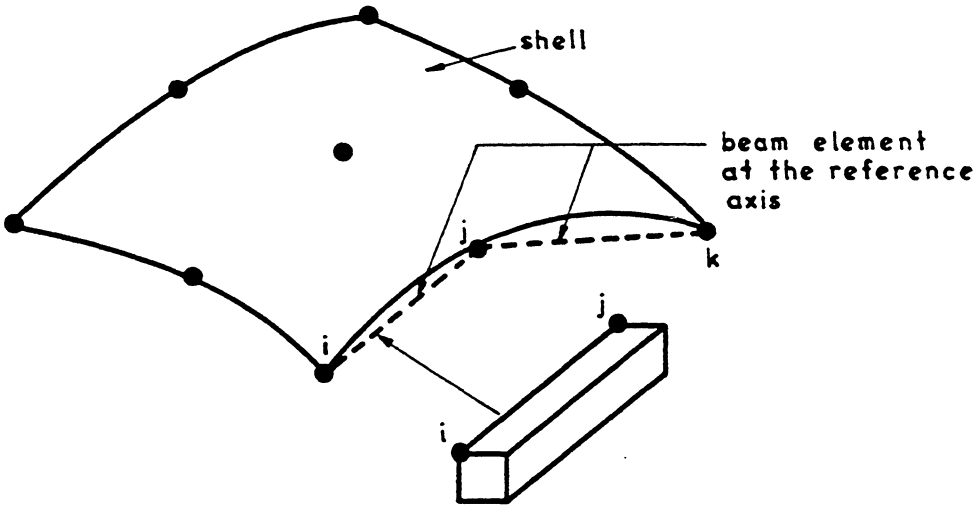

(a) CONFIGURATION OF 2 BEAMS ALONG EACH SIDE OF A SHELL ELEMENT

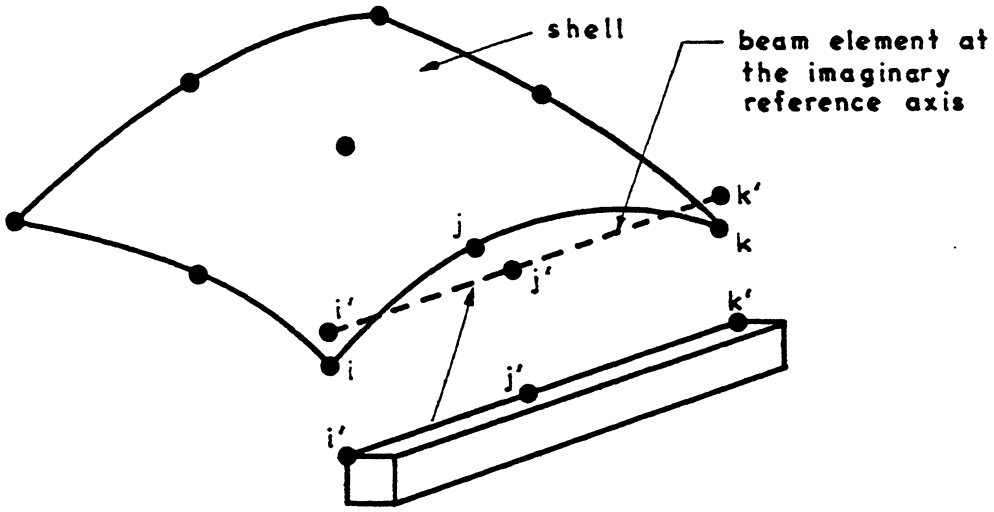

(b) CONFIGURATION OF ONE BEAM ALONG EACH SIDE OF A SHELL ELEMENT

FIG. 7.2 POSSIBLE CONFIGURATION OF STRAIGHT BEAM ELEMENT CONNECTED TO THE PRESENT SHELL ELEMENT

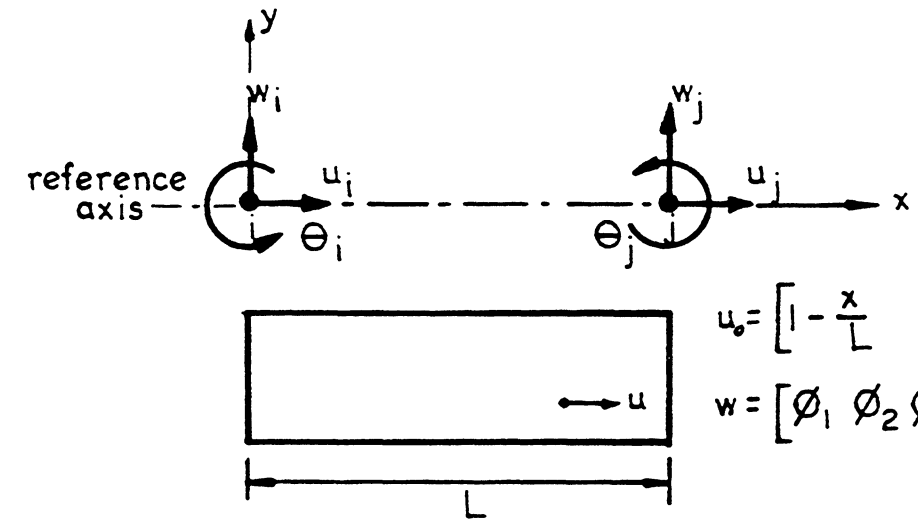

$$u_o = \begin{bmatrix} 1 - \frac{x}{L} & \frac{x}{L} \end{bmatrix} \begin{bmatrix} u_i \\ u_j \end{bmatrix}$$

$$w = \begin{bmatrix} \phi_1 & \phi_2 & \phi_3 & \phi_4 \end{bmatrix} \begin{bmatrix} w_i \\ w_j \\ \Theta_i \\ \Theta_j \end{bmatrix}$$

(a) CCB BEAM

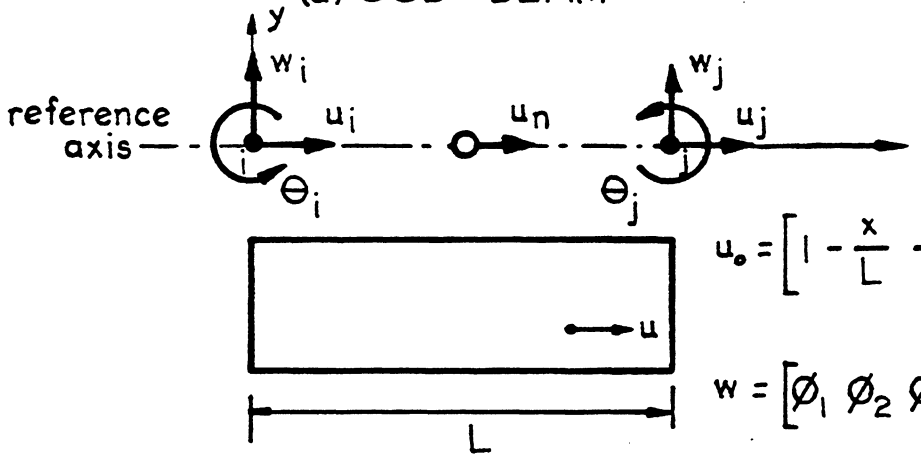

$$u_o = \begin{bmatrix} 1 - \frac{x}{L} & \frac{x}{L} & 4\frac{x}{L}(1 - \frac{x}{L}) \end{bmatrix} \begin{bmatrix} u_i \\ u_j \\ u_n \end{bmatrix}$$

$$w = \begin{bmatrix} \phi_1 & \phi_2 & \phi_3 & \phi_4 \end{bmatrix} \begin{bmatrix} w_i \\ w_j \\ \Theta_i \\ \Theta_j \end{bmatrix}$$

(b) CLB BEAM

$$u = u_o - y \frac{dw}{dx}$$

$$\phi_1 = 1 + 2\left(\frac{x}{L}\right)^3 - 3\left(\frac{x}{L}\right)^2 \qquad \phi_2 = 3\left(\frac{x}{L}\right)^2 - 2\left(\frac{x}{L}\right)^3$$

$$\phi_3 = L\left(\frac{x}{L} - 2\left(\frac{x}{L}\right)^2 + \left(\frac{x}{L}\right)^3\right) \qquad \phi_4 = -L\left(\left(\frac{x}{L}\right)^2 - \left(\frac{x}{L}\right)^3\right)$$

FIG. 7.3 GEOMETRY AND DISPLACEMENT FUNCTIONS FOR DIFFERENT BEAM MODELS

immediately that a constant axial strain constraint is imposed in the CCB beam element at the reference axis.

To show the effects of this artificial constraint on the behavior of the CCB beam element, a cantilever beam with stiffnesses EA and EI, modelled first by one CCB and second by one CLB is analyzed. The reference axis is assumed to be at a distance d above the neutral axis of the beam. The results of the analyses are compared with those from the elementary beam theory and are summarized in Table 7.1.

The CCB can only represent exactly the cases where constant strain exists at the reference axis. Examples are: constant axial load ($R_1 = 1$, $R_3 = d$), and constant axial load plus a constant moment ($R_1 = 1$). However, in the case of linear moment ($R_2 = 1$), the CCB gives a vertical displacement of:

$$r_2 = \frac{L^3}{4EI} + \frac{L^3}{12E(I + Ad^2)}$$

corresponding to an error of:

$$-\frac{L^3}{12EI} + \frac{L^3}{12E(I + Ad^2)}$$

For d = h/2, the vertical displacement is found to be 19% less than the exact value. This discrepancy can be corrected by mesh refinement, however.

The CLB, on the other hand, gives the correct displacements for the three different load cases studied, independent of the location of the reference axis relative to the neutral axis.

It is therefore concluded that the incompatible axial displacement degree of freedom u_n is necessary for the correct modelling of the

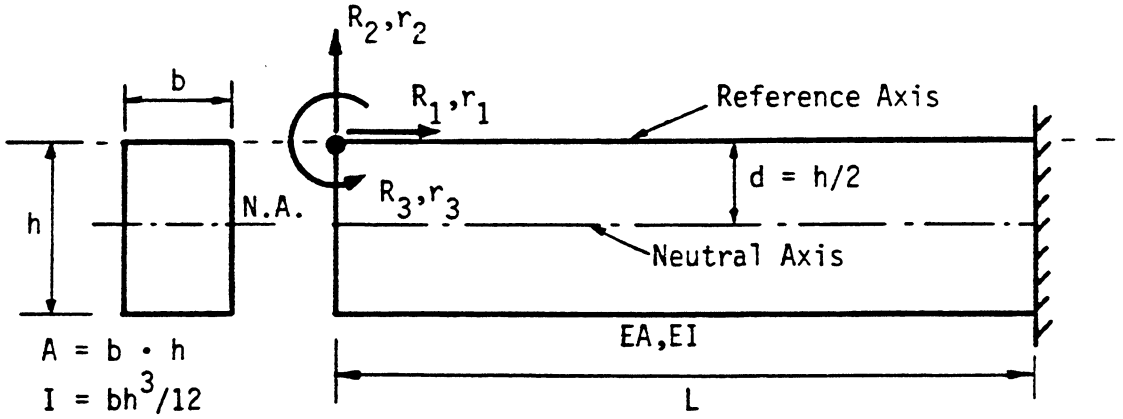

TABLE 7.1 DISPLACEMENTS COMPARISON FOR CANTILEVER BEAM WITH REFERENCE AXIS PLACED AT DIFFERENT LOCATION

Loading	Displacement	Exact (Beam Theory)	$d \neq 0$ CCB	$d \neq 0$ CLB
$R_1 = 1$	r_1	$\frac{L}{EA} + \frac{Ld^2}{EI}$	$\frac{L}{EA} + \frac{Ld^2}{EI}$	$\frac{L}{EA} + \frac{Ld^2}{EI}$
	r_2	$\frac{L^2d}{2EI}$	$\frac{L^2d}{2EI}$	$\frac{L^2d}{2EI}$
	r_3	$-\frac{Ld}{EI}$	$-\frac{Ld}{EI}$	$-\frac{Ld}{EI}$
$R_2 = 1$	r_1	$\frac{L^2d}{2EI}$	$\frac{L^2d}{2EI}$	$\frac{L^2d}{2EI}$
	r_2	$\frac{L^3}{3EI}$	$\frac{L^3}{4EI} + \frac{L^3}{12E(I+Ad^2)}$	$\frac{L^3}{3EI}$
	r_3	$-\frac{L^2}{2EI}$	$-\frac{L^2}{2EI}$	$-\frac{L^2}{2EI}$
$R_1 = 1$ $R_3 = d$	r_1	$\frac{L}{EA}$	$\frac{L}{EA}$	$\frac{L}{EA}$
	r_2	0	0	0
	r_3	0	0	0

bending stiffness and to take into account the shifting of the neutral axis due to cracking and other material nonlinearities in a reinforced concrete beam.

7.3.2 Geometry and Displacement Fields

The geometry of the beam element is shown in Fig. 7.4. The beam element has a rectangular cross section, of length L, and has local axes x, y, and z, with unit vectors $\hat{x}$, $\hat{y}$, and $\hat{z}$, respectively. The beam geometric center is described by the offsets e_y and e_z relative to the $\hat{x}$ axis.

The vector $\hat{x}$ is defined by the vector $\overline{IJ}$ joining node i and node j, normalized to unit magnitude.

The vector $\hat{z}$ is perpendicular to the plane spanned by the vectors $\overline{IJ}$ and $\overline{IK}$, normalized to unit magnitude

$$\hat{z} = \frac{\overline{IJ} \times \overline{IK}}{|\overline{IJ} \times \overline{IK}|}$$

where $\overline{IK}$ is the vector joining node i and node k. The location of node k must not lie along the x axis and the resulting $\hat{z}$ vector must be parallel to one of the principal axes.

The $\hat{y}$ vector is perpendicular to the $\hat{x}$ and $\hat{z}$ vectors

$$\hat{y} = \hat{z} \times \hat{x} .$$

There are 13 DOF for the beam element. Six DOF are associated with each of the two end nodes, namely u_i, v_i, w_i, θ_{x_i}, θ_{y_i}, and θ_{z_i}, and an internal mid-side axial degree of freedom u_n, which is eliminated at the element level, leaving only 12 DOF for the beam element.

The displacement fields of the beam element on its local x axis are:

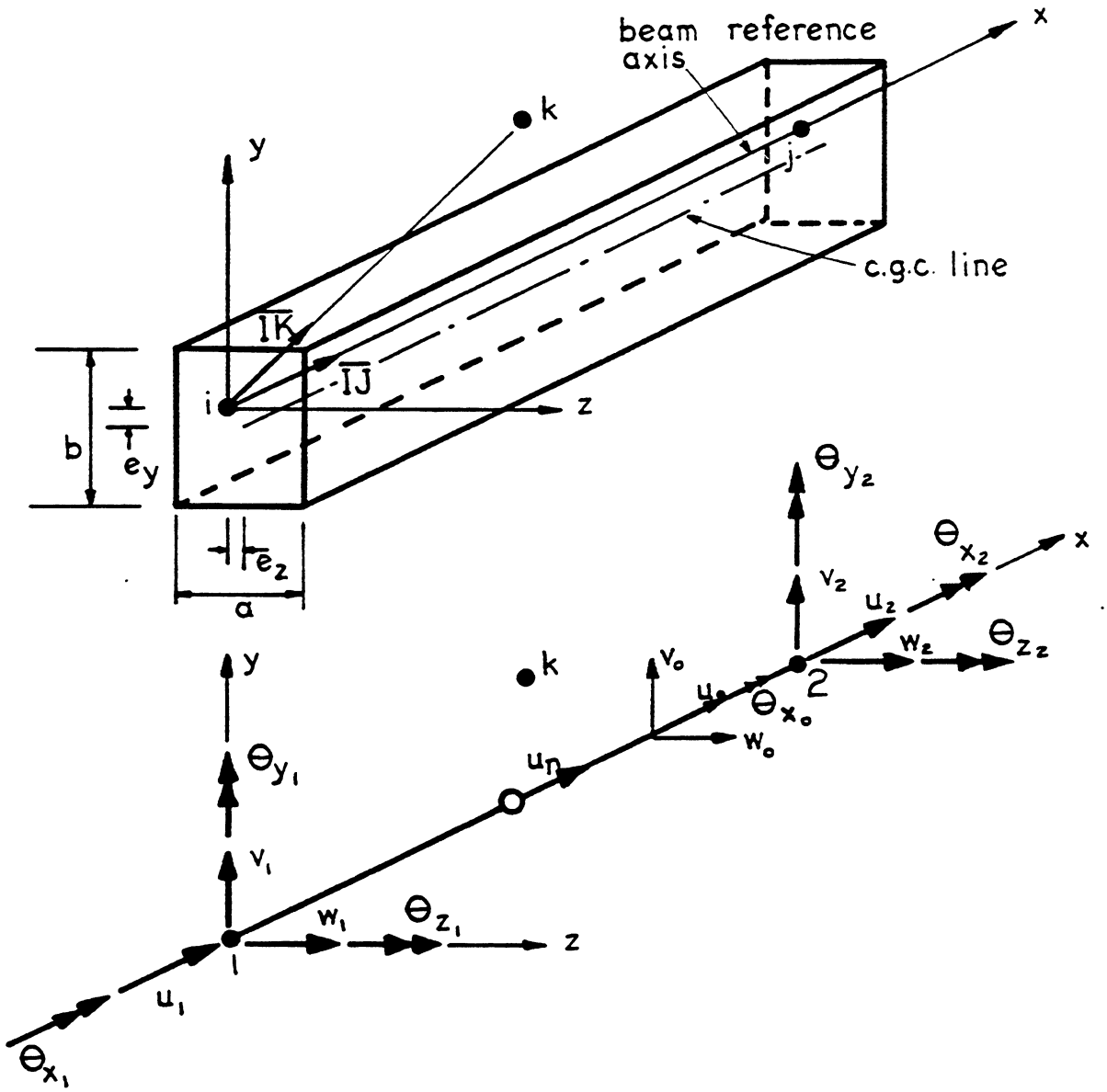

$$\underset{\sim}{S}_a^T = \left[S_{u_1}\ S_{u_2}\ S_{v_1}\ S_{v_2}\ S_{\theta_{z_1}}\ S_{\theta_{z_2}}\ S_{w_1}\ S_{w_2}\ S_{\theta_{y_1}}\ S_{\theta_{y_2}}\ S_{\theta_{x_1}}\ S_{\theta_{x_2}} \right]$$

$$\underset{\sim}{v}_a^T = \left[u_1\ \ u_2\ \ v_1\ \ v_2\ \ \Theta_{z_1}\ \Theta_{z_2}\ w_1\ \ w_2\ \ \Theta_{y_1}\ \Theta_{y_2}\ \Theta_{x_1}\ \Theta_{x_2} \right]$$

FIG. 7.4 3D BEAM ELEMENT - GEOMETRY AND DEGREES OF FREEDOM

$$u_o = \begin{bmatrix} 1 - \frac{x}{L} & \frac{x}{L} & 4(1-\frac{x}{L})\frac{x}{L} \end{bmatrix} \begin{bmatrix} u_1 \\ u_2 \\ u_n \end{bmatrix} \tag{7.1a}$$

$$v_o = \begin{bmatrix} \phi_1 & \phi_2 & \phi_3 & \phi_4 \end{bmatrix} \begin{bmatrix} v_1 \\ v_2 \\ \theta_{z_1} \\ \theta_{z_2} \end{bmatrix} \tag{7.1b}$$

$$w_o = \begin{bmatrix} \phi_1 & \phi_2 & -\phi_3 & -\phi_4 \end{bmatrix} \begin{bmatrix} w_1 \\ w_2 \\ \theta_{y_1} \\ \theta_{y_2} \end{bmatrix} \tag{7.1c}$$

where

$$\phi_1 = 1 + 2(\frac{x}{L})^3 - 3(\frac{x}{L})^2$$

$$\phi_2 = 3(\frac{x}{L})^2 - 2(\frac{x}{L})^3$$

$$\phi_3 = L\left[\frac{x}{L} - 2(\frac{x}{L})^2 + (\frac{x}{L})^3\right]$$

$$\phi_4 = -L\left[(\frac{x}{L})^2 - (\frac{x}{L})^3\right]$$

The axial displacement, u_x, at any point within the beam element can be obtained by assuming the Euler-Bernoulli's beam kinematics

$$u_x = u_o - z\frac{dw_o}{dx} - y\frac{dv_o}{dx} \tag{7.2}$$

The axial strain ε_x is then obtained by differentiating u_x with

respect to x

$$\varepsilon_x = \frac{du_x}{dx}$$

$$= \frac{du_o}{dx} - z\frac{d^2w_o}{dx^2} - y\frac{d^2v_o}{dx^2} \tag{7.3}$$

Substituting Eq. 7.1a, Eq. 7.1b, and Eq. 7.1c into Eq. 7.3, the resulting strain-displacement relationship is:

$$\varepsilon_x = \underset{\sim}{B}_u \underset{\sim}{u} - y\,\underset{\sim}{B}_v \underset{\sim}{v} - z\,\underset{\sim}{B}_w \underset{\sim}{w} \tag{7.4}$$

where

$$\underset{\sim}{B}_u = \left[-\frac{1}{L}\ \ \frac{1}{L}\left(\frac{1}{L} - \frac{2x}{L^2}\right)\cdot 4\right]$$

$$\underset{\sim}{B}_v = \left[\phi_{1,xx}\ \ \phi_{2,xx}\ \ \phi_{3,xx}\ \ \phi_{4,xx}\right]$$

$$\underset{\sim}{B}_w = \left[\phi_{1,xx}\ \ \phi_{2,xx}\ \ -\phi_{3,xx}\ \ -\phi_{4,xx}\right]$$

$$\underset{\sim}{u}^T = \left[u_1\ \ u_2\ \ u_n\right]$$

$$\underset{\sim}{v}^T = \left[v_1\ \ v_2\ \ \theta_{z_1}\ \ \theta_{z_2}\right]$$

$$\underset{\sim}{w}^T = \left[w_1\ \ w_2\ \ \theta_{y_i}\ \ \theta_{y_2}\right]$$

and $_{,xx}$ represents the second derivative with respect to x.

The rotation about the x axis, θ_{x_o}, is assumed to be linear

$$\theta_{x_o} = \left[1 - \frac{x}{L}\ \ \frac{x}{L}\right]\begin{bmatrix}\theta_{x_1}\\ \theta_{x_2}\end{bmatrix} \tag{7.5}$$

and the twist α along the reference axis x is:

$$\alpha = \frac{d\theta_{x_o}}{dx} = \left[-\frac{1}{L} \quad \frac{1}{L}\right] \begin{bmatrix} \theta_{x_1} \\ \theta_{x_2} \end{bmatrix} \tag{7.6}$$

$$= \underset{\sim}{B}_{\theta} \, \underset{\sim}{\theta}_{x}$$

Note that unrestrained warping torsion is assumed in Eq. 7.3. This leads to the uncoupling of the torsional degrees of freedom from the other degrees of freedom.

7.3.3 Element Elastic Stiffness

Following the same procedure as described in Chapter 6, the elastic stiffness of a reinforced concrete beam can be obtained.

$$\underset{\sim}{k}_e = \int_{V_1} E \, \varepsilon_x \, \delta\varepsilon_x \, dv + \int_L GJ \, \alpha \, \delta\alpha \, dx \tag{7.7}$$

where E and ε_x are functions of the local x, y, and z axes; and the torsional stiffness GJ is a function of x.

Using the strain displacements relationships, Eq. 7.4 and Eq. 7.6, Eq. 7.7 can be rewritten:

$$\underset{\sim}{k}_e = \int_0^L \int_{-\frac{b}{2}}^{\frac{b}{2}} \int_{-\frac{a}{2}}^{\frac{a}{2}} [\underset{\sim}{B}_u \; -y\underset{\sim}{B}_v \; -z\underset{\sim}{B}_w]^T \, E \, [\underset{\sim}{B}_u \; -y\underset{\sim}{B}_v \; -z\underset{\sim}{B}_w] \, dz \, dy \, dx$$

$$+ \int_0^L \underset{\sim}{B}_{\theta}^T \, GJ \, \underset{\sim}{B}_{\theta} \, dx \tag{7.8}$$

where a and b are the beam's cross-sectional dimensions.

For a reinforced concrete beam section divided into N_z equal layers in the z' direction and N_y equal layers in the y' direction and reinforced with N_s steel reinforcing bars (Fig. 7.5), the beam stiffness can be obtained explicitly when the material in each filament is assumed to be constant along the beam element. The result is:

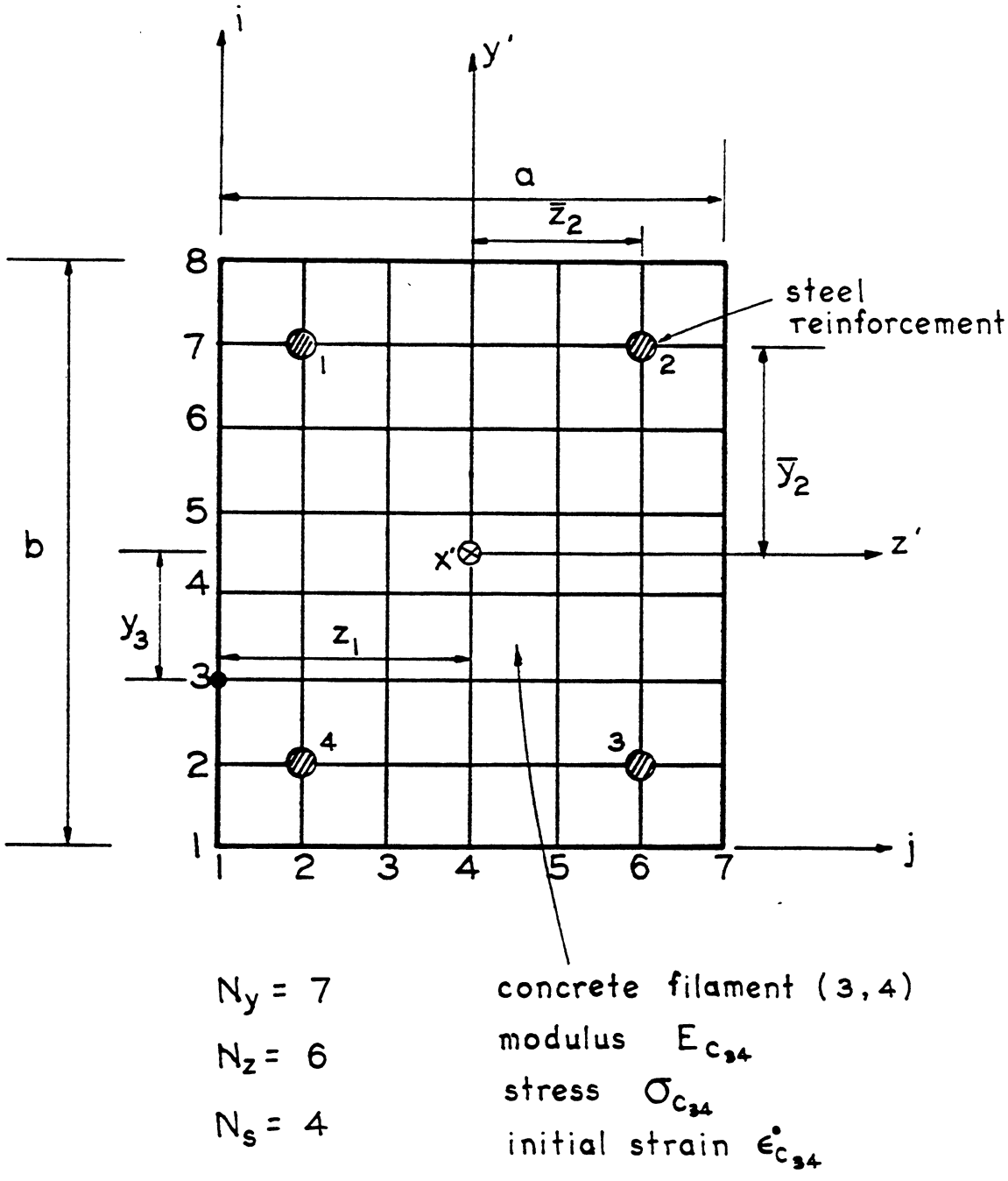

FIG. 7.5 TYPICAL CROSS SECTION OF A REINFORCED CONCRETE BEAM ELEMENT

$$\underset{\sim}{k}_e = \begin{bmatrix} \underset{\sim}{K}_{uu} & \underset{\sim}{K}_{uv} & \underset{\sim}{K}_{uw} & 0 \\ & \underset{\sim}{K}_{vv} & \underset{\sim}{K}_{vw} & 0 \\ \text{SYMM.} & & \underset{\sim}{K}_{ww} & 0 \\ & & & \underset{\sim}{K}_{\theta\theta} \end{bmatrix} \tag{7.9}$$

where the submatrices

$$\underset{\sim}{K}_{uu} = \int_0^L \underset{\sim}{B}_u^T D_{uu} \underset{\sim}{B}_u \, dx$$

$$\underset{\sim}{K}_{uv} = \int_0^L \underset{\sim}{B}_u^T D_{uv} \underset{\sim}{B}_v \, dx$$

$$\underset{\sim}{K}_{uw} = \int_0^L \underset{\sim}{B}_u^T D_{uw} \underset{\sim}{B}_w \, dx$$

$$\underset{\sim}{K}_{vv} = \int_0^L \underset{\sim}{B}_v^T D_{vv} \underset{\sim}{B}_v \, dx$$

$$\underset{\sim}{K}_{vw} = \int_0^L \underset{\sim}{B}_v^T D_{vw} \underset{\sim}{B}_w \, dx$$

$$\underset{\sim}{K}_{ww} = \int_0^L \underset{\sim}{B}_w^T D_{ww} \underset{\sim}{B}_w \, dx$$

$$\underset{\sim}{K}_{\theta\theta} = \int_0^L \underset{\sim}{B}_\theta^T GJ \underset{\sim}{B}_\theta \, dx$$

and

$$D_{uu} = \sum_{j=1}^{N_z} \sum_{i=1}^{N_y} (z_j - z_{j+1})(y_i - y_{i+1}) E_{c_{ij}} + \sum_{l=1}^{N_s} E_{s_l} A_{s_l}$$

$$D_{uv} = -\tfrac{1}{2} \sum_{j=1}^{N_z} \sum_{i=1}^{N_y} (z_j - z_{j+1})(y_i^2 - y_{i+1}^2) E_{c_{ij}} - \sum_{l=1}^{N_s} E_{s_l} A_{s_l} \bar{y}_l$$

$$D_{uw} = -\tfrac{1}{2} \sum_{j=1}^{N_z} \sum_{i=1}^{N_y} (z_j^2 - z_{j+1}^2)(y_i - y_{i+1}) E_{c_{ij}} - \sum_{l=1}^{N_s} E_{s_l} A_{s_l} \bar{z}_l$$

$$D_{vv} = \frac{1}{3} \sum_{j=1}^{N_z} \sum_{i=1}^{N_y} (z_j - z_{j+1})(y_i^3 - y_{i+1}^3) E_{c_{ij}} + \sum_{l=1}^{N_s} E_{s_l} A_{s_l} \bar{y}_l^2$$

$$D_{vw} = \frac{1}{4} \sum_{j=1}^{N_z} \sum_{i=1}^{N_y} (z_j^2 - z_{j+1}^2)(y_i^2 - y_{i+1}^2) E_{c_{ij}} + \sum_{l=1}^{N_s} E_{s_l} A_{s_l} \bar{z}_l \bar{y}_l$$

$$D_{ww} = \frac{1}{3} \sum_{j=1}^{N_z} \sum_{i=1}^{N_y} (z_j^3 - z_{j+1}^3)(y_i - y_{i+1}) E_{c_{ij}} + \sum_{l=1}^{N_s} E_{s_l} A_{s_l} \bar{z}_l^2$$

$E_{c_{ij}}$ = Uniaxial modulus of elasticity for concrete

E_{s_l} = Uniaxial modulus of elasticity for steel

The submatrices of Eq. 7.9 after integration is performed are:

$$\underset{\sim}{K}_{uu} = \begin{bmatrix} \frac{1}{L} & -\frac{1}{L} & 0 \\ & \frac{1}{L} & 0 \\ \text{SYMM.} & & \frac{16}{3L} \end{bmatrix} D_{uu} \qquad (7.10a)$$

$$\underset{\sim}{K}_{uv} = \begin{bmatrix} 0 & 0 & \frac{1}{L} & -\frac{1}{L} \\ 0 & 0 & -\frac{1}{L} & \frac{1}{L} \\ -\frac{8}{L^2} & \frac{8}{L^2} & -\frac{4}{L} & -\frac{4}{L} \end{bmatrix} D_{uv} \qquad (7.10b)$$

$$\underset{\sim}{K}_{uw} = \begin{bmatrix} 0 & 0 & -\frac{1}{L} & \frac{1}{L} \\ 0 & 0 & \frac{1}{L} & -\frac{1}{L} \\ -\frac{8}{L^2} & \frac{8}{L^2} & \frac{4}{L} & \frac{4}{L} \end{bmatrix} D_{uw} \qquad (7.10c)$$

$$\underset{\sim}{K}_{w} = \begin{bmatrix} \frac{12}{L^3} & -\frac{12}{L^3} & \frac{6}{L^2} & \frac{6}{L^2} \\ & \frac{12}{L^3} & -\frac{6}{L^2} & \frac{6}{L^2} \\ & & \frac{4}{L} & \frac{2}{L} \\ \text{SYMM.} & & & \frac{4}{L} \end{bmatrix} D_{vv} \qquad (7.10d)$$

$$\underset{\sim}{K}_{vw} = \begin{bmatrix} \frac{12}{L^3} & -\frac{12}{L^3} & -\frac{6}{L^2} & -\frac{6}{L^2} \\ -\frac{12}{L^3} & \frac{12}{L^3} & \frac{6}{L^2} & \frac{6}{L^2} \\ \frac{6}{L^2} & -\frac{6}{L^2} & -\frac{4}{L} & -\frac{2}{L} \\ \frac{6}{L^2} & -\frac{6}{L^2} & -\frac{2}{L} & -\frac{4}{L} \end{bmatrix} D_{vw} \qquad (7.10e)$$

$$\underset{\sim}{K}_{ww} = \begin{bmatrix} \frac{12}{L^3} & -\frac{12}{L^3} & -\frac{6}{L^2} & -\frac{6}{L^2} \\ & \frac{12}{L^3} & \frac{6}{L^2} & \frac{6}{L^2} \\ & & \frac{4}{L} & \frac{2}{L} \\ \text{SYMM.} & & & \frac{4}{L} \end{bmatrix} D_{ww} \qquad (7.10f)$$

$$\underset{\sim}{K}_{\theta\theta} = \begin{bmatrix} \frac{1}{L} & -\frac{1}{L} \\ -\frac{1}{L} & \frac{1}{L} \end{bmatrix} GJ \qquad (7.10g)$$

The stiffness $\underset{\sim}{k}_e$ can be rearranged so that the last row contains the displacement degree of freedom u_n. In matrix form,

$$\left[\begin{array}{c|c} \underset{\sim}{k}_{aa} & \underset{\sim}{k}_{ab} \\ \hline \underset{\sim}{k}_{ba} & k_{bb} \end{array}\right] \left[\begin{array}{c} \underset{\sim}{v}_a \\ \hline u_n \end{array}\right] = \left[\begin{array}{c} \underset{\sim}{S}_a \\ \hline S_u \end{array}\right] \qquad (7.11)$$

where $\underset{\sim}{v}_a^T = [\, u_1 \; u_2 \; v_1 \; v_2 \; \theta_{z_1} \; \theta_{z_2} \; w_1 \; w_2 \; \theta_{y_1} \; \theta_{y_2} \; \theta_{x_1} \; \theta_{x_2} \,]$

$$k_{bb} = \frac{16}{3L} D_{uu}$$

$$\underset{\sim}{k}_{ba} = [\, 0 \;\; 0 \;\; -\frac{8}{L^2} D_{uv} \;\; \frac{8}{L^2} D_{uv} \;\; -\frac{4}{L} D_{uv} \;\; -\frac{4}{L} D_{uv} \;\; -\frac{8}{L^2} D_{uw} \;\; \frac{8}{L^2} D_{uw}$$

$$\frac{4}{L} D_{uw} \;\; \frac{4}{L} D_{uw} \;\; 0 \;\; 0 \,]$$

$$\underset{\sim}{k}_{ab} = \underset{\sim}{k}_{ba}^T$$

Using static condensation with $S_u = 0$, the final beam elastic stiffness $\underset{\sim}{k}_a$ is:

$$\underset{\sim}{k}_a = \underset{\sim}{k}_{aa} - \frac{1}{k_{bb}} \underset{\sim}{k}_{ab} \underset{\sim}{k}_{ba} \qquad (7.12)$$

relating the element load $\underset{\sim}{S}_a$ and the displacement $\underset{\sim}{v}_a$.

$$\underset{\sim}{S}_a = \underset{\sim}{k}_a \underset{\sim}{v}_a$$

7.3.4 Element Geometric Stiffness

The nonlinear strains component η_{ij} for the beam element obtained by making use of Eq. 2.42 is:

$$\eta_{xx} = \tfrac{1}{2}\left(\frac{\partial u_o}{\partial x}\right)^2 + \tfrac{1}{2}\left(\frac{\partial v_o}{\partial x}\right)^2 + \tfrac{1}{2}\left(\frac{\partial w_o}{\partial x}\right)^2 \tag{7.13}$$

The beam geometric stiffness can be obtained by substituting the assumed beam displacement fields (Eq. 7.1a, Eq. 7.1b, and Eq. 7.1c) into Eq. 7.13 and evaluating the expression:

$$\underset{\sim}{k}_g = \int_{V_1} \sigma\eta_{xx}\, \delta\eta_{xx}\, dv \tag{7.14}$$

This approach has been used by Kang [74] and Aldstedt [24].

However, when constant axial force is assumed in the beam element, the beam behaves like a truss element in carrying the axial load. Consequently, a more simple truss element geometric stiffness can be used. Furthermore, when the equilibrium correction is performed on the solution, the exact tangent stiffness need not be formed. The displacement fields in this case become:

$$u_o = \begin{bmatrix} 1 - \frac{x}{L} & \frac{x}{L} \end{bmatrix} \begin{bmatrix} u_1 \\ u_2 \end{bmatrix} \tag{7.15a}$$

$$v_o = \begin{bmatrix} 1 - \frac{x}{L} & \frac{x}{L} \end{bmatrix} \begin{bmatrix} v_1 \\ v_2 \end{bmatrix} \tag{7.15b}$$

$$w_o = \begin{bmatrix} 1 - \frac{x}{L} & \frac{x}{L} \end{bmatrix} \begin{bmatrix} w_1 \\ w_2 \end{bmatrix} \tag{7.15c}$$

Substituting Eq. 7.15a, Eq. 7.15b, and Eq. 7.15c into Eq. 7.13 and the results into Eq. 7.14, the resulting beam geometric stiffness is:

$$\underset{\sim}{k}_g = \frac{P}{L}\begin{bmatrix} 1 & -1 & 0 & 0 & 0 & 0 & 0 & 0 & 0 & 0 & 0 & 0 \\ & 1 & 0 & 0 & 0 & 0 & 0 & 0 & 0 & 0 & 0 & 0 \\ & & 1 & -1 & 0 & 0 & 0 & 0 & 0 & 0 & 0 & 0 \\ & & & 1 & 0 & 0 & 0 & 0 & 0 & 0 & 0 & 0 \\ & & & & 0 & 0 & 0 & 0 & 0 & 0 & 0 & 0 \\ & & & & & 0 & 0 & 0 & 0 & 0 & 0 & 0 \\ & & & & & & 1 & -1 & 0 & 0 & 0 & 0 \\ & & & & & & & 1 & 0 & 0 & 0 & 0 \\ & & \text{SYMM.} & & & & & & 0 & 0 & 0 & 0 \\ & & & & & & & & & 0 & 0 & 0 \\ & & & & & & & & & & 0 & 0 \\ & & & & & & & & & & & 0 \end{bmatrix} \qquad (7.16)$$

where the axial force P is:

$$P = \sum_{j=1}^{N_z} \sum_{i=1}^{N_y} (z_j - z_{j+1})(y_i - y_{i+1})\, \sigma_{c_{ij}} + \sum_{l=1}^{N_s} A_{s_l}\, \sigma_{s_l}$$

and $\underset{\sim}{S}_a = \underset{\sim}{k}_g \underset{\sim}{v}_a$

7.3.5 Element Internal Resisting Load

The internal resisting load $\underset{\sim}{S}_I$ due to the stresses σ_c in the concrete filaments, σ_s in the steel filaments and the torque T_x in the beam can be obtained by evaluating

$$\underset{\sim}{S}_I = \int_{v_1} \underset{\sim}{B}^T \sigma \, dv + \int_L \underset{\sim}{B}_\theta^T T_x \, dx$$

$$= \int_0^L \int_{-\frac{b}{2}}^{\frac{b}{2}} \int_{-\frac{a}{2}}^{\frac{a}{2}} [\underset{\sim}{B}_{u_o} - y\, \underset{\sim}{B}_v - z\, \underset{\sim}{B}_w]^T \sigma \, dz \, dy \, dx + \int_0^L \underset{\sim}{B}_\theta^T T_x \, dx \qquad (7.17)$$

and

$$\underset{\sim}{B}_{u_o} = \left[-\frac{1}{L} \quad \frac{1}{L} \right] \tag{7.18}$$

By assuming the stress σ in a filament to be constant at a section x, Eq. 7.17 can be integrated to obtain:

$$\underset{\sim}{S}_I = \int_0^L \begin{bmatrix} \underset{\sim}{B}_{u_o}^T \sigma_u \\ \underset{\sim}{B}_v^T \sigma_v \\ \underset{\sim}{B}_w^T \sigma_w \end{bmatrix} dx + \int_0^L \underset{\sim}{B}_\theta^T T_x \, dx \tag{7.19}$$

where

$$\sigma_u = \sum_{j=1}^{N_z} \sum_{i=1}^{N_y} (z_j - z_{j+1})(y_i - y_{i+1}) \sigma_{c_{ij}} + \sum_{l=1}^{N_s} A_{s_l} \sigma_{s_l}$$

$$\sigma_v = -\tfrac{1}{2} \sum_{j=1}^{N_z} \sum_{i=1}^{N_y} (z_j - z_{j+1})(y_i^2 - y_{i+1}^2) \sigma_{c_{ij}} - \tfrac{1}{2} \sum_{l=1}^{N_s} \bar{y}_l A_{s_l} \sigma_{s_l}$$

$$\sigma_w = -\tfrac{1}{2} \sum_{j=1}^{N_z} \sum_{i=1}^{N_y} (z_j^2 - z_{j+1}^2)(y_i - y_{i+1}) \sigma_{c_{ij}} - \tfrac{1}{2} \sum_{l=1}^{N_s} \bar{z}_l A_{s_l} \sigma_{s_l}$$

In the longitudinal x direction, $\underset{\sim}{S}_I$ is integrated numerically using a two-point Gaussian quadrature.

$$\underset{\sim}{S}_I = w_1 \begin{bmatrix} \underset{\sim}{B}_{u_o}^T \sigma_u \\ \underset{\sim}{B}_v^T \sigma_v \\ \underset{\sim}{B}_w^T \sigma_w \end{bmatrix}_{x_1 = \frac{L}{2} - \frac{\sqrt{3}L}{6}} + w_2 \begin{bmatrix} \underset{\sim}{B}_{u_o}^T \sigma_u \\ \underset{\sim}{B}_v^T \sigma_v \\ \underset{\sim}{B}_w^T \sigma_w \end{bmatrix}_{x_2 = \frac{L}{2} + \frac{\sqrt{3}L}{6}} + \begin{bmatrix} 0 \\ 0 \\ 0 \\ \underset{\sim}{S}_\theta^T \end{bmatrix} \tag{7.20}$$

where $w_1 = w_2 = \frac{L}{2}$

$$\underset{\sim}{S}_I^T = [\, \underset{\sim}{S}_{u_o} \;\; \underset{\sim}{S}_v \;\; \underset{\sim}{S}_w \;\; \underset{\sim}{S}_\theta \,]^T$$

$$\underset{\sim}{S}_{u_o} = [\, S_{u_1} \;\; S_{u_2} \,]$$

$$\underset{\sim}{S}_v = [\, S_{v_1} \;\; S_{v_2} \;\; S_{\theta_{z_1}} \;\; S_{\theta_{z_2}} \,]$$

$$\underset{\sim}{S}_w = [\, S_{w_1} \;\; S_{w_2} \;\; S_{\theta_{y_1}} \;\; S_{\theta_{y_2}} \,]$$

$$\underset{\sim}{S}_\theta = [\, S_{\theta_{x_1}} \;\; S_{\theta_{x_2}} \,] = [\, T_x - T_x \,]$$

Note that in Eq. 7.17 the strain displacement transformation $\underset{\sim}{B}_{u_o}$ (Eq. 7.18) is used instead of $\underset{\sim}{B}_u$ (Eq. 7.1a) in order to enforce the zero force constraint for the internal degree of freedom u_n.

7.3.6 Element Load due to Initial Strain

The initial axial strains ε_c^o in the concrete filaments due to the effects of creep and shrinkage give rise to the clamping forces $\underset{\sim}{S}_o$, where $\underset{\sim}{S}_o$ is calculated as:

$$\underset{\sim}{S}_o = \int_0^L \int_{-\frac{b}{2}}^{\frac{b}{2}} \int_{-\frac{a}{2}}^{\frac{a}{2}} [\underset{\sim}{B}_{u_o} \; -y\underset{\sim}{B}_v \; -z\underset{\sim}{B}_w]^T \, E \, \varepsilon_c^o \, dz \, dy \, dx \qquad (7.21)$$

in which E and ε_c^o are functions of x, y, and z.

Following the same procedure used for the computation of $\underset{\sim}{S}_I$ and assuming ε_c^o and E to be constant in a filament at a section x, the results are:

$$\underset{\sim}{S}_o = w_1 \left[\begin{matrix} \underset{\sim}{B}_{u_o}^T \varepsilon_u \\ \underset{\sim}{B}_v^T \varepsilon_v \\ \underset{\sim}{B}_w^T \varepsilon_w \end{matrix} \right]_{x_1 = \frac{L}{2} - \frac{\sqrt{3}L}{6}} + w_2 \left[\begin{matrix} \underset{\sim}{B}_{u_o} \varepsilon_u \\ \underset{\sim}{B}_v \varepsilon_v \\ \underset{\sim}{B}_w \varepsilon_w \end{matrix} \right]_{x_2 = \frac{L}{2} + \frac{\sqrt{3}L}{6}} \tag{7.22}$$

where

$$\varepsilon_u = \sum_{j=1}^{N_z} \sum_{i=1}^{N_y} (z_j - z_{j+1})(y_i - y_{i+1})\, E_{c_{ij}}\, \varepsilon^o_{c_{ij}}$$

$$\varepsilon_v = -\tfrac{1}{2} \sum_{j=1}^{N_z} \sum_{i=1}^{N_y} (z_j - z_{j+1})(y_i^2 - y_{i+1}^2)\, E_{c_{ij}}\, \varepsilon^o_{c_{ij}}$$

$$\varepsilon_w = -\tfrac{1}{2} \sum_{j=1}^{N_z} \sum_{i=1}^{N_y} (z_j^2 - z_{j+1}^2)(y_i - y_{i+1})\, E_{c_{ij}}\, \varepsilon^o_{c_{ij}}$$

$$\underset{\sim}{S}_o = \left[S^o_{u_1} \;\; S^o_{u_2} \;\; S^o_{v_1} \;\; S^o_{v_2} \;\; S^o_{\theta_{z_1}} \;\; S^o_{\theta_{z_2}} \;\; S^o_{w_1} \;\; S^o_{w_2} \;\; S^o_{\theta_{y_1}} \;\; S^o_{\theta_{y_2}} \right]$$

7.3.7 Transformation and the Assembly of the Beam Element

Before the beam's stiffnesses and the load vectors can be assembled, they must be transformed to a set of global degrees of freedom.

The beam element (Fig. 7.6) has the local degrees of freedom $\underset{\sim}{v}_a$ and the global degrees of freedom $\underset{\sim}{r}$. The two systems are related by an orthogonal matrix $\underset{\sim}{A}$, such that:

$$\underset{\sim}{v}_a = \underset{\sim}{A}\, \underset{\sim}{r} \tag{7.23}$$

where

$$\underset{\sim}{r}^T = \left[U_i \; V_i \; W_i \; \theta_{X_i} \; \theta_{Y_i} \; \theta_{Z_i} \; U_j \; V_j \; W_j \; \theta_{X_j} \; \theta_{Y_j} \; \theta_{Z_j} \right]$$

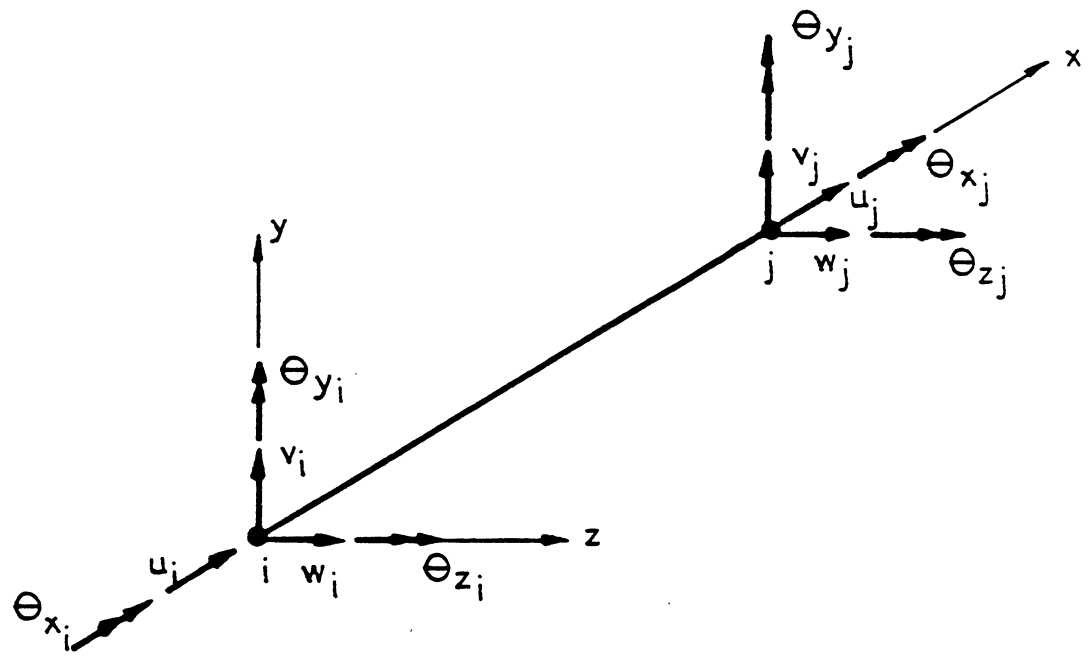

(a) LOCAL D.O.F.

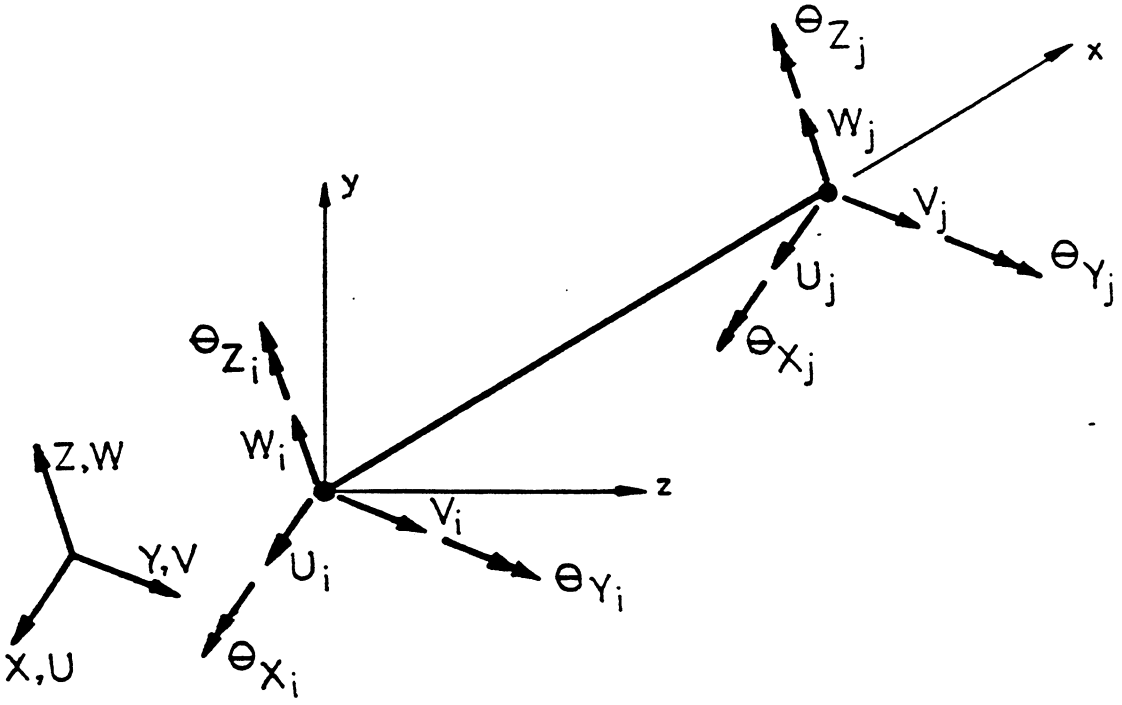

(b) GLOBAL D.O.F.

FIG. 7.6 LOCAL AND GLOBAL DOF FOR THE BEAM ELEMENT

$$\underset{\sim}{A} = \begin{bmatrix}
a_{11} & a_{12} & a_{13} & 0 & 0 & 0 & 0 & 0 & 0 & 0 & 0 & 0 \\
0 & 0 & 0 & 0 & 0 & 0 & a_{11} & a_{12} & a_{13} & 0 & 0 & 0 \\
a_{21} & a_{22} & a_{23} & 0 & 0 & 0 & 0 & 0 & 0 & 0 & 0 & 0 \\
0 & 0 & 0 & 0 & 0 & 0 & a_{21} & a_{22} & a_{23} & 0 & 0 & 0 \\
0 & 0 & 0 & a_{31} & a_{32} & a_{33} & 0 & 0 & 0 & 0 & 0 & 0 \\
0 & 0 & 0 & 0 & 0 & 0 & 0 & 0 & 0 & a_{31} & a_{32} & a_{33} \\
a_{31} & a_{32} & a_{33} & 0 & 0 & 0 & 0 & 0 & 0 & 0 & 0 & 0 \\
0 & 0 & 0 & 0 & 0 & 0 & a_{31} & a_{32} & a_{33} & 0 & 0 & 0 \\
0 & 0 & 0 & a_{21} & a_{22} & a_{23} & 0 & 0 & 0 & 0 & 0 & 0 \\
0 & 0 & 0 & 0 & 0 & 0 & 0 & 0 & 0 & a_{21} & a_{22} & a_{23} \\
0 & 0 & 0 & a_{11} & a_{12} & a_{13} & 0 & 0 & 0 & 0 & 0 & 0 \\
0 & 0 & 0 & 0 & 0 & 0 & 0 & 0 & 0 & a_{11} & a_{12} & a_{13}
\end{bmatrix}$$

$$[\, a_{11} \;\; a_{12} \;\; a_{13} \,] = [\, \hat{x}_1 \;\; \hat{x}_2 \;\; \hat{x}_3 \,]$$

$$[\, a_{21} \;\; a_{22} \;\; a_{23} \,] = [\, \hat{y}_1 \;\; \hat{y}_2 \;\; \hat{y}_3 \,]$$

$$[\, a_{31} \;\; a_{32} \;\; a_{33} \,] = [\, \hat{z}_1 \;\; \hat{z}_2 \;\; \hat{z}_3 \,]$$

The transformation on the stiffnesses $\underset{\sim}{k}_e$ and $\underset{\sim}{k}_g$ are:

$$\underset{\sim}{K}_E = \underset{\sim}{A}^T \underset{\sim}{k}_e \underset{\sim}{A} \tag{7.24}$$

$$\underset{\sim}{K}_G = \underset{\sim}{A}^T \underset{\sim}{k}_g \underset{\sim}{A} \tag{7.25}$$

and the transformation on the load vectors, $\underset{\sim}{S}_I$ and $\underset{\sim}{S}_o$, are:

$$\underset{\sim}{R}^I = \underset{\sim}{A}^T \underset{\sim}{S}_I \tag{7.26}$$

$$\underset{\sim}{R}^o = \underset{\sim}{A}^T \underset{\sim}{S}_o$$

7.4 Eccentric Edge Beam

In this study, beam elements are connected to shell elements at discrete points by means of rigid links to form a shell-beam system (Fig. 7.7). The beam element's degrees of freedom are chosen to be the master, and the degrees of freedom of the nodes where the beams are connected to the shell are slave.

For small rotations, the master-slave relationship for the degrees of freedom at node i is:

$$\begin{bmatrix} u_s \\ v_s \\ w_s \\ \alpha_1 \\ \alpha_2 \\ \alpha_3 \end{bmatrix}_i = \begin{bmatrix} 1 & 0 & 0 & 0 & e_Z & -e_Y \\ 0 & 1 & 0 & -e_Z & 0 & e_X \\ 0 & 0 & 1 & e_Y & -e_X & 0 \\ 0 & 0 & 0 & V_{1X} & V_{1Y} & V_{1Z} \\ 0 & 0 & 0 & V_{2X} & V_{2Y} & V_{2Z} \\ 0 & 0 & 0 & V_{3X} & V_{3Y} & V_{2Z} \end{bmatrix}_i \begin{bmatrix} u_b \\ v_b \\ w_b \\ \theta_X \\ \theta_Y \\ \theta_Z \end{bmatrix}_I \tag{7.28a}$$

$$\underset{\sim}{U}_{s_i} = \underset{\sim}{T}_i \, \underset{\sim}{U}_{b_I} \tag{7.28b}$$

where

$$\begin{bmatrix} e_X \\ e_Y \\ e_Z \end{bmatrix}_i = \begin{bmatrix} X_s \\ Y_s \\ Z_s \end{bmatrix}_i - \begin{bmatrix} X_b \\ Y_b \\ Z_b \end{bmatrix}_I$$

and, V_{iX}, V_{iY}, and V_{iZ} are the components of the surface vector $\underset{\sim}{V}_i$, i=1,2,3, of the shell described in Section 6.2.1.

The shell stiffness $\underset{\sim}{K}_E^{ij}$ relating the forces corresponding to the degrees of freedom at node i and the displacement degrees of freedom

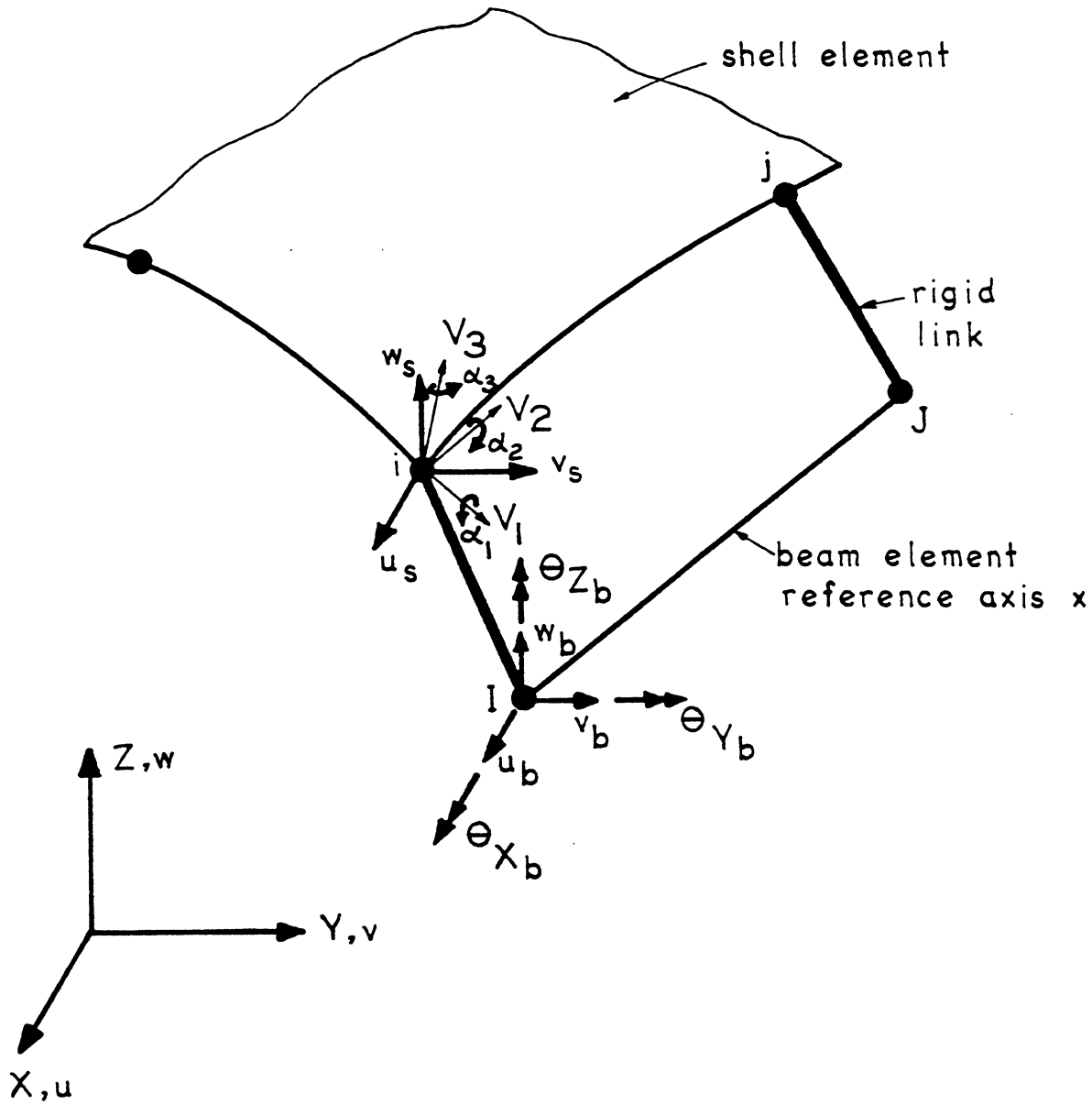

FIG. 7.7 GEOMETRY AND DEGREES OF FREEDOM OF A SHELL-BEAM SYSTEM

at node j is:

$$\begin{bmatrix} R_x \\ R_y \\ R_z \\ M_1 \\ M_2 \end{bmatrix}_i = \underset{\sim}{K}_E^{ij} \begin{bmatrix} u_s \\ v_s \\ w_s \\ \alpha_1 \\ \alpha_2 \end{bmatrix}_j$$

where $\underset{\sim}{K}_E^{ij}$ is a 5×5 matrix described in Section 6.2.4.

The stiffness $(\underset{\sim}{K}_E^{ij})$ at the master's degrees of freedom is:

$$(\underset{\sim}{K}_E^{ij})_I = \underset{\sim}{T}_i^T \left[\begin{array}{c|c} \underset{\sim}{K}_E^{ij} & 0 \\ \hline 0 & 0 \end{array}\right] \underset{\sim}{T}_j \tag{7.29}$$

where the stiffness associated with the rotation α_3 about the shell normal $\underset{\sim}{V}_3$ is assumed to be zero.

In Eq. 7.29, $(\underset{\sim}{K}_E^{ij})_I$ is a 6×6 matrix and $\underset{\sim}{T}_i$ is the transformation matrix described by Eq. 7.28a. When node i on the shell is not connected by a rigid link to a beam, $\underset{\sim}{T}_i$ is an identity matrix $\underset{\sim}{I}$.

The nodal loads $\underset{\sim}{R}_i$ at node i are similarly transformed:

$$(\underset{\sim}{R}_i)_I = \underset{\sim}{T}_i^T \underset{\sim}{R}_i \tag{7.30}$$

Alternately, the beam stiffness can be transformed to the shell's degrees of freedom and subsequently added to the shell stiffness. However, it is found that the imposition of the boundary conditions becomes more difficult when the actual points of support do not lie on the shell, Fig. 7.8. In this case, appropriate transformations

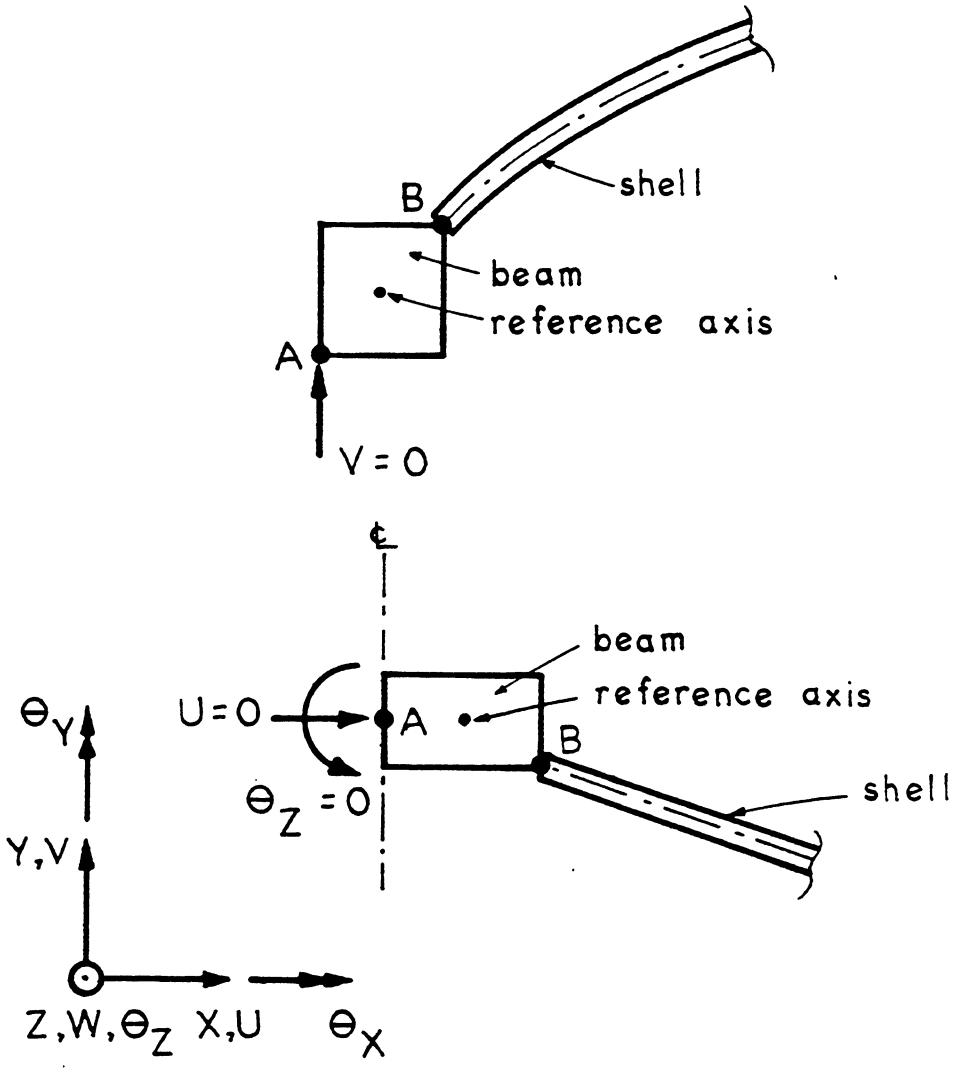

FIG. 7.8 EXAMPLES OF BOUNDARY CONDITIONS WHICH CANNOT BE COMPLETELY DESCRIBED BY THE SHELL'S DEGREES OF FREEDOM

are required to transform the shell's stiffness at the degrees of freedom (Point B in Fig. 7.8) to the degrees of freedom at the supporting point (Point A in Fig. 7.8).

In the present adopted model, the reference axis can always be chosen such that the points of support lie on it, and consequently, the boundary conditions can be imposed directly.

7.5 Material Model for the Beam Element

The material models for the concrete and steel described in Chapter 3, specialized to a one-dimensional stress state, are used.

However, a material law for the torsion still remains to be defined. In the present study, an effective torsional stiffness approach is used.

For the present beam element, bending action and the torsional action are assumed to be completely uncoupled. Consequently, the interactions between the stresses from the two different sources are ignored.

7.5.1 Torque-Twist Relationship

In the present study, a trilinear model is used to represent the torsional response of a reinforced concrete beam. Figure 7.9 shows a typical torque-twist response for pure torsion of a rectangular reinforced concrete beam. The response is almost linear until first cracking occurs, and then nonlinear onwards.

Three distinct points are required to completely define the shape of the curve.

(1) The torque at first cracking, T_{cr}, and the corresponding α_{cr}.

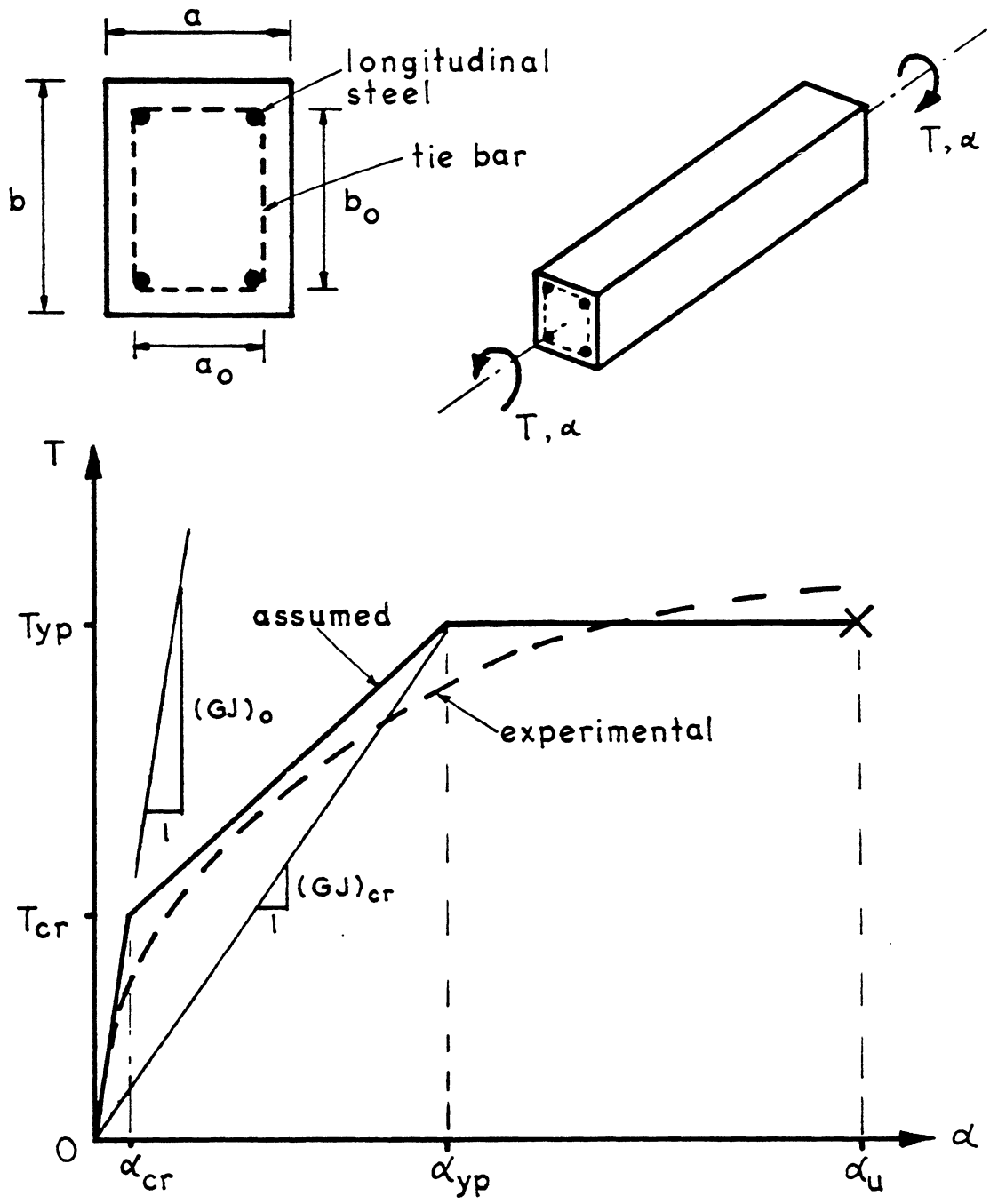

FIG. 7.9 TYPICAL TORQUE-TWIST RELATIONSHIP FOR A RECTANGULAR REINFORCED CONCRETE BEAM UNDER PURE TORSION

(2) The torque at first full yielding of all the reinforcement, T_{yp}, and the corresponding α_{yp}.

(3) The twist at ultimate failure, α_u.

7.5.2 Elastic Response and Cracking in Torsion

Experimental investigations show that the response is almost linear under pure torsion until cracking occurs.

Excluding the contribution from the steel reinforcement, the torsional stiffness $(GJ)_o$ for an uncracked section can be found by using the classical theory for unrestrained warping torsion [120]. In general, $(GJ)_o$ can be represented by:

$$(GJ)_o = \kappa a^3 b \cdot G \tag{7.30}$$

where κ is assumed to be of the form:

$$\kappa = 0.333 - \frac{0.224}{(b/a)} + \frac{0.032}{(b/a)^2} \tag{7.31}$$

$$b \geq a$$

The maximum shearing stress is:

$$\tau_{max} = \frac{T}{\beta a^2 b} \tag{7.32}$$

where β is another assumed function,

$$\beta = 0.333 - \frac{0.223}{(b/a)} + \frac{0.098}{(b/a)^2} \tag{7.33}$$

$$b \geq a$$

The assumed functions κ and β are compared with the exact solutions [120], using an infinite series, and the results are shown in

the following table.

b/a (b > a)	VALUE OF κ		VALUE OF β	
	EXACT [120]	EQ. 7.31	EXACT [120]	EQ. 7.33
1.0	0.141	0.141	0.208	0.208
1.2	0.166	0.169	0.219	0.215
1.5	0.196	0.198	0.231	0.228
2.0	0.229	0.229	0.246	0.246
2.5	0.249	0.249	0.258	0.259
3.0	0.263	0.262	0.267	0.270
4.0	0.281	0.279	0.282	0.230
5.0	0.291	0.289	0.291	0.292
10.0	0.312	0.311	0.312	0.312
∞	0.333	0.333	0.333	0.333

It is observed that close agreement exists between the theoretical values and the values obtained from the assumed empirical functions.

For pure torsional moment on the beam, the maximum tensile stress is numerically equal to the maximum shear stress, τ_{max}, in Eq. 7.32. Consequently, the torsional moment existing in the concrete beam at first cracking is:

$$T_{cr} = \beta\, a^2\, b\, f_t' \tag{7.34}$$

where f_t' is the uniaxial tensile strength of the concrete.

The corresponding twist at the cracking torque is:

$$\alpha_{cr} = \frac{T_{cr}}{(GJ)_o} \tag{7.35}$$

7.5.3 Post-Cracking Stiffness, Yielding and Failure

Lampert [121] has studied the post-cracking behavior of reinforced concrete beams. Based upon the space truss analogy, the post-cracking stiffness $(GJ)_{cr}$ is found to be:

$$(GJ)_{cr} = \frac{4E_s(a_o b_o)^3}{u^2} \cdot W \tag{7.36}$$

where

$$W = \frac{1}{\frac{1}{\rho_h} + \frac{1}{2}\left(\frac{1}{\rho_s} + \frac{1}{\rho_s'}\right) + 4n\lambda \frac{a_o b_o}{ut}} \tag{7.37}$$

$$\rho_s = \frac{2A_s^b}{a_o b_o}$$

$$\rho_s' = \frac{2A_s^t}{a_o b_o}$$

$$\rho_h = \frac{2A_h u}{a_o b_o s}$$

u = perimeter of the core = $2(a_o + b_o)$

A_s^t = total top steel area

A_s^b = total bottom steel area

A_h = hoop steel area

s = spacing of the hoop reinforcement

The parameter λ is included in Eq. 7.37 to take into account warping and the change in the shear modulus of the concrete, and n and t are uncertainty parameters.

Ignoring the concrete contribution in shear, λ then assumes a zero value.

The post-cracking stiffness now simplifies to:

$$(GJ)_{cr} = \frac{4E_s(a_o b_o)^3}{u^2} \frac{1}{\frac{1}{\rho_h} + \frac{1}{2}\left(\frac{1}{\rho_s} + \frac{1}{\rho_s'}\right)} \tag{7.38}$$

The torque required to cause full yielding of the longitudinal and the hoop steel reinforcement can be again found by using the space truss analogy. The yielding torque obtained by Lampert [121], assuming an elasto-plastic material for the reinforcement, is:

$$T_{yp} = 2\, a_o b_o \frac{A_h f_{h_y}}{s \tan\theta} \tag{7.39}$$

where θ is the crack inclination and

$$\tan\theta = \sqrt{\frac{A_s}{2(a_o + b_o)} \cdot \frac{s}{A_h} \cdot \frac{f_{s_y}}{f_{h_y}}} \tag{7.40}$$

A_s = total area of the longitudinal steel

A_h = area of one hoop reinforcing bar

s = spacing of the hoop reinforcement

f_{s_y} = yield strength of the longitudinal steel reinforcement

f_{h_y} = yield strength of the hoop reinforcement

The deformation corresponding to the condition of first full yielding is:

$$\alpha_{yp} = \frac{T_{yp}}{(GJ)_{cr}} \tag{7.41}$$

Failure is assumed when the maximum shearing strain in the concrete extreme fiber reaches an ultimate value, γ_u. This value usually lies in the range of 0.01 and 0.02. A conservative lower bound value for α_u suggested by Collins et al [122] based upon the minimum value of γ_u is:

$$\alpha_u = 0.01 \frac{a_o + b_o}{a_o b_o} \tag{7.42}$$

7.5.4 Overlay Model for Torsion

A trilinear torque-twist response as shown in Fig. 7.10a is modelled by two components, each exhibiting elasto-plastic behavior (Fig. 7.10b), such that the torsional stiffness GJ and the torque T of the beam are:

$$GJ = GJ_1 + GJ_2 \tag{7.43}$$

$$T = T_1 + T_2 \tag{7.44}$$

The stiffnesses GJ_1 and GJ_2 can be found by solving the simultaneous equations:

$$GJ_1 \alpha_{cr} + GJ_2 \alpha_{cr} = T_{cr} \tag{7.45a}$$

$$GJ_1 \alpha_{cr} + GJ_2 \alpha_{yp} = T_{yp} \tag{7.45b}$$

The solutions are:

$$GJ_1 = \frac{T_{cr} - \psi \alpha_{cr}}{\alpha_{cr}} \tag{7.46}$$

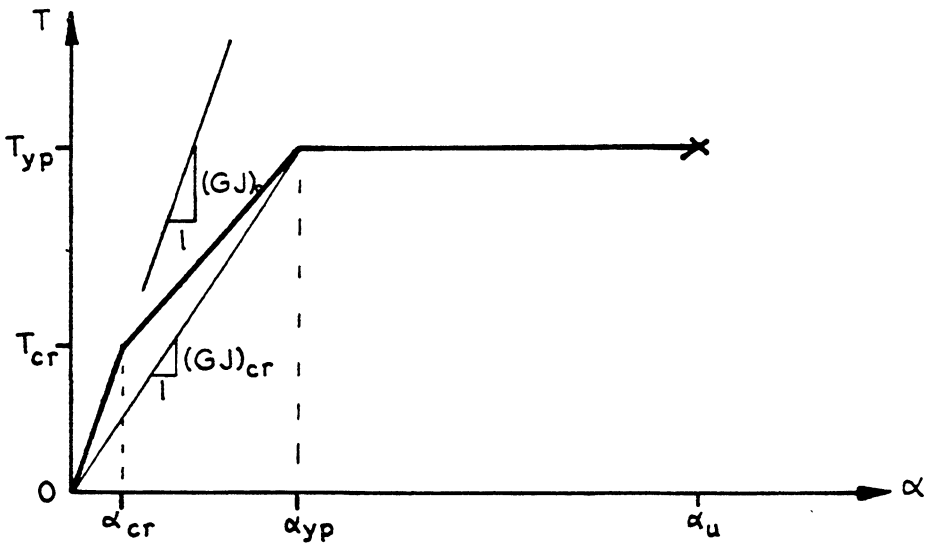

(a) ASSUMED TORQUE TWIST RESPONSE

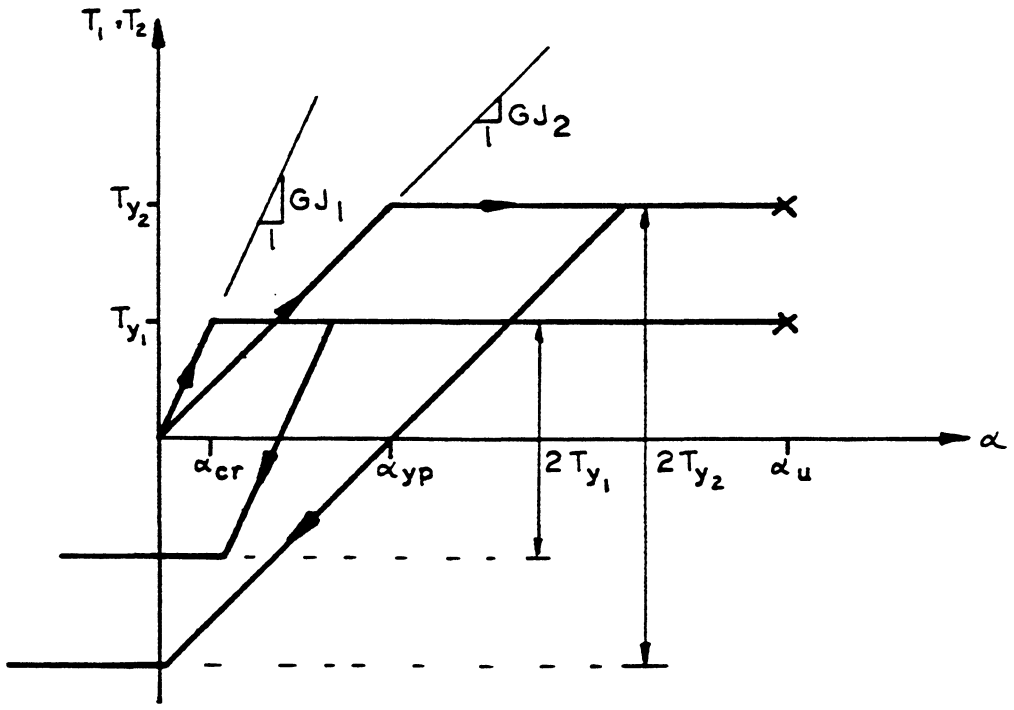

(b) OVERLAY MODEL FOR TORQUE TWIST RELATIONSHIP

FIG. 7.10 OVERLAY MODEL FOR TRILINEAR TORQUE-TWIST RELATIONSHIP

$$GJ_2 = \psi \tag{7.47}$$

$$\psi = \frac{T_{yp} - T_{cr}}{\alpha_{yp} - \alpha_{cr}}$$

The yielding torques for the two components are:

$$T_{y_1} = GJ_1 \alpha_{cr} \tag{7.48}$$

$$T_{y_2} = GJ_2 \alpha_{yp} \tag{7.49}$$

The use of the overlay model allows the modelling of inelastic unloading easily. It is assumed that inelastic unloading of each component is elastic with its initial stiffness (Fig. 7.10b). The resulting inelastic unloading response is shown in Fig. 7.11 for unloading after cracked and unloading after yielded.

7.6 Large Displacement Analysis

In the analysis including nonlinear geometry, the geometry of the beam and the beam's local axes x, y, and z have to be updated. The procedure described herein is restricted to large displacements and small incremental rigid body rotations.

To update the beam element's local axes, a procedure based upon average rotation of the beam element's axes is adopted.

It is assumed that the equilibrium configuration at step i-1 and the incremental nodal displacements at the current step i are known.

Referring to Fig. 7.12, the relative displacements between the two ends of the beam element can be found from the incremental nodal

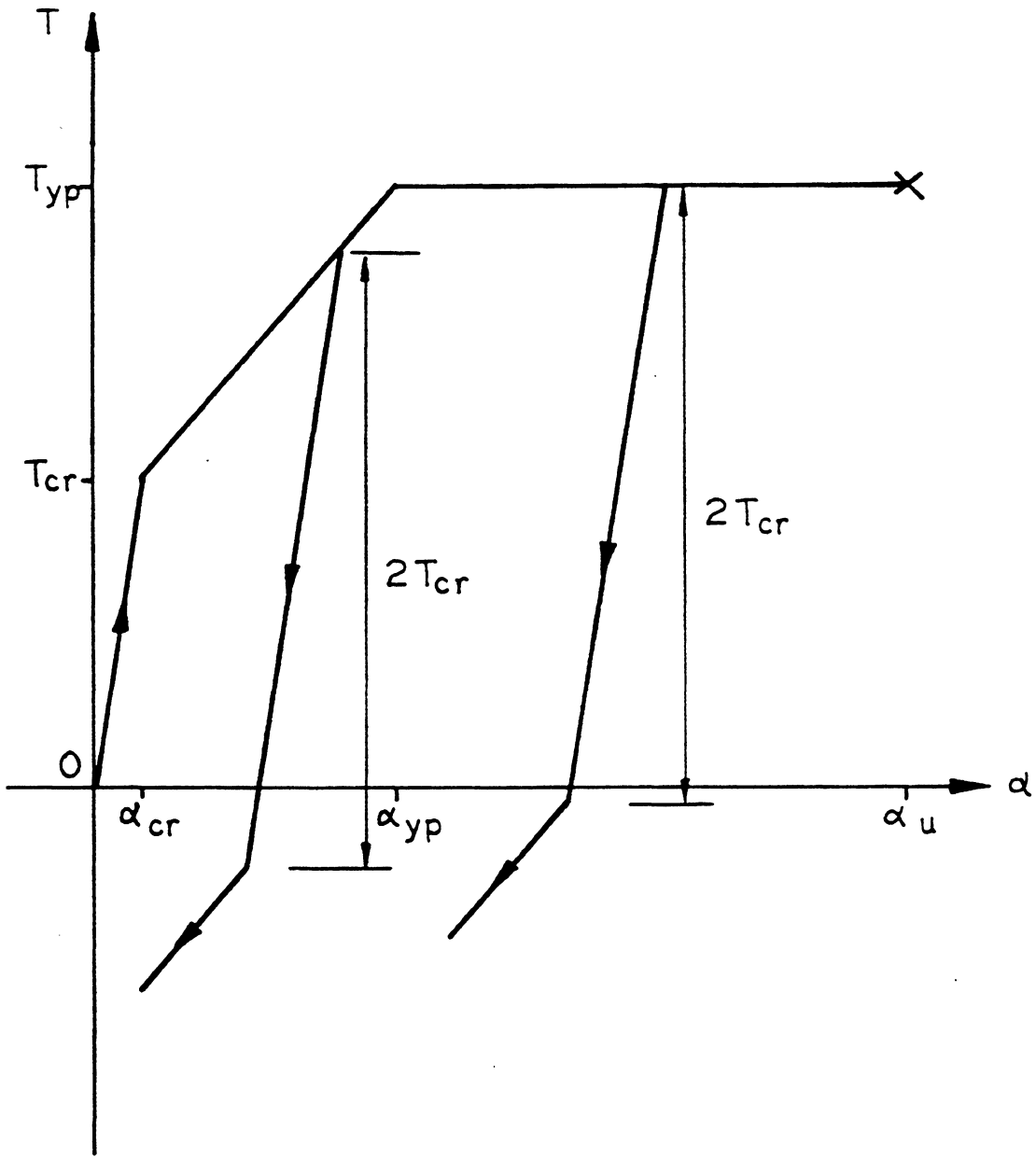

FIG. 7.11 INELASTIC UNLOADING IN TORSION FOR THE OVERLAY MODEL

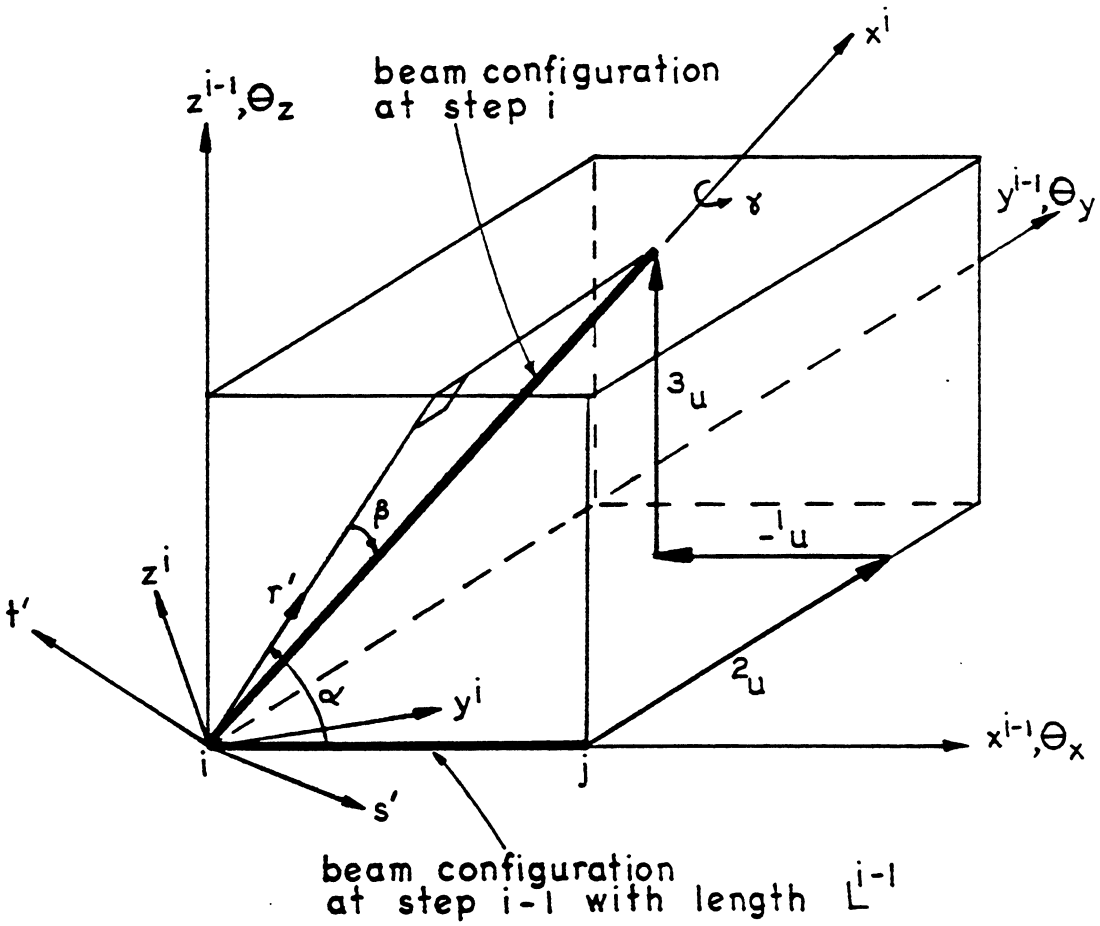

FIG. 7.12 TRANSFORMATION OF THE BEAM LOCAL AXES IN A LARGE DISPLACEMENT ANALYSIS

displacements relative to the x^{i-1}, y^{i-1}, and z^{i-1} axes. They are:

$$ {}^1u = \Delta u_j - \Delta u_i \tag{7.50a} $$

$$ {}^2u = \Delta v_j - \Delta v_i \tag{7.50b} $$

$$ {}^3u = \Delta w_j - \Delta w_i \tag{7.50c} $$

The new coordinate axes x^i, y^i, and z^i at step i, with unit vectors $\underset{\sim}{\hat{x}}^i$, $\underset{\sim}{\hat{y}}^i$, and $\underset{\sim}{\hat{z}}^i$, are obtained as a result of a series of motions. The rotation α about the -ve y^{i-1} axis transform x^{i-1}, y^{i-1}, and z^{i-1} to r', y^{i-1} and t'. The rotation β about the t' axis brings r', y^{i-1} and t' to x^i, s' and t'. Finally, the rotation γ about the x^i axis rotates x^i, s' and t' to the final direction x^i, y^i, and z^i.

The three angles (α, β and γ) that describe the motions can be found by simple geometry with reference to Fig. 7.12.

$$ \cos\alpha = \frac{L^{i-1} + {}^1u}{[(L^{i-1} + {}^1u)^2 + {}^3u^2]^{\frac{1}{2}}} \tag{7.51a} $$

$$ \sin\alpha = \frac{{}^3u}{[(L^{i-1} + {}^1u)^2 + {}^3u^2]^{\frac{1}{2}}} \tag{7.51b} $$

$$ \cos\beta = \frac{[(L^{i-1} + {}^1u)^2 + {}^3u^2]^{\frac{1}{2}}}{[(L^{i-1} + {}^1u)^2 + {}^2u^2 + {}^3u^2]^{\frac{1}{2}}} \tag{7.51c} $$

$$ \sin\beta = \frac{{}^2u}{[(L^{i-1} + {}^1u)^2 + {}^2u^2 + {}^3u^2]^{\frac{1}{2}}} \tag{7.51d} $$

$$ \gamma = \tfrac{1}{2}(\theta_{x_j} + \theta_{x_i}) \tag{7.51e} $$

The transformation between the unit vectors $\hat{x}^i$, $\hat{y}^i$, $\hat{z}^i$ at step i and the unit vectors $\hat{x}^{i-1}$, $\hat{y}^{i-1}$, $\hat{z}^{i-1}$ at step i-1 is therefore:

$$\begin{bmatrix} \hat{\underset{\sim}{x}}^T \\ \hat{\underset{\sim}{y}}^T \\ \hat{\underset{\sim}{z}}^T \end{bmatrix}_i = \underbrace{\begin{bmatrix} 1 & 0 & 0 \\ 0 & \cos\gamma & \sin\gamma \\ 0 & -\sin\gamma & \cos\gamma \end{bmatrix}_i}_{\gamma \text{ motion}} \cdot \underbrace{\begin{bmatrix} \cos\beta & \sin\beta & 0 \\ -\sin\beta & \cos\beta & 0 \\ 0 & 0 & 1 \end{bmatrix}_i}_{\beta \text{ motion}}$$

$$\cdot \underbrace{\begin{bmatrix} \cos\alpha & 0 & \sin\alpha \\ 0 & 1 & 0 \\ -\sin\alpha & 0 & \cos\alpha \end{bmatrix}_i}_{\alpha \text{ motion}} \begin{bmatrix} \hat{\underset{\sim}{x}}^T \\ \hat{\underset{\sim}{y}}^T \\ \hat{\underset{\sim}{z}}^T \end{bmatrix}_{i-1} \tag{7.52}$$

Carrying out the matrix multiplication in Eq. 7.52, the required transformation matrix T is:

$$\underset{\sim}{T} = \begin{bmatrix} \cos\alpha\cos\beta & \sin\beta & \cos\beta\sin\alpha \\ (-\cos\gamma\sin\beta\cos\alpha - \sin\gamma\sin\alpha) & \cos\gamma\cos\beta & (-\cos\gamma\sin\beta\sin\alpha + \sin\gamma\cos\alpha) \\ (\sin\gamma\sin\beta\cos\alpha - \cos\gamma\sin\alpha) & -\sin\gamma\cos\beta & (\sin\gamma\sin\beta\sin\alpha + \cos\gamma\cos\alpha) \end{bmatrix}_i \tag{7.53}$$

The nodal point coordinates of the beam are updated once nodal displacement increments at node j are known in the global coordinate axes,

$$\begin{bmatrix} X^i \\ Y^i \\ Z^i \end{bmatrix}_j = \begin{bmatrix} X^{i-1} \\ Y^{i-1} \\ Z^{i-1} \end{bmatrix}_j + \begin{bmatrix} \Delta u \\ \Delta v \\ \Delta w \end{bmatrix}_j \tag{7.54}$$

and the new member length L^i can be found based on this new geometry.

The increment in the axial strain due to axial elongation is:

$$\Delta\varepsilon = \frac{L^i - L^{i-1}}{L^o} \tag{7.55}$$

where L^o is the original unstretched member length.

Note that for an axial member, the use of the strain expression of Eq. 2.42 is analogous to computing the strain increment as:

$$\Delta\varepsilon' = \frac{L^i - L^{i-1}}{L^{i-1}} \tag{7.56}$$

For small strains, no distinction needs to be made between L^o and L^{i-1}. Consequently, the strain $\Delta\varepsilon'$ and $\Delta\varepsilon$ are approximately equal.

The axial displacements increment in the beam element coordinate axes are then adjusted:

$$u_1 = 0$$

$$u_2 = \Delta\varepsilon\, L^{i-1}$$

and the strain increment at any location within the beam element can be found by making use of the strain-displacement relationship of Eq. 7.4.

The total strain at the i^{th} step is obtained by a summation of all the previous strain increments. For small strains and small incremental rigid body rotations, this closely approximates the exact total strain.

8. SOLUTION STRATEGY FOR NONLINEAR ANALYSIS

8.1 General

The solution of the equation of the form:

$$\underset{\sim}{K}\,\underset{\sim}{r} = \underset{\sim}{R}$$

which is nonlinear, in general, has to resort to either a step-by-step procedure, an iterative procedure, or a combination of the two.

The solution is relatively trivial if the load is single valued in displacement. This is generally not the case for a structural system that exhibits strain softening or a snap-through phenomenon, where the load is multi-valued in displacement. Special treatment has to be given for these cases, as will be discussed later.

8.1.1 Step-by-Step Method

In this method, the load $\underset{\sim}{R}$ is divided into a number of small increments, $\Delta\underset{\sim}{R}$, and the response, $\underset{\sim}{r}$, is obtained by the summation of each of the $\Delta\underset{\sim}{r}$. Mathematically, this can be recast as:

$$\underset{\sim i}{K}\,\Delta\underset{\sim i}{r} = \Delta\underset{\sim i}{R}$$

$$\underset{\sim i}{r} = \underset{\sim i-1}{r} + \Delta\underset{\sim i}{r}$$

where i represents the i^{th} load step.

The solution tends to drift away from the true path unless $\Delta\underset{\sim i}{R}$ is chosen to be very small.

A more accurate solution can be obtained when the residuals $\Delta\underset{\sim i-1}{R^u}$ from the previous step are added to the current load increment $\Delta\underset{\sim i}{R}$ for the solution of $\Delta\underset{\sim i}{r}$. The computational procedure is:

$$\underset{\sim}{K}_i \, \Delta \underset{\sim}{r}_i = \Delta \underset{\sim}{R}_i + \Delta \underset{\sim}{R}^u_{i-1}$$

$$\underset{\sim}{r}_i = \underset{\sim}{r}_{i-1} + \Delta \underset{\sim}{r}_i$$

Geometrically, the two methods are shown in Fig. 8.1a and Fig. 8.1b.

8.1.2 Iterative Method

Several variants of the method are available. Among them, the two most commonly used methods in solving nonlinear structural problems are the Newton-Raphson's and the Secant methods.

8.1.2.1 Newton-Raphson's Iterative Method

The total value of $\underset{\sim}{R}$ is applied and the values of $\underset{\sim}{K}$ and $\underset{\sim}{r}$ are continuously updated until convergence is achieved (Fig. 8.1c).

Computationally, the following steps are involved.

$$\underset{\sim}{K}_i \, \Delta \underset{\sim}{r}_i = \underset{\sim}{R} - \underset{\sim}{R}_i$$

$$\underset{\sim}{r}_i = \underset{\sim}{r}_{i-1} + \Delta \underset{\sim}{r}_i$$

$$\underset{\sim}{R}_{i+1} = \underset{\sim}{K}_{i+1} \, \underset{\sim}{r}_i$$

Convergence is said to have been achieved if $||\underset{\sim}{r}_i - \underset{\sim}{r}_{i-1}|| \leq C$, where C is some convergence norm.

The Quasi-Newton's method (Fig. 8.1d) assumes a constant $\underset{\sim}{K}_i$, which is equal to the initial stiffness, $\underset{\sim}{K}_o$. Convergence is slower in this case.

8.1.2.2 Secant Method

In this method, the secant value, $\underset{\sim}{K}_{s_i}$, is continuously updated until $\underset{\sim}{r}_i$ and $\underset{\sim}{r}_{i-1}$ are close to within a reasonable limit (Fig. 8.1e).

Computationally, this is as follows:

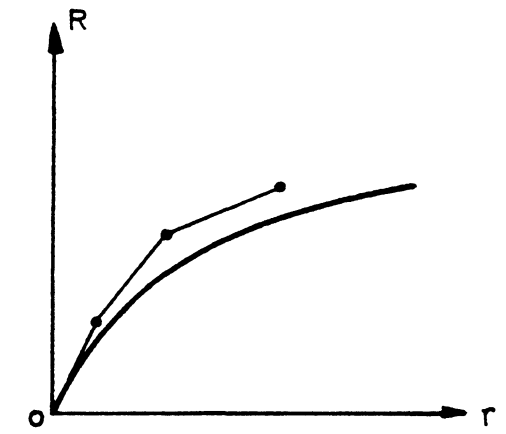

(a) PURE INCREMENTAL

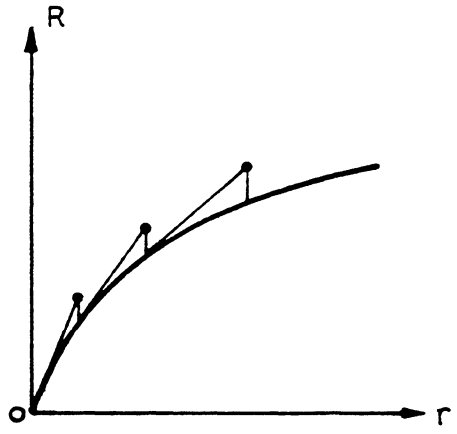

(b) INCREMENTAL WITH RESIDUAL CORRECTIONS

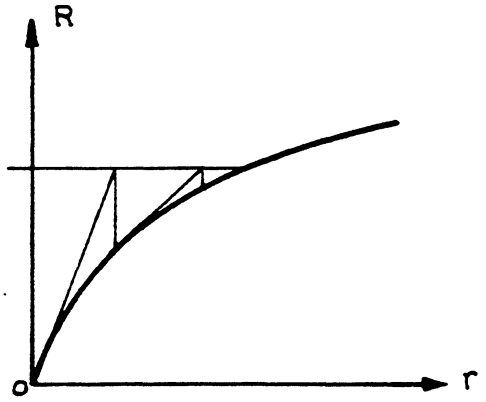

(c) NEWTON-RAPHSON'S METHOD

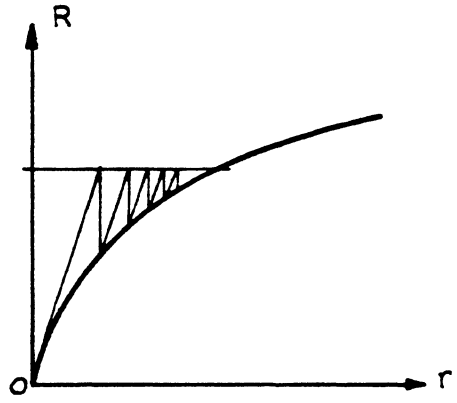

(d) QUASI-NEWTON'S METHOD

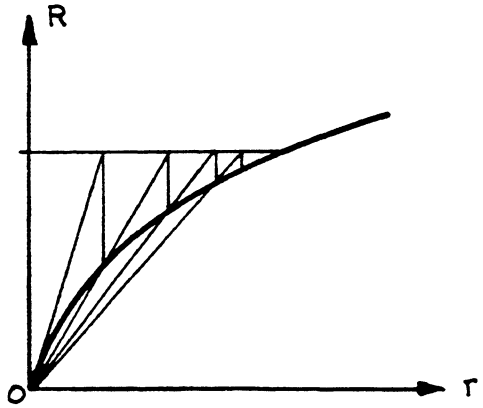

(e) SECANT METHOD

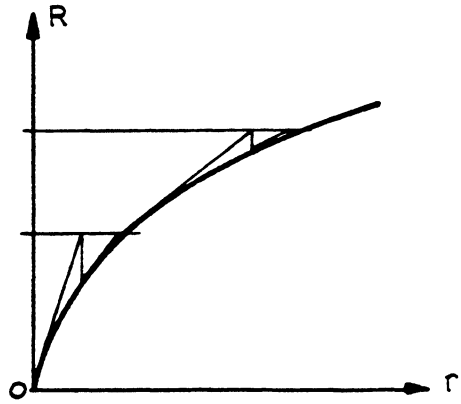

(f) COMBINED INCREMENTAL AND ITERATIVE

FIG. 8.1 SCHEMATICS OF THE SOLUTION PROCEDURE IN A NONLINEAR PROBLEM

$$\underset{\sim}{K}_{s_i}\ \underset{\sim}{r}_i = \underset{\sim}{R}$$

$$\underset{\sim}{K}_{s_{i+1}} = \frac{\underset{\sim}{R} - \underset{\sim}{R}^u_i}{\underset{\sim}{r}_i}$$

$$\underset{\sim}{R}^u_i = \text{Residual at step i.}$$

Convergence is very fast for both the Newton-Raphson's method and the Secant method. In fact, it can be shown that the Newton-Raphson's method converges quadratically while the convergence of the Secant method is of the order of 1.62 [123].

8.1.2.3 Step-Iterative Method

While it is very costly to perform a full Newton-Raphson's method or the Secant method due to constant updating of the stiffness, a considerable savings can be achieved if the matrix $\underset{\sim}{K}$ is only updated and triangularized at the beginning of the step i (Fig. 8.1f). In this way, only back-substitution is involved in obtaining the $\Delta\underset{\sim}{r}_i$ in the subsequent iterations.

8.2 Automatic Load Generation

Along the solution path, the stiffness of a structure changes due to the nonlinearities it involves. This will cause a different truncation error in the solution when a constant size of load step is used. A larger truncation error may either cause drift off from the the true solution or convergence may never be achieved. Therefore, an automatic load generation capability is essential so that the load step can be adjusted according to the nonlinearities of the structure.

Søreide [35] developed a scheme based upon a constant truncation error in the displacements. This will yield an approximately

equal number of iteration cycles for the solution to converge at all steps.

Bergan [124], by monitoring the ratio of the generalized current stiffness to the generalized initial stiffness, obtains a constant rate of change in the stiffness of the structure.

The simplest approach, however, is to impose a maximum displacement increment of a selected degree of freedom.

8.3 Solution Procedure Involving Strain Softening and Instability

When a structure exhibits strain softening or snap-through, the stiffness at some point in the solution path is non-positive definite (Fig. 8.2). The conventional methods for solving the nonlinear set of equations, as discussed in Section 8.1, are not applicable without modification.

Various schemes have been proposed in the past to circumvent the difficulties which arise in treating the non-positive definiteness of the stiffness matrix and passing over the limit point when the determinant of the stiffness changes sign, points A, B, and B' in Fig. 8.2. Here some of the numerical schemes will be reviewed to form the basis for the selection of a numerical scheme to be used in the present study.

8.3.1 Imposed Displacement via the Change of Independent Variable

Argyris [125] first introduced this method and chose the displacement rather than the load as the independent variable. However, the loss of the symmetry and the banded nature of the resulting stiffness matrix have placed some restrictions on its use.

8.3.2 Augmenting the Stiffness Matrix

This method has been used by Whiteman et al [126] in solving frame type structures and is later generalized by Sharifi [127].

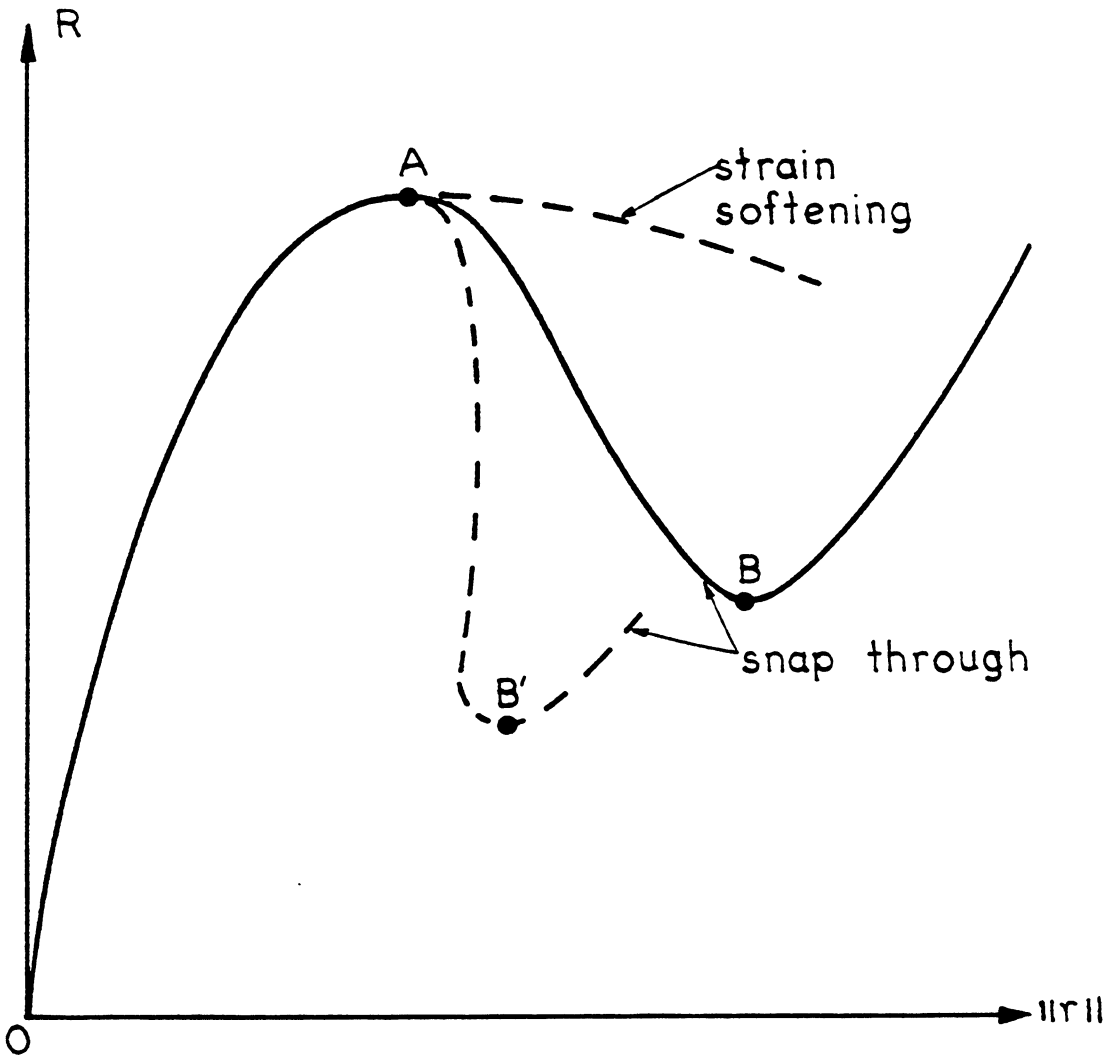

FIG. 8.2 TYPICAL LOAD-DISPLACEMENT RESPONSE FOR STRUCTURE WITH NON-POSITIVE DEFINITE STIFFNESS MATRIX

The method involves augmenting the structure with a set of linear generalized springs at each of the loaded joints so that the stiffness of the complete system, including the generalized springs, is positive definite. The method is illustrated by a simple truss in Fig. 8.3.

However, due to the coupling of all the loaded degrees of freedom produced by the generalized spring system, the augmented stiffness matrix is generally a full matrix. The maximum increase in the solution time in solving the system of equations, as shown by Sharifi [127], may be as much as 25%. The unbanded nature of the stiffness matrix may also cause numerical problems when the augmented spring stiffness is chosen to be too large in value. On the other hand, if the spring stiffness is chosen to be too small, it may have no effect on the resulting stiffness.

8.3.3 Orthogonalizing Techniques

Bergan [128] developed an iterative scheme in which the iteration is carried out with variable load level. The idea is to adjust the external load so that the residual is always perpendicular to the external load. This should theoretically give the smallest residual in the least squares sense and hence converge quickly to the true solution. However, Powell et al [129] have found that the scheme does not produce consistent improvements in reliability and speed of convergence.

8.3.4 Double Step Method

The solution at any instant is obtained in two steps by solving for the displacements $\underset{\sim}{r}^u$ and $\underset{\sim}{r}^e$ of two independent load conditions $\underset{\sim}{R}^u$ and $\underset{\sim}{R}^e$. The final solution is then obtained so that a certain constraint, $\underset{\sim}{C} = \underset{\sim}{0}$ betweeen the displacements $\underset{\sim}{r}^u$ and $\underset{\sim}{r}^e$, is satisfied.

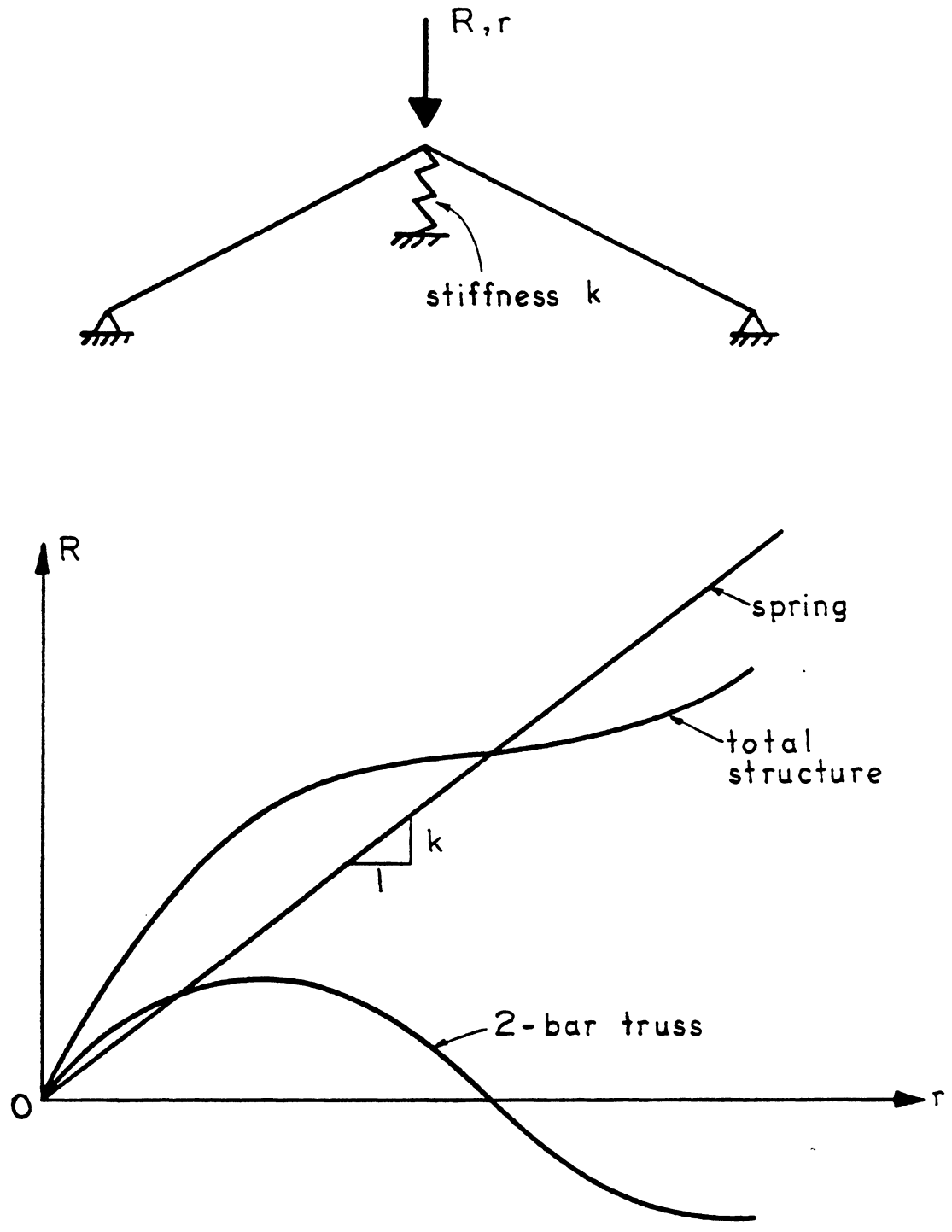

FIG. 8.3 LOAD-DISPLACEMENT RESPONSE OF AN AUGMENTED 2-BAR TRUSS STRUCTURE

In mathematical terms:

$$\underset{n\times n}{[\ K\ ]}\ \underset{n\times 1}{[\ r^u}\ |\ \underset{n\times 1}{r^e\ ]} = \underset{n\times 1}{[\ R^u}\ |\ \underset{n\times 1}{R^e\ ]} \tag{8.1a}$$

$$\underset{\sim}{C}(\underset{\sim}{r}^u, \phi^i \underset{\sim}{r}^e) = \underset{\sim}{0} \tag{8.1b}$$

Equation 8.1a is used to solve for n $\underset{\sim}{r}^u$ and n $\underset{\sim}{r}^e$ and Eq. 8.1b is used to solve for the load factor ϕ^i so that the constraint equation $\underset{\sim}{C} = \underset{\sim}{0}$ is satisfied. The matrix $\underset{\sim}{K}$ can be non-positive definite, provided that it is not singular. In general, $\underset{\sim}{r}^u$ is the displacement vector due to the unbalanced load $\underset{\sim}{R}^u$ and $\underset{\sim}{r}^e$ is the displacement vector due to some reference external load $\underset{\sim}{R}^e$.

Frey [130] computes the increment of displacement $\Delta\underset{\sim}{r}_i$ in the i^{th} step as follows:

$$\Delta\underset{\sim}{r}_i = \Delta\underset{\sim}{r}^u \text{ for } \det \underset{\sim}{K}_{i-1} \cdot \det \underset{\sim}{K}_i > 0 \tag{8.2a}$$

$$\Delta\underset{\sim}{r}_i = -\Delta\underset{\sim}{r}^e + \Delta\underset{\sim}{r}^u \text{ for } \det \underset{\sim}{K}_{i-1} \cdot \det \underset{\sim}{K}_i < 0 \tag{8.2b}$$

Equation 8.2a means that conventional Newton-Raphson's iteration is used when no sign change is detected in the determinant of the stiffness matrix in two consecutive steps. Equation 8.2b means that the direction of the external load increment is reversed when performing iteration when a sign change is detected in the determinant of the stiffness matrix in two consecutive steps.

Bergan [124] has also used a similar technique but iteration is not performed to avoid numerical problems in the vicinity of limit load where the stiffness is nearly singular.

Powell et al [129] use the constraint condition:

$$r_n^u + \phi^i r_n^e = \delta \tag{8.3}$$

for imposed deformation, where δ is the prescribed displacement at the n^{th} degree of freedom. This method is identical with Batoz et al [131].

$$\underset{\sim}{R}^{e^T} [\underset{\sim}{r}^u + \phi^i \underset{\sim}{r}^e] = 0 \tag{8.4}$$

corresponds to the iteration with constant work constraint.

Ramm [132] uses the constant arc constraint and, for proportional loading, it can be expressed as:

$$(\phi^1, \underset{\sim}{r}^1) \cdot (\phi^i, \underset{\sim}{r}^i) = 0 \tag{8.5}$$

where $(\phi^1, \underset{\sim}{r}^1)$ represents the tangent at the current state 1 along the deformation path and $(\phi^i, \underset{\sim}{r}^i)$ is some vector in the space span by ϕ^i and $\underset{\sim}{r}^i$. Equation 8.5 means that the iterative path is always normal to the tangent plane span by $(\phi^1, \underset{\sim}{r}^1)$. The vector $\underset{\sim}{r}^i$ is again formed in two steps:

$$\underset{\sim}{r}^i = \phi^i \underset{\sim}{r}^e + \underset{\sim}{r}^u \tag{8.6}$$

Substituting Eq. 8.6 into Eq. 8.5, the unknown load factor ϕ^i can be found.

The idea of the normal plane of Ramm [132] is related to that of Crisfield [133]. They are both modified versions of the Riks-Wempner method [134,135]. However, in Crisfield's approach, the constraint approach is not followed.

It should be mentioned that Frey [130] and Bergan [124] iterate with constant external load steps, but Powell [129] and Ramm [132] iterate with variable external load.

8.3.5 Solution Scheme in the Present Study

A number of numerical schemes have been presented in the previous section. The double step method seems to be the most general and is well suited for solving problems with strain softening and instability. The key lies in the proper choice of the constraint.

The approaches of Frey [130], Bergan [124], and Ramm [132] require the tangent stiffness to be exact. This means that the stiffness has to be reformed at the end of every iteration. The computational effort is therefore high.

The imposed deformation of Powell [129] does not require the exact tangent stiffness to be formed, provided that the load is single valued in the displacement component n. This only involves a proper choice of the n^{th} displacement degree of freedom to be constrained. As demonstrated by Powell et al [129], an iteration with constant imposed deformation also yielded a more rapidly converged solution compared to the conventional iteration with constant load step.

It is because of the economy, speed of convergence, and the simplicity of the imposed deformation of Powell [129] that the same numerical scheme is used in the present study.

8.4 Termination of the Solution

Depending on the objective of the analysis, different criteria can be used. The criteria may be chosen to satisfy either the serviceability or the safety requirements.

In the present study, both criteria will be used. To find the ultimate load capacity of the structure, the solution is stopped once a negative eigenvalue is detected in the stiffness matrix. To satisfy

the serviceability requirement, the displacement is imposed progressively until the maximum allowable value is exceeded. Typically, this is the case in studying the post-buckling behavior of a structure.

The two criteria used are illustrated in a typical load displacement diagram for a structure with instability (Fig. 8.4).

8.5 Description of the Present Numerical Technique

An automatic load generation based upon limiting the n^{th} imposed displacement increment δ_{max} at the beginning of the displacement step is used. The constraint equations are:

$$r_n^u + \phi^i r_n^e = \delta_{max} \quad \text{for first iteration}$$

$$r_n^u + \phi^i r_n^e = 0 \quad \text{for subsequent iterations}$$

In order to guard against excessive load being put on the system in any displacement increment, the load factor ϕ^i is limited such that:

$$\phi^i \leq \phi_{max}$$

The convergence criteria can be controlled either by force or displacement in absolute magnitude or it can be expressed as a fraction of an incremental external force or displacement.

The iterative path in the present numerical technique can be geometrically interpreted as in Fig. 8.5. The method, when applied to a single degree of freedom system with snap-through phenomenon, converges at the first iteration and good agreement is observed. The results are presented in Fig. 8.6 and Table 8.1.

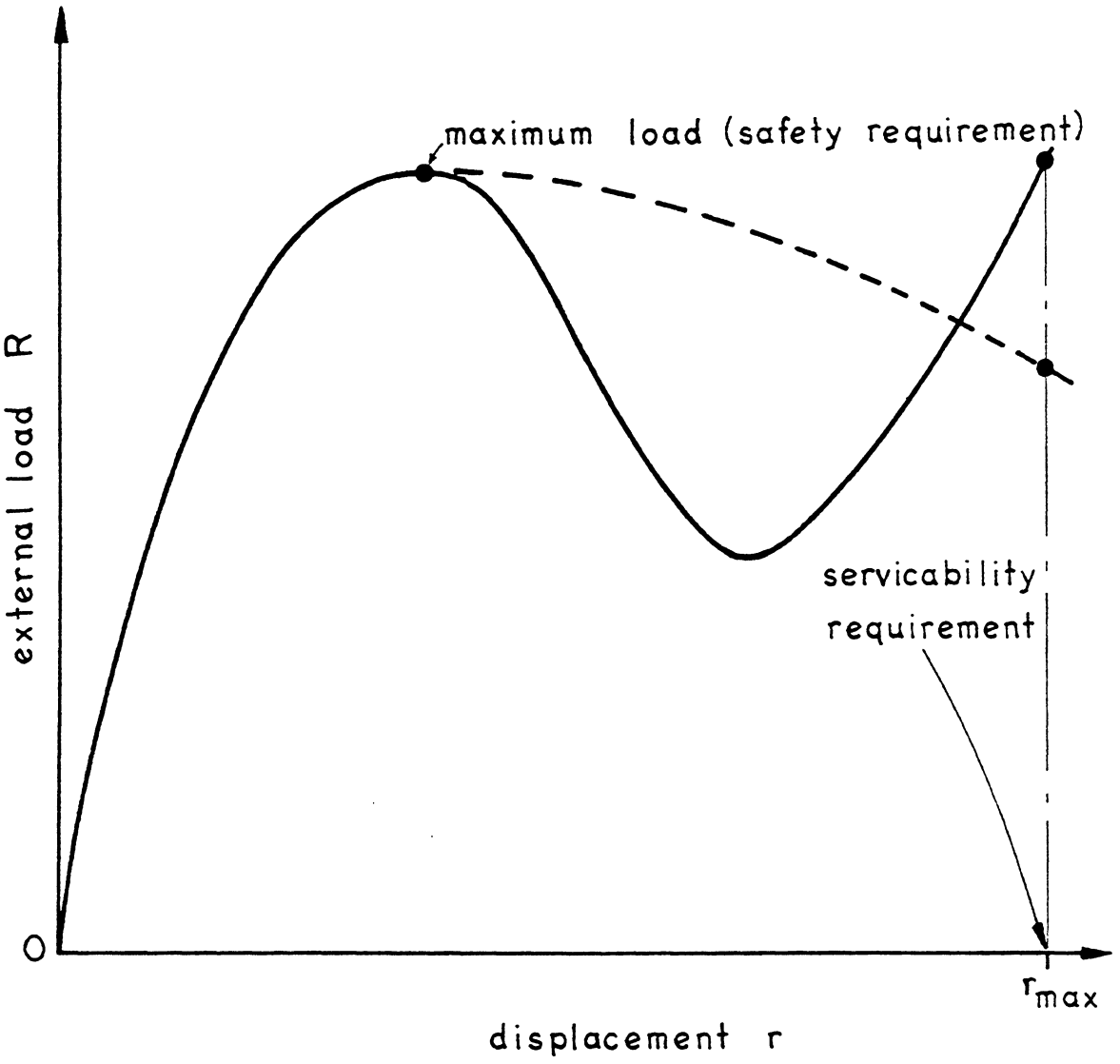

FIG. 8.4 TERMINATION OF SOLUTION

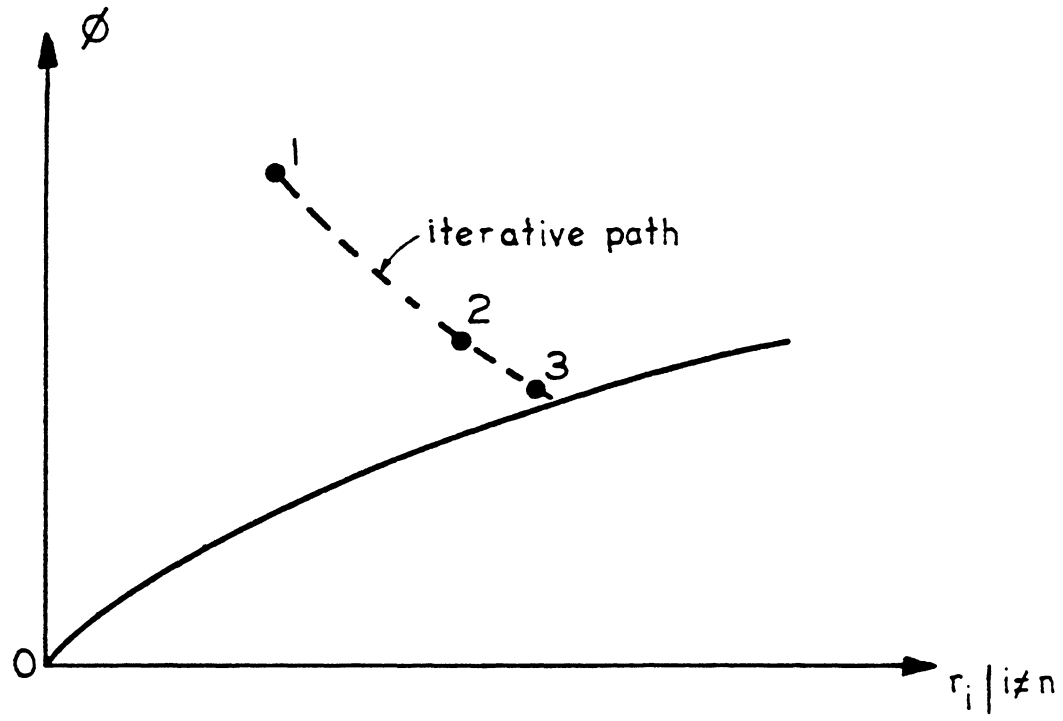

LOAD VS. DISPLACEMENT OF THE UNCONSTRAINED D.O.F.

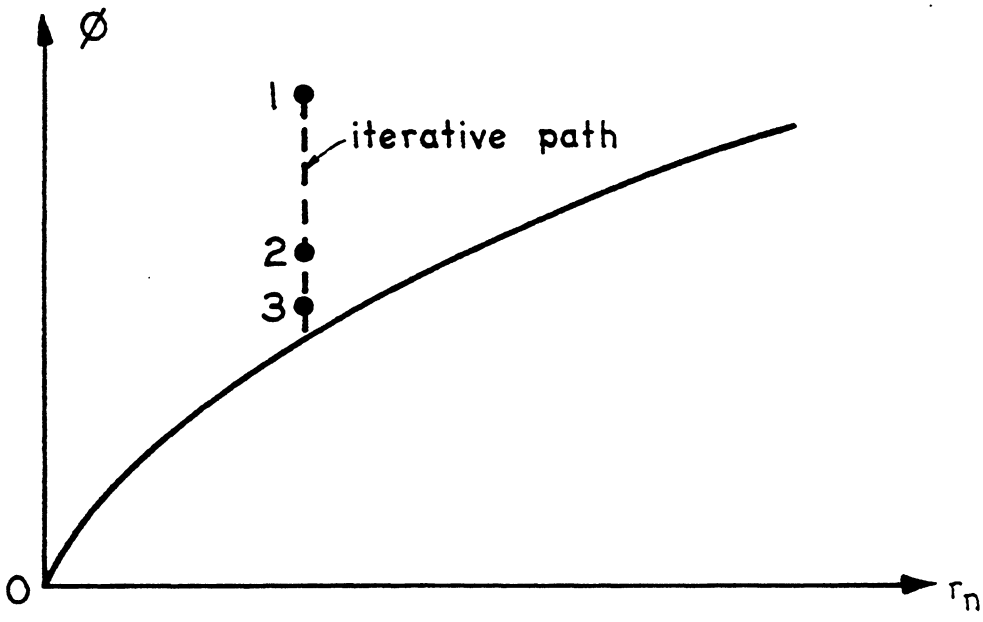

LOAD VS. DISPLACEMENT OF THE CONSTRAINED D.O.F. n

FIG. 8.5 ITERATIVE PATH FOR IMPOSED DISPLACEMENT

TABLE 8.1 ITERATIVE PROCEDURE FOR TWO BAR TRUSS WITH CONSTANT IMPOSED DISPLACEMENT

Load Step	Itr.	Displ. Increment (δ)	R_{ref}	$R_u = R_E - R_I$	K_T (Ignore K_G)	$\Delta r_e = K_T^{-1} R_{ref}$	$\Delta r_u = K_T^{-1} R_u$	$\frac{\Delta\phi}{\Delta r_e} = \frac{(\delta - \Delta r_u)}{\Delta r_e}$	$R_E = \Sigma\Delta\phi \cdot R_{ref}$	R_I	r_{TOT}
1	1	2.0	250.0	0.0	304.75	0.82	0.0	2.44	610.0	460.0	2.0
	2	0.0	250.0	150.0	227.1	1.10	0.66	-0.6	460.0	460.0	2.0
2	1	4.0	250.0	0.0	227.1	1.10	0.0	3.64	1370.0	399.0	6.0
	2	0.0	250.0	971.0	37.69	6.63	25.76	-3.89	399.0	399.0	6.0
3	1	4.0	250.0	0.0	37.69	6.63	0.0	0.61	550.0	-399.0	10.0
	2	0.0	250.0	949.0	37.69	6.63	25.18	-3.80	-399.0	-399.0	10.0
4	1	4.0	250.0	0.0	37.69	6.63	0.0	0.608	-248.0	-460.0	14.0
	2	0.0	250.0	212.0	227.1	1.10	0.933	-0.848	-460.0	-460.0	14.0
5	1	4.0	250.0	0.0	227.1	1.10	0.0	3.64	450.0	737.8	18.0
	2	0.0	250.0	-287.8	353.7	0.707	-0.814	1.15	737.8	737.8	18.0
6	1	2.0	250.0	0.0	353.7	0.707	0.0	2.83	1445.0	2498.3	20.0
	2	0.0	250.0	-1053.3	294.7	0.848	-3.574	4.21	2498.3	2498.3	20.0

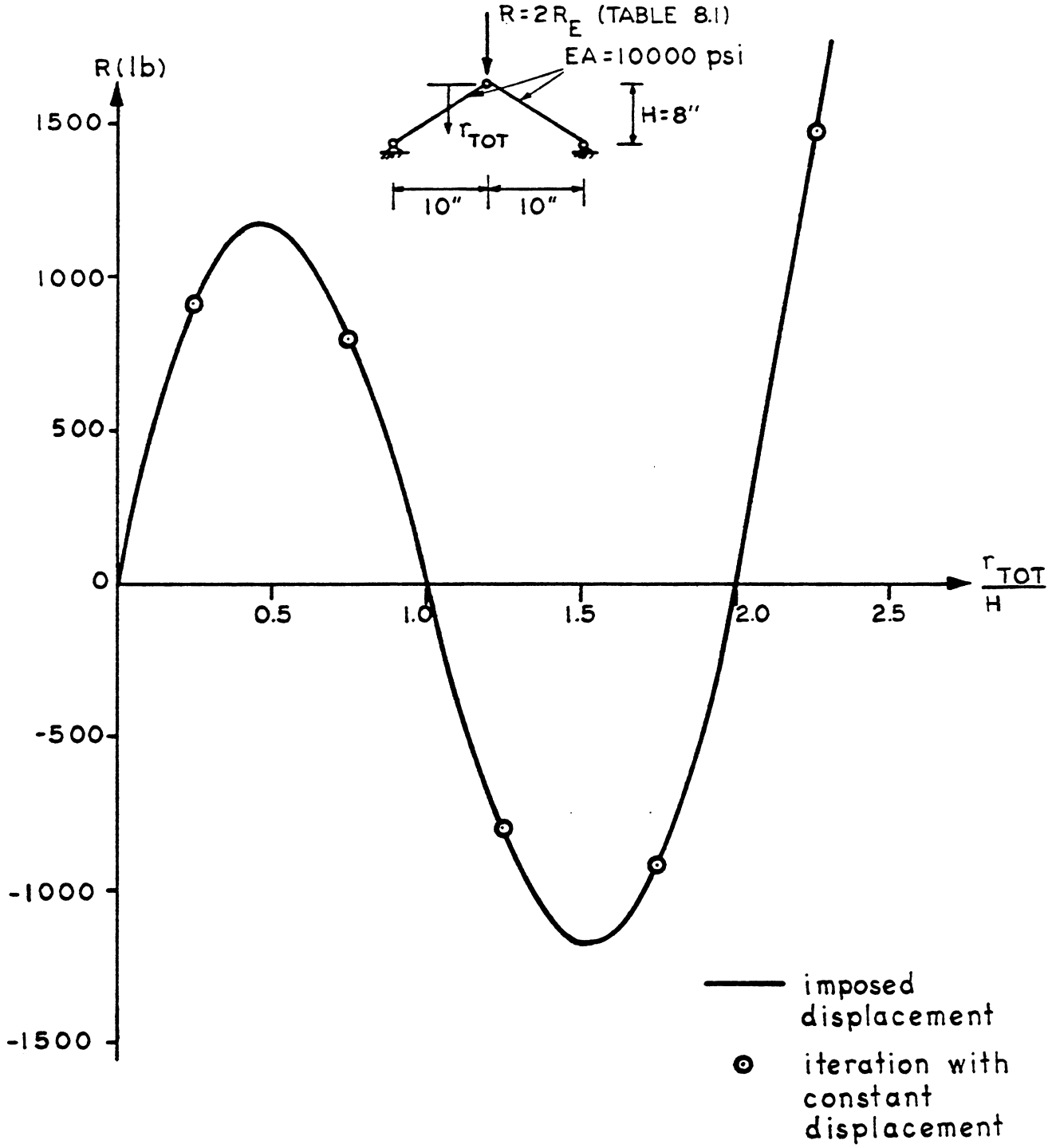

FIG. 8.6 SNAP-THROUGH OF A 2-BAR TRUSS SOLVED BY ITERATION WITH CONSTANT IMPOSED DISPLACEMENT

9. COMPUTER PROGRAM

9.1 General

A computer program called NASHL (Nonlinear Analysis of Reinforced Concrete ShelLs with Edge Beams) has been developed to trace the structural response of reinforced concrete shells with edge beams including nonlinear material and geometry, and the time dependent effects of creep and shrinkage.

The program is coded in FORTRAN IV and has been tested on the CDC7600 computer of the University of California, Berkeley. The blank common is dynamically dimensioned within the program so that the central memory of the computer can be used efficiently. The equation solver used is based upon Gaussian Elimination and the total number of equations are stored in blocked forms [136]. The blocking of the equations has made it possible to analyze a large structural system where both the total number of equations and bandwidth are large [137,138].

The computer program consists of a main program NASHL and three library elements: shell element (ASHL), beam element (BEAM) and boundary spring element (BOUND). The shell and the beam element can be either used separately or integrated to form a system consisting of shell and beam elements. The element data are stored in slow speed storage system using tapes and drums, so that each element forms a separate module, thus allowing the addition of new elements if desired.

The functions performed by each element library routine are:

1. Input the element data and initialize the arrays, store the information on tape MTS1.
2. Form the element stiffness using the element data stored on tape MTS1.

3. Perform state determinations, update the states and the stresses as well as the geometry of the element if desired. Store the new information on tape MTS2.
4. Compute the internal resulting forces due to the updated stresses stored on tape MTS2.
5. Output the element states and stresses if desired.

A detailed description of the input for the program is described in Appendix A.

9.2 Flow Chart for the Computer Program NASHL

A flow chart for the computer program is shown in Fig. 9.1.

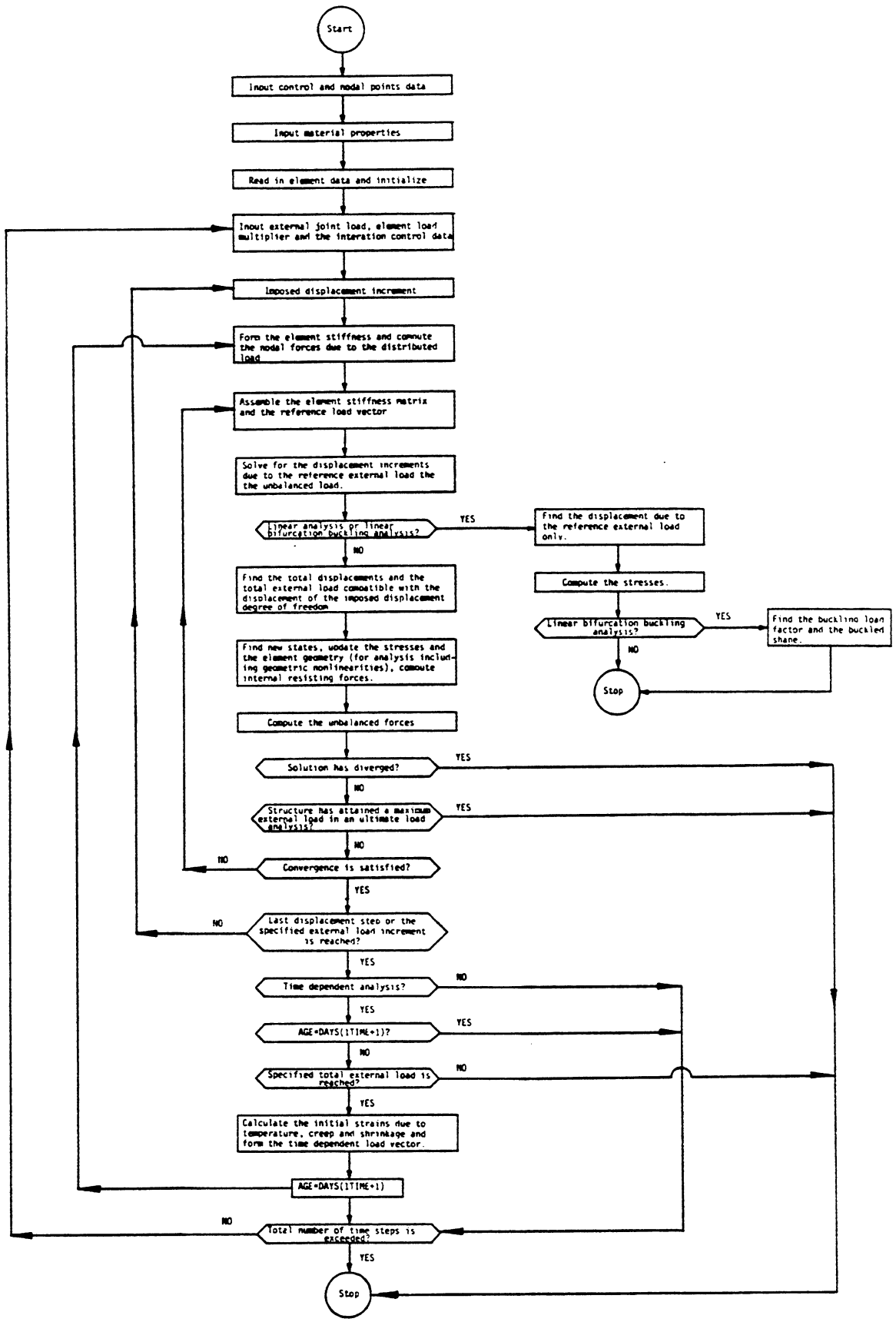

FIG. 9.1 FLOW CHART FOR THE COMPUTER PROGRAM NASHL

10. NUMERICAL STUDIES

10.1 General

In this chapter, numerical examples are solved using the computer program NASHL, developed in the present study, to verify the proposed method of analysis.

The examples also serve as a means to demonstrate the range of complexities of the problems that can be analyzed and the effects of nonlinear material, nonlinear geometry and the time dependent phenomenon of creep and shrinkage on the results obtained.

The examples are subdivided into three categories:

(1) Linear elastic structures with nonlinear geometry.

(2) Reinforced concrete beams and plates.

(3) Reinforced concrete shells with edge members.

The results for each group of examples will be presented in separate sections and, finally, the computational effort for some selected examples will also be summarized.

10.2 Linear Elastic Structures

In this group of examples, emphasis is placed on the verification of the present method of handling geometric nonlinearities, both for the shell element and the beam element, by adopting a small strains, small incremental rigid body rotation theory.

It is found that the use of the complete strain-displacement relationship of Eq. 2.12 is necessary in solving large displacement problems so that the strains due to the rotations are properly accounted for. Retaining only the linear terms requires that the incremental displacements and rotations be unnecessarily small in order to obtain

the correct solutions. This fact is illustrated in the first and the second examples in this section.

The use of the numerical scheme as discussed in Chapter 8 in solving the buckling of shell due to finite displacement is demonstrated in the third and fourth examples. The third example also serves to verify the present treatment of the pressure load.

Finally, the fifth example verifies the treatment of nonlinear geometry for the beam element.

10.2.1 Pure Bending of Plate Strip

A cantilever plate strip of length 10 in., width 1 in. and thickness 0.1 in. is subjected to an end moment M. This is a large rotation problem and the exact solution for the deformed shape is a circular arc of length 10 in. and with a radius R, where

$$R = \frac{EI}{M}$$

The moment required to bend the plate into a complete circle is M_o, where

$$M_o = \frac{2\pi EI}{L}$$

The plate is modelled by 4 equal sized shell elements and the geometry and the material properties of the structure are shown in Fig. 10.1.

The calculated deformed shape for the load level of 0.1 M_o and 0.2 M_o are shown in Fig. 10.1. It can be observed that good agreement exists between the theoretical and the calculated values when all nonlinear terms in the strain-displacement relationship are used.

At a load level of 0.2 M_o, the error in the vertical tip deflection is 0.2% and for the horizontal tip deflection, an error of 4.0%

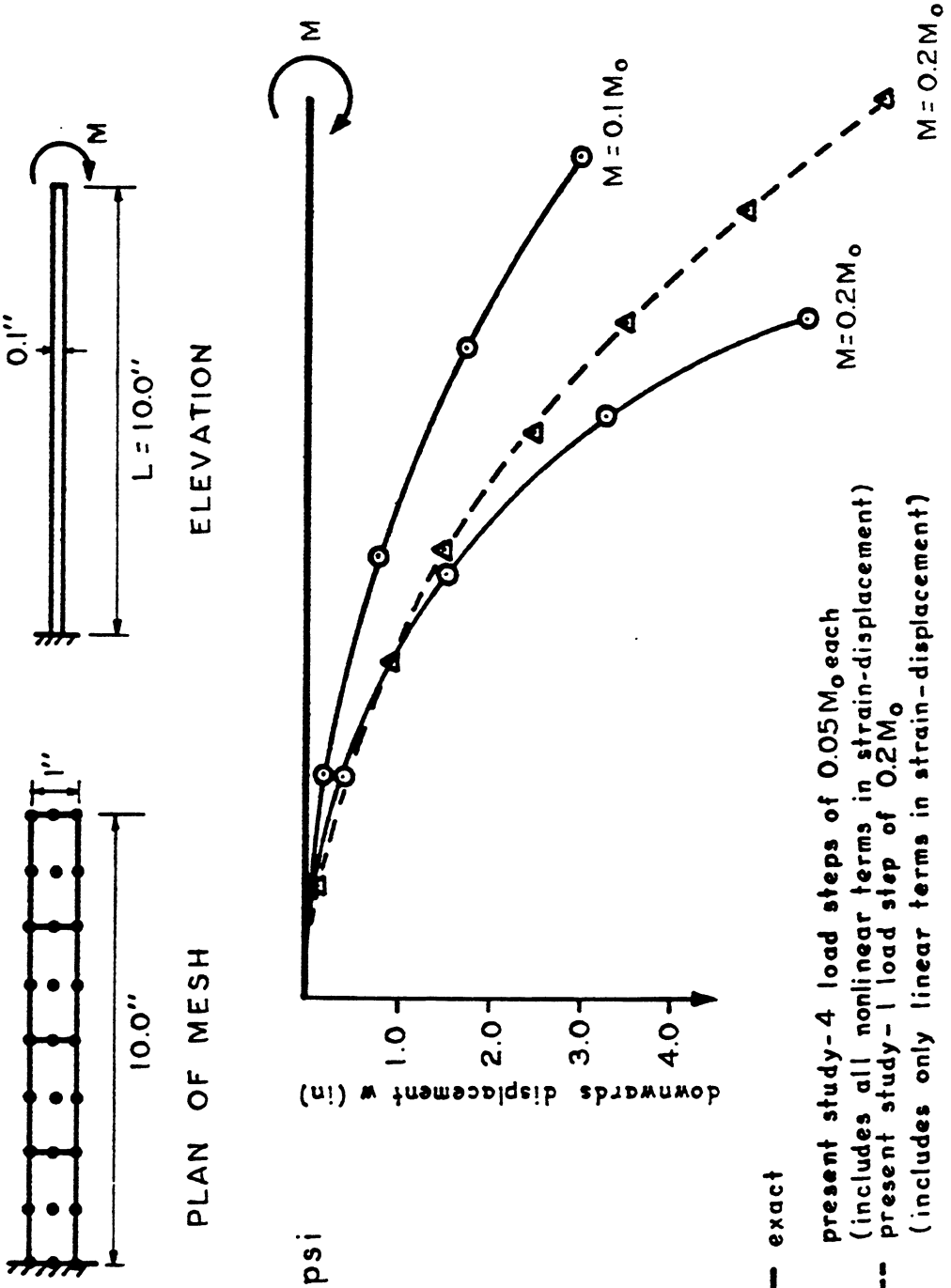

FIG. 10.1 PURE BENDING OF PLATE STRIP (EX. 10.2.1) - DEFORMED SHAPE OF CANTILEVER PLATE STRIP DUE TO END MOMENT

is observed. The internal bending moment (not shown) shows an error of about 2.0% near the support.

For an analysis with one load step of 0.2 M_o and retaining only the linear terms in the strain-displacement relationship, a significant error in the deformed shape occurs (Fig. 10.1).

This example demonstrates that the nonlinear terms in the strain-displacement relationship should be retained and that large rotation problems can be solved by using the present method and subdividing the total load into load steps such that large rotations become a series of small rotations. In the present analysis, a total end rotation of 0.4π radians is obtained in 4 steps, each of 0.1π radians each.

10.2.2 Large Displacement Analysis of a Simply Supported Square Plate

A simply supported 16-in. square plate subjected to a uniform vertical load, analyzed by Levy [139] with the use of trigonometrical series, is re-analyzed here. The edges are restrained against horizontal movement and the load is conservative.

The geometry and the material properties are shown in Fig. 10.2. Due to the symmetry of the structure, only one-quarter of the plate is modelled with a mesh of 2 x 2 shell elements. The solution is obtained by using 4 equal loads with increments of 3.0 psi each, giving a total load of 12.0 psi.

The load-displacement response for the plate is shown and compared with Levy's solution [139] in Fig. 10.2. The structure exhibits a distinct stiffening effect due to the development of the in-plane membrane forces.

The load vs. the stresses at selected points are also compared and the results are shown in Fig. 10.3. Agreement with Levy's solution

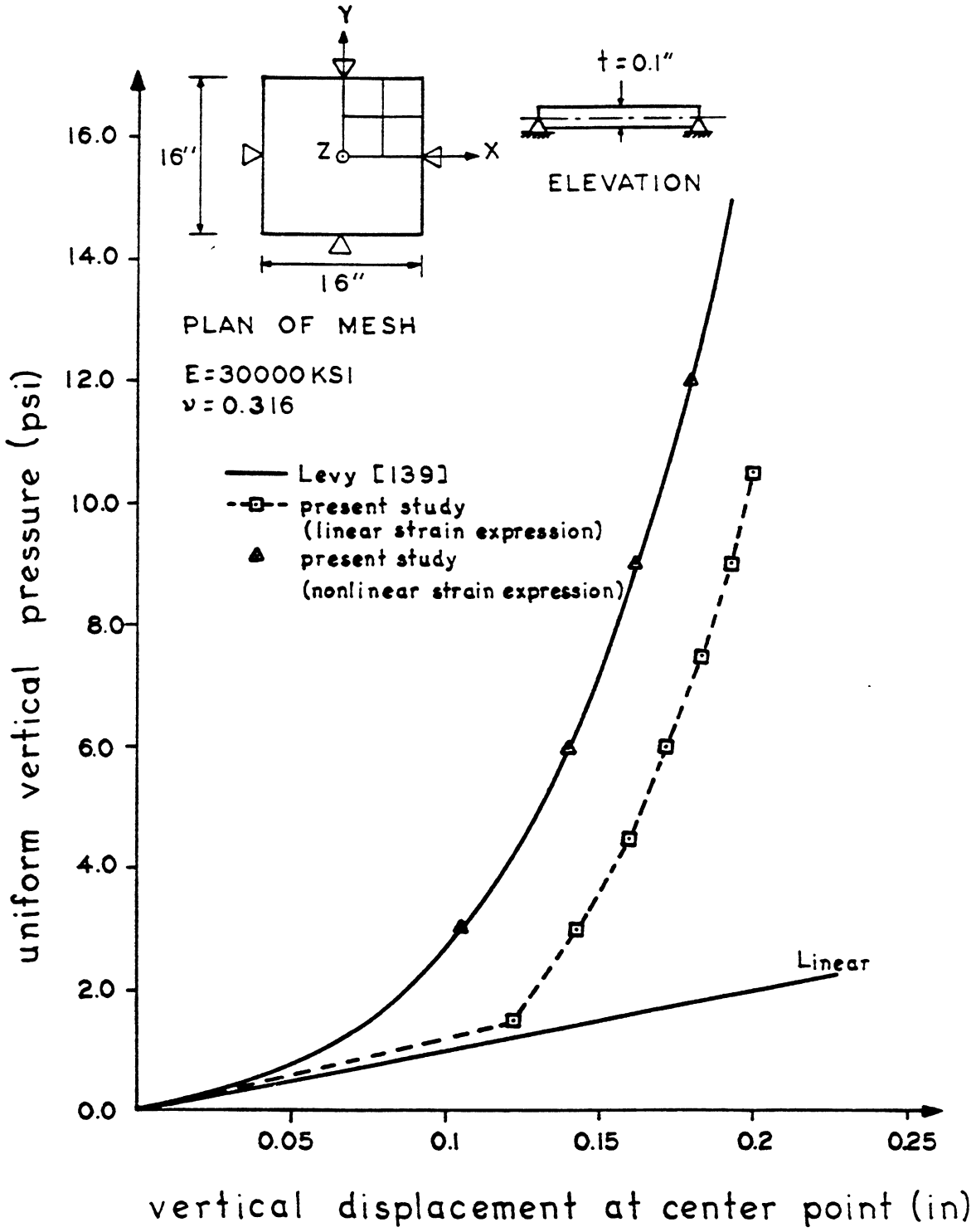

FIG. 10.2 LARGE DISPLACEMENT ANALYSIS OF A SIMPLY SUPPORTED SQUARE PLATE (EX. 10.2.2) - LOAD VS. CENTER POINT VERTICAL DISPLACEMENT

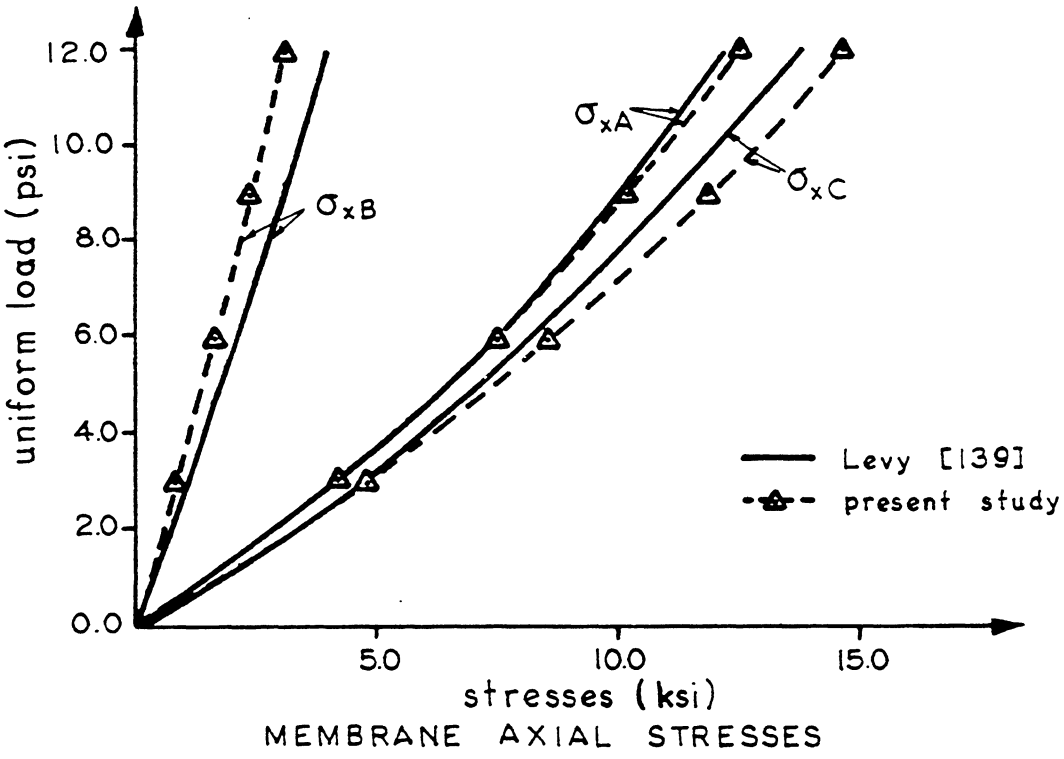

MEMBRANE AXIAL STRESSES

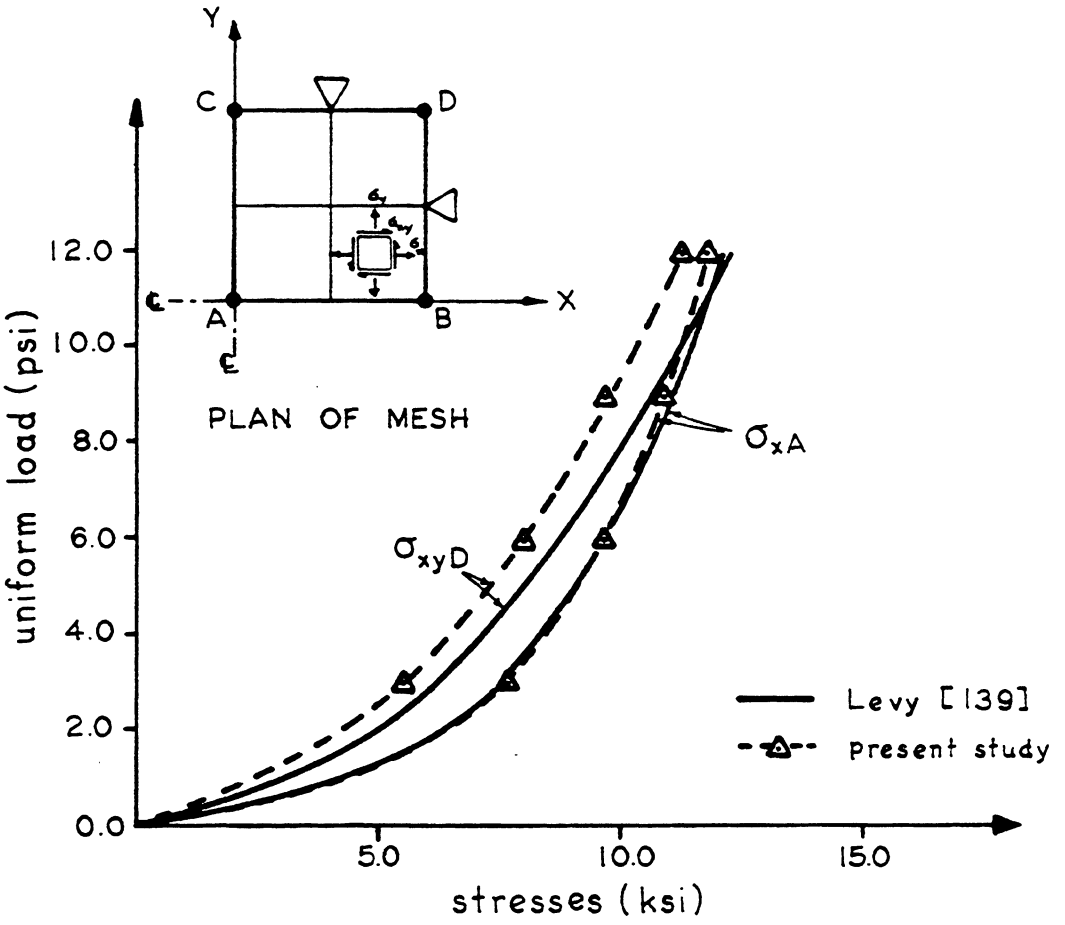

MEMBRANE SHEAR AND BENDING STRESSES

FIG. 10.3 LARGE DISPLACEMENT ANALYSIS OF A SIMPLY SUPPORTED SQUARE PLATE (EX. 10.2.2) - COMPARISON OF STRESSES

is generally good; however, the discrepancies in σ_{xB} and σ_{xyD} at a load level of 12.0 psi reach 15.0% and 10.0%, respectively.

Again, for an analysis using only the linear strain expression (Fig. 10.2), the displacement response of the plate cannot be predicted correctly even when the load increment is halved to an increment of 1.5 psi.

This example further validates the present treatment of nonlinear geometry in two dimensions. The correlation between the results of the present analysis and those of Levy's solution are satisfactory considering the coarse mesh of the structure used.

10.2.3 Symmetrical Buckling of Circular Arch due to Uniform Pressure

An end clamped shallow circular arch subjected to a uniform pressure is analyzed to verify the present numerical technique in solving a snap-through problem and to demonstrate the use of equilibrium correction in treating the pressure loading.

The geometry and the material properties are shown in Fig. 10.4. Due to the symmetry of the structure, one-half of the arch is modelled by 6 equal sized shell elements. The response of the structure is obtained by imposing the control vertical displacement w_o in 10 equal displacement steps of 0.5 in. each.

The load displacement response is shown in Fig. 10.4, together with the finite element solution obtained by Sharifi [127] and the analytical solution of Schreyer [140]. It can be seen that good agreement exists.

It is interesting to note that Sharifi [127], who used 10 beam elements for half the arch and only a linear strain-displacement relationship, obtained a solution which by using 60 load increments is not

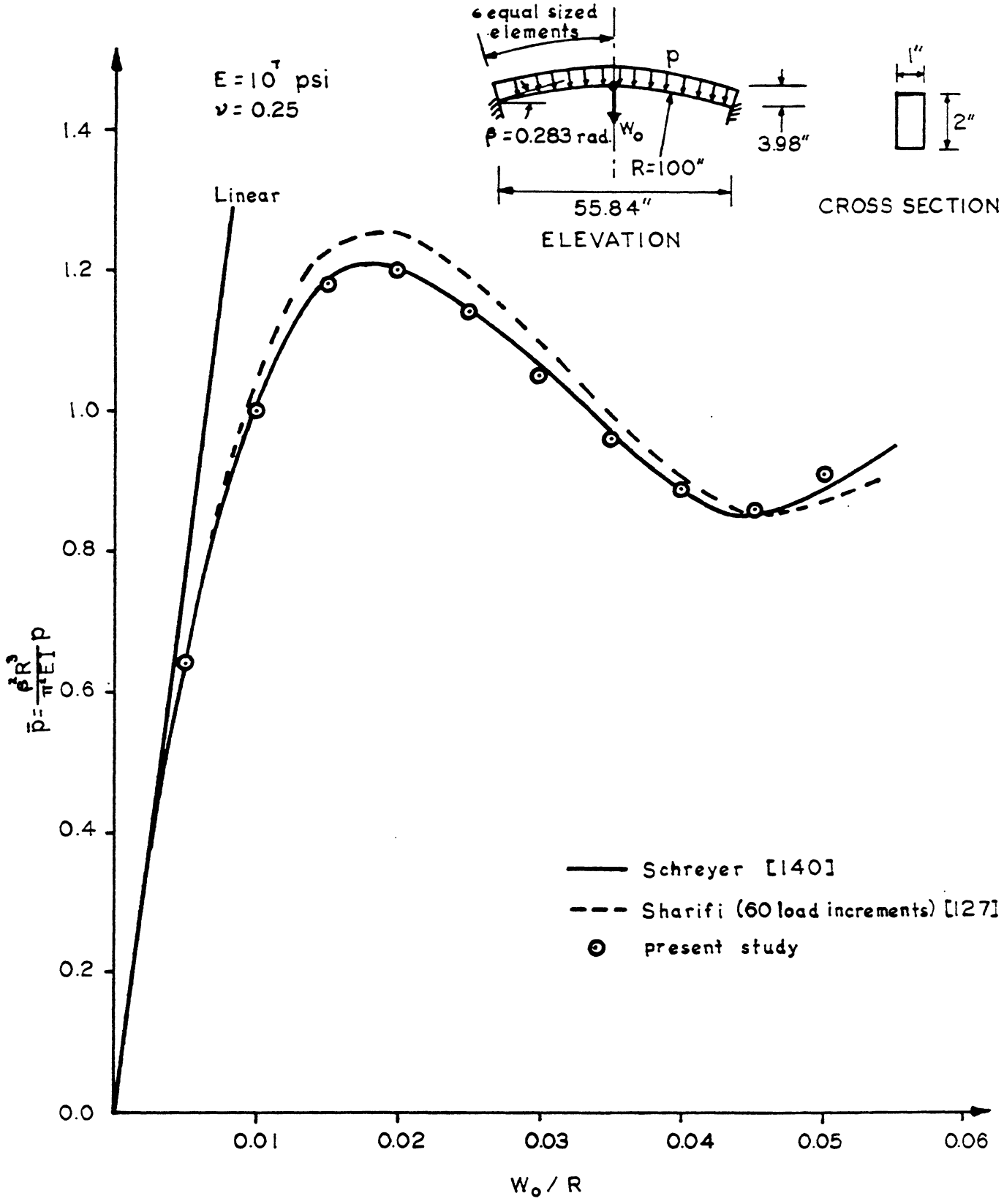

FIG. 10.4 SYMMETRICAL BUCKLING OF CIRCULAR ARCH DUE TO UNIFORM PRESSURE p (EX. 10.2.3) - LOAD VS. CENTRAL VERTICAL DOWNWARDS DISPLACEMENT

as close to that of Schreyer [140] as is the present study. The present method of analysis predicts the correct response for relatively large load steps.

A statical check has been made at mid-span at a load level of $p = 748$ psi ($\bar{p} = 0.91, w_o/R = 0.05$). Taking into account the change in geometry and summing the moments about the support point, the difference between the external and internal moment is found to be 1.0%. Also the difference between the external and internal horizontal and vertical forces are, respectively, 1.0% and 2.0%.

10.2.4 Buckling of a Hinged Spherical Shell

A spherical shell, square in plan, and hinged all around the edges, and loaded with a concentrated load at the crown, has been analyzed by Leicester [141] with a series solution using shallow shell theory. The problem has also been solved by many investigators [142, 25] as a standard example to test their formulation of the nonlinear geometry problem and the prediction of the buckling load of the shell.

The geometry and material properties are shown in Fig. 10.5. Due to the symmetry of the structure, one-quarter of the shell is modelled with a mesh of 2 x 2 shell elements. The vertical displacement at the crown, w_o, has been chosen as the imposed displacement degree of freedom. The complete load displacement response is obtained in 12 displacement increments of w_o, each equal to 1.0 in.

The load displacement response is shown in Fig. 10.5, together with the series solution of Leicester [141] and the finite element solution of Dhatt [142]. It can be seen that the ascending branch of the load displacement response and the buckling load correlate well with Leicester's and Dhatt's solutions. Although there are some

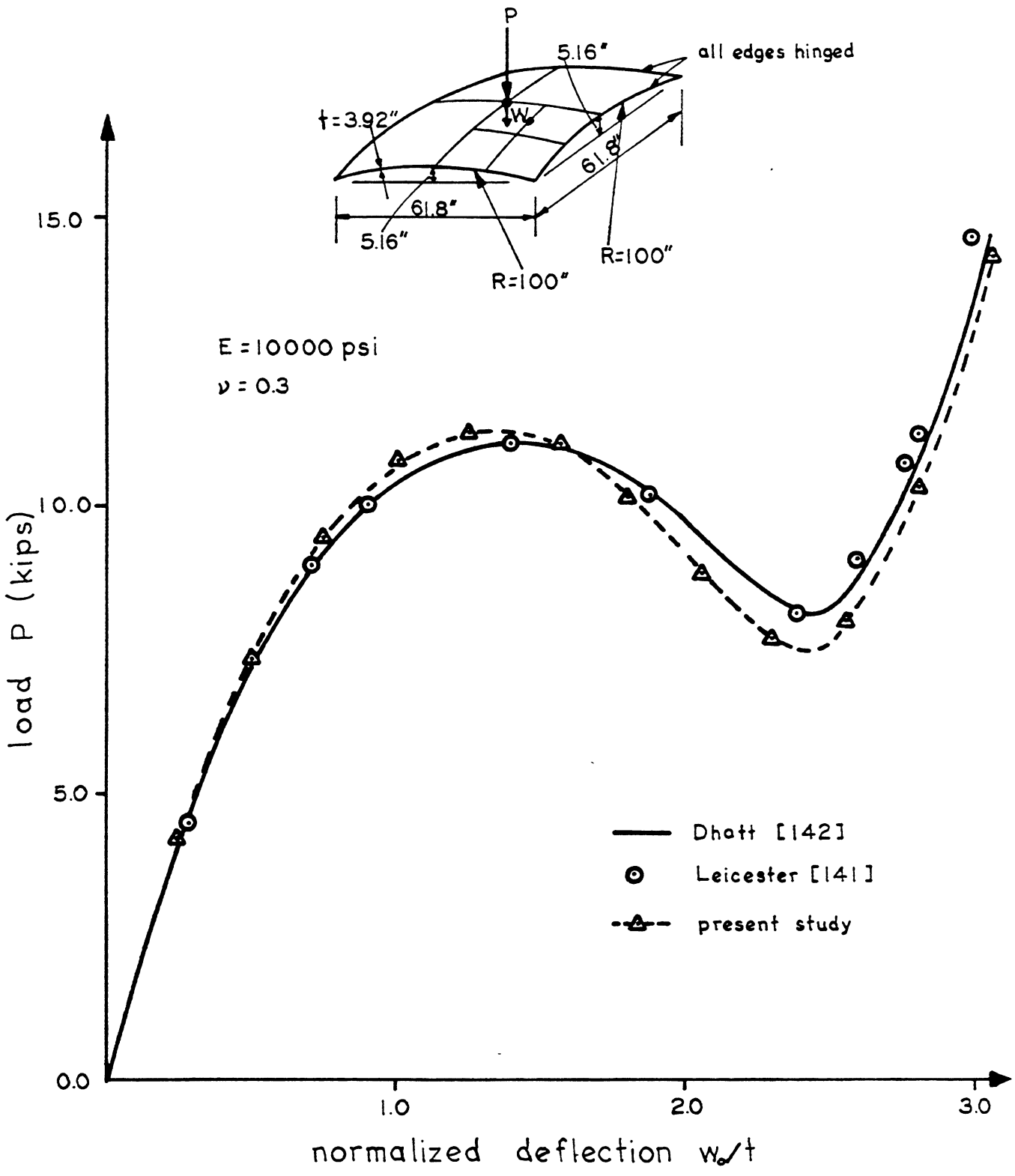

FIG. 10.5 BUCKLING OF A HINGED SPHERICAL SHELL (EX. 10.2.4) - LOAD VS. CROWN POINT VERTICAL DOWNWARDS DISPLACEMENT

discrepancies in the vicinity of the early post-buckling response, the discrepancy diminishes when the structure starts to stiffen up.

10.2.5 45° Curved Beam

A planar circularly curved cantilever beam subtends a horizontal angle at 45° is analyzed. It has constant square cross section and is subjected to a concentrated end load P normal to the plane containing the curve. The analysis in this example serves the purpose of verifying the treatment of the nonlinear geometry in the present 3D beam element and as a cross-check between the results for the present beam element and the present shell element.

The geometry and the material properties are shown in Fig. 10.6. The structure is first modelled by 8 equal sized beam elements and secondly by 4 equal sized shell elements. The vertical tip displacement, w, is chosen to be the imposed degree of freedom. Equal increments of 5 in. in w are used.

The load vs. the tip displacements, u, v, and w are shown in Fig. 10.6 and compare very well with the numerical solutions obtained by Bathe et al [31], who also used a 3D beam element. However, the treatment of the nonlinear geometry used by Bathe et al [31] is slightly different than the present study.

A statical check has been made at the support point A (Fig. 10.6), at a load of P = 295 lb. Using the deformed geometry of the curved beam, which is modelled by beam elements, the results are summarized in the following:

End shear	=	293 lb.
External load	=	295 lb.
End moment	=	17.4 in-k

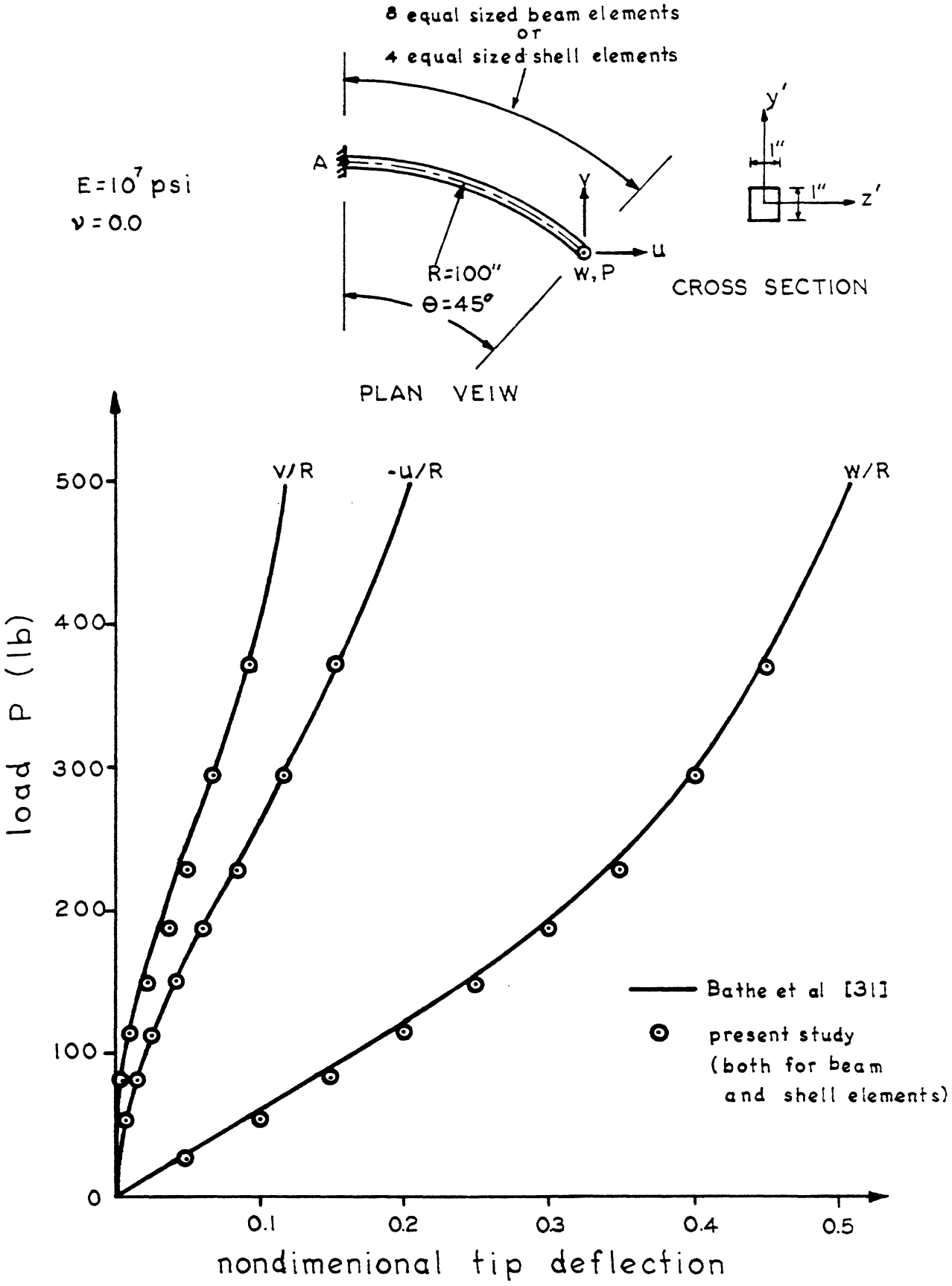

FIG. 10.6 45° CURVED BEAM (EX. 10.2.5) - LOAD VS. TIP DISPLACEMENTS

External moment = 17.4 in-k

End torque = 6.6 in-k

External torque = 6.6 in-k

It can be observed that excellent agreement exists between the internal and the external forces even for this large displacement with w = 40 in. For the analysis using the shell elements instead of the 3D beam elements, similar results for the displacements and the internal forces were found, giving a cross-check on the two element types being used in the present study.

10.3 Reinforced Concrete Beams and Plates

The purpose of this group of examples is to verify the concrete and steel material models. When applicable, the numerical results are also compared with experimental results in order to verify the present method of analysis.

The first example is a hypothetical beam with horizontal restraint. It serves as an example to demonstrate the effects of nonlinear geometry in a reinforced concrete structure. The second example is a slab where biaxial stress states exist. The third example is a column subjected to uniaxial bending where the effects of nonlinear geometry and time dependent creep and shrinkage are demonstrated. The fourth example is to study column behavior under biaxial bending, for a short time loading, with different slenderness ratios.

10.3.1 Reinforced Concrete Beam

A hypothetical reinforced concrete beam, restrained against horizontal movement at the supports, is analyzed to verify the present material models for the concrete and steel under uniaxial stress states, and to demonstrate the effects of nonlinear geometry in a reinforced

concrete structure. The same example was studied by Kang [74] and Van Greunen [26].

The geometry, the loading, and the material properties are shown in Fig. 10.7. Due to symmetry, one-half of the structure is modelled by 3 shell elements. The thickness of the beam is divided into 6 equal layers of concrete. The load displacement response is obtained by imposing the vertical displacement at mid-span.

The structure with linear material (Case 1) exhibits a distinct stiffening effect due to the development of the in-plane tensile forces in the beam. The external load, q, carried by the structure can be found by considering equilibrium of the deformed structure:

$$q = \frac{8}{L^2} (M + P\Delta) \tag{10.1}$$

where M, P, and Δ are the internal moment, the axial force, and the vertical displacement at mid-span of the beam.

It can be seen from Eq. 10.1 that the stiffening effect is due to the $P\Delta$ contribution. For a linear material, q is a monotonic increasing function of the displacement.

Ignoring the change in geometry of the structure, a continuous degradation in stiffness results due to the effects of cracking and nonlinear behavior of the concrete and yielding of the steel. This case is not plotted in Fig. 10.7, but has been solved both by Kang [74] and Van Greunen [26]. However, as shown in Fig. 10.7, including both the effects of material and geometric nonlinearities, the behavior of the beam is almost linear after initial cracking without any substantial degradation in stiffness. Further cracking is offset by an increase in stiffness due to the $P\Delta$ effect.

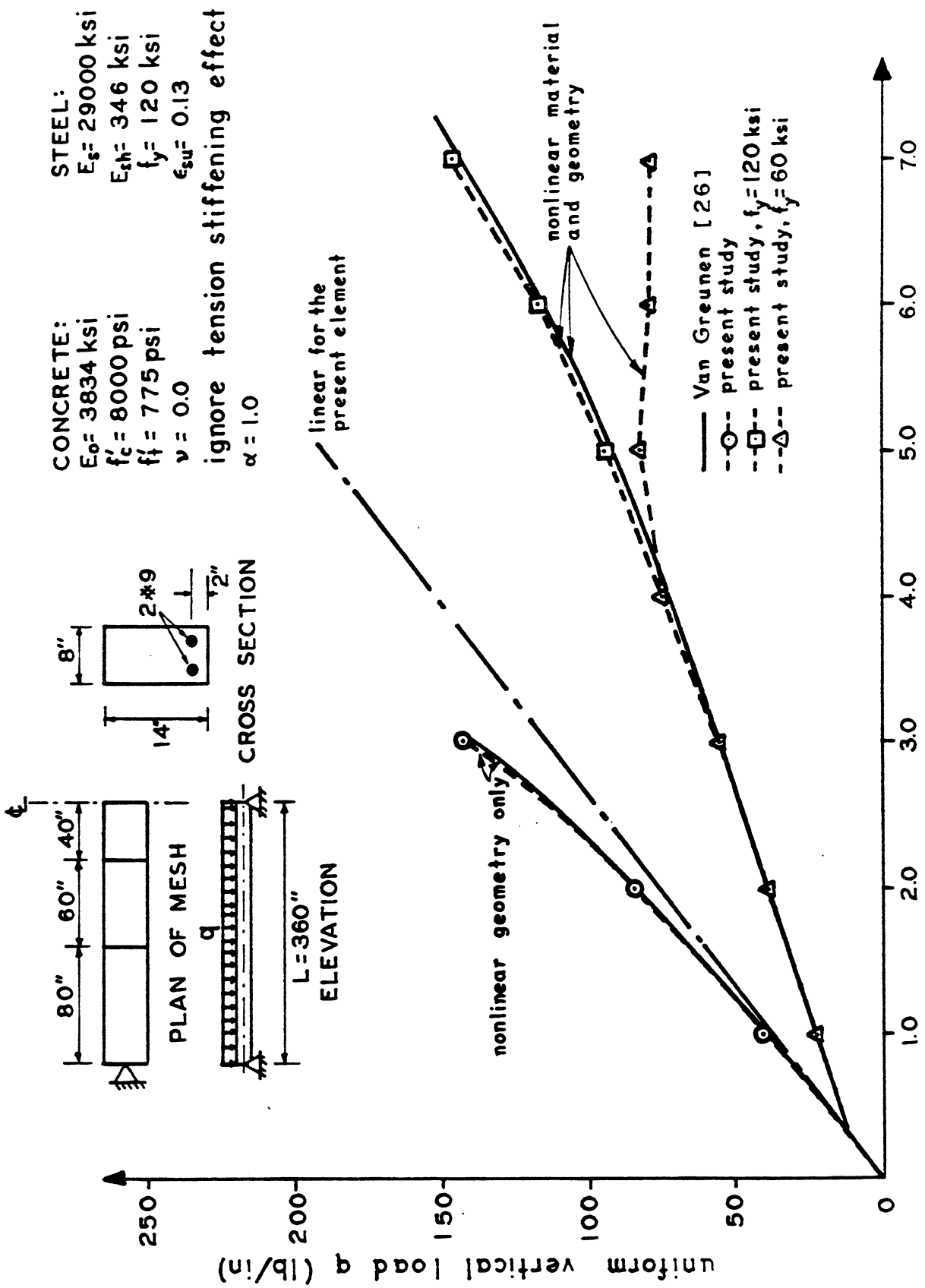

FIG. 10.7 REINFORCED CONCRETE BEAM (EX. 10.3.1) - LOAD VS. MID-SPAN VERTICAL DOWNWARDS DISPLACEMENT

For the case of f_y = 60 ksi (Case 2), the yielding of the reinforcement at a load level of about 70.0 lb/in. causes a substantial loss of stiffness and the material nonlinearities then dominate the behavior. The beam finally fails in a ductile manner at a load of 82 lb/in.

However, for f_y = 120 ksi (Case 3), a stiffening effect is observed at a later post-cracking stage. At a load level of 146 lb/in., the maximum concrete compressive stress is 6.9 ksi, while the maximum steel tensile stress is 109 ksi. These indicate that a further increase in load is possible. The extrapolated ultimate load, assuming full yielding of the reinforcement, is found to be 164 lb/in.

The load displacement responses for the three cases are shown in Fig. 10.7 and good agreement is observed between the results of the present analyses and those of Van Greunen [26].

To demonstrate the importance of the nonlinear geometry in the analyses, the present results for the ultimate loads are compared with those obtained from beam theory by assuming a uniform compressive stress distribution for concrete. In this case, beam theory gives an ultimate load of 80 lb/in. and 149 lb/in. for f_y = 60 ksi and f_y = 120 ksi, respectively. The ultimate loads obtained in this study are 82 lb/in. and 164 lb/in., which represent an increase of 2% and 10% over those of beam theory.

The importance of the nonlinear geometry in certain types of reinforced concrete structures is demonstrated in this example.

10.3.2 McNeice Slab

An isotropically reinforced concrete slab, simply supported at the four corners, was tested by McNeice [143]. The same slab has been

analyzed by many investigators, among them are Lin [8], Kabir [11], and Van Greunen [26].

Due to the lack of experimental data, the following set of material properties, which has been used by other investigators [8,11,26], is used in the present analysis.

Concrete		Steel	
E_o	= 4150 ksi	E_s	= 29000 ksi
f'_c	= 5.5 ksi	E_{sh}	= 0
f'_t	= 0.55 ksi	f_y	= 60 ksi
ν	= 0.15	σ_{su}	= 0.1 in/in.
α	= 1.0		

The tension stiffening effect in the concrete is included as an added stiffness to the steel.

The geometry and the reinforcement of the slab are shown in Fig. 10.8. Due to symmetry, one-quarter of the slab is modelled by a mesh of 2 x 2 shell elements. The thickness of the slab is divided into 6 equal layers, and the reinforcement is represented by an equivalent smeared single layer of steel of 0.011 in. thick. The transverse displacement at the center of the slab is chosen to be the imposed displacement degree of freedom where each imposed displacement increment equals 0.1 in. In this example, nonlinear geometry is not included.

The analysis is first carried out for the slab with no horizontal restraint and, secondly, with horizontal restraint.

The load vs. the vertical displacement at point A for the two cases are shown in Fig. 10.8 and are compared with the experimental results of McNeice [143].

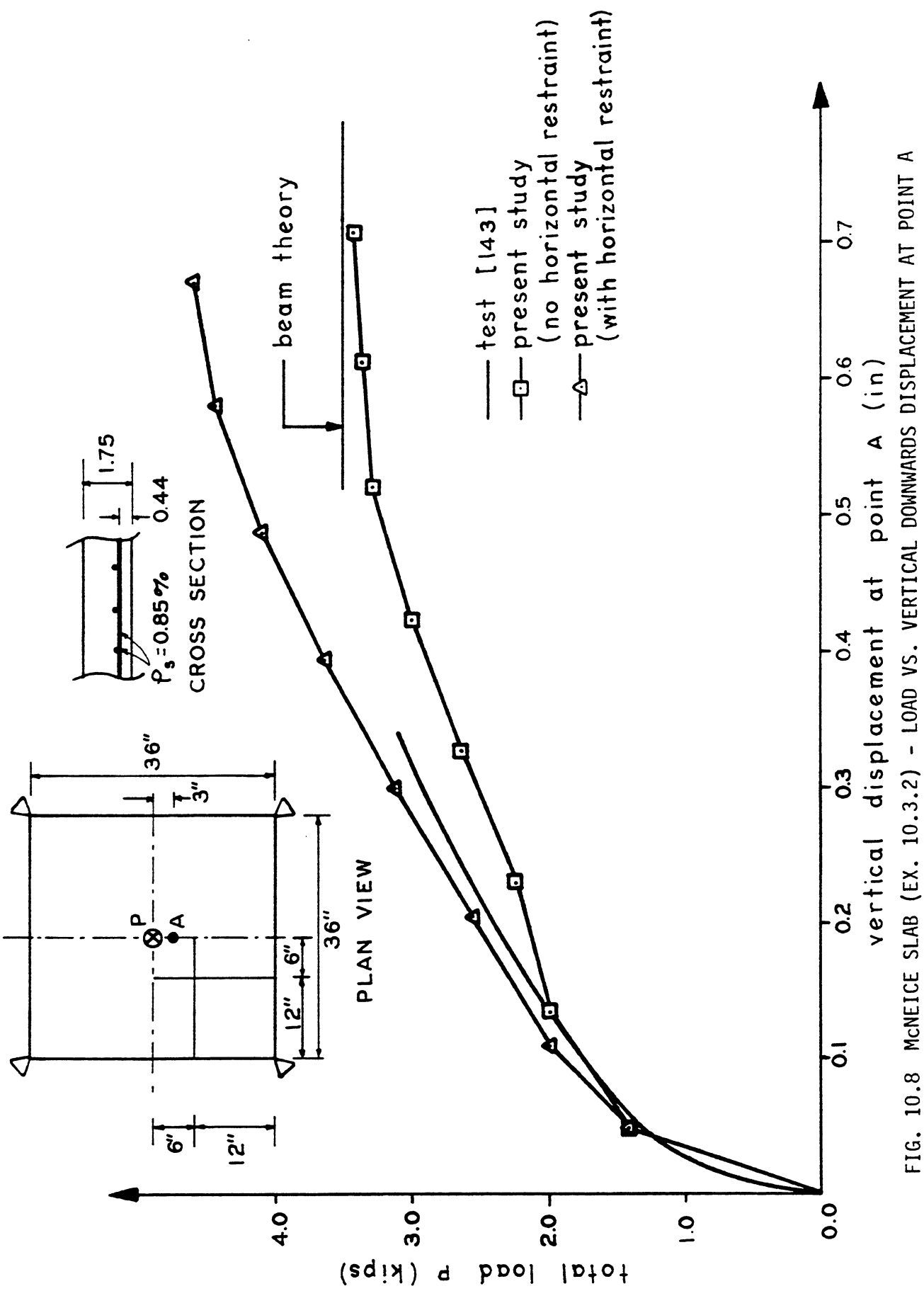

FIG. 10.8 McNEICE SLAB (EX. 10.3.2) - LOAD VS. VERTICAL DOWNWARDS DISPLACEMENT AT POINT A

The neutral axis of the slab will shift upwards because of cracking in the concrete. This will develop the in-plane membrane forces due to the rotations of the cross sections when the supporting points are restrained against horizontal movement. These membrane forces will tend to prevent the potential cracking and redistribute the stresses in the slab and, as a consequence, a stiffer and a stronger structure results. On the other hand, when horizontal movement is permitted, these membrane forces cannot be developed and the resulting load carrying capacity reaches an ultimate load similar to that based upon beam theory by assuming a full yield moment exists at the mid-span cross section of the slab.

The load vs. the maximum concrete compressive stresses and the magnified steel stresses (average steel stresses + average tensile stresses in the concrete between primary cracks) at point C are shown in Fig. 10.9. The stiffening due to the horizontal restraint is again noted.

The existence of the horizontal restraint also causes some redistribution in stresses; and, as a result, the crack patterns will be different. The modes of failure are essentially the same, namely by yielding of the reinforcing steel at mid-span, but the crack directions are slightly different. This is shown in Fig. 10.10 for the two different support conditions.

To show the magnitude of the membrane forces developed, the internal forces at mid-span are integrated to obtain the horizontal reaction. For the case where the slab is restrained horizontally, a reaction of 6.8 k in compression is obtained at a load of 4620 lb. However, when there is no horizontal restraint, the total axial force

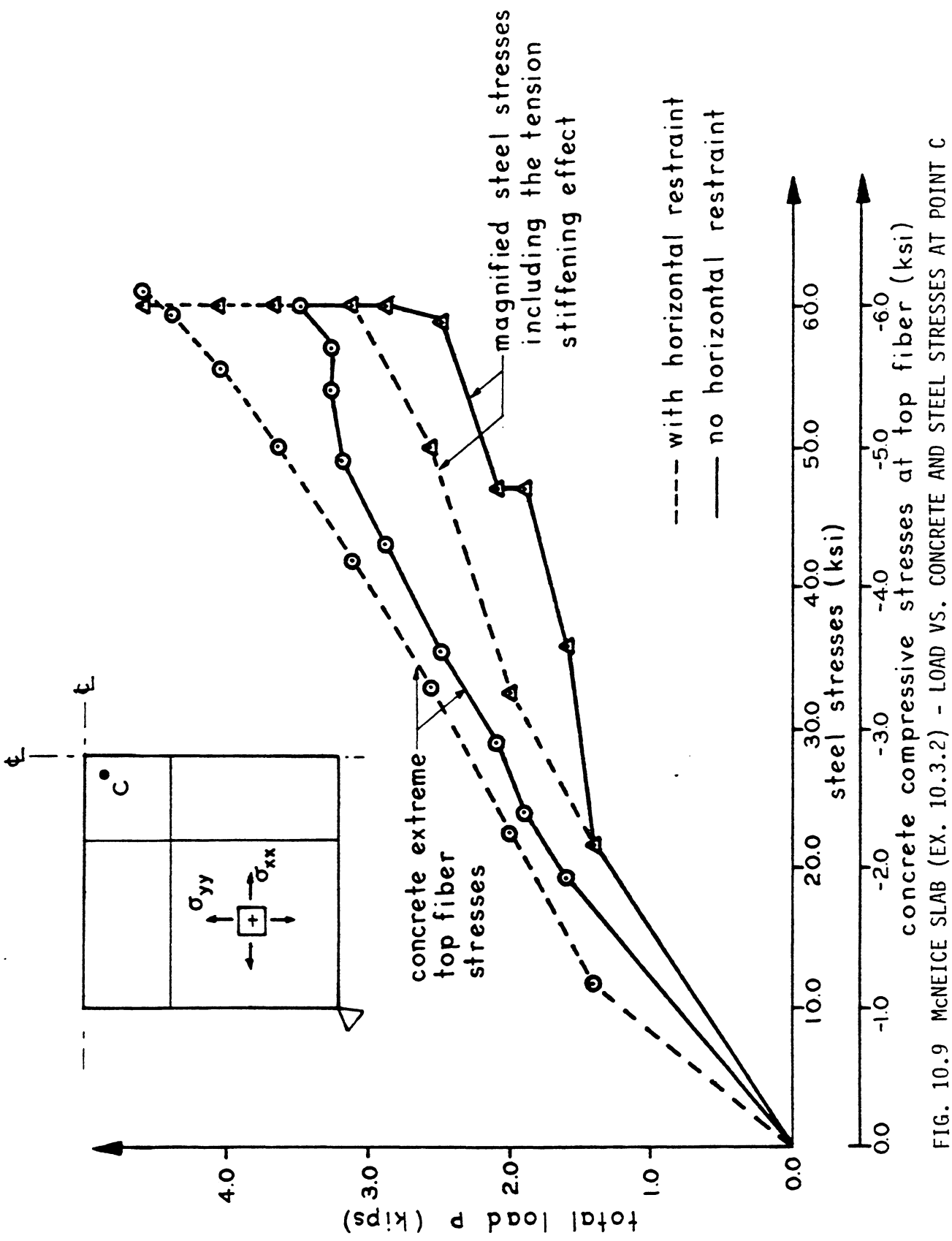

FIG. 10.9 McNEICE SLAB (EX. 10.3.2) - LOAD VS. CONCRETE AND STEEL STRESSES AT POINT C

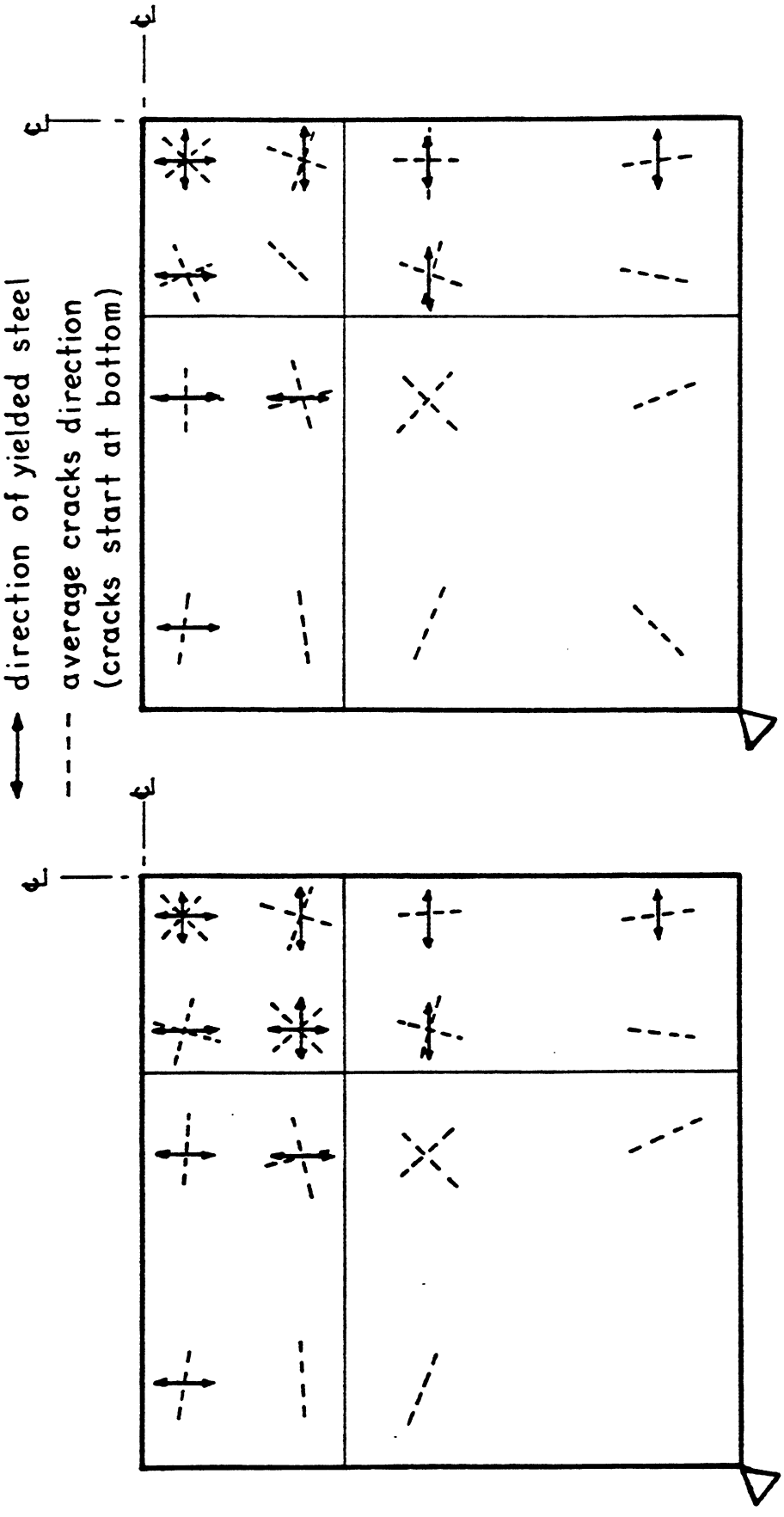

FIG. 10.10 McNEICE SLAB (EX. 10.3.2) - CRACK PATTERNS

at mid-span is negligibly small, having a value of 54 lb. in compression, at a load of 3480 lb.

The two cases studied, which represent the two extremes in a simply supported system, clearly demonstrate the important influence of the horizontal restraint. The actual supporting condition will generally lie somewhere between them. This uncertainty in the actual boundary condition will further complicate the nonlinear analysis of a reinforced concrete structure.

10.3.3 Sustained Load on a Reinforced Concrete Column

A series of columns with different slenderness ratios have been tested by Hellesland et al [144] for long time loading. The columns are eccentrically loaded. At 28 days after casting, a load of 34.5 k is applied and sustained on the structure over a period of 3 months. The structure is then loaded to failure.

In this example, one of the columns tested by Hellesland et al [144] will be analyzed. The column is first analyzed for instantaneous loading and, secondly, for sustained load, including the effects of creep and shrinkage.

The geometry and the reinforcement arrangement of the column are shown in Fig. 10.11. The stirrups in the enlarged sections of the actual test model are not modelled in the present analysis. Instead, four #5 bars are assumed to exist.

Due to symmetry, one-half of the structure is modelled by 9 beam elements, where 2 equally sized elements are used in the enlarged section and 7 beam elements, as shown in Fig. 10.11, are used for the smaller section. The cross section of the column is divided into 10 equal layers about the axis of bending and only one layer is used about

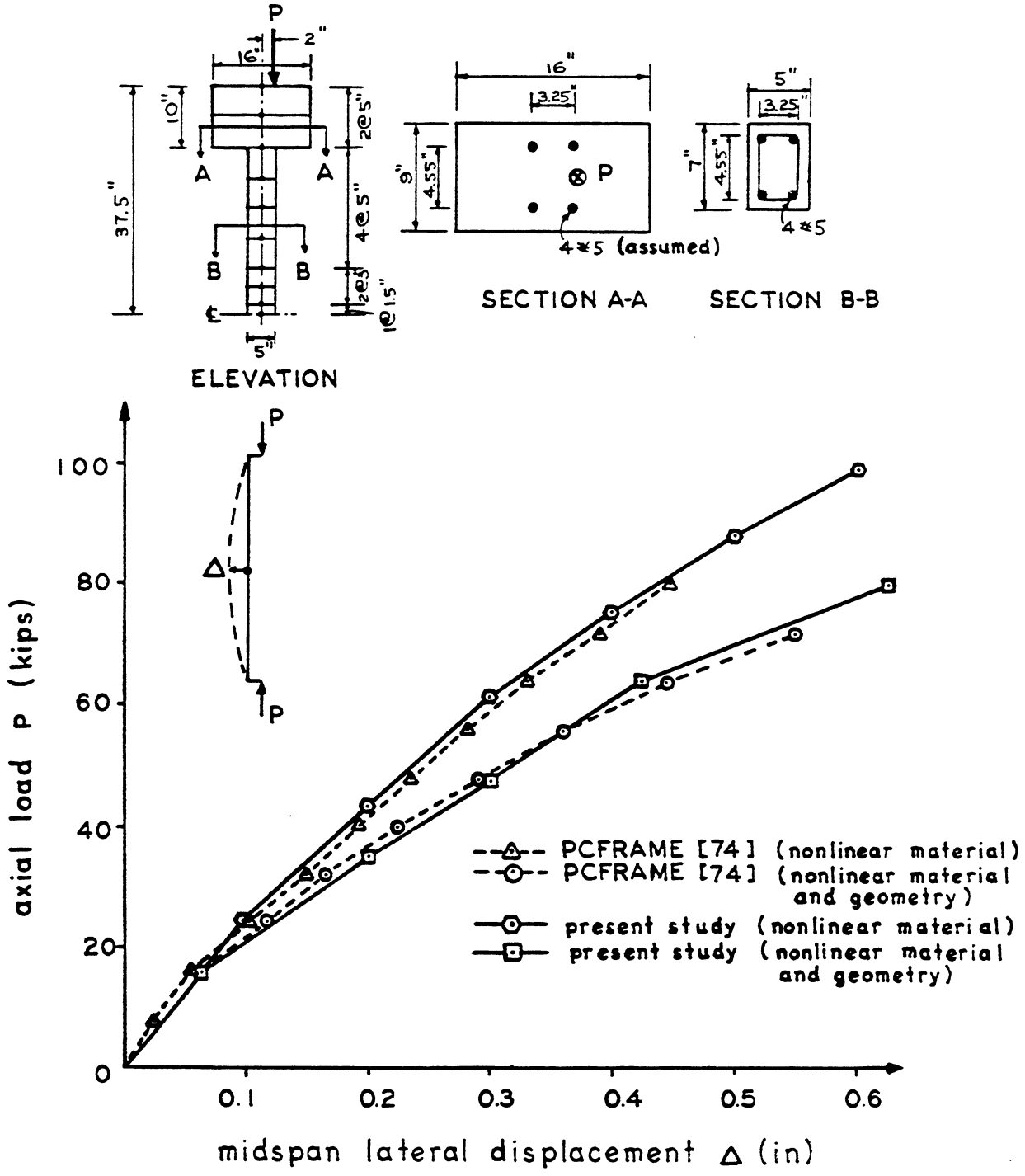

FIG. 10.11 SHORT TIME LOADING ON A REINFORCED CONCRETE COLUMN (EX. 10.3.3) - LOAD VS. MID-SPAN LATERAL DISPLACEMENT

the other axis.

The material properties are as follows:

Concrete		Steel	
E_o	$= 4.15 \times 10^3$ ksi	E_s	$= 30.6 \times 10^3$ ksi
f'_c	= 5.3 ksi	E_{sh}	= 0.0
f'_t	= 0.437 ksi	f_y	= 59.0 ksi
ν	= 0.0	ε_{su}	= 0.1

Tension stiffening is ignored.

For the analyses including creep and shrinkage, ACI recommendations for these effects are followed. The 3 months' sustained load period is divided into one time step.

For short time loading, the analyses for the cases where geometric nonlinearities are included and excluded are presented in Fig. 10.11. The results are compared with those obtained from the computer program PCFRAME [74] to test the reinforced concrete beam model. The slight discrepancy is due to the different concrete models used. The importance of the PΔ effect is particularly noted.

For the analyses including creep and shrinkage, both the cases with and without nonlinear geometry are included. The load-displacement responses are shown in Fig. 10.12, together with the experimental results of Hellesland et al [144]. In the experimental curve, the strain softening branch is deliberately excluded for clarity.

Good correlation between the experimental curve and the analytical curve is observed for the case where nonlinear geometry is included in the analysis. The present analysis gives an ultimate load of 77.0 k vs. the experimental load of 80.0 k. Failure is caused by cracking

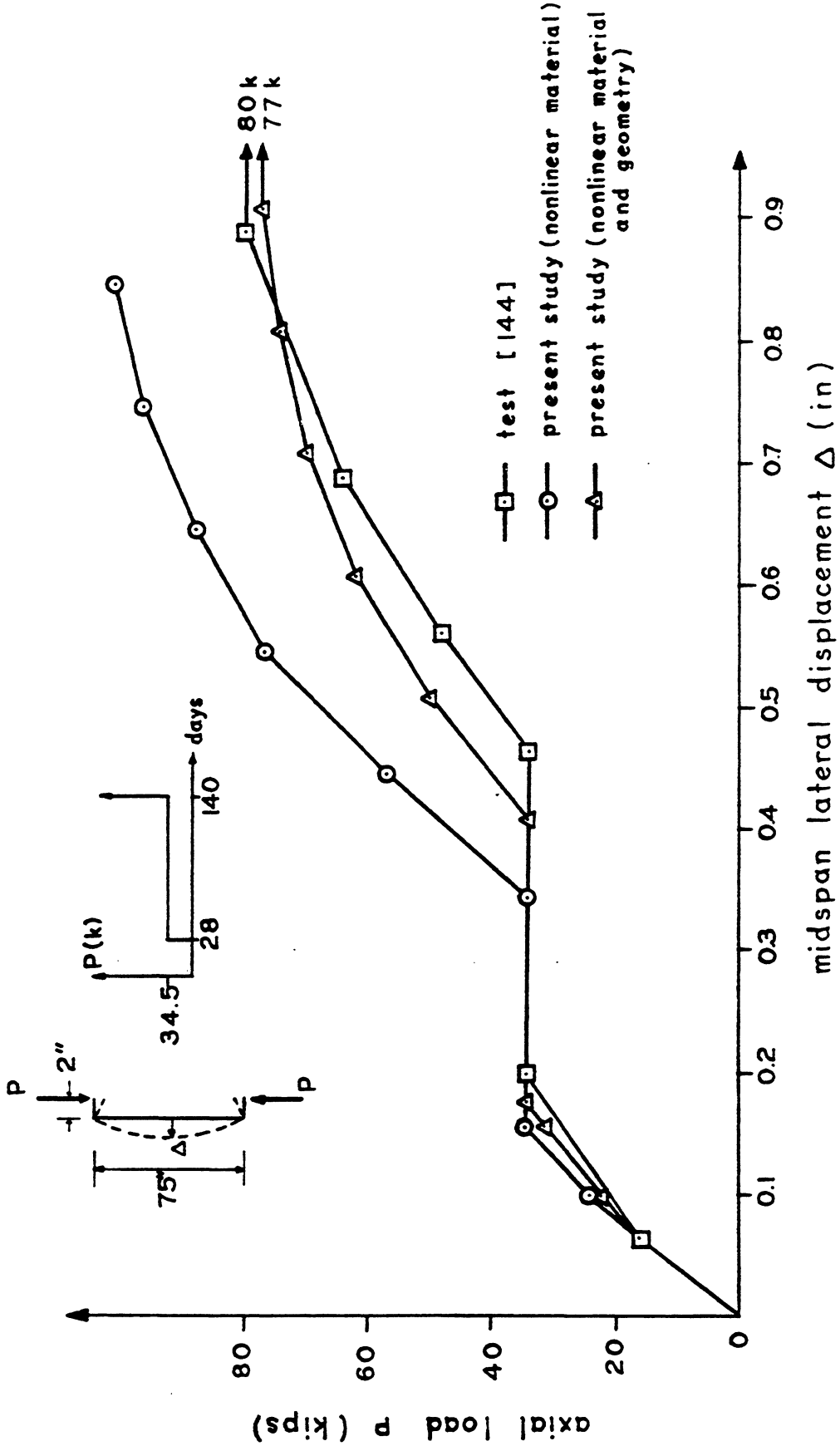

FIG. 10.12 SUSTAINED LOAD ON A REINFORCED CONCRETE COLUMN (EX. 10.3.3) - LOAD VS. MID-SPAN LATERAL DISPLACEMENT

in the concrete and yielding of the reinforcing steel.

However, when the change in geometry is not accounted for in the analysis, a much higher ultimate load will be predicted. At a load of 102.0 k, the maximum tensile stress in the steel is 36.8 ksi, indicating an ultimate strength well over 102.0 k should be anticipated for this case.

This example demonstrates the importance of including creep and shrinkage, and the nonlinear geometry in the prediction of the true load carrying capacity of a reinforced concrete column. The increase in lateral displacement due to creep and shrinkage of the concrete is further amplified by the PΔ effect and the column finally fails by yielding of the steel reinforcement.

The applicability of the present method of analysis to this example is well demonstrated.

10.3.4. Biaxial Bending of a Reinforced Concrete Column

One feature of the present beam element is its ability to handle problems in biaxial bending. It is the purpose of this example to demonstrate this capability and to study the effect of nonlinear geometry on columns with different slenderness ratios under short time loading.

A series of four hypothetical reinforced concrete columns loaded eccentrically in two directions is chosen for the present analysis, including both the material and geometric nonlinearities. They all have identical cross sections and reinforcement but different lengths.

The geometry, the reinforcement arrangement, and the material properties are shown in Fig. 10.13. The column lengths are 50 in., 100 in., 200 in., and 400 in.

Due to symmetry, one-half of the column is modelled by 8 equally

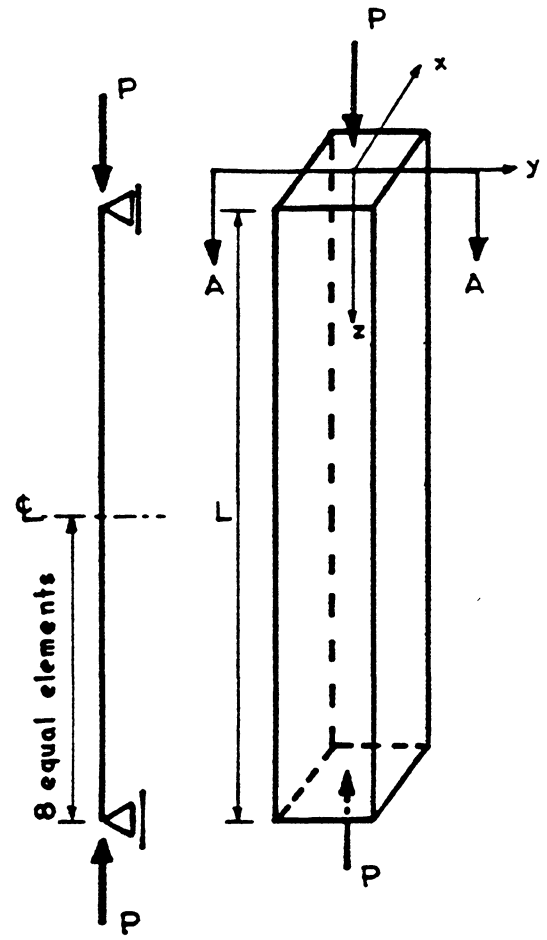

IDEALIZED STRUCTURE

ISOMERIC VIEW OF COLUMN

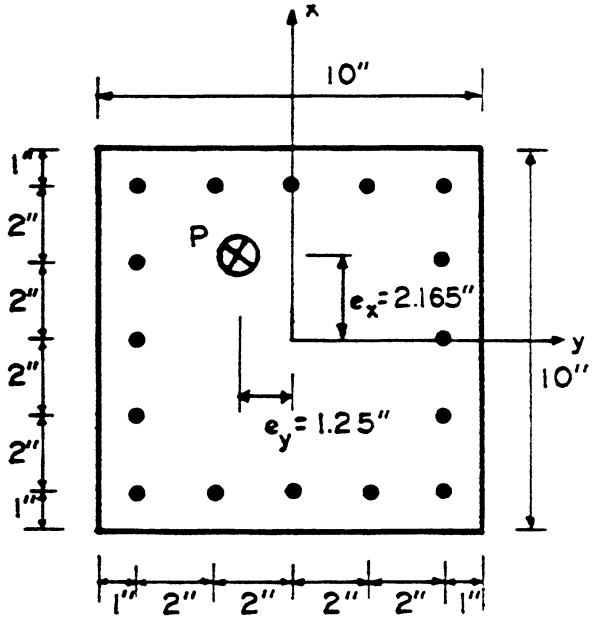

SECTION A-A

CONCRETE MATERIAL

f'_c = 4000 psi

f'_t = 10 psi

E_o = 3.6×10^6 psi

$\epsilon_c = 2.2 f'_c / E_o$

STEEL MATERIAL

f_y = 36600 psi

E_s = 30×10^6 psi

E_{sh} = 0.0

ignore tension stiffening effect

FIG. 10.13 BIAXIAL BENDING OF A REINFORCED CONCRETE COLUMN (EX. 10.3.4) - GEOMETRY AND MATERIAL PROPERTIES

sized beam elements. The cross section of the column is divided into 10 layers in each of the two directions, giving a total of 100 longitudinal filaments. Imposed deformations are again used to obtain the load-displacement response.

The resulting load-displacement curves are shown in Fig. 10.14 and are compared with those obtained by Warner [145], who assumes a cosine function for the deformed shape. It is observed that good agreement exists between the two solutions for short to intermediate columns having lengths of 50 in. and 100 in. For longer columns, L = 200 in., Warner [145] predicts a stiffer structure because the nonlinear geometry cannot be adequately accounted for by his assumed cosine deflected shape.

As can be seen in Fig. 10.14, the increase in column length decreases the ultimate load from 317 k for L = 50 in. to 111 k for L = 400 in. This represents a 65% decrease in strength for an 800% increase in slenderness ratio. However, it should be noted that when nonlinear geometry is not included in the analyses, the ultimate loads for all columns should be close to that of L = 50 in.

It is interesting to note that for the longer column, L = 400 in., the bifurcation load does not govern the design. The ratio of the ultimate load to the bifurcation load is 0.37. Indicating bifurcation analysis is on the unsafe side.

The progressive crack patterns for the column with L = 200 in. are shown in Fig. 10.15. It fails by yielding of the reinforcement and cracking and yielding of the concrete. It should be noted that the orientation of the plane of bending rotates, as indicated by the ratio u_x/u_y in Fig. 10.15, because of cracking and other material

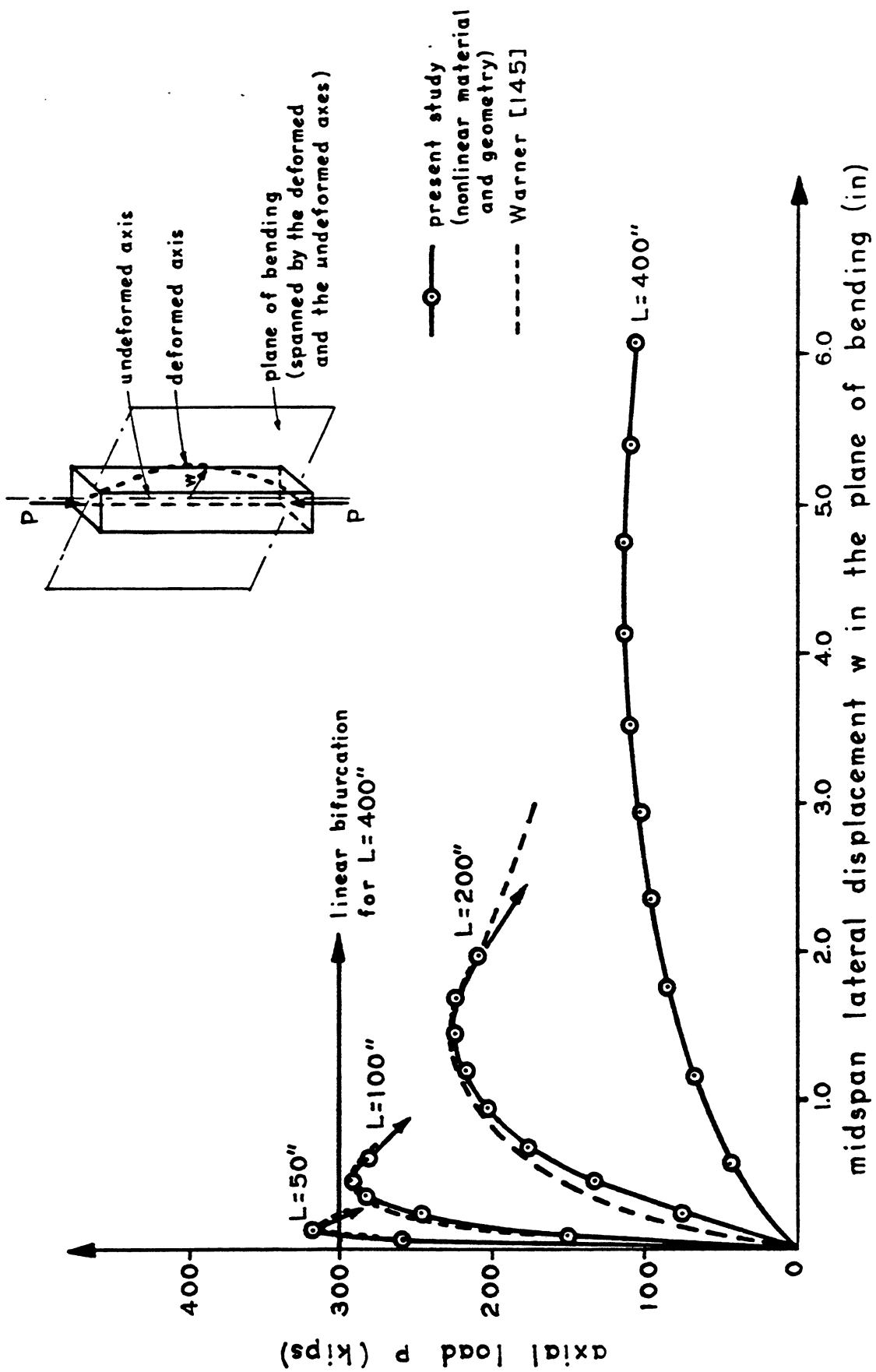

FIG. 10.14 BIAXIAL BENDING OF A REINFORCED CONCRETE COLUMN (EX. 10.3.4) - LOAD VS. LATERAL DISPLACEMENT w IN THE PLANE OF BENDING FOR DIFFERENT COLUMN LENGTHS

LOAD P (kips)	CRACK PATTERNS	DISPLACEMENT u_x (in)	DISPLACEMENT u_y (in)	u_x/u_y
75.3	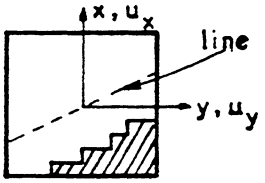	-0.2	0.119	-1.68
132.7	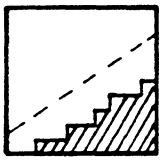	-0.4	0.241	-1.66
176.1	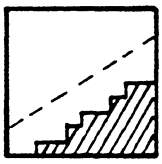	-0.6	0.367	-1.63
204.3		-0.8	0.501	-1.60
218.3		-1.0	0.647	-1.54
224.6	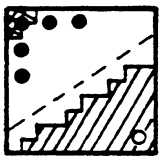	-1.2	0.796	-1.51
223.8	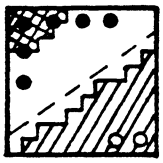	-1.4	0.957	-1.46

FIG. 10.15 BIAXIAL BENDING OF A REINFORCED CONCRETE COLUMN (EX. 10.3.4) - CRACK PATTERNS AT MID-LENGTH OF COLUMN WITH L = 200 IN.

nonlinearities. The total rotation of this plane is 4.4° at failure (P = 224 k). This rotation also induces a maximum torsional moment of 140 in.-lb. Similar behavior is observed for other columns.

A statical check has been carried out at the mid-length of the column. For the column length L = 200 in., and at a load of 224 k, the internal moments at the mid-length are:

$$M_{i_x} = 494 \text{ in.-k}$$

$$M_{i_y} = 798 \text{ in.-k}$$

The external moments are:

$$M_{e_x} = P \cdot e_y + P \cdot u_y = 280 + 214 = 494 \text{ in.-k}$$

$$M_{e_y} = P \cdot e_x - P \cdot u_x = 484 + 313 = 797 \text{ in.-k}$$

The above equilibrium check indicates the important contribution of the PΔ effect.

As a conclusion, the ultimate load analysis of long columns under biaxial bending can only be obtained by a fully nonlinear analysis, including both the effects of material and geometric nonlinearities. The time dependent effects of creep and shrinkage, although not included in the present analyses, should be investigated. Bifurcation analysis or an analysis including nonlinear material only will be on the unconservative side.

10.4 Reinforced Concrete Shells

In this last group of examples, a cylindrical shell and an HP gabled shell are analyzed. The two examples serve the purpose of verifying the present method of analysis in a complete system made up of shell elements and beam elements.

The important effects of the nonlinear geometry in a shell structure are demonstrated in the cylindrical shell example. The

time dependent effects of creep and shrinkage coupled with nonlinear material and geometry will be illustrated in the final comprehensive HP shell example.

10.4.1 Cylindrical Shell

A series of eleven cylindrical shells, simply supported at the two ends and constructued of reinforced concrete, have been tested by Bouma et al [146]. The shells are 1/8 scaled models of actual full scale structures, and they have identical cross sections and edge beams, but different span lengths and amounts of reinforcement. The loadings on the models are the roof load of 41 psf and a load of 33.6 lb/ft. on the edge beam, and an additional 25% of the roof load to account for the live load. The total load on the model is therefore 3360 lb. In the test, this load is proportionally increased until failure occurs.

In this example, the shell designated A2 in the test [146] is chosen. A linear analysis of the unreinforced shell is first performed to test the finite element model. Then nonlinear analyses are carried out to determine the nonlinear response and the ultimate load capacity of the shell.

1. Linear Analysis

The geometry of the shell is shown in Fig. 10.16. Due to symmetry, one-quarter of the shell is modelled by 6 shell elements and 6 beam elements, as shown in Fig. 10.17. The shell element is divided into 6 layers through the thickness while 10 layers are used for each of the two directions of the beam's cross section.

The loading on the model is scaled proportionally to obtain a reference load of 1.0 psi of the shell's surface and 7.87 lb/in. in the edge beam. The distributed load is replaced by the tributary

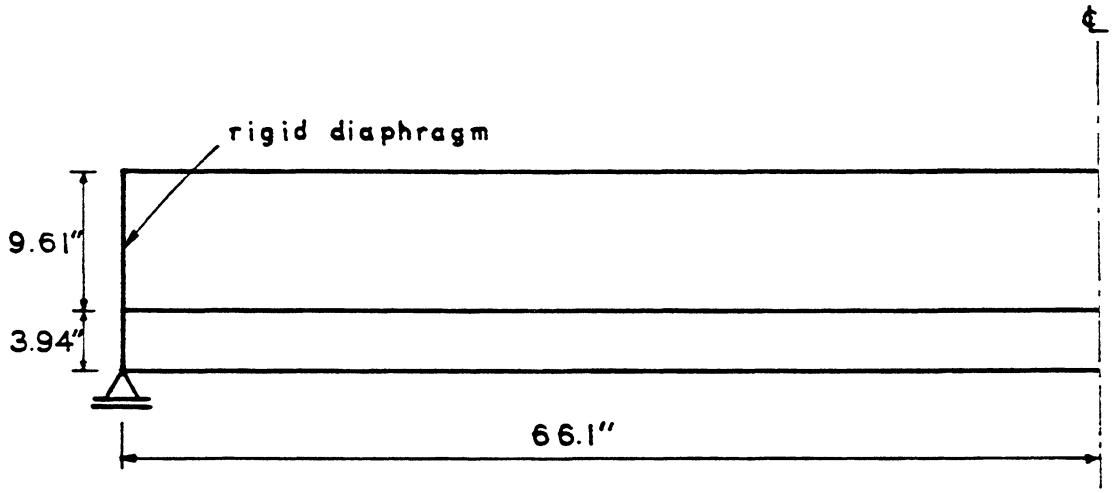

ELEVATION

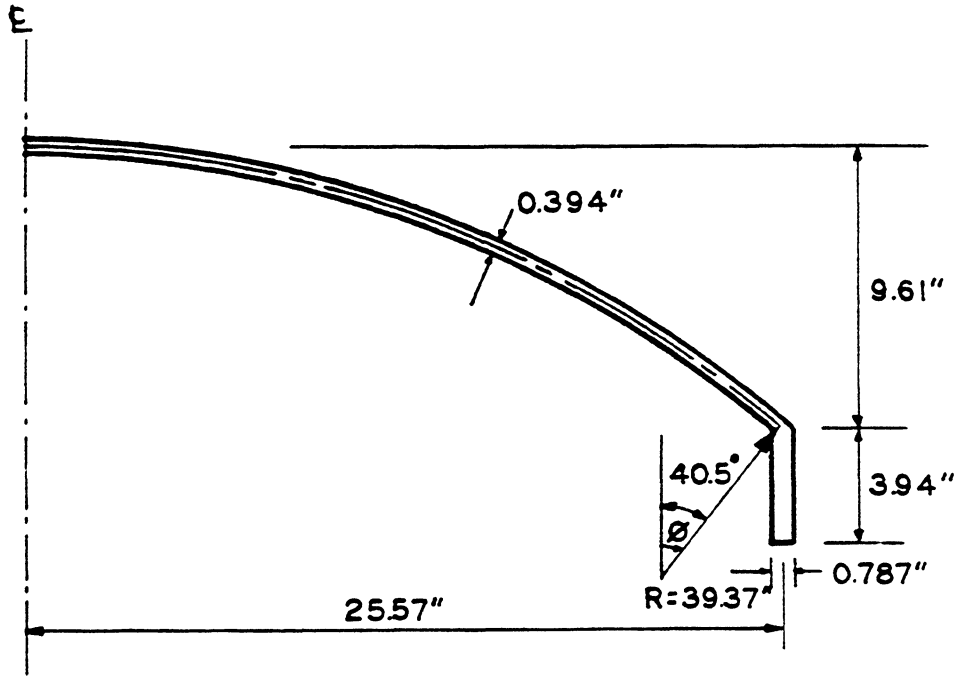

CROSS SECTION

FIG. 10.16 CYLINDRICAL SHELL (EX. 10.4.1) - GEOMETRY OF THE SHELL

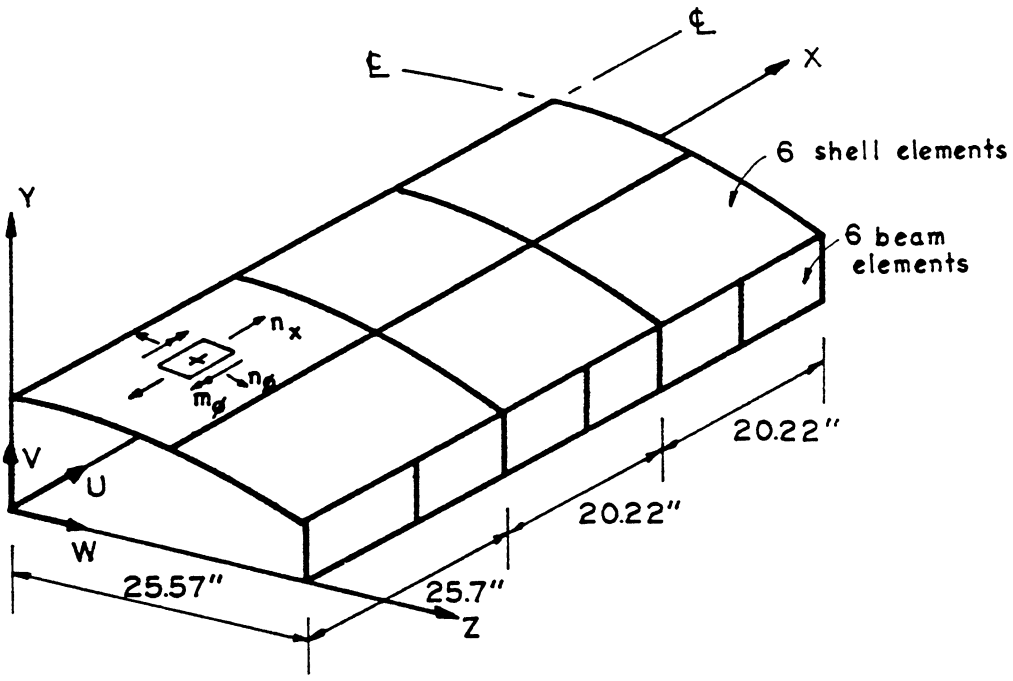

MESH LAYOUT AND +VE DIRECTION OF DISPLACEMENT AND FORCE

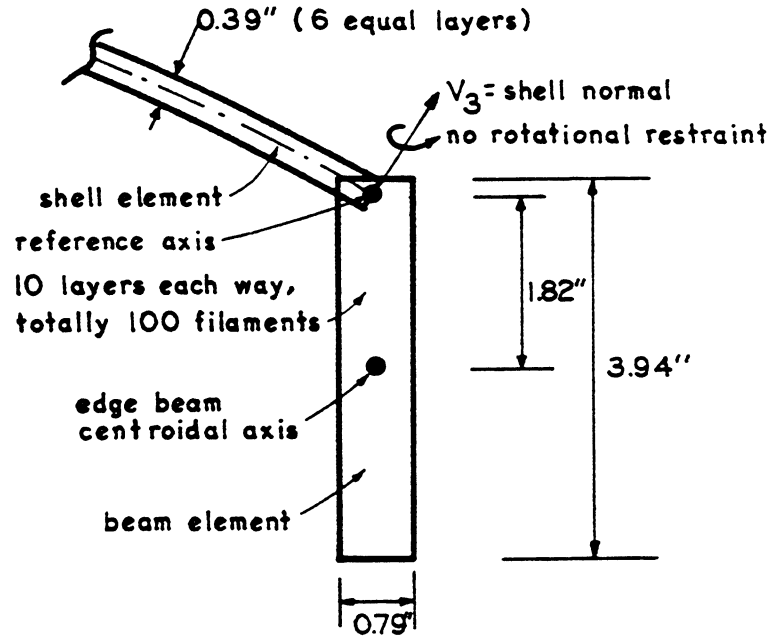

MODELLING OF ECCENTRIC EDGE BEAM

FIG. 10.17 CYLINDRICAL SHELL (EX. 10.4.1) - MESH LAYOUT AND THE MODELLING OF EDGE BEAM

nodal loads in the analysis.

The material properties of the shell are assumed to be:

$$E = 4.35 \times 10^3 \text{ ksi}$$

$$\nu = 0.3$$

The results are compared with those obtained from the computer program MULEL [108], which is based upon analytical solution using the Donnell-Jenkins equations for the shell and ordinary beam theory for the edge beam. The comparisons are presented in Fig. 10.18 to Fig. 10.20 for the displacements, membrane stress resultants in the shell, and the edge beam stress resultants at the reference axis. It can be seen that good agreement exists between the results of the present analysis and those from MULEL, even for the relatively coarse mesh used in the present study.

It should also be kept in mind that although the bending moments in the edge beams are continuous across adjacent beam elements at the locations where the forces are transferred to the beams, they are not continuous when the stress resultants are evaluated at some other locations because of the discontinuities in the axial forces. However, the moments at the mid-lengths of the beam elements are still close to the exact values.

In this example, the modelling of the composite shell-beam system by a non-composite system is proven to be satisfactory.

2. Nonlinear Analysis

The reinforced concrete shell is first analyzed including non-linear material alone and, secondly, including both material and geometric nonlinearities. Similar analyses have been made by Arnesen [15] by modelling the edge beam as concentric with the shell.

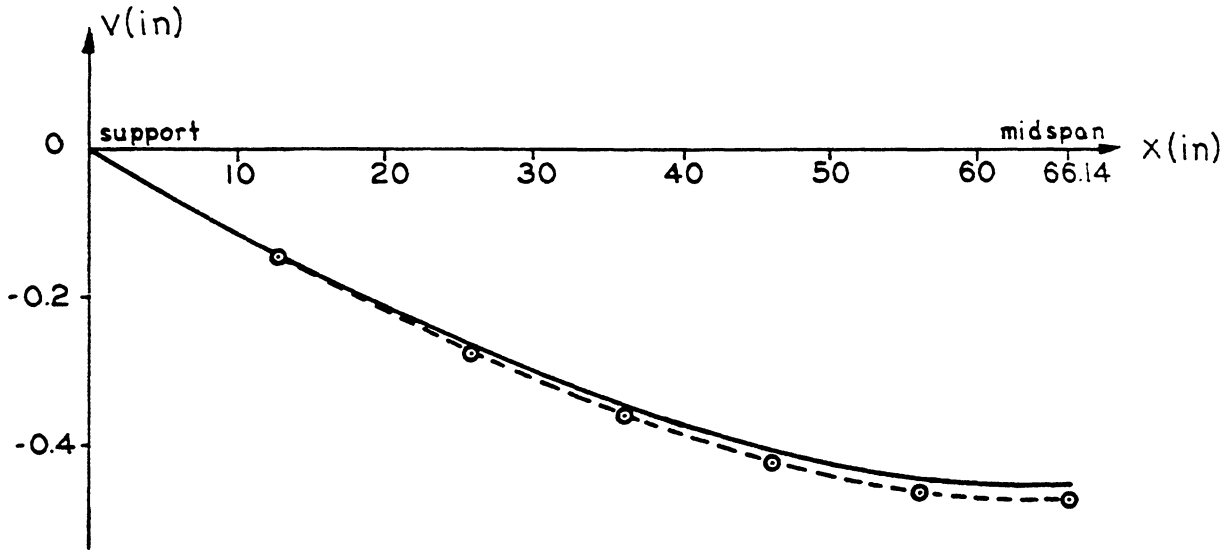

VERTICAL DISPLACEMENT V ALONG EDGE BEAM

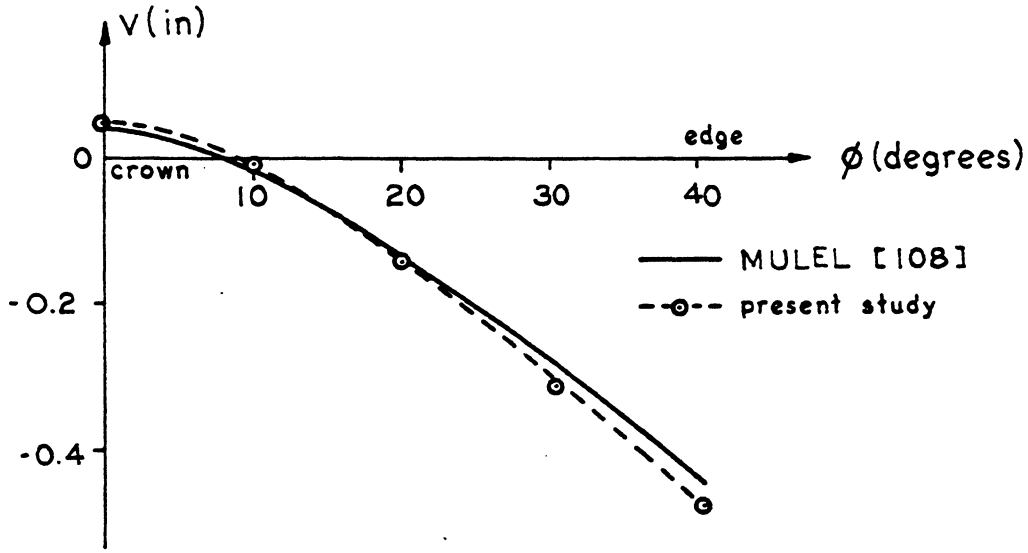

VERTICAL DISPLACEMENT V AT MIDSPAN

FIG. 10.18 CYLINDRICAL SHELL - LINEAR ANALYSIS (EX. 10.4.1) - DISPLACEMENT PROFILES FOR 1.0 PSI OF SHELL LOAD AND 7.87 LB/IN. IN THE EDGE BEAM

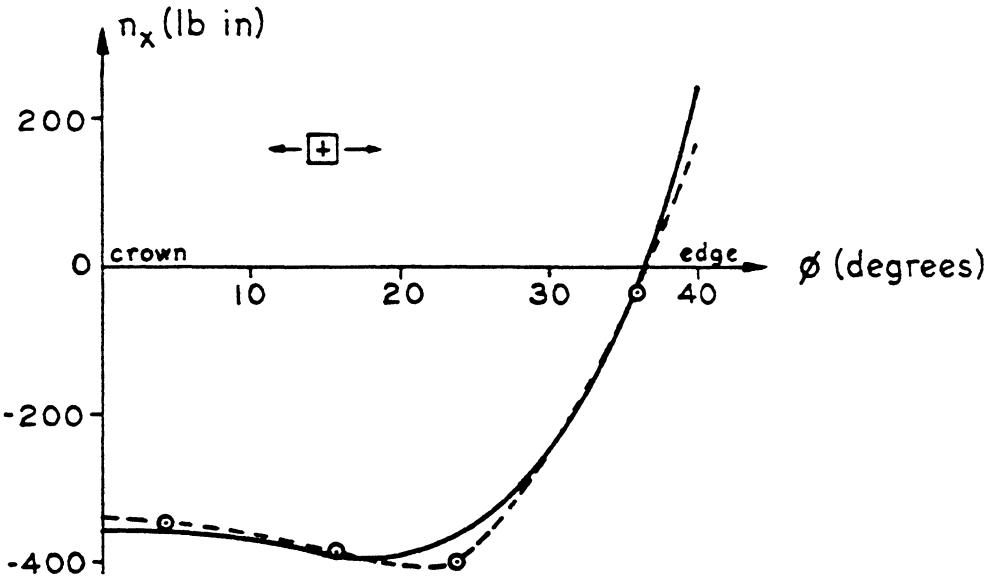

SHELL MEMBRANE FORCE n_x AT MIDSPAN

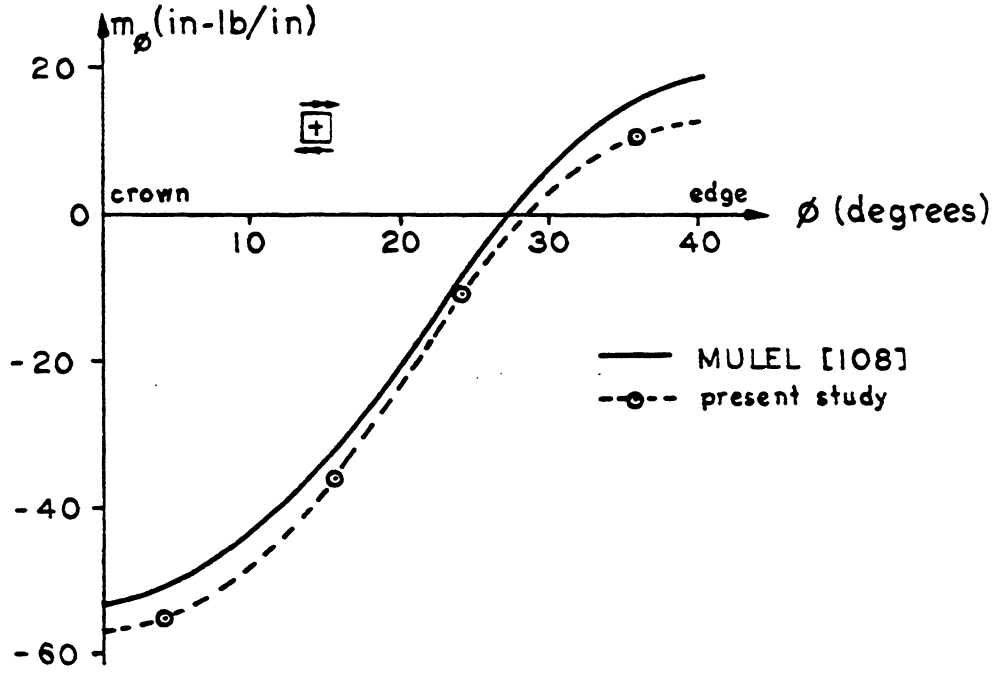

SHELL TRANSVERSE BENDING MOMENT $m_ø$ AT MIDSPAN

FIG. 10.19 CYLINDRICAL SHELL - LINEAR ANALYSIS (EX. 10.4.1) - SHELL STRESS RESULTANTS AT MID-SPAN FOR 1.0 PSI OF SHELL LOAD AND 7.87 LB/IN. IN THE EDGE BEAM

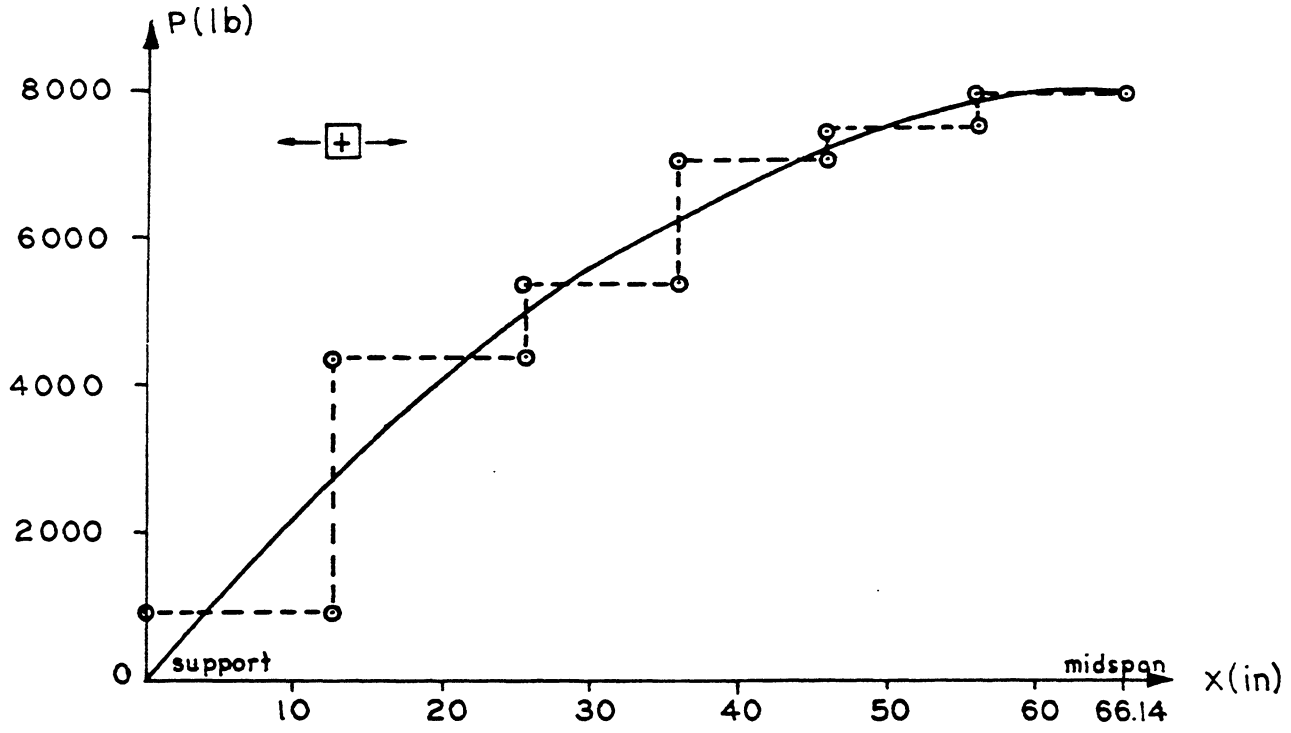

AXIAL FORCE P IN THE EDGE BEAM

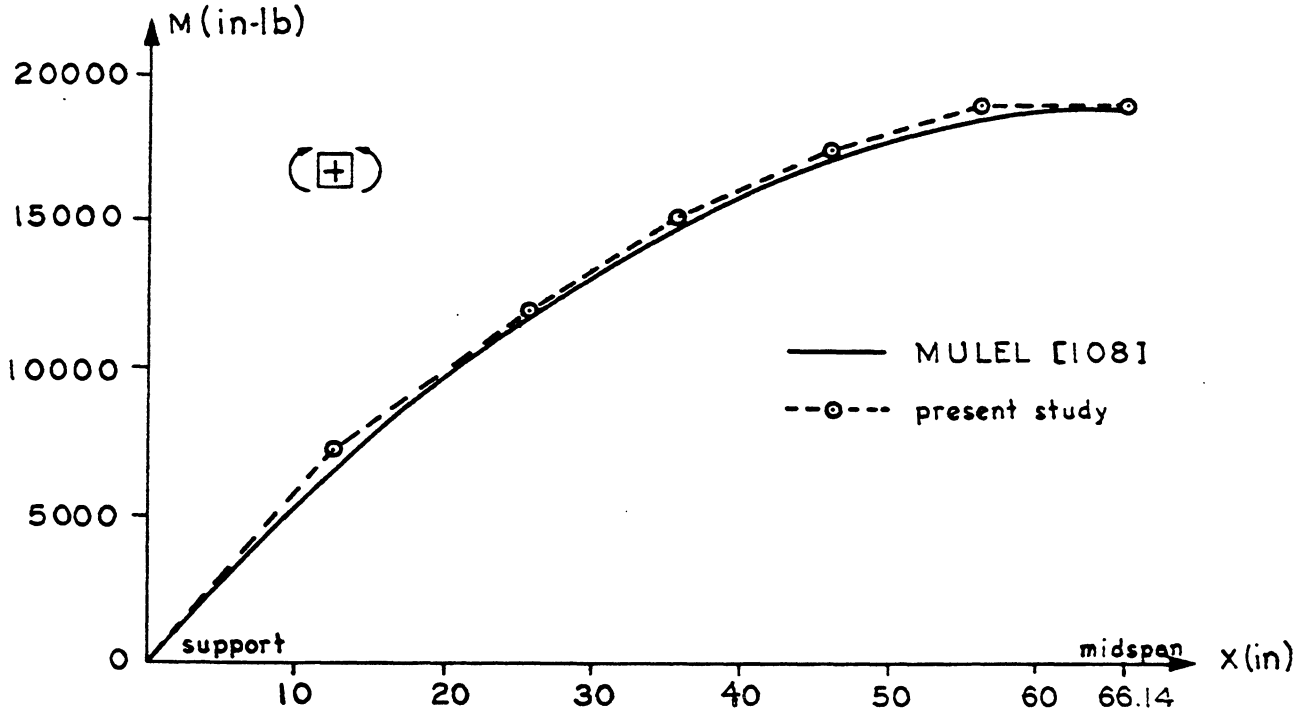

LONGITUDINAL BENDING MOMENT M ABOUT THE REFERENCE AXIS

FIG. 10.20 CYLINDRICAL SHELL - LINEAR ANALYSIS (EX. 10.4.1) - EDGE BEAM STRESS RESULTANTS ABOUT THE REFERENCE AXIS AT MID-SPAN FOR 1.0 PSI OF SHELL LOAD AND 7.87 LB/IN. IN THE EDGE BEAM

The same mesh layout used in the linear analysis is again used. The reinforcement details, as given in the paper [146], are shown in Fig. 10.21. The total steel area in the edge beam is replaced by 10 equally spaced steel filaments. No data is given regarding the hoop reinforcement in the edge beam, and it is therefore assumed here. The diagonal reinforcement layout is the same as that used by Arnesen [15].

The material data for the concrete and steel show a substantial scattering in the tests and the mean values are therefore adopted here. The material properties are summarized in the following:

Concrete		Steel	
E_o	$= 4.37 \times 10^3$ ksi	E_s	$= 29.9 \times 10^3$ ksi
f'_c	= 4.12 ksi	E_{sh}	= 0.0
f'_t	= 0.711 ksi	f_y	= 42.7 ksi
ν	= 0.3 (assumed)	ε_{su}	= 0.1
ε_c	$= 2\, f'_c/E_o$		
α	= 1.0		

Here, the cube strength and the modulus of rupture are used for f'_c and f'_t, respectively.

The tension stiffening effect is accounted for by increasing the steel stiffness. The tension stiffening factor described in Chapter 3 is used for the shell. However, they are arbitrarily scaled down by a factor of 0.325 in the edge beam to ensure that the post-cracking stiffness is smaller than the uncracked stiffness.

The material properties used by Arnesen [15] are slightly different. He used those listed on the following page.

The total steel area in the edge beam is 0.174 in^2 in the present analysis while Arnesen [15] used 0.197 in^2.

Concrete		Steel	
E_o	= 4.35×10^3 ksi	E_s	= 30.5×10^3 ksi
f'_c	= 4.35 ksi	E_{sh}	= 0.29×10^3 ksi
f'_t	= 0.65 ksi	f_y	= 42.8 ksi (shell)
ν	= 0.3	f_y	= 40.6 ksi (beam)
		f_u	= 53.7 ksi (shell)
		f_u	= 53.1 ksi (beam)

where f_u is the ultimate strength of the steel.

The resulting load-displacement response for the shell, obtained by an imposed vertical displacement increment of 0.1 in. for the edge beam at mid-span, is presented in Fig. 10.22, together with test results of Bouma et al [146] and the analytical results of Arnesen [15]. The agreement between the present analytical results and the tests are satisfactory for the case where nonlinear geometry is included.

The distinct increase in stiffness due to the increase in the T-C couple when nonlinear geometry is included is particularly noted. For the analysis including nonlinear material only, an ultimate load of 8.4 k is obtained. This is close to the value obtained from the beam theory. However, when nonlinear geometry is included in the analysis, an ultimate load of 10.2 k is obtained. This represents a 21% increase in strength over the case where nonlinear geometry is not considered.

The experimental ultimate load reported in [146] is 11.8 k. The ultimate load obtained in the present analysis is therefore 14% lower than the experimental value.

Investigating the mode of failure for the case where nonlinear geometry is included indicates that the shell sustained initial yielding of the longitudinal steel causing larger displacements and

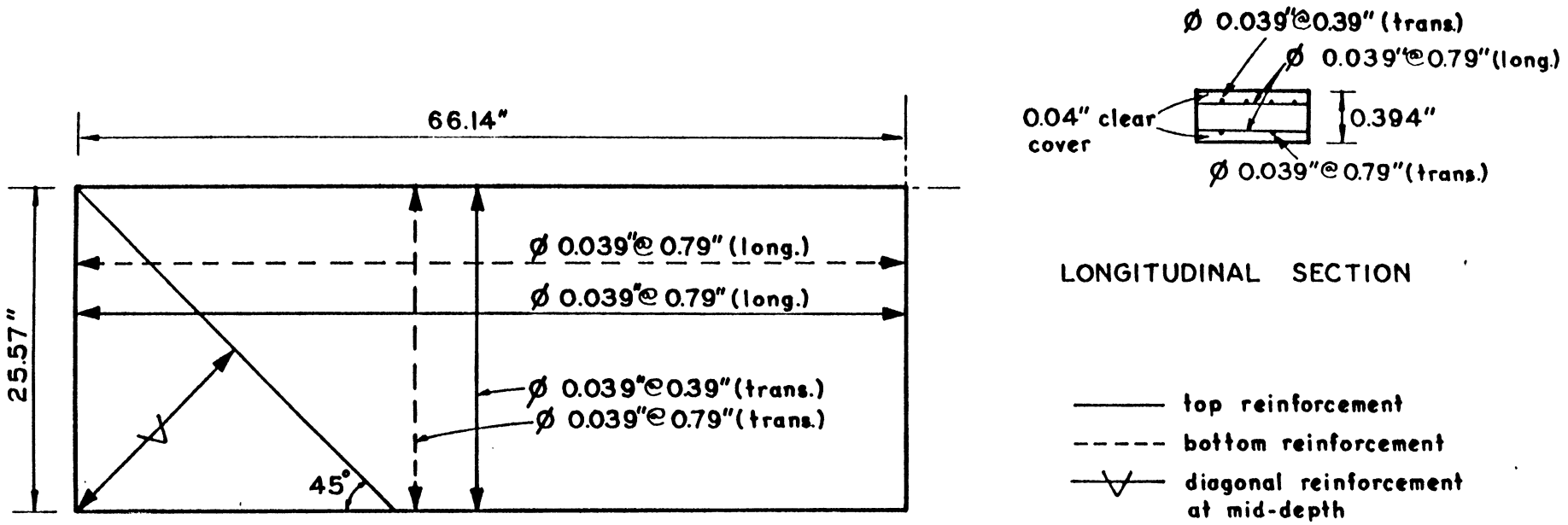

FIG. 10.21 CYLINDRICAL SHELL - NONLINEAR ANALYSIS (EX. 10.4.1) - REINFORCEMENT LAYOUT FOR THE SHELL AND THE EDGE BEAM

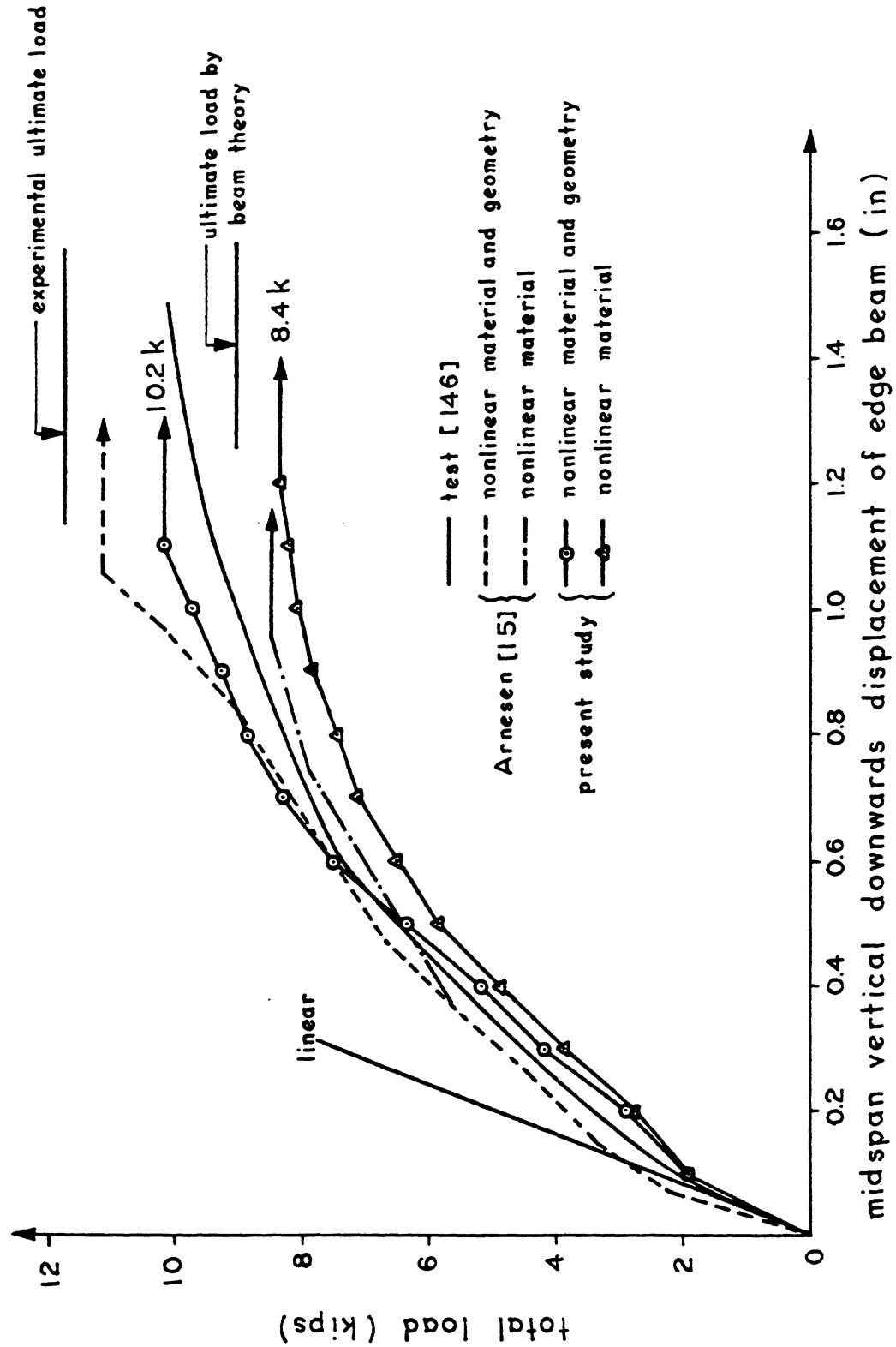

FIG. 10.22 CYLINDRICAL SHELL - NONLINEAR ANALYSIS (EX. 10.4.1) - LOAD VS. MID-SPAN EDGE BEAM VERTICAL DISPLACEMENT

more cracking and then finally failed in diagonal tension near the supporting points. The crack patterns are shown in Fig. 10.23.

This failure mode suggests that a more refined steel stress-strain relationship has to be used in order to obtain a better correlation in the ultimate load range. The modelling of the steel reinforcement as an elasto-plastic material is insufficient in this case.

A plot of the total load vs. the tensile forces at mid-span is shown in Fig. 10.24. The smaller tensile forces for the same external load is noted for the analysis with nonlinear material and geometry. This decrease in the tensile forces is due to the increase in the moment arm due to the change in geometry of the structure.

At a total load of 8.4 k, which corresponds to the ultimate load of the shell when nonlinear geometry is excluded, the tensile force, T_1, at mid-span is 14.8 k. The moment arm, d, can be found by assuming T_1 to be at the centroid of the edge beam.

$$d = \frac{M_e}{T_1} = 9.38 \text{ in.}$$

where M_e is the external moment in equilibrium with the T-C couple produced by T_1.

When the change in geometry is considered, an increase in moment arm of $\Delta = 0.76$ in. is obtained. The tensile force in this case is decreased to T_2:

$$T_2 = \frac{M_e}{(d+\Delta)} = 13.7 \text{ k}$$

which is in good agreement with the analysis including nonlinear geometry which gives a tensile force of 13.5 k.

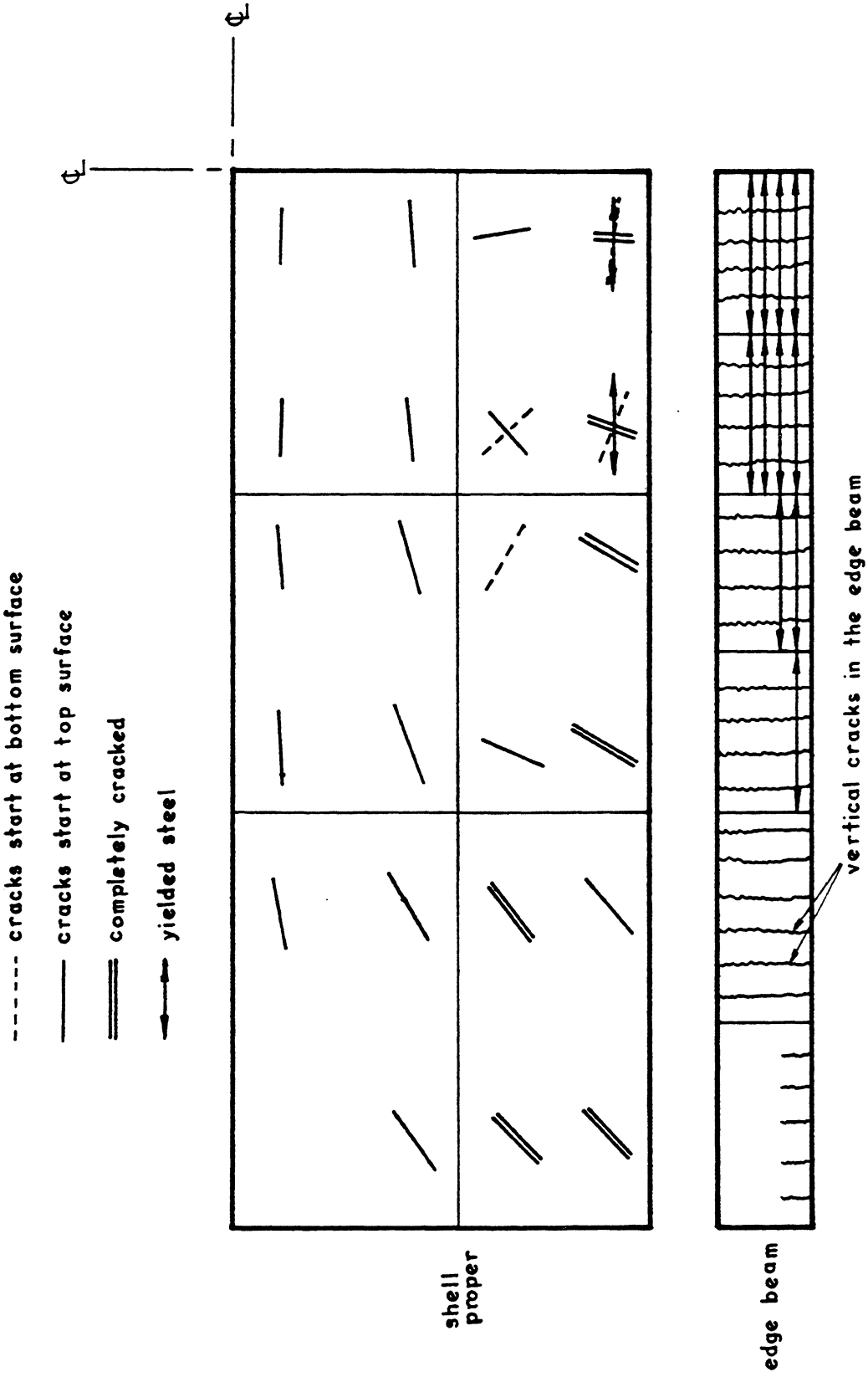

FIG. 10.23 CYLINDRICAL SHELL - ANALYSIS WITH NONLINEAR MATERIAL AND GEOMETRY (EX. 10.4.1) - CRACK PATTERN AT A TOTAL LOAD OF 10.2k

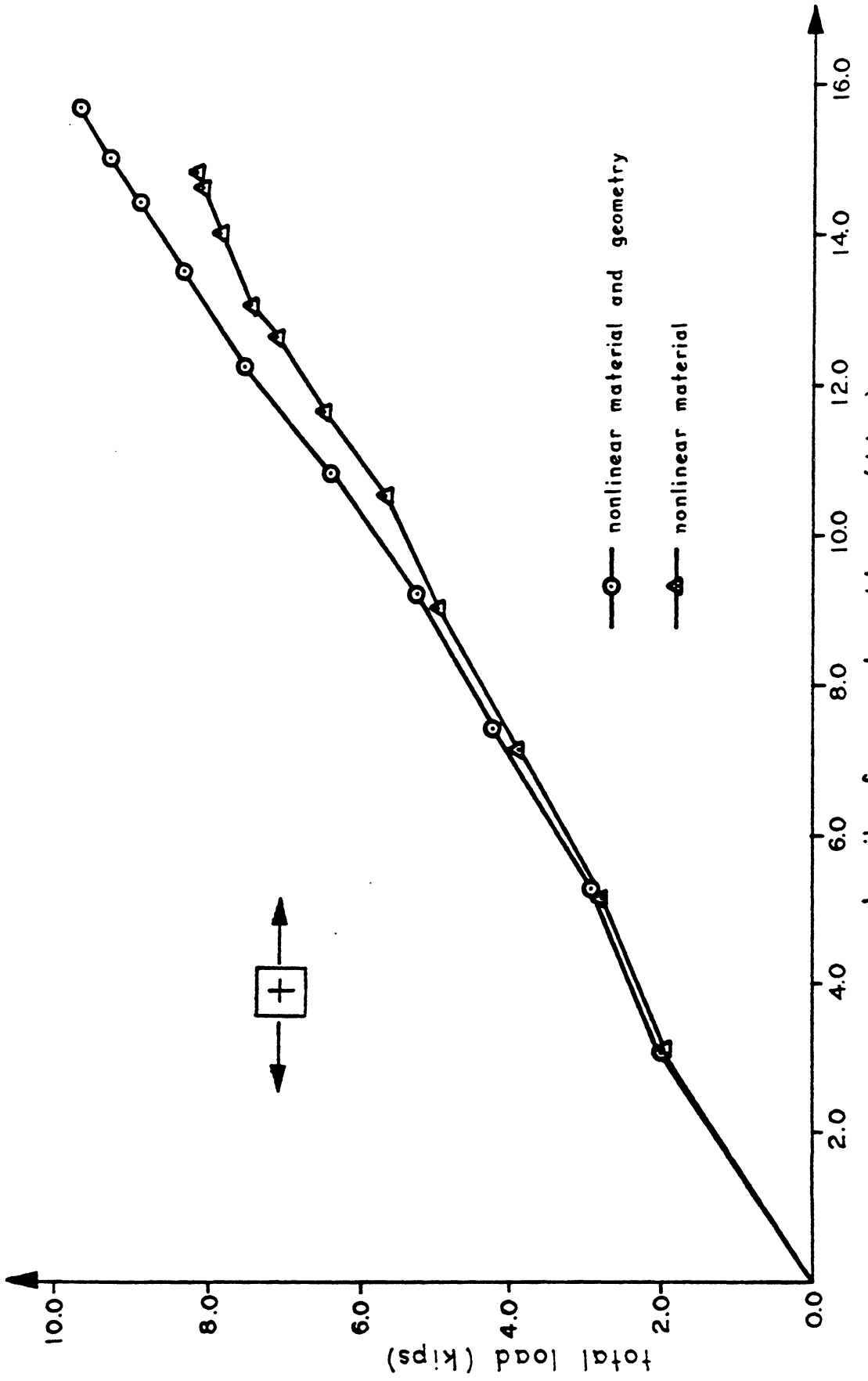

FIG. 10.24 CYLINDRICAL SHELL - NONLINEAR ANALYSIS (EX. 10.4.1) - LOAD VS. LONGITUDINAL TENSILE FORCE AT MID-SPAN

A statical check has also been carried out at mid-span, for the case where nonlinear geometry is included, at a load of 9.7 k just before the shell fails. Taking into account the deformed geometry, the results are:

Tensile force	=	7.86 k
Compressive force	=	-7.97 k
External Moment	=	80.6 in-k
Internal Moment	=	80.4 in-k

The agreements are good to within 1%.

In this example, the importance of including the change in geometry in the analysis of a cylindrical shell is demonstrated. The ultimate load analysis also requires a more refined material model for the steel reinforcement to get even better agreement with the experimental result.

10.4.2 Gabled HP Shell

In this example, a gabled HP shell is analyzed to determine its response behavior under the influence of dead and live loads on the shell. The importance of the nonlinear geometry and of the creep and shrinkage effects are demonstrated.

The geometry of the gabled HP shell used in the present example is shown in Fig. 10.25. The shell spans 80 ft. and has a rise of 8 ft. and a constant thickness of 3 in. The size of the crown beams and the edge beams are, respectively, B x H and b x h.

Linear analyses on a series of such HP shells with different crown beam sizes have been reported by Schnobrich [118] and Kabir [11]. In Kabir's analyses, he assumes the crown beams and the edge beams to be concentric with the shell, and they are modelled by triangular flat

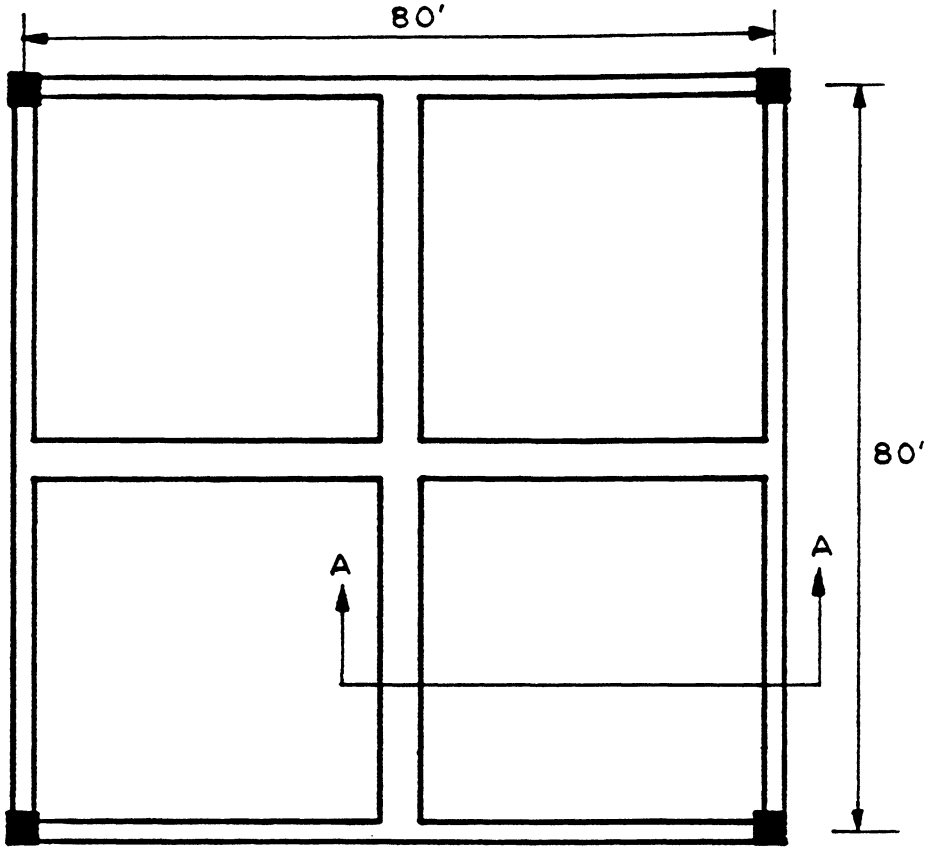

PLAN VIEW

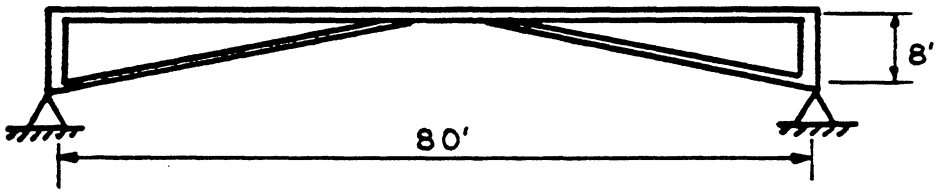

ELEVATION

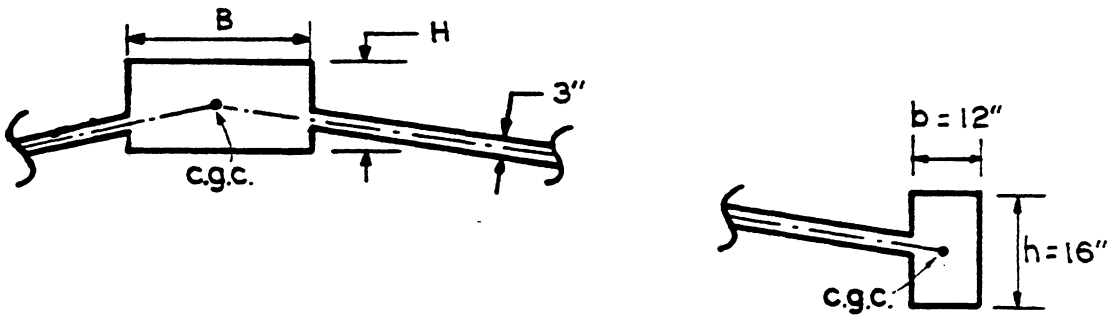

SECTION A-A

FIG. 10.25 HP GABLED SHELL (EX. 10.4.2) - GEOMETRY OF THE GABLED HP SHELL

shell elements. On the other hand, Schnobrich assumes the crown beams to be placed eccentrically above the shell and the crown beams and the edge beams are modelled by a higher order beam element which has a displacement field compatible with the shell element he has used.

In this example, a linear analysis for the total dead load on the shell is first carried out to verify the present finite element model of the HP shell. Then a nonlinear analysis for dead load and multiples of live load of 20 psf on the horizontal projection of the shell is performed to determine its ultimate load capacity under short time loading. Finally, the nonlinear behavior of the gabled HP shell including creep and shrinkage effects is investigated. The modes of failure and the ultimate load capacity of the shell for different nonlinear analyses are then compared. Design recommendations are then drawn based upon the results of the present analyses.

1. Linear Analysis

Linear analyses for the shell subjected to dead load are performed for two shells which have equally sized edge beams with b = 12 in. and h = 16 in. The crown beam sizes, on the other hand, are different. Their dimensions (B x H) are, respectively, 24 x 8 in. and 48 x 12 in.

The analysis is first carried out for the shell with the smaller crown beam (B x H = 24 x 8 in.) and, secondly, for the one with the larger crown beam (B x H = 48 x 12 in.).

The mesh layout for the present analysis is shown in Fig. 10.26. Due to symmetry, only one-quarter of the shell is modelled.

Only the dead load of the shell and those of the crown and the edge beams are considered. Consistent nodal forces are used.

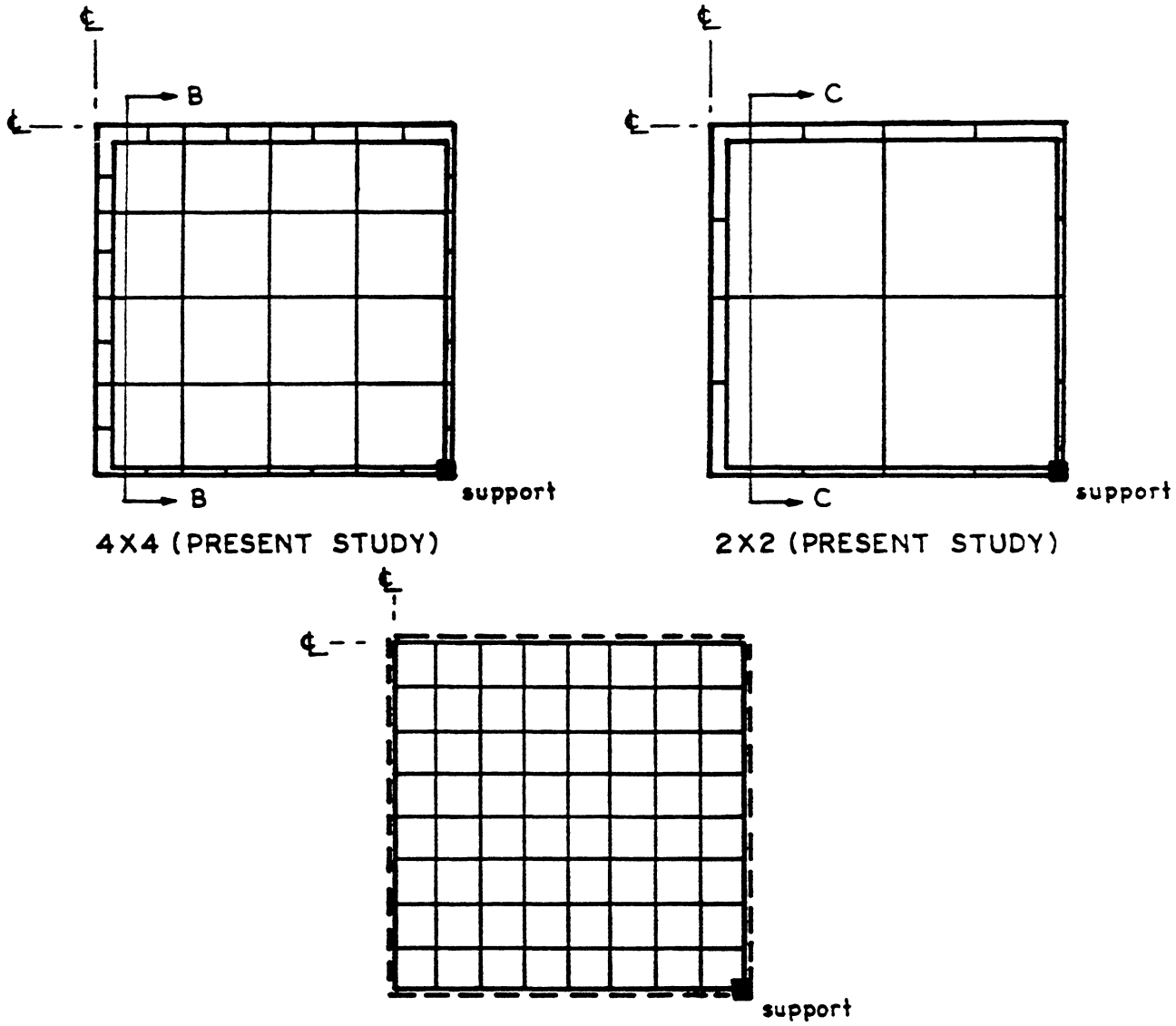

(a) MESH LAYOUT FOR THE GABLED HP SHELL

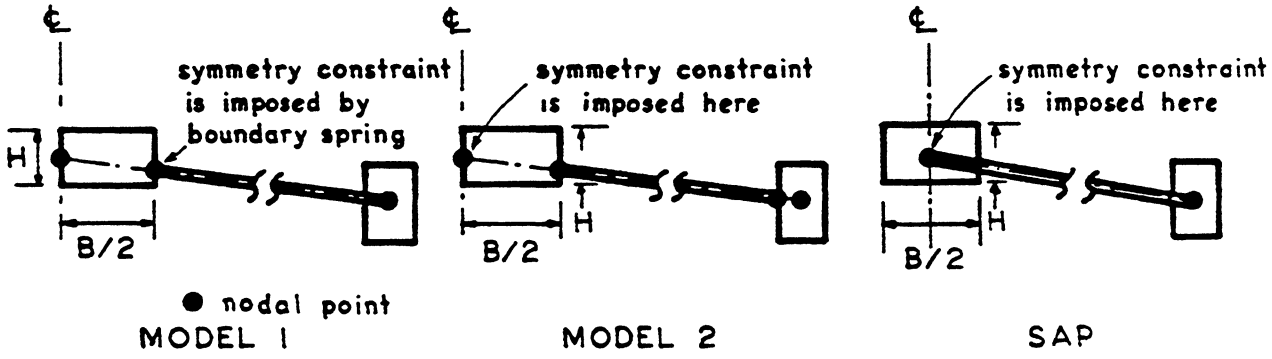

(b) MODELLING OF THE EDGE AND CROWN BEAMS

FIG. 10.26 HP GABLED SHELL (EX. 10.4.2) - MESH LAYOUT AND THE MODELLING OF THE EDGE AND THE CROWN BEAMS

In an attempt to model the crown beam's weight distribution as closely as possible, the crown beam is modelled in two different ways, shown as Model 1 and Model 2 in Fig. 10.26.

In Model 1, the stiffness of the crown beam is transformed to the shell element's degrees of freedom and the symmetry constraint is imposed by the use of boundary spring elements.

In Model 2, the stiffness of the shell is transformed to the degrees of freedom of the beam and the symmetry constraint is imposed by striking out the corresponding rows and columns in the assembled stiffness matrix.

The material properties for the two shells are:

$$E_o = 3.0 \times 10^3 \text{ ksi}$$

$$\nu = 0.15$$

The results for the linear analysis of the shell due to the total dead load with the smaller crown beam are shown in Fig. 10.27 to Fig. 10.31. The agreement between the results of the present analysis and those of Kabir [11] and Schnobrich [118] are good. Furthermore, it is noted that modelling the crown beam as Model 1 or Model 2 gives very little difference in the results.

These indicate that the response is insensitive to the different crown beam models for this shell with a 24 x 8 in. crown beam.

For the shell with the larger crown beam (B x H = 48 x 12 in.), the results of the present analysis with the crown beam Model 2 compare well with those from SAP [138] with an 8 x 8 mesh of the shell (Fig. 10.26). Selected results are shown in Fig. 10.32 to Fig. 10.35.

The important influence of the crown beam's weight and its distribution on the overall behavior of the shell is particularly noted.

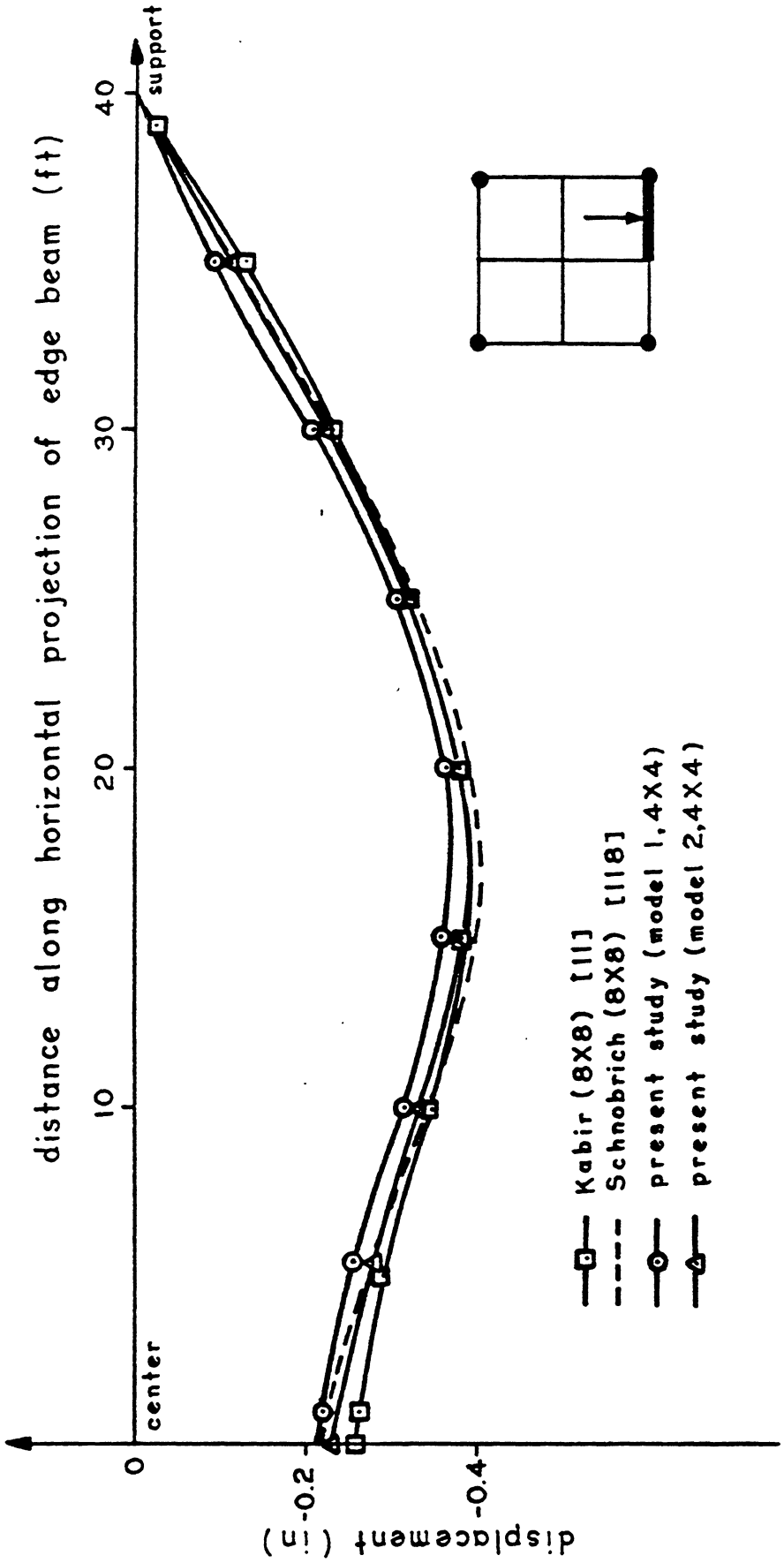

FIG. 10.27 HP GABLED SHELL - LINEAR ANALYSIS (EX. 10.4.2) - VERTICAL EDGE BEAM DISPLACEMENT (+ve UPWARDS) DUE TO TOTAL DEAD LOAD ONLY (B x H = 24 x 8 in.)

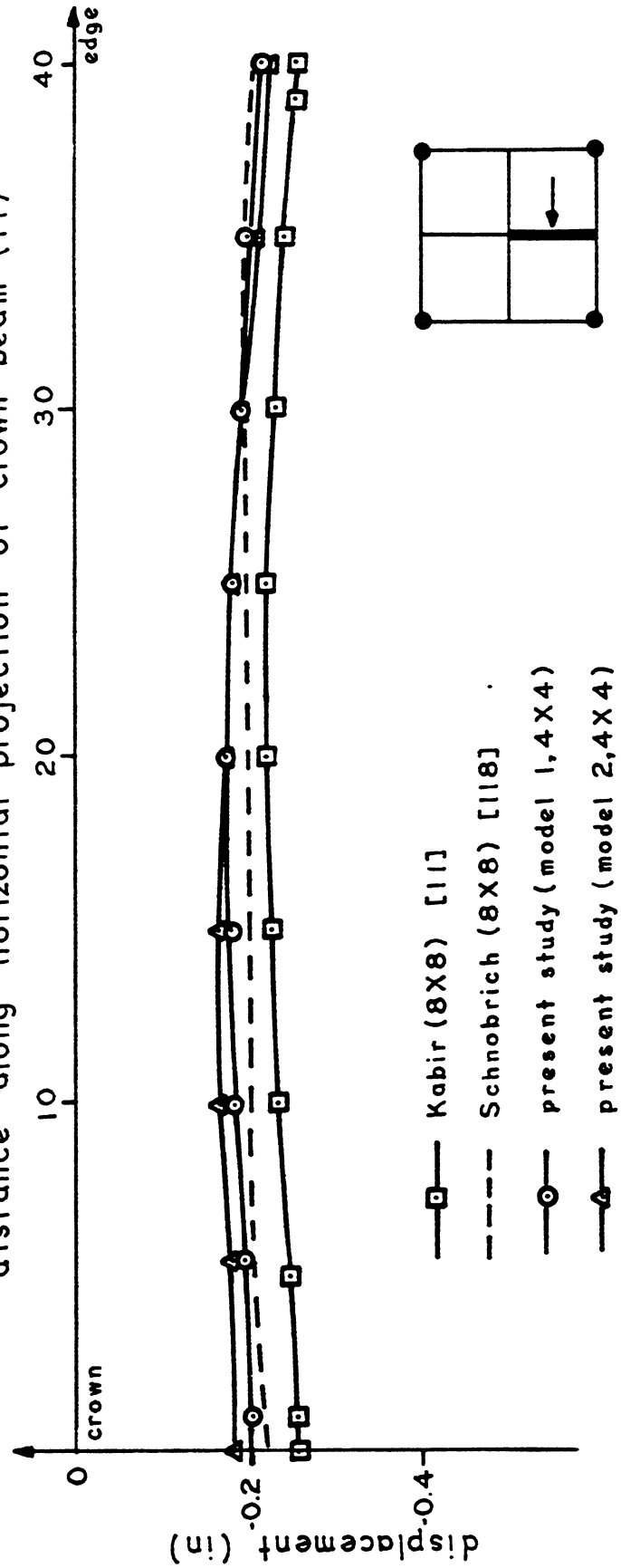

FIG. 10.28 HP GABLED SHELL - LINEAR ANALYSIS (EX. 10.4.2) - VERTICAL CROWN BEAM DISPLACEMENT (+ve UPWARDS) DUE TO TOTAL DEAD LOAD ONLY (B x H = 24 x 8 in.)

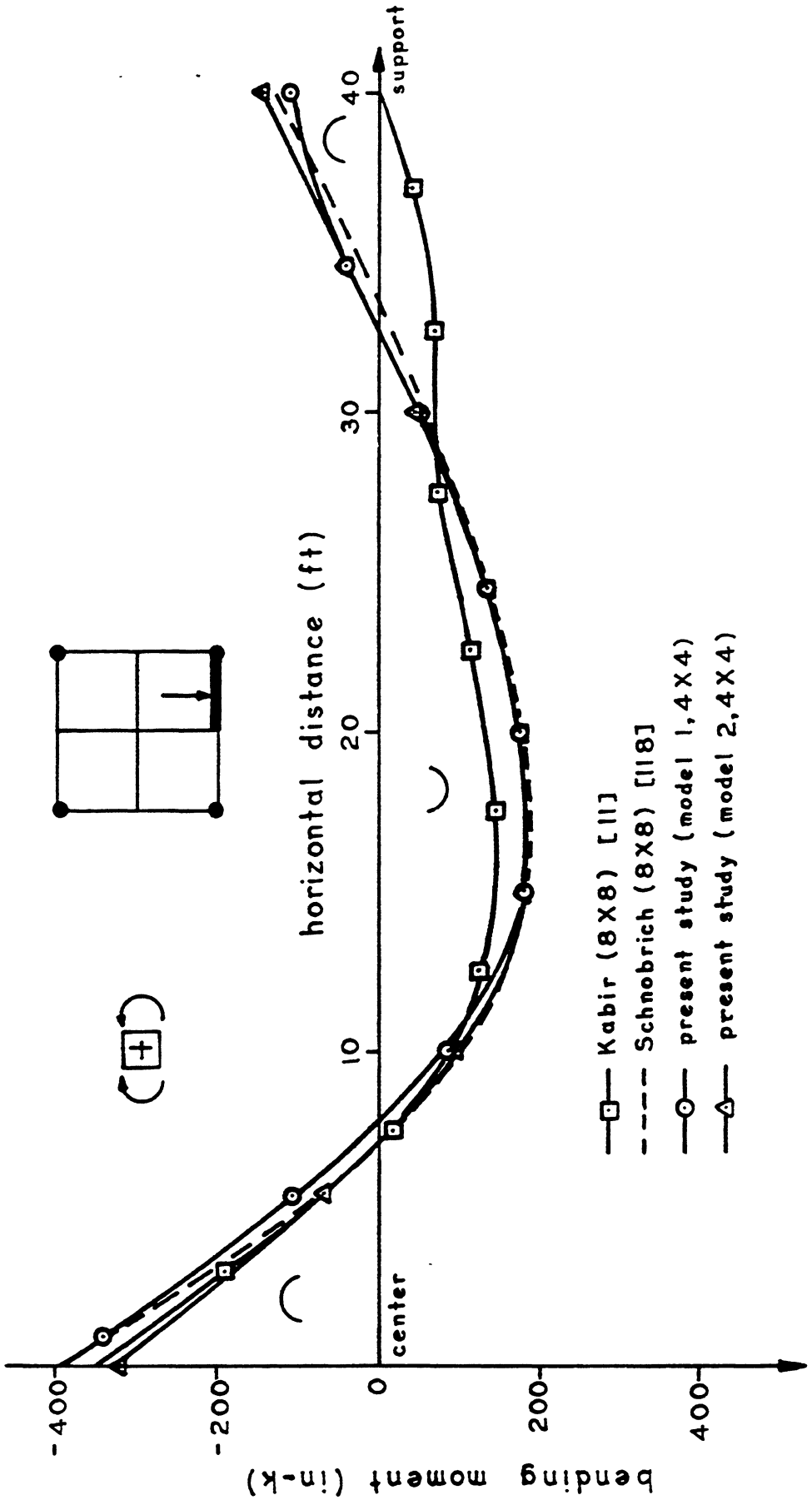

FIG. 10.29 HP GABLED SHELL - LINEAR ANALYSIS (EX. 10.4.2) - BENDING MOMENT IN THE EDGE BEAM DUE TO TOTAL DEAD LOAD ONLY (B x H = 24 x 8 in.)

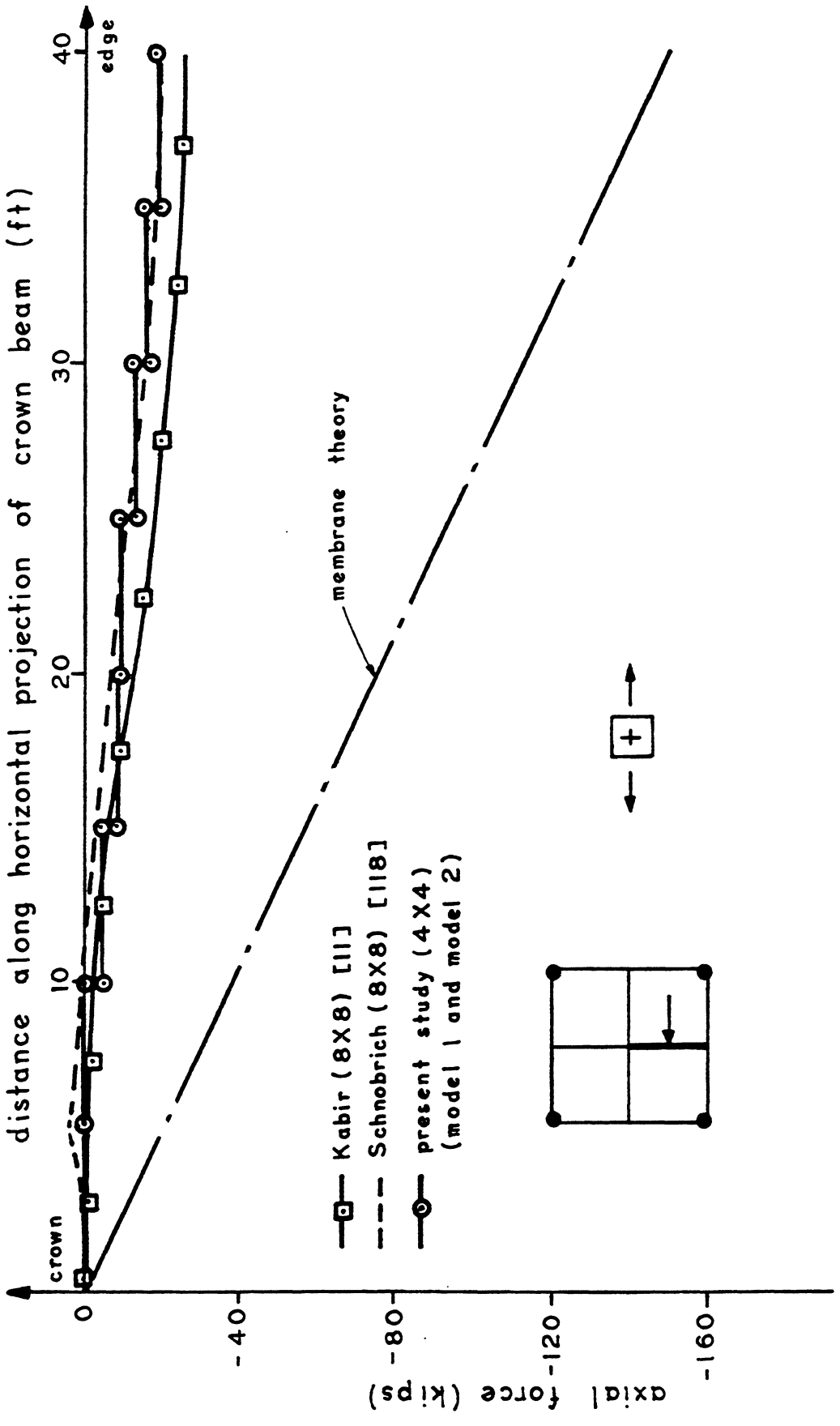

FIG. 10.30 HP GABLED SHELL - LINEAR ANALYSIS (EX. 10.4.2) - AXIAL FORCE IN THE CROWN BEAM DUE TO TOTAL DEAD LOAD ONLY (B x H = 24 x 8 in.)

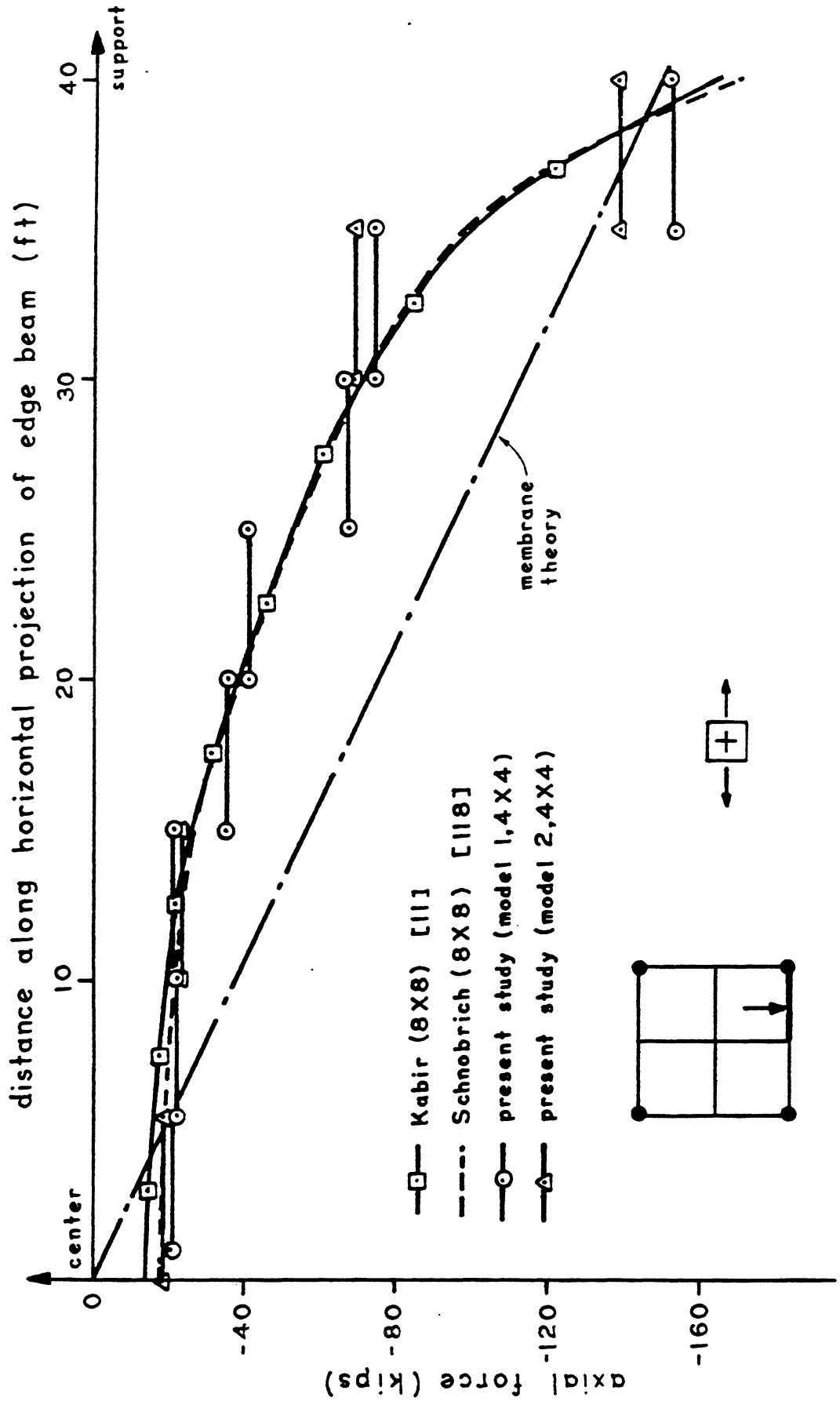

FIG. 10.31 GABLED HP SHELL - LINEAR ANALYSIS (EX. 10.4.2) - AXIAL FORCE IN THE EDGE BEAM DUE TO TOTAL DEAD LOAD ONLY ($B \times H = 24 \times 8$ in.)

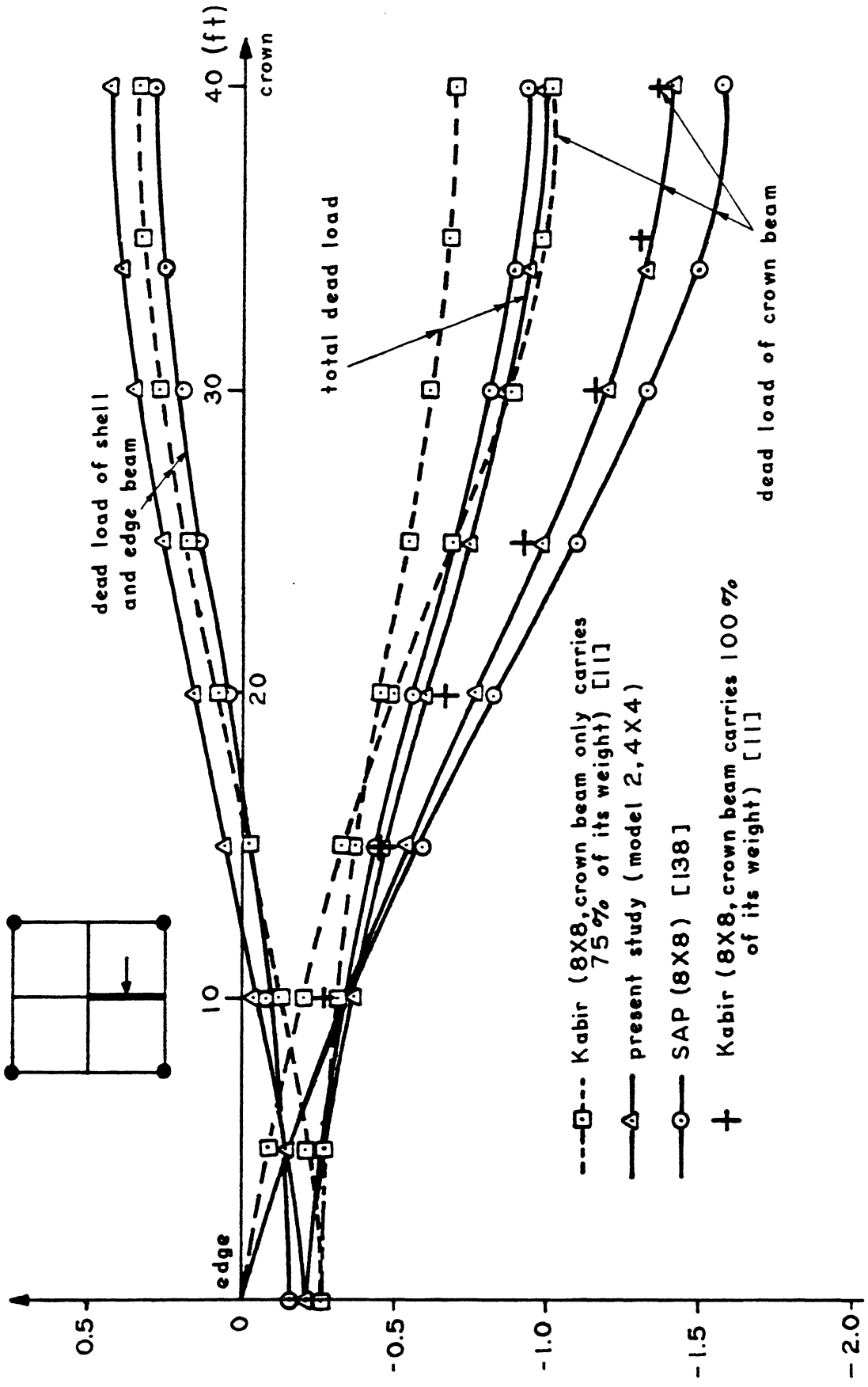

FIG. 10.32 GABLED HP SHELL - LINEAR ANALYSIS (EX. 10.4.2) - VERTICAL CROWN BEAM DISPLACEMENT (+ve UPWARDS) DUE TO VARIOUS DEAD LOADS (B x H = 48 x 12 in.)

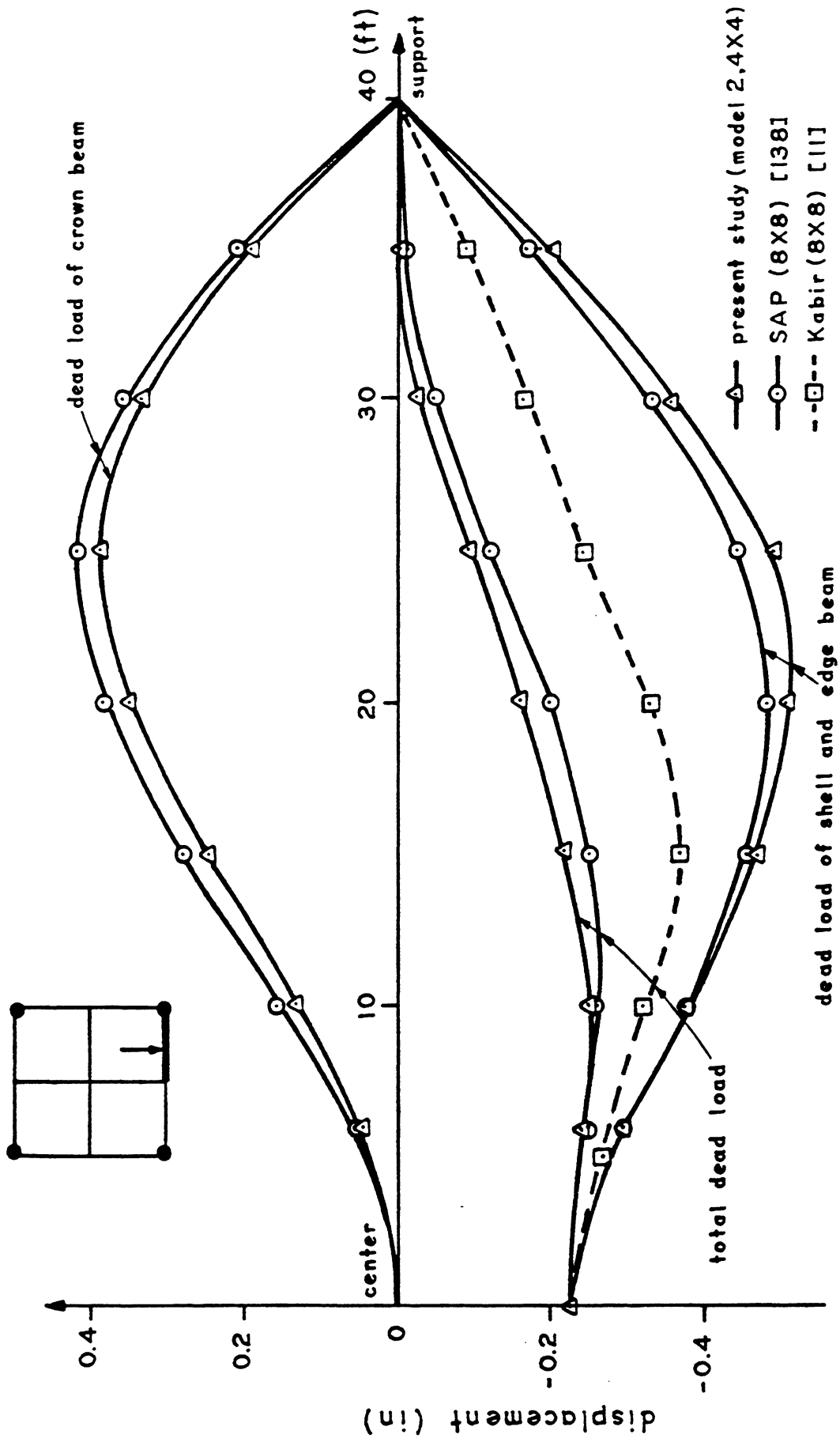

FIG. 10.33 GABLED HP SHELL - LINEAR ANALYSIS (EX. 10.4.2) - VERTICAL EDGE BEAM DISPLACEMENT (+ve UPWARDS) DUE TO VARIOUS DEAD LOADS (B x H = 48 x 12 in.)

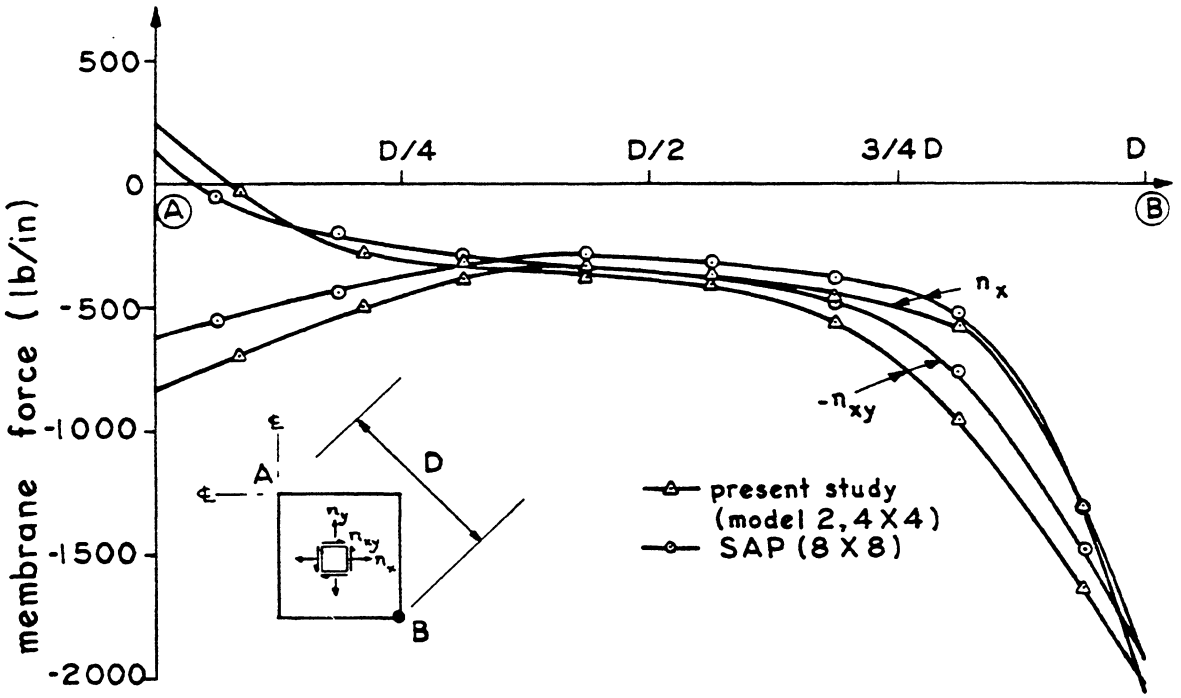

SHELL MEMBRANE FORCE

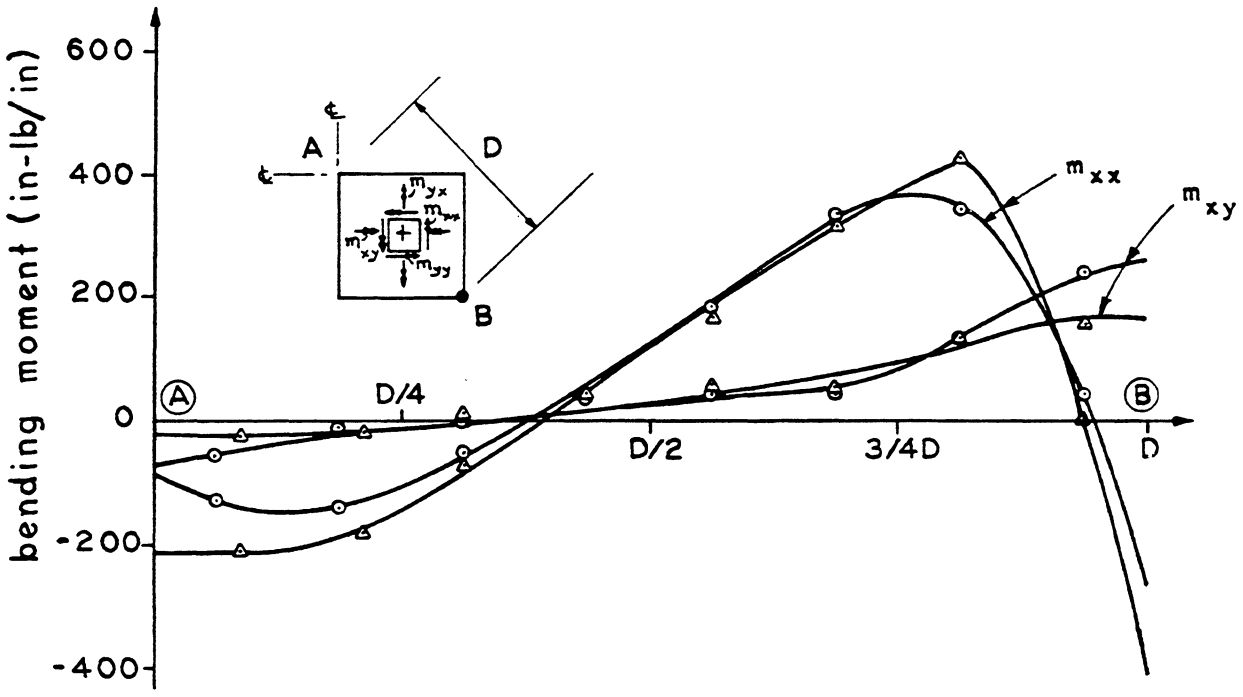

SHELL BENDING MOMENT

FIG. 10.34 GABLED HP SHELL - LINEAR ANALYSIS (EX. 10.4.2) - SHELL MEMBRANE FORCE AND BENDING MOMENT ALONG A-B UNDER TOTAL DEAD LOAD ONLY (B x H = 48 x 12 in.)

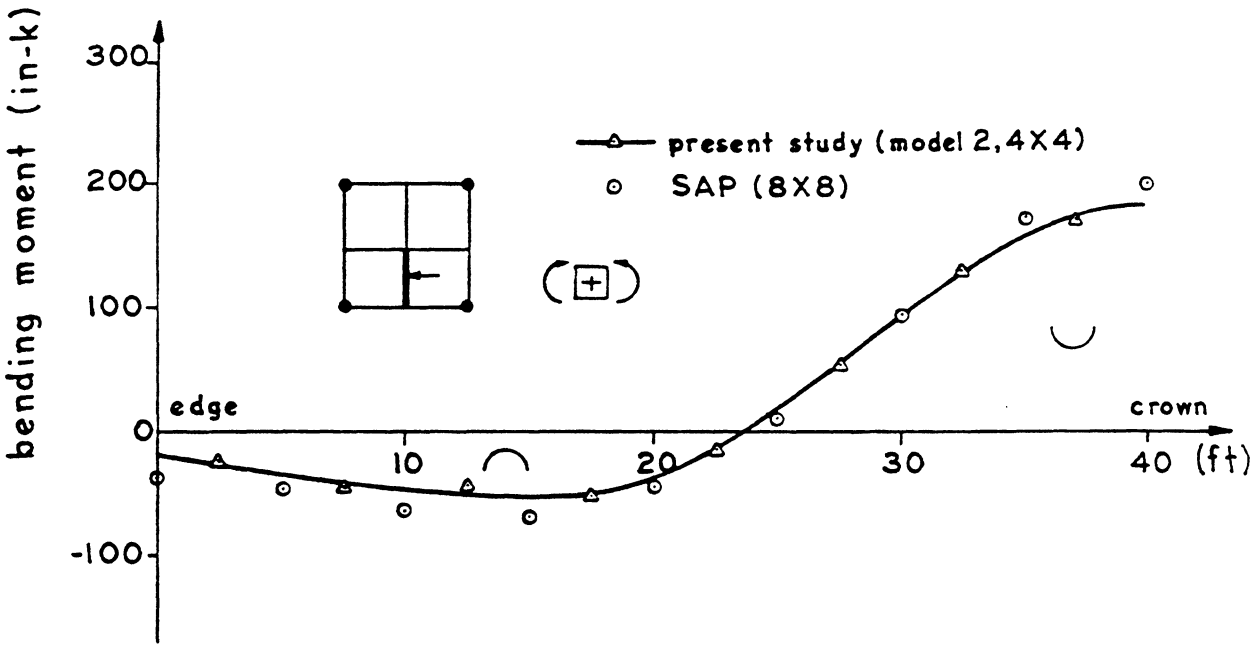

BENDING MOMENT IN THE CROWN BEAM

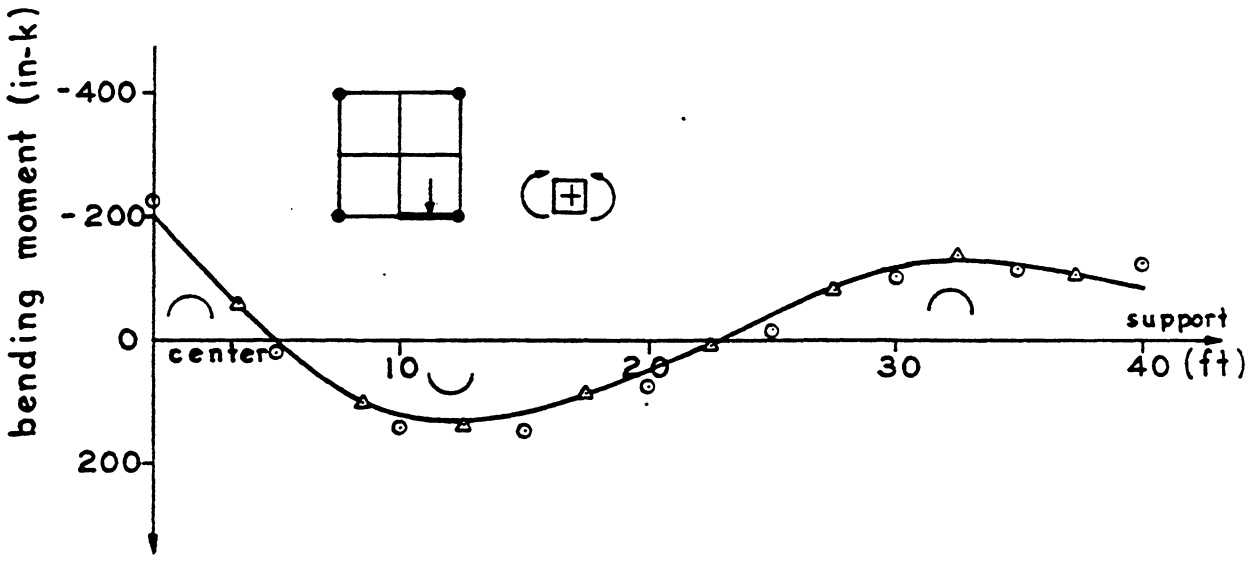

BENDING MOMENT IN THE EDGE BEAM

FIG. 10.35 GABLED HP SHELL - LINEAR ANALYSIS (EX. 10.4.2) - BENDING MOMENT IN THE CROWN AND EDGE BEAMS UNDER TOTAL DEAD LOAD ONLY (B x H = 48 x 12 in.)

With reference to Fig. 10.32, the crown beam vertical displacement under the combined dead weight of the shell and the edge beam show very little difference in results between the present analysis, SAP and Kabir's. However, under the total dead load, including the crown beam weight, substantial deviation exists between Kabir's results and those of the present analysis and SAP. This discrepancy is attributed to Kabir's analytical model in which it is believed that 75% of the crown beam's weight is actually carried by the crown beam while the remaining 25% is distributed to and carried by the shell. When the crown beam dead load contribution is increased by 33% in Kabir's solution in order to properly account for the total crown beam dead load carried by the crown beam, the vertical displacement along the crown beam due to its own weight (Fig. 10.32) is again in close agreement between the three solutions. This illustrates that great care must be exercised in the analytical modelling of the structure, especially at the boundaries.

To show the effects of the positioning of the crown beam relative to the shell, the results of the present analysis with no crown beam eccentricity are compared with those of Schnobrich [118] with the crown beam placed eccentrically above the shell. In Fig. 10.36 and Fig. 10.37, it can be seen that when the crown beam is placed eccentrically above the shell, both the axial force in the crown and the edge beams are slightly increased. However, the bending moment in the crown beam is decreased drastically.

The behavior of the shell with the larger crown beam is also sensitive to the imposed boundary conditions on the crown beam boundary at the plane of symmetry. For the reinforced concrete shell case to

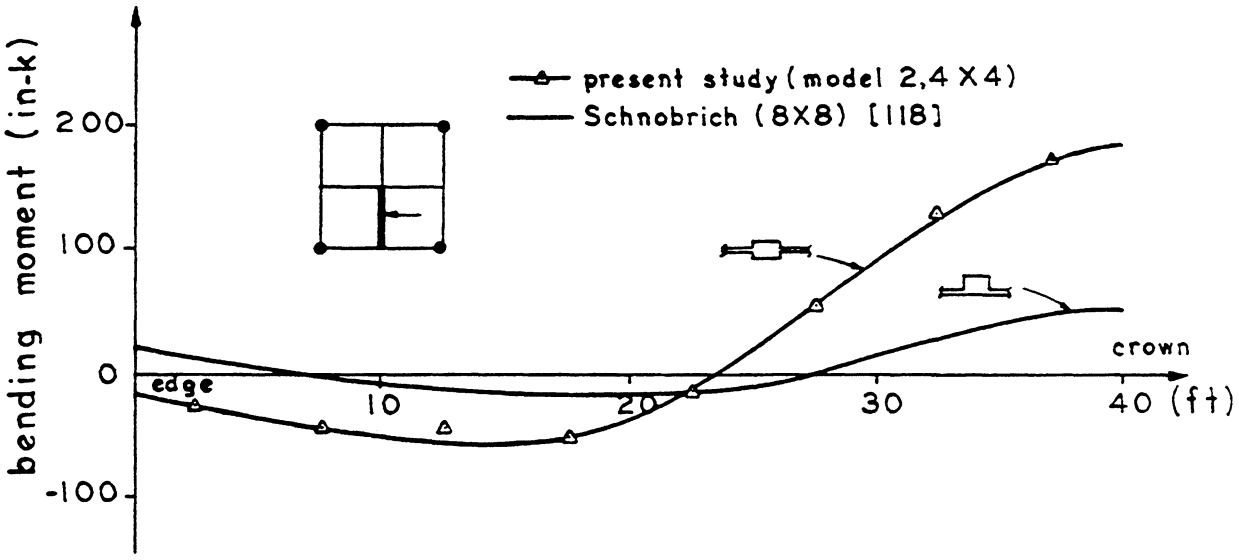

BENDING MOMENT IN THE CROWN BEAM

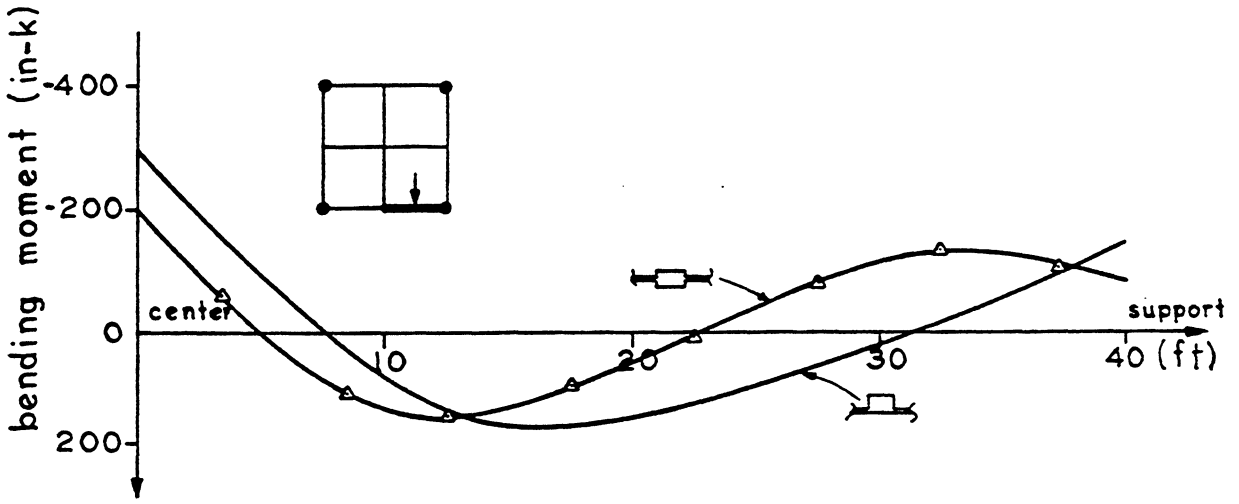

BENDING MOMENT IN THE EDGE BEAM

FIG. 10.36 GABLED HP SHELL - LINEAR ANALYSIS (EX. 10.4.2) - BENDING MOMENT IN THE CROWN AND EDGE BEAMS UNDER TOTAL DEAD LOAD SHOWING EFFECT OF CROWN BEAM ECCENTRICITY (B x H = 48 x 12 in.)

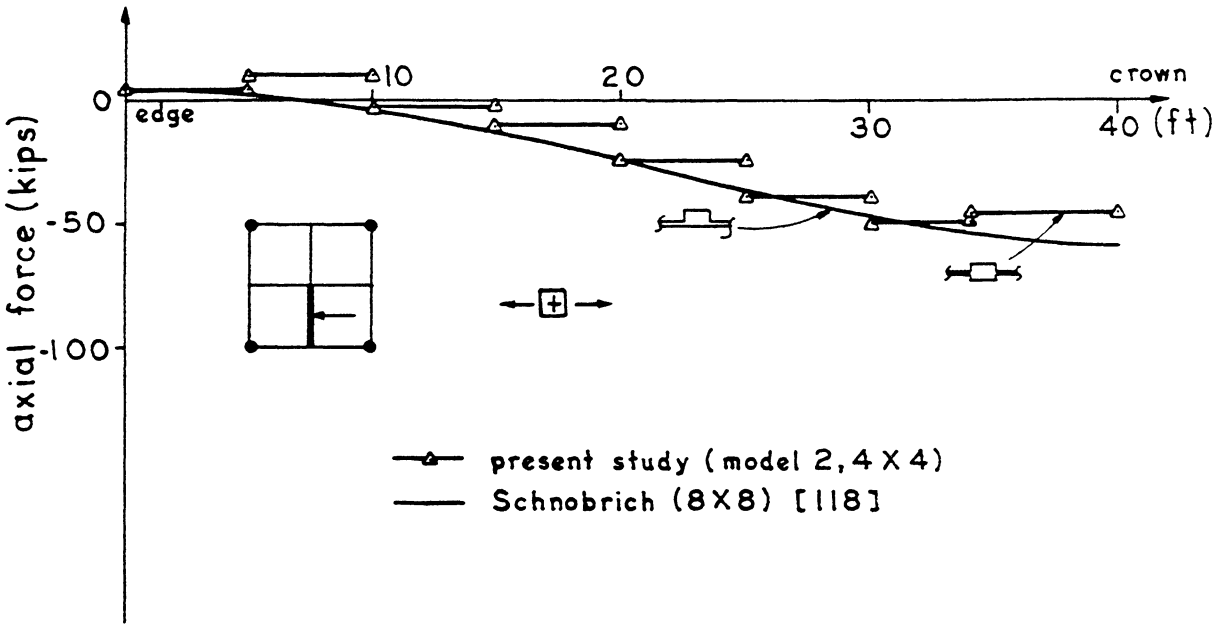

AXIAL FORCE IN THE CROWN BEAM

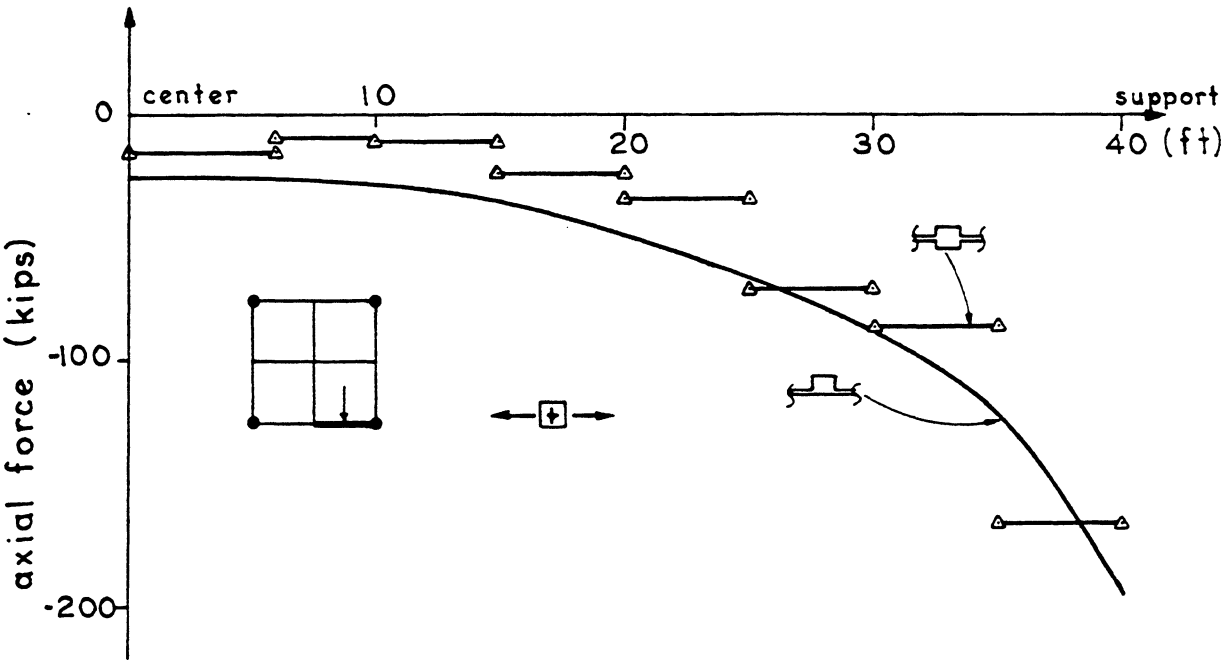

AXIAL FORCE IN THE EDGE BEAM

FIG. 10.37 GABLED HP SHELL - LINEAR ANALYSIS (EX. 10.4.2) - AXIAL FORCE IN THE CROWN AND EDGE BEAMS UNDER TOTAL DEAD LOAD SHOWING EFFECT OF CROWN BEAM ECCENTRICITY (B x H = 48 x 12 in.)

be described later, Model 1 and Model 2 (Fig. 10.26) give somewhat different results as can be seen from the displacement profiles of the crown and the edge beams depicted in Fig. 10.38. The comparison for the unreinforced shell with the large crown beam (B x H = 48 x 12 in.) have not been carried out for the crown beam Model 1 and Model 2 but it is believed that similar differences as those shown in Fig. 10.38 would occur.

To illustrate the effects on the internal forces due to the presence of the larger crown beam, a statical check has been carried out at Section B-B (Fig. 10.26) for a quarter of each of the two unreinforced shells with crown beam Model 2. The results are summarized in the following table for total dead load (shell + edge beam + crown beam) on the structure.

Axial Forces	B x H = 24 x 8 in.	B x H = 48 x 12 in.
Shell Crown Beam Edge Beam	-165 k (84%) - 15 k (7%) - 17 k (9%)	-183 k (75%) - 46 k (19%) - 14 k (6%)
Total Compressive Forces (C) at B-B	-197 k (100%)	-243 k (100%)
Horizontal Reactions (H)	196 k	239 k
Differences (C+H)	- 1 k	- 4 k

It can be seen that about 10% of the total axial force at Section B-B is being transferred from the shell proper to the crown

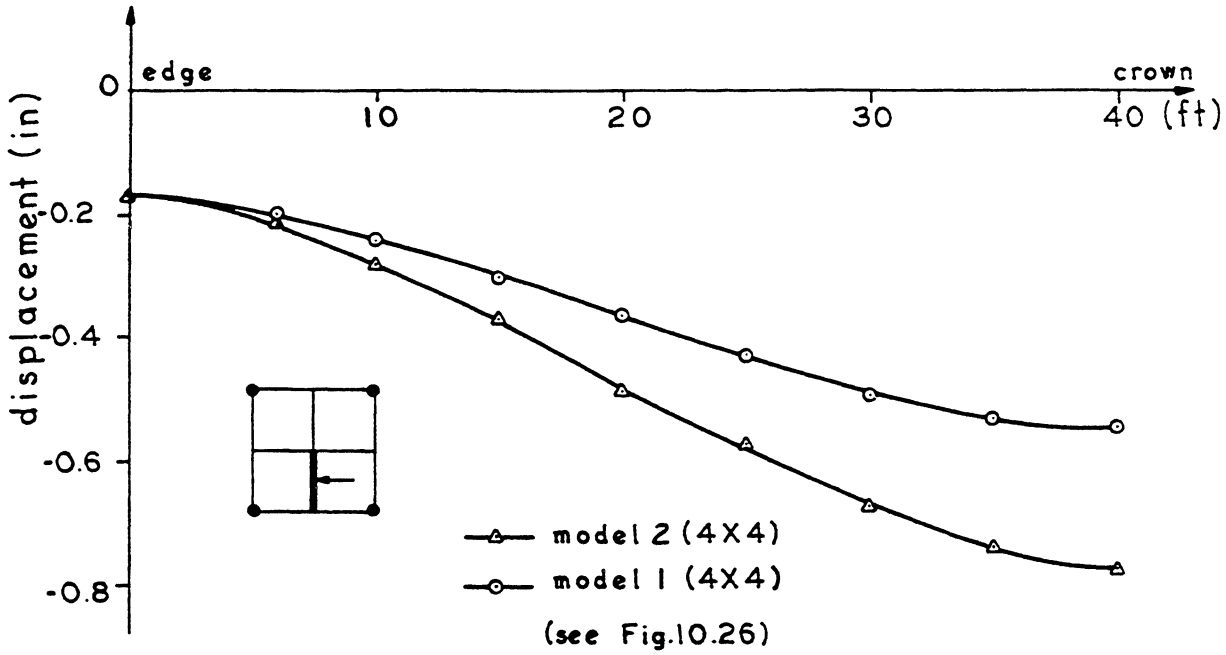

VERTICAL DISPLACEMENT OF CROWN BEAM

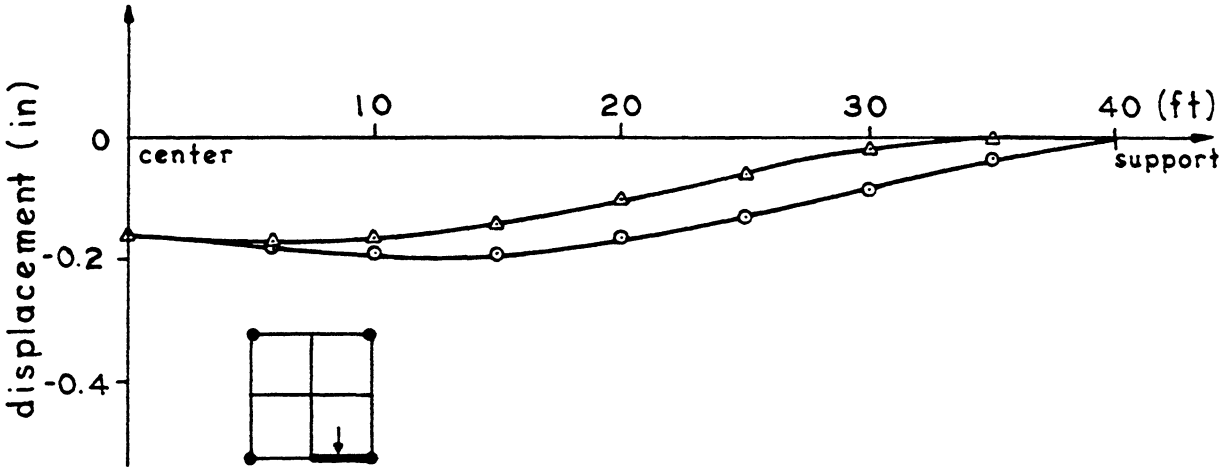

VERTICAL DISPLACEMENT OF EDGE BEAM

FIG. 10.38 GABLED HP SHELL - LINEAR ANALYSIS (EX. 10.4.2) - VERTICAL DISPLACEMENTS OF THE CROWN AND EDGE BEAMS (+ve UPWARDS) FOR THE REINFORCED CONCRETE SHELL UNDER TOTAL DEAD LOAD SHOWING EFFECT OF THE IMPOSED BOUNDARY CONDITION AT THE CROWN BEAM (B x H = 48 x 12 in.)

beam for a size increase in the crown beam from B x H = 24 x 8 in. to B x H = 48 x 12 in.

The linear analyses for the two gabled HP shells demonstrate that larger crown beams are more sensitive to their location relative to the shell, its weight and its distribution, and the boundary conditions being imposed on them at the plane of structural symmetry (Model 1 vs. Model 2). A substantial stress redistribution is also noted for a change in sizes of the crown beams.

2. Nonlinear Analysis for Short Time Loading

In order to emphasize the effects of the nonlinear geometry on a reinforced concrete gabled HP shell, the shell with a 48 x 12 in. crown beam which carries a larger axial force in the crown beam is chosen for the analysis. Here crown beam Model 2 (Fig. 10.26) is used.

The geometry and the reinforcement layout are shown in Fig. 10.39. The crown beam is divided into 10 equal layers through the thickness while only one layer is used across the width of the crown beam. The edge beam is divided into 10 equal layers, both through the depth and across the width of the edge beam. For the shell proper, 6 equal layers are used through its depth. The steel reinforcement is represented by discrete reinforcement in the crown and the edge beams, while 2 layers of smeared steel are used in the shell proper, each running in the direction of the generators.

The material properties for the concrete and steel are:

Concrete		Steel	
E_o	= 3.33×10^3 ksi	E_s	= 29.0×10^3 ksi
f'_c	= 3.0 ksi	E_{sh}	= 0.0
f'_t	= 0.471 ksi	f_y	= 60.0 ksi

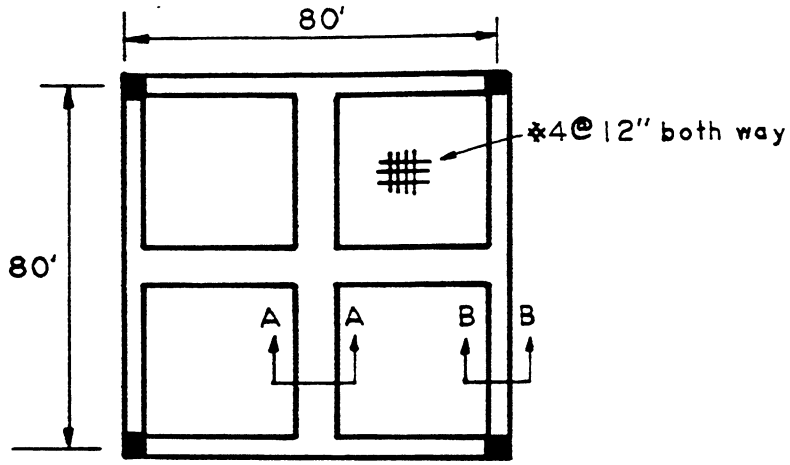

PLAN

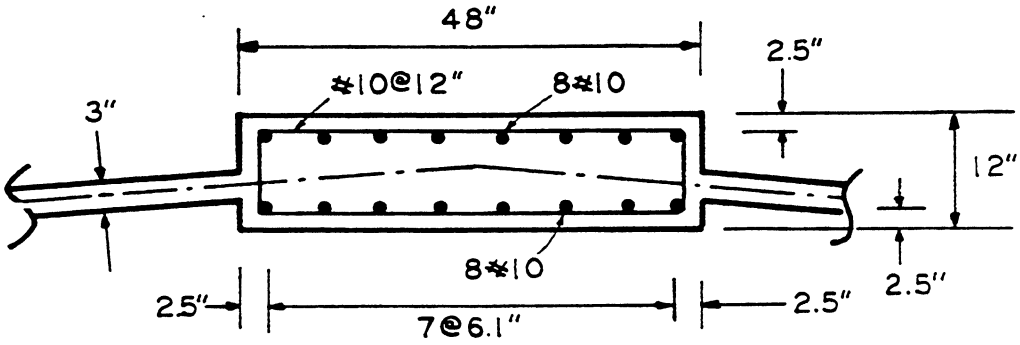

SECTION A-A

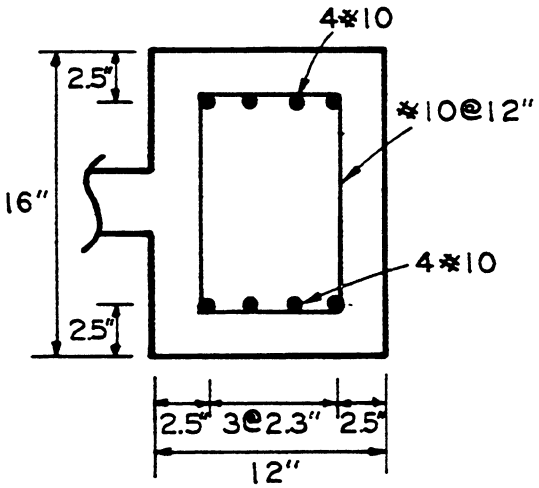

SECTION B-B

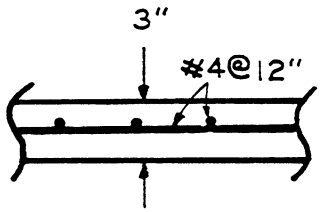

SHELL PROPER

FIG. 10.39 GABLED HP SHELL (EX. 10.4.2) - REINFORCEMENT LAYOUT
(B x H = 48 x 12 in.)

Concrete		Steel
ν	= 0.15	ε_{su} = 0.1
α	= 0.5	
ε_c	= $2 f'_c/E_o$	

The tension stiffening effects are accounted for by increasing the steel moduli. The default tension stiffening factors described in Chapter 3 are used for the shell. However, for the crown and the edge beams, these default values are scaled in such a way that the initial post-cracking axial stiffnesses are equal to half of the uncracked axial stiffnesses.

The results for the dead load linear analysis compare well for a 2 x 2 mesh and a 4 x 4 mesh of the shell (Fig. 10.26), and they are shown in Fig. 10.40.

The shell with linear material and nonlinear geometry is first analyzed to investigate the effects of nonlinear geometry. The shell is modelled by a 2 x 2 mesh. The live load is increased incrementally following the application of the total dead load of the shell. The vertical displacement at the crown of the shell is chosen to be the imposed displacement degree of freedom.

The load vs. the vertical displacement at the crown is shown in Fig. 10.41. The response is almost linear up to a load of DL+10LL. The continuous change in the geometry of the shell finally causes local instability in the vicinity of the crown at a load of DL+11.8LL. Further increase in the vertical displacement of the crown causes a decrease in the external load.

The displaced shape of the shell at a load of DL+11.8LL is

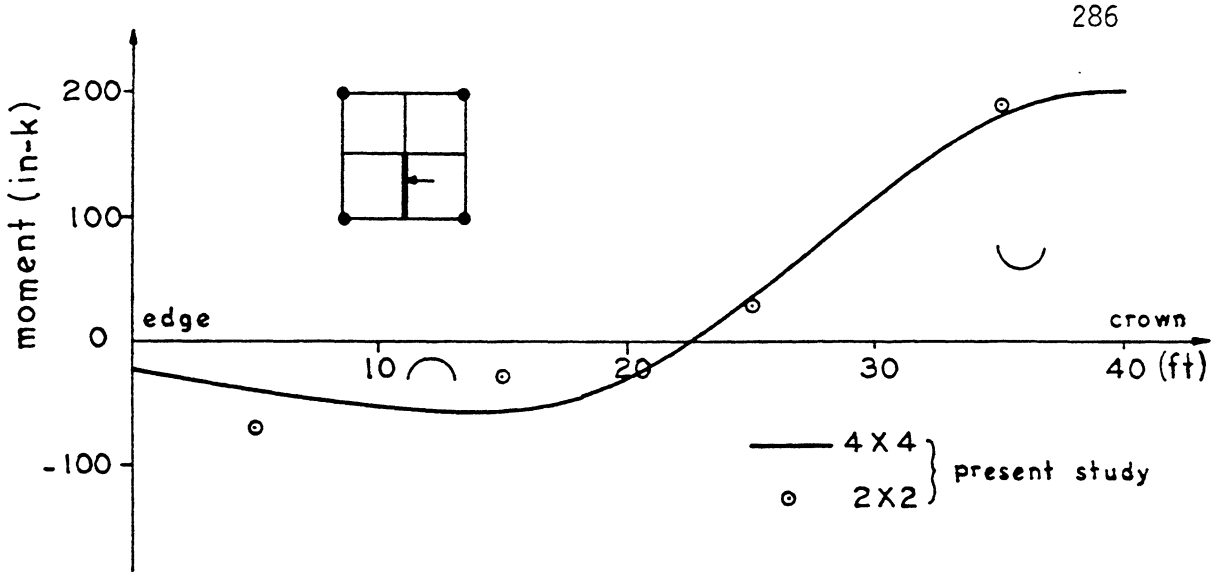

BENDING MOMENT IN THE CROWN BEAM

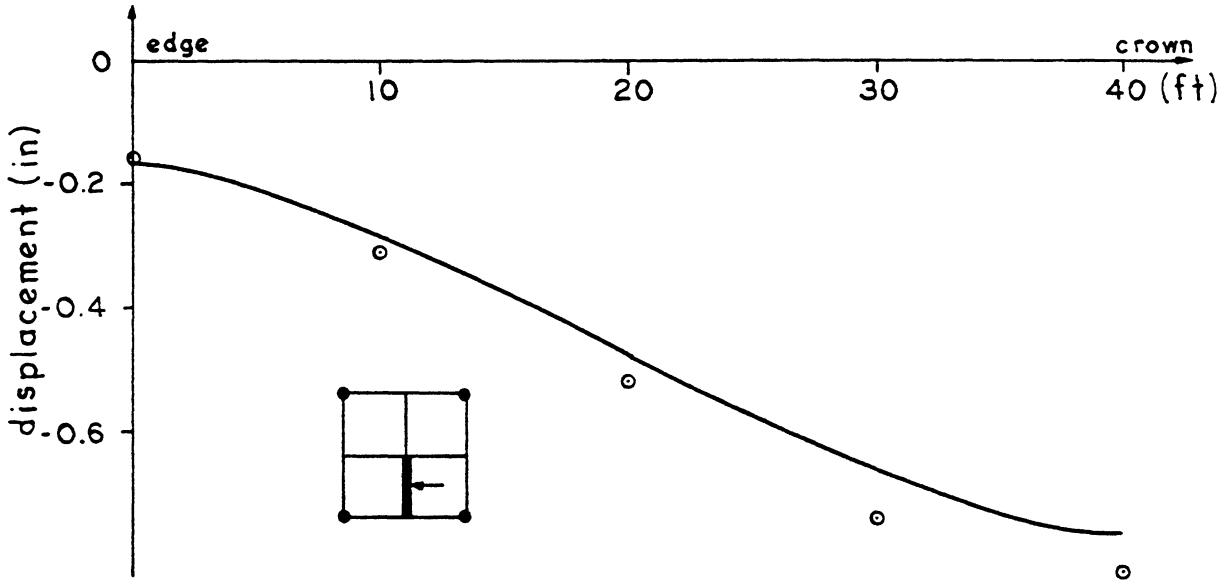

VERTICAL DISPLACEMENT OF THE CROWN BEAM

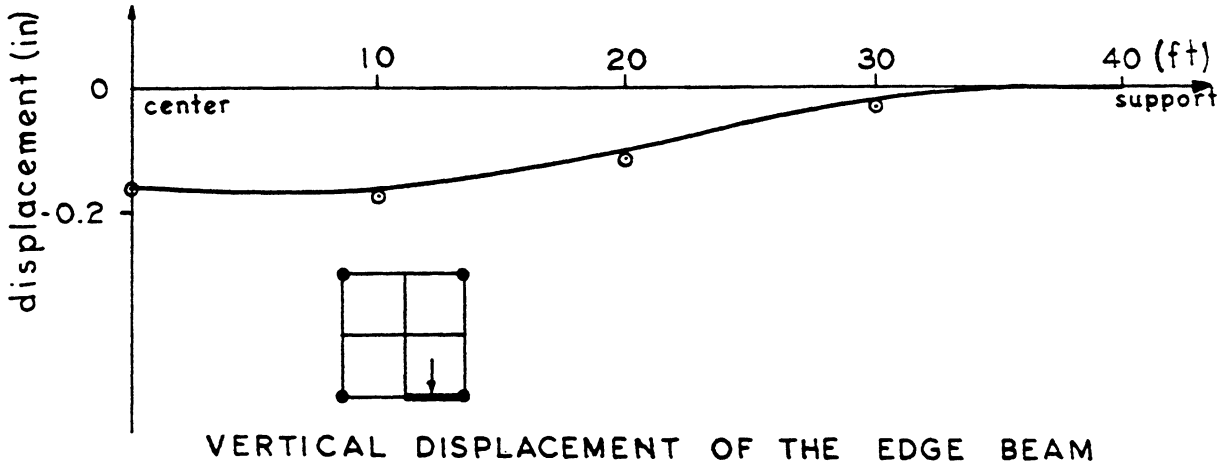

VERTICAL DISPLACEMENT OF THE EDGE BEAM

FIG. 10.40 GABLED HP SHELL - LINEAR ANALYSIS (EX. 10.4.2) - COMPARISON OF RESULTS FOR THE COARSE (2 x 2) AND FINE (4 x 4) MESHES FOR THE REINFORCED CONCRETE SHELL UNDER TOTAL DEAD LOAD ONLY (B x H = 48 x 12 in.)

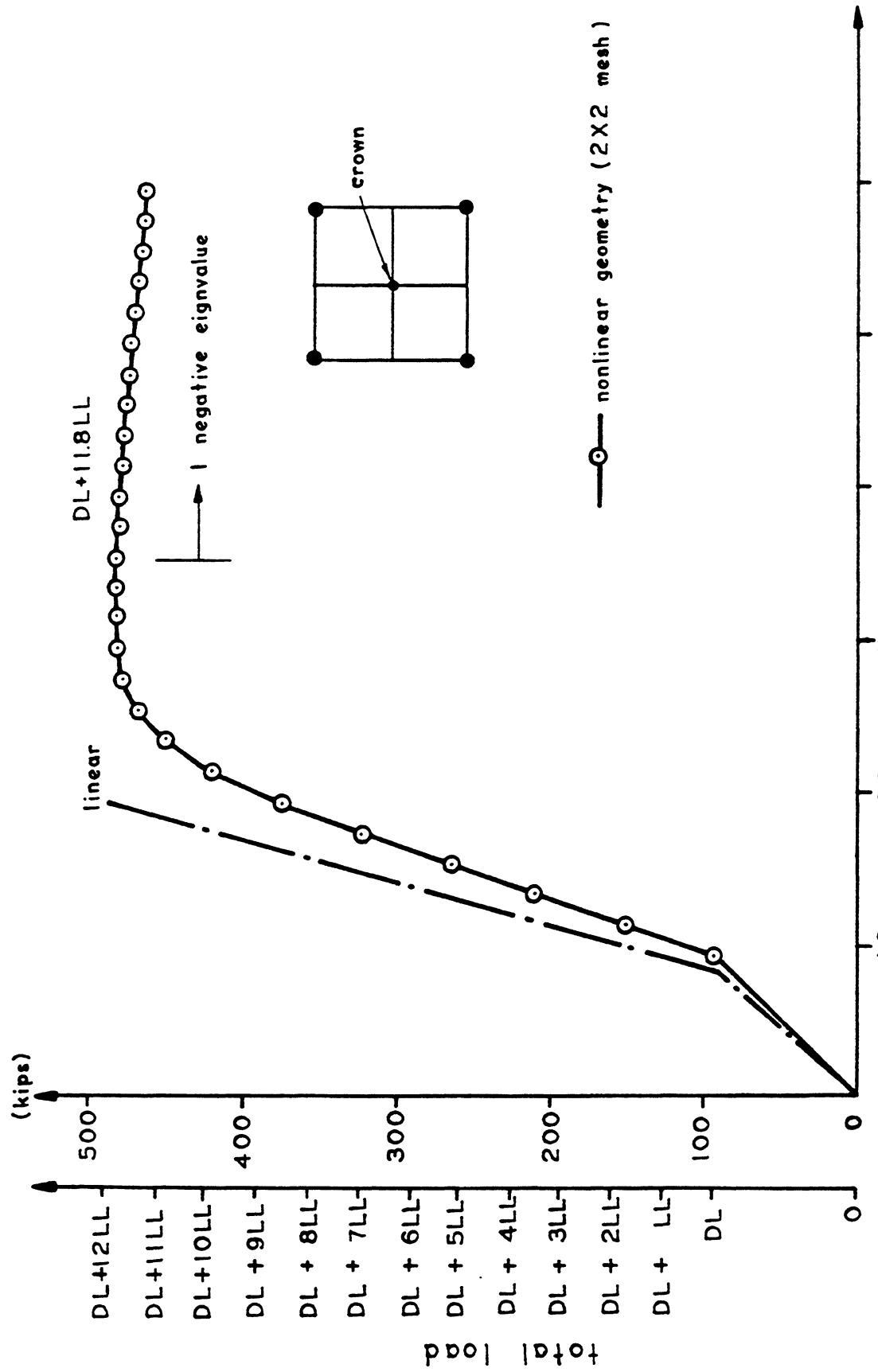

FIG. 10.41 GABLED HP SHELL - ANALYSIS FOR SHORT TIME LOADING WITH NONLINEAR GEOMETRY (EX. 10.4.2) - LOAD VS. VERTICAL DOWNWARDS DISPLACEMENT AT CROWN POINT FOR 2 x 2 MESH (B x H = 48 x 12 in.)

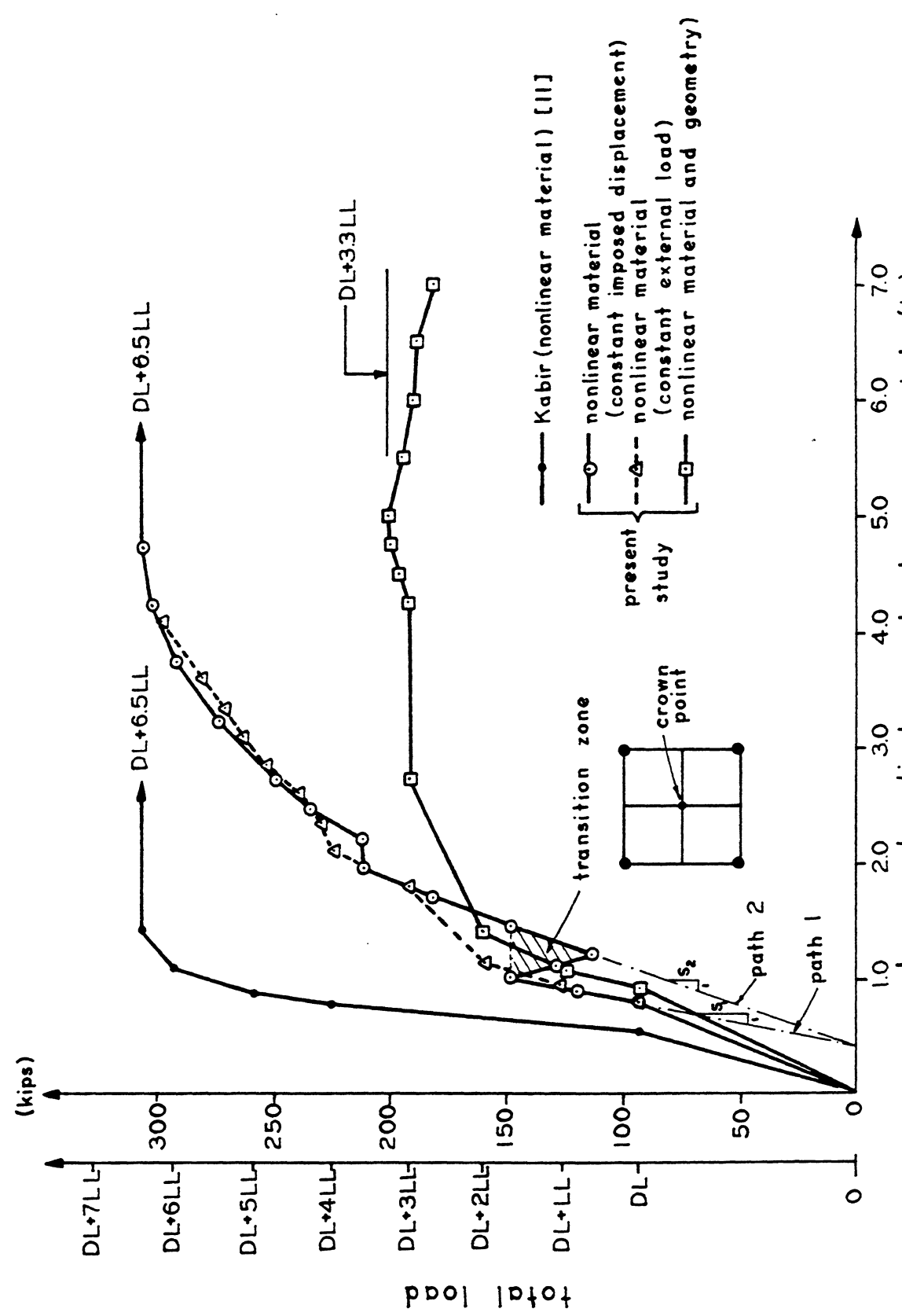

FIG. 10.43 GABLED HP SHELL - NONLINEAR ANALYSIS FOR SHORT TIME LOADING (EX. 10.4.2) - LOAD VS. VERTICAL DOWNWARDS DISPLACEMENT AT CROWN POINT FOR 4 x 4 MESH (B x H = 48 x 12 in.)

shape of this transition zone is largely dependent on the extent of the cracked regions and the tensile forces being retained in the cracked concrete. When iteration is carried out for a constant imposed external load, this transition zone cannot be detected. However, the major part of the load displacement response remains essentially the same (Fig. 10.43). The slight discrepancy is due to the larger convergence tolerance used for the case where iteration is performed with constant imposed external load.

In order to avoid the ambiguity of the transition zone, iteration with constant imposed external load is used in the earlier stage which is finally replaced by an iterative scheme with constant imposed displacement at a later stage in order to find the ultimate load correctly. This technique is used for the analysis where both nonlinear material and geometry are included.

A large decrease in the ultimate load from DL+6.5LL to DL+3.3LL is noted when nonlinear geometry is included in the analysis.

It is interesting to note that Kabir [11] has the same ultimate load as in the present study although the linear solutions are different. This indicates that the ultimate load is insensitive to the distribution of the crown beam's weight.

A statical check has been made at Section B-B (Fig. 10.26) at the ultimate load for the analyses with and without nonlinear geometry and the results are summarized in the table on the following page. Again, it is observed that there is a continuous build up of axial forces in crown beam when nonlinear geometry is included in the analysis.

Axial Forces	Nonlinear Material	Nonlinear Material and Geometry
Shell Crown Beam Edge Beam	-506 k (63%) -229 k (28%) - 70 k (9%)	-313 k (60%) -200 k (38%) - 14 k (2%)
Total C	-805 k (100%)	-527 k (100%)
Horizontal Reaction	+760 k	+507 k
Differences	- 45 k	- 20 k

3. Analysis for the Time Dependent Effects of Creep and Shrinkage

To study the effects of creep and shrinkage on the ultimate load capacity of the shell, the reinforced concrete shell is analyzed for a sustained dead load from 28 days to 180 days. At the end of the 180 days, the shell is loaded to failure by the addition of multiples of live load.

The 5-month time period is divided into 6 time steps: 28 - 32 - 40 - 60 - 100 - 140 - 180 days. Standard values recommended by ACI Committee 209 [64], described in Chapter 4, are used for the time dependent material properties.

The analysis is first performed with a mesh of 2 x 2. Both the analyses with and without nonlinear geometry are included. The analysis is then further substantiated with the analysis including nonlinear material and geometry for a 4 x 4 mesh of the shell.

The resulting load displacement responses are shown in Fig. 10.44. Here, the analysis including nonlinear material only again shows a transition zone due to the use of the iterative scheme with constant imposed displacement.

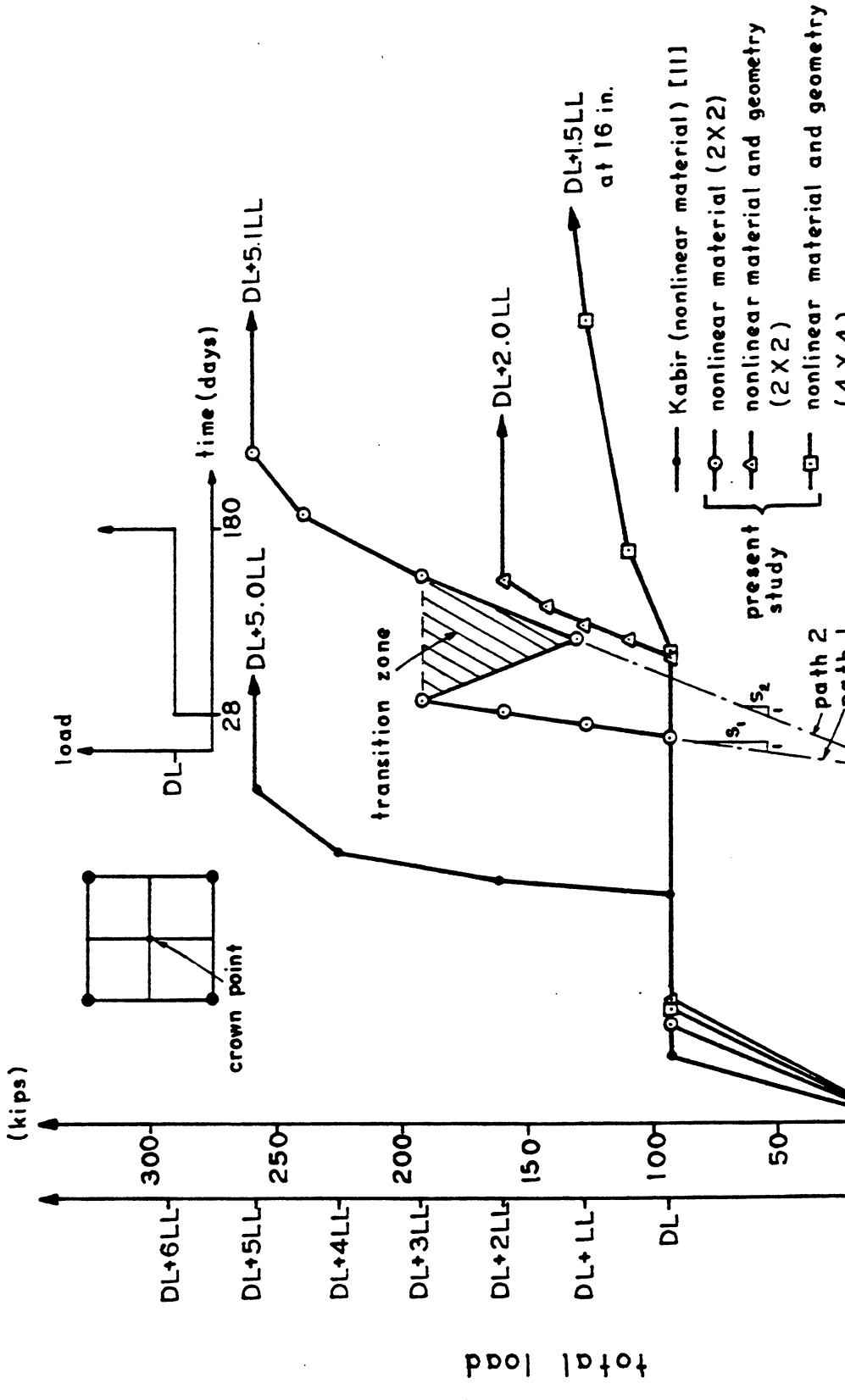

FIG. 10.44 GABLED HP SHELL - TIME DEPENDENT ANALYSIS (EX. 10.4.2) - LOAD VS. VERTICAL DOWNWARDS DISPLACEMENT AT CROWN POINT UNDER SUSTAINED LOAD (B x H = 48 x 12 in.)

The decrease in the ultimate load capacity of the shell due to the change in geometry is particularly noted. For a 2 x 2 mesh, the ultimate load drops from DL+5.1LL to DL+2.0LL when nonlinear geometry is included. The analysis with a 4 x 4 mesh gives an ultimate load of DL+1.5LL, however.

The results for the analysis including nonlinear geometry for a 2 x 2 mesh and a 4 x 4 mesh are in good agreement prior to the application of the live load. Selected results are shown from Fig. 10.45 to Fig. 10.49, together with some of the results obtained by Kabir [11]. A decrease in the compressive stresses in the shell and an increase in the axial forces and bending moments in the crown beams are noted.

The difference in the results between the present analysis with nonlinear material only and those of Kabir is due to a sign error by Kabir in the transformation of the creep and the shrinkage strains. A closer agreement in the internal forces of the crown beam (not shown) is observed when the sign is reversed in an analysis by the present method to make it consistent with that of Kabir.

The crack patterns for a 4 x 4 mesh of the shell under the combined effects of nonlinear material and geometry and that of creep and shrinkage at ages of 28 days and 180 days are compared in Fig. 10.50. It can be seen that at 180 days,the increase in the bending moment and the displacement in the crown beam result in some additional cracking in the crown beams and near the supports. The crack pattern (not shown) for the analysis with a 2 x 2 mesh, on the other hand, does not have any crack in the crown beam at 180 days, however. This earlier cracking associated with the 4 x 4 mesh leads to a lower ultimate load of the shell.

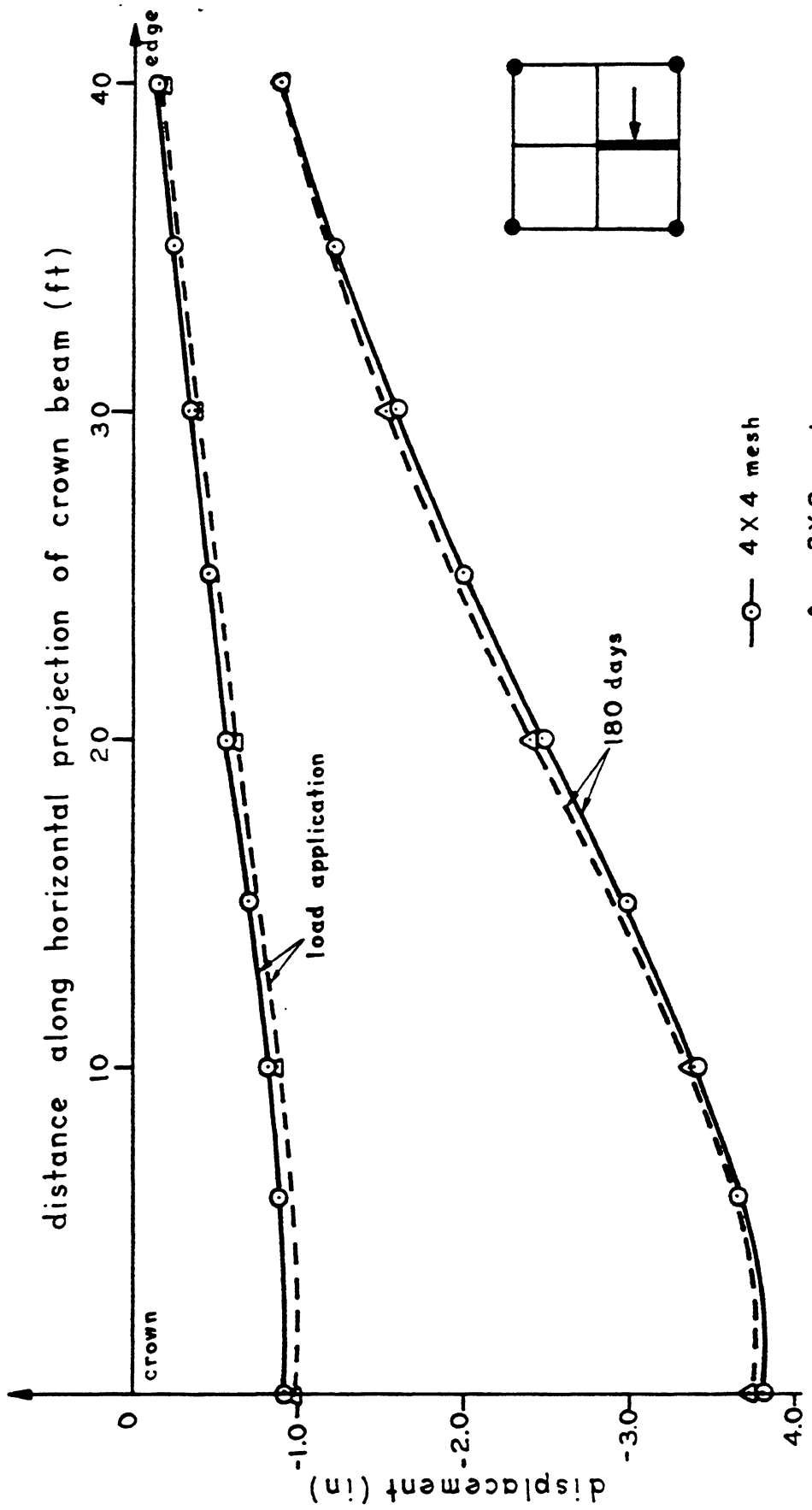

FIG. 10.45 GABLED HP SHELL - TIME DEPENDENT ANALYSIS WITH NONLINEAR MATERIAL AND GEOMETRY (EX. 10.4.2) - VERTICAL CROWN BEAM DISPLACEMENT FOR SUSTAINED TOTAL DEAD LOAD ON THE SHELL FOR 2 x 2 AND 4 x 4 MESHES (B x H = 48 x 12 in.)

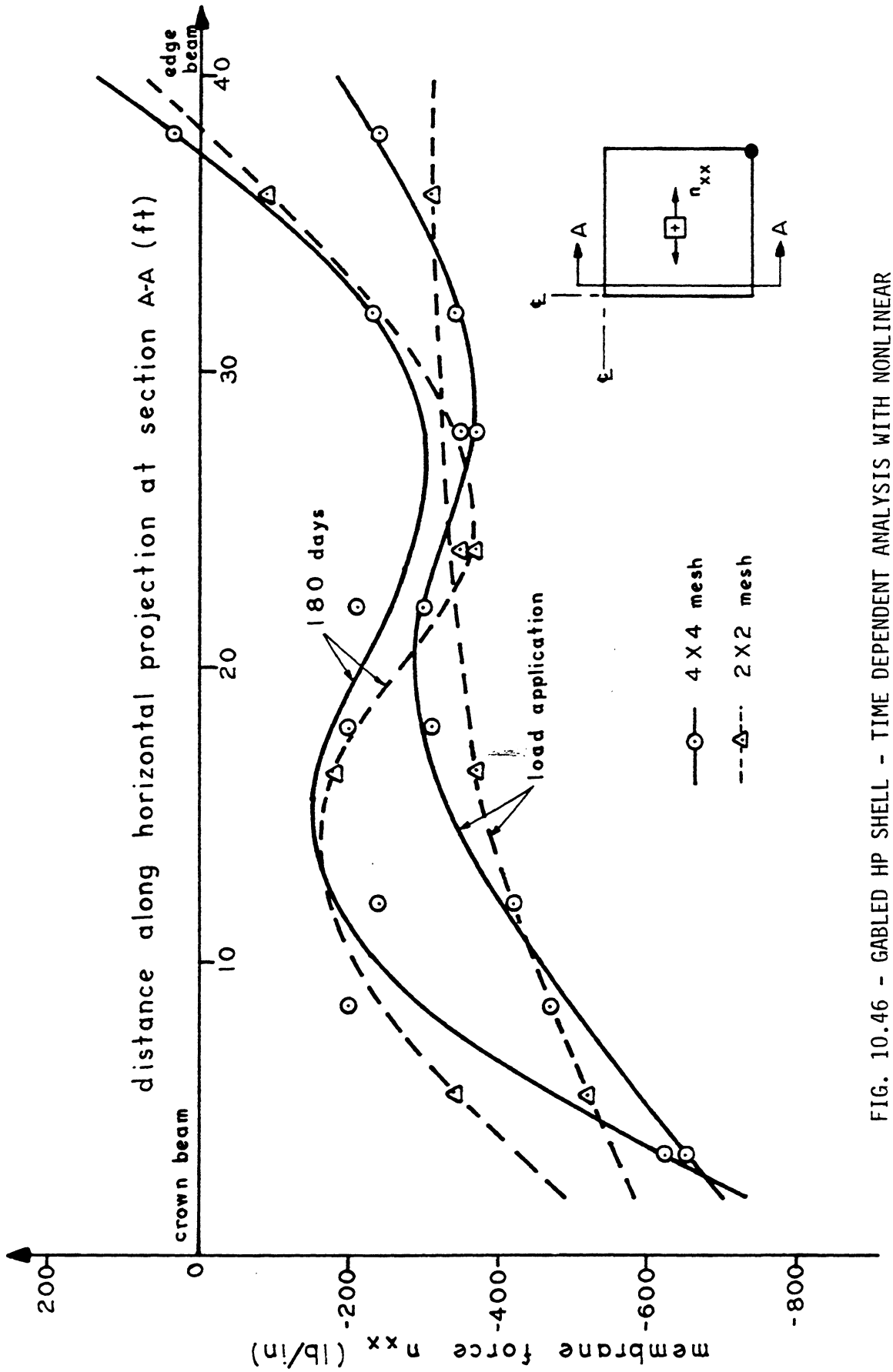

FIG. 10.46 - GABLED HP SHELL - TIME DEPENDENT ANALYSIS WITH NONLINEAR MATERIAL AND GEOMETRY (EX. 10.4.2) - SHELL MEMBRANE STRESS n_{xx} AT SECTION A-A FOR SUSTAINED TOTAL DEAD LOAD ON THE SHELL FOR 2 x 2 AND 4 x 4 MESHES (B x H = 48 x 12 in.)

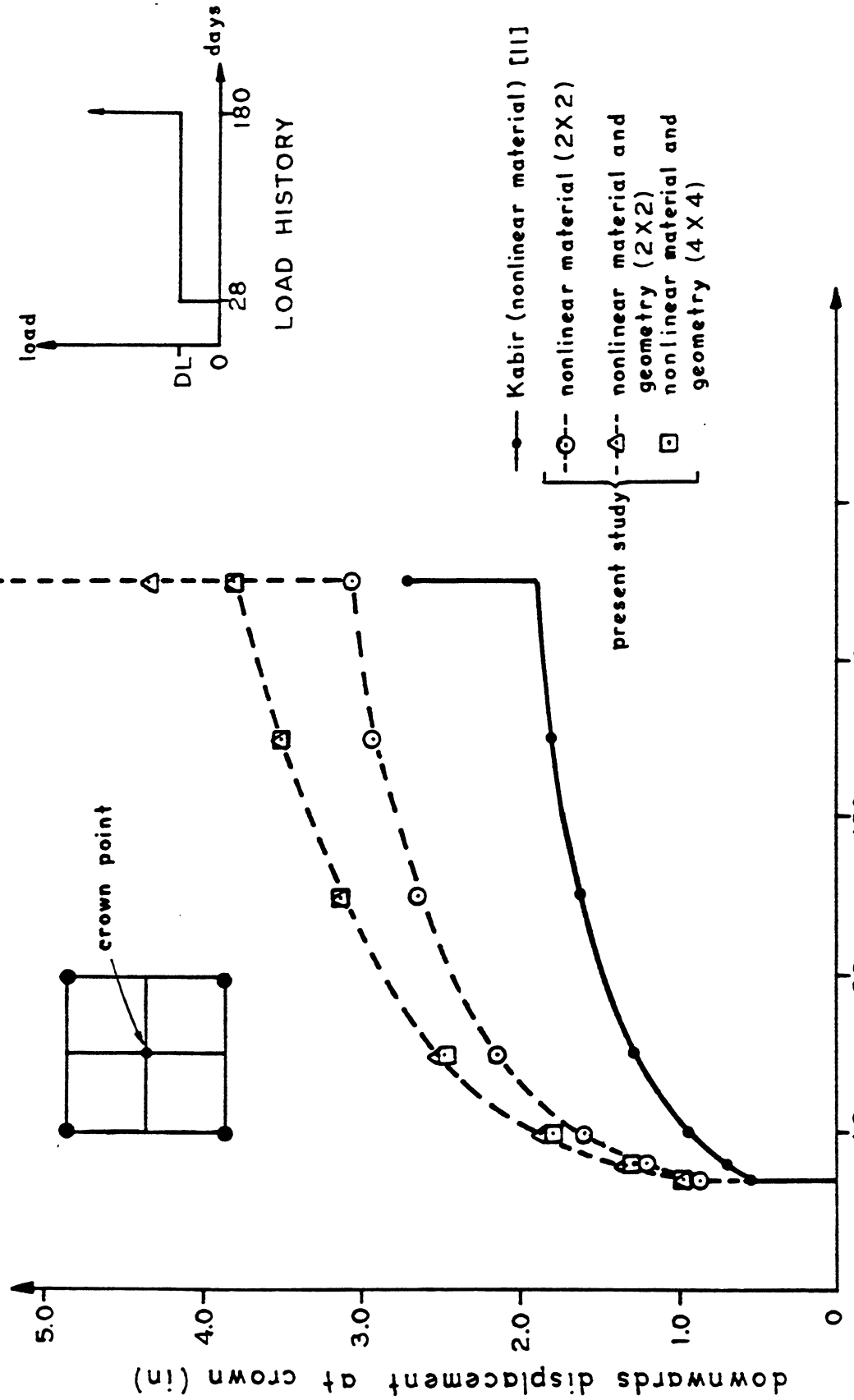

FIG. 10.47 GABLED HP SHELL - TIME DEPENDENT ANALYSIS (EX. 10.4.2) - TIME VARIATION OF VERTICAL CROWN POINT DISPLACEMENT FOR THE APPLIED LOAD HISTORY, FOR 2 x 2 AND 4 x 4 MESHES (B x H = 48 x 12 in.)

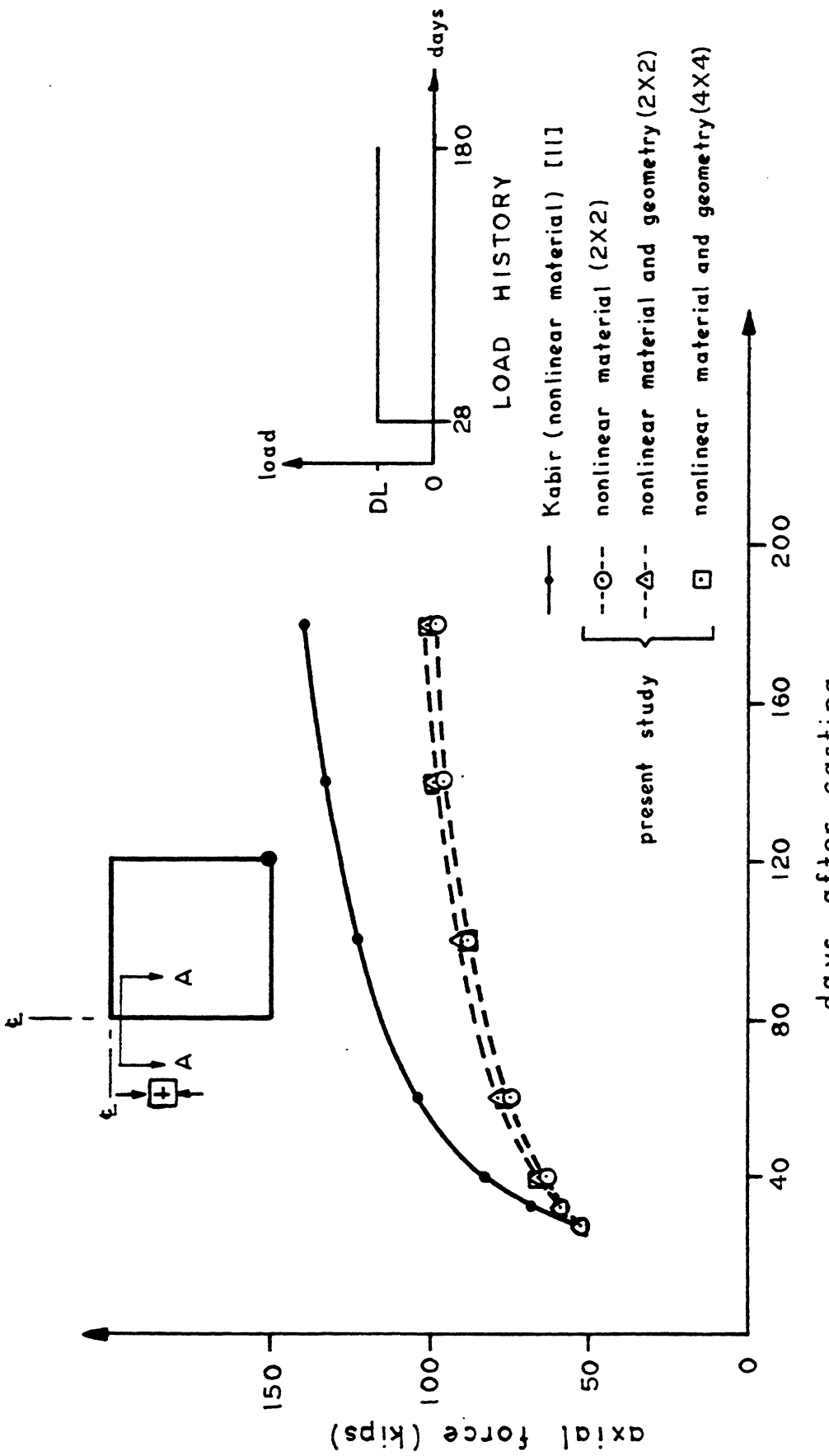

FIG. 10.48 GABLED HP SHELL - TIME DEPENDENT ANALYSIS (EX. 10.4.2) - TIME VARIATION OF AXIAL FORCE IN THE CROWN BEAM AT SECTION A-A FOR SUSTAINED TOTAL DEAD LOAD ON THE SHELL, FOR 2 x 2 AND 4 x 4 MESHES (B x H = 48 x 12 in.)

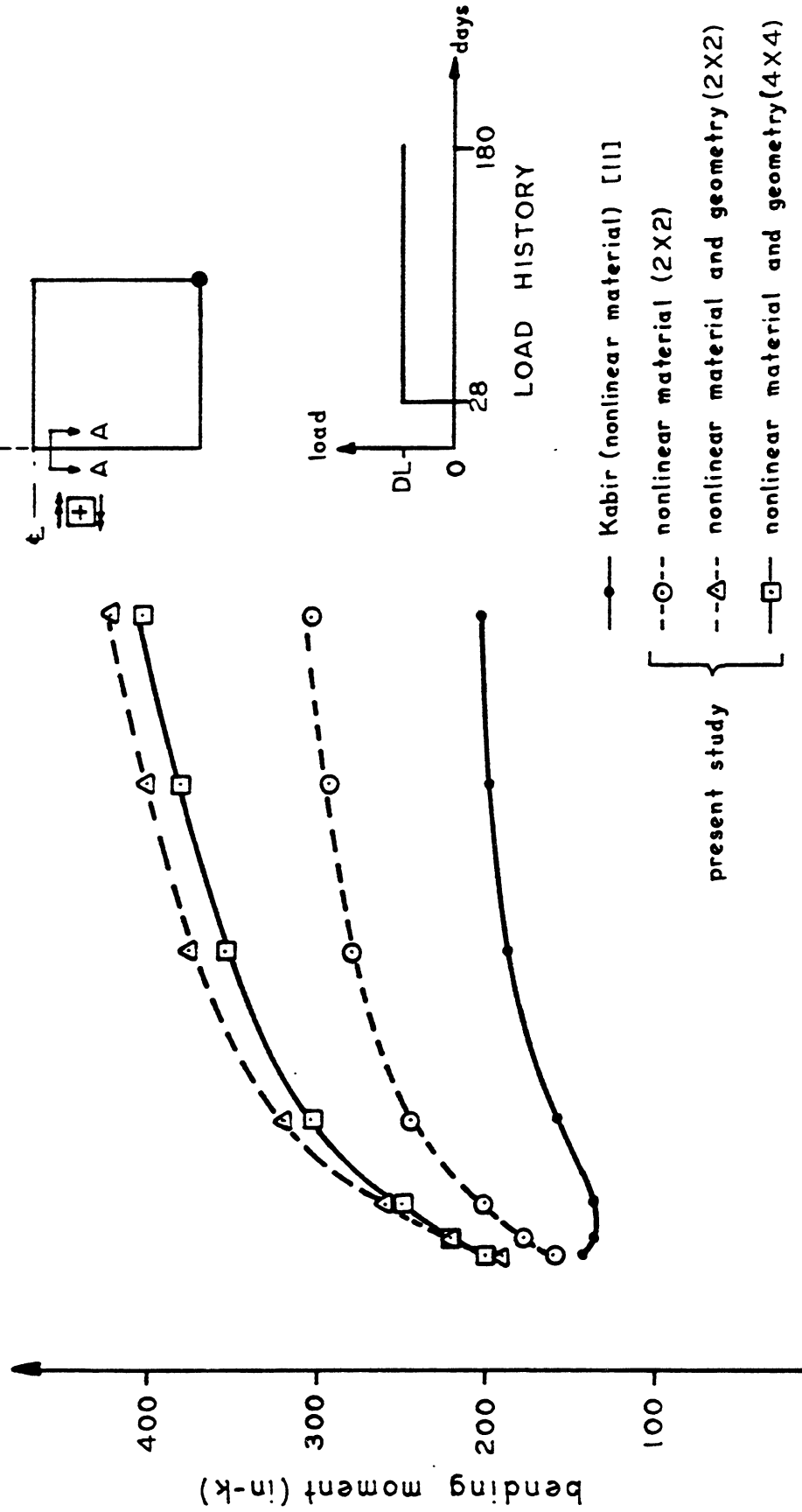

FIG. 10.49 GABLED HP SHELL - TIME DEPENDENT ANALYSIS (EX. 10.4.2) - TIME VARIATION OF BENDING MOMENT IN THE CROWN BEAM AT SECTION A-A FOR SUSTAINED TOTAL DEAD LOAD ON THE SHELL, FOR 2 x 2 AND 4 x 4 MESHES (B x H = 48 x 12 in.)

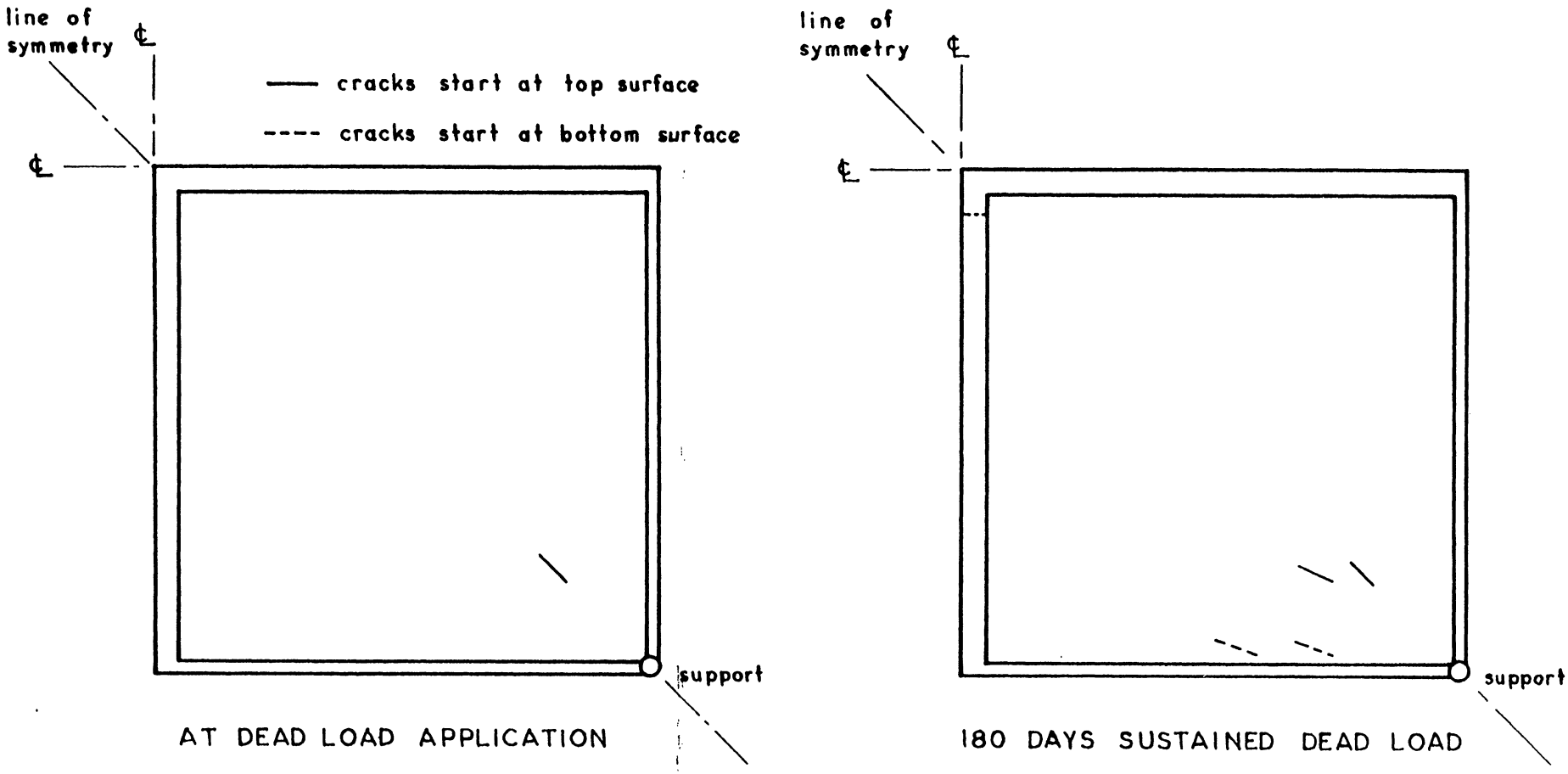

FIG. 10.50 GABLED HP SHELL - TIME DEPENDENT ANALYSIS WITH NONLINEAR MATERIAL AND GEOMETRY (EX. 10.4.2) - CRACK PATTERNS FOR SUSTAINED TOTAL DEAD LOAD ON THE SHELL FOR 4 x 4 MESH (B x H = 48 x 12 in.)

To see the amount of redistribution in the internal forces due to the nonlinear geometry or due to the combined effects of creep and shrinkage and nonlinear geometry, a statical check at Section B-B (Fig. 10.26) for the shell under total dead load is again carried out for a 4 x 4 mesh. The results are summarized in the following table.

Axial Forces	NL Material (28 days)	NL Material and Geometry (28 days)	NL Material and Geometry and Creep and Shrinkage (180 days)
Shell Crown Beam Edge Beam	-174 k (72%) - 53 k (22%) - 15 k (6%)	-173 k (71%) - 55 k (23%) - 14 k (6%)	-113 k (48%) -102 k (43%) - 22 k (9%)
Total C	-242 k (100%)	-242 k (100%)	-237 k (100%)
Horizontal Reaction	238 k	238 k	234 k
Differences	- 4 k	- 4 k	- 3 k

It can be seen that a significant amount of axial force is being redistributed from the shell to the crown beam under the influence of creep and shrinkage.

Due to creep and shrinkage, the shell tends to shrink, the restraints offered by the stiffner crown and the edge beams will then cause a redistribution of the axial forces from the shell to the crown and the edge beams. This increase in the axial forces will in turn cause a further increase in the displacements and bending moments in the crown beams due to the PΔ effects.

4. Modes of Failure

The load displacement responses for all the analyses except for

the case with linear material and nonlinear geometry are summarized in Fig. 10.51. The transition zones are deliberately omitted for clarity since they do not have any physical meaning when a monotonic increasing load is applied to the shell.

The ultimate load for a 4 x 4 mesh of the shell drops from DL+6.5LL to DL+1.5LL when nonlinear geometry and the effects of creep and shrinkage are included. This can be understood by studying the crack patterns of the 4 x 4 mesh of the shell for different analyses, as shown in Fig. 10.52.

For the analysis including nonlinear material only, the cracks first start near the support and propagate upwards along the diagonal. The shell fails by splitting along the diagonal and the yielding of the reinforcement. The response is therefore quite ductile.

For the analysis including nonlinear material and geometry, the shell first cracks near the support, which coupled with the increase in the displacements and the bending moments in the crown beams due to the nonlinear geometry effects, finally causes splitting along the diagonal of the shell. The failure mode is more brittle in this case.

In the case where creep and shrinkage and the nonlinear geometry are included in the analysis, cracking occurs in the crown beams at 180 days and tends to amplify the nonlinear geometry effects which, in turn, causes more cracking in the supporting members. Without the help of the supporting members, the shell cannot stand by itself and it fails in a sudden brittle manner.

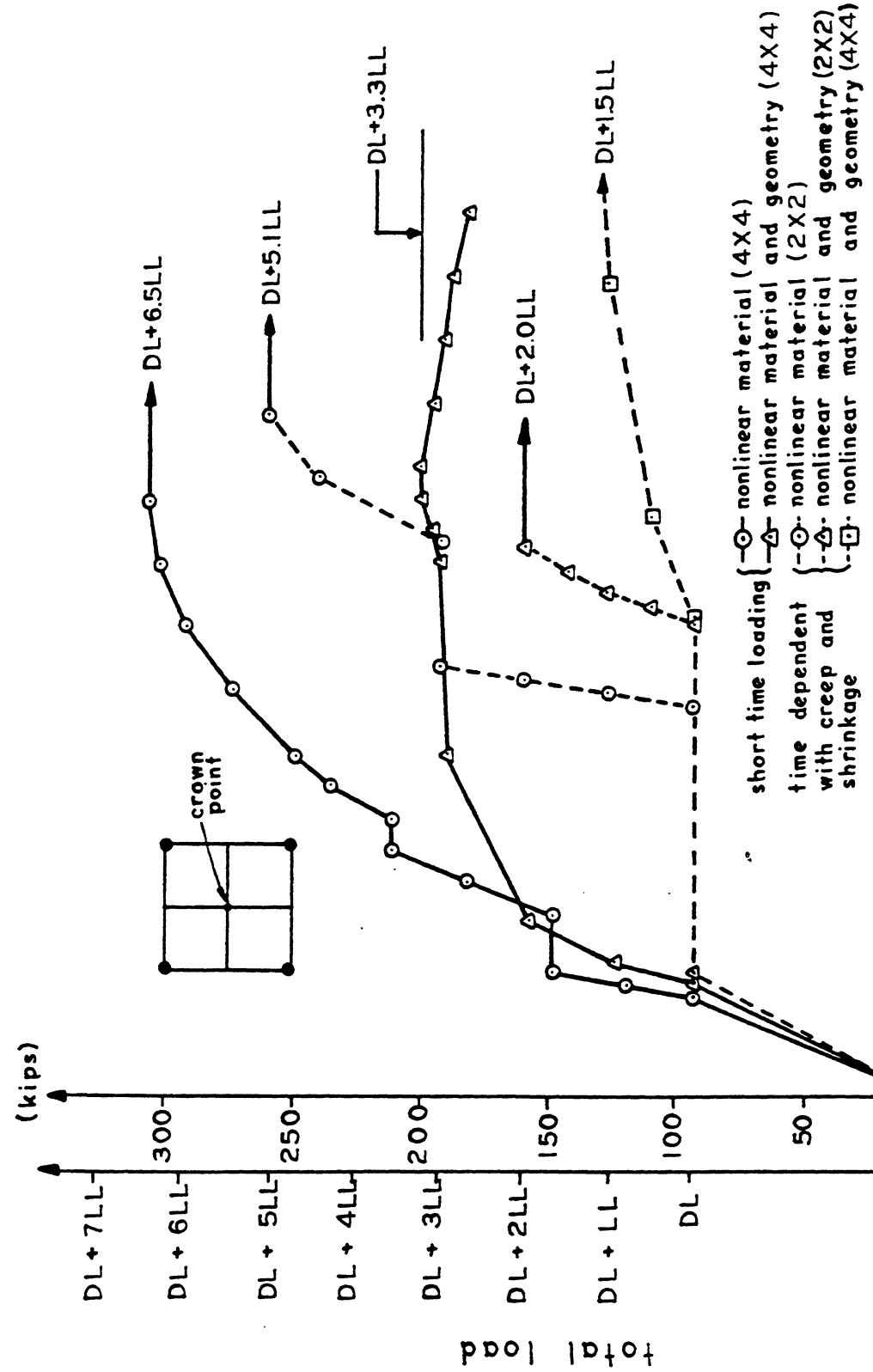

FIG. 10.51 GABLED HP SHELL - NONLINEAR ANALYSIS (EX. 10.4.2) - COMPARISON OF LOAD VS. CROWN POINT VERTICAL DOWNWARDS DISPLACEMENT FOR INSTANTANEOUS AND SUSTAINED LOAD (B x H = 48 x 12 in.)

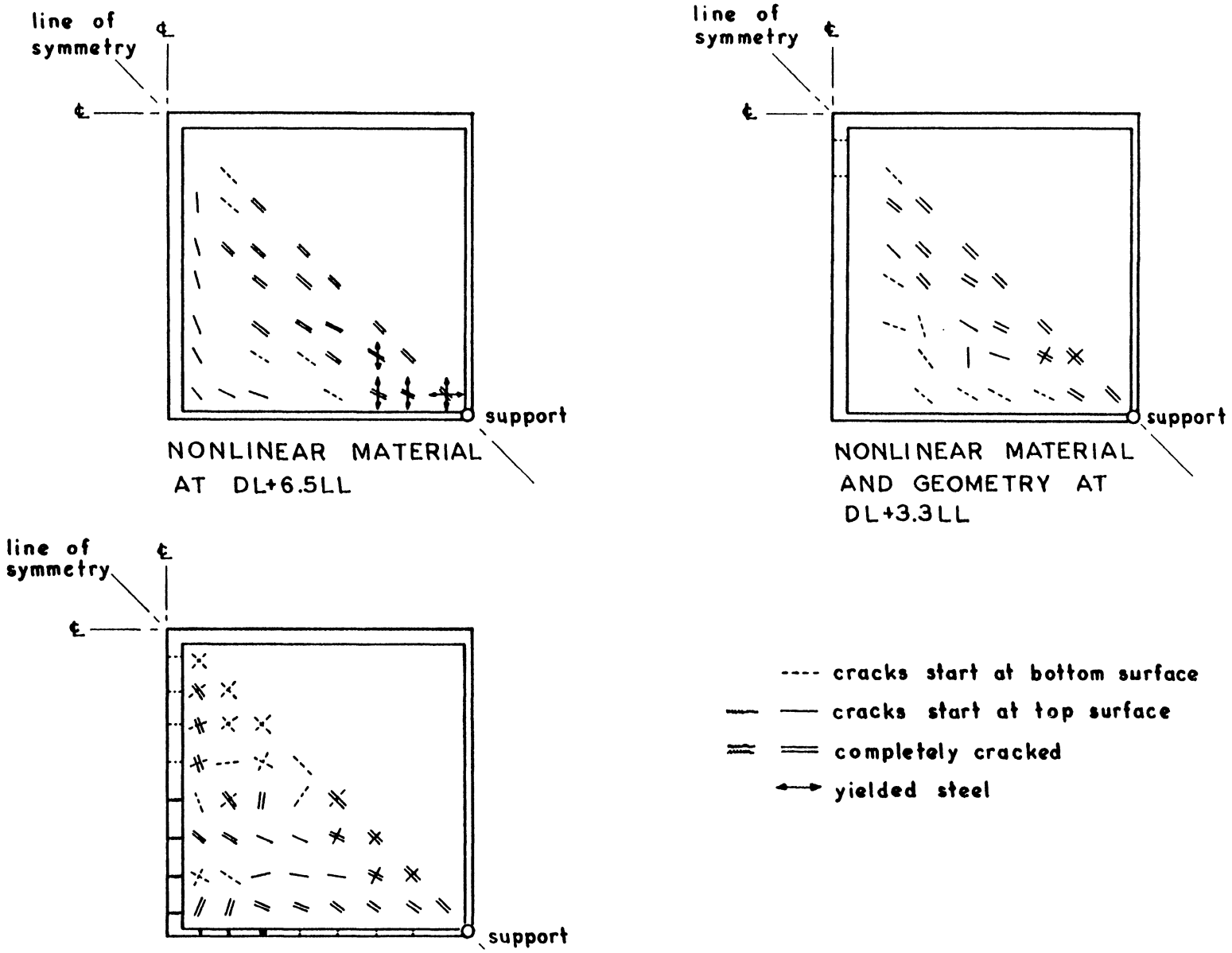

FIG. 10.52 GABLED HP SHELL - NONLINEAR ANALYSIS (EX. 10.4.2) - COMPARISON OF CRACK PATTERNS AT FAILURE FOR 4 x 4 MESH FOR VARIOUS ANALYSES (B x H = 48 x 12 in.)

5. Conclusions

The effects of the nonlinear geometry coupled with creep and shrinkage are shown to be significant in the gabled HP shell with a 48 x 12 in. crown beam. The decrease in the ultimate load from DL+6.5LL to DL+3.3LL due to the nonlinear geometry is observed. The combined effects of creep and shrinkage and of nonlinear geometry decrease the ultimate load from DL+6.5LL to DL+1.5LL, while an analysis including creep and shrinkage and only nonlinear material effects gives an ultimate load of DL+5.1LL.

The significant stress redistribution as a result of creep and shrinkage, which couples with nonlinear geometry has a detrimental effect on the structural behavior. The crown beam must therefore be designed with care so as to minimize its weight. It can also be positioned eccentrically above the shell so that its bending moment will be decreased. In these ways, the effects of the nonlinear geometry can be minimized.

The mode of failure reveals that the shell first cracks near the supports and the cracking is accelerated by the nonlinear geometry effects in the crown region. A better design is to thicken the shell near the supports and to provide reinforcement against possible local bending.

The use of membrane theory as a design tool must be used with care and the true assessment of the ultimate load capacity can be carried out only by performing a fully nonlinear analysis including both the nonlinear material and geometry and the effects of creep and shrinkage.

10.5 Computer Time

The examples described in this chapter were run on the CDC 7600 computer at the Lawrence Berkeley Laboratory of the University of California, Berkeley. The computer time required in some selected examples are summarized in Table 10.1.

The computing algorithm used by the Lawrence Berkeley Laboratory for the computation of the total job CUS is:

Total CUS = 3* (CP + SS) + 0.5 BLD + ITO

where

CP = actual computer time (seconds) used for executing the problem

SS = system seconds

BLD = LCM buffer loads in computing units (CU). This is a measure of the input-output activities between the central memory and the peripheral storage.

ITO = interference to other jobs (CU).

In general, the SS and the ITO usually contribute a fraction of the total CUS.

The major factors affecting the total CUS are the size of the problem, total number of elements, number of layers used through the thickness, the frequency of reforming the stiffness matrix, and the total number of iterations. For the shell element used in the present study, the total CUS is also a function of the number of integration points across the surface of the shell.

For all the examples studied in this chapter, the stiffness is reformed every iteration. A convergence norm ranging from 5% to 15% of the maximum incremental displacement in the first iteration of an increment is generally used.

Example	Nonlinear Material	Nonlinear Geometry	Time Dependent Creep and Shrinkage	Shell Element			3D Beam Element		No. of Equations	Bandwidth	Total Number of Iterations	CP Time (sec)	BLD (computing units)	Total Job CUS
				No. of Elements	Integration Scheme	No. of Layers of Concrete	No. of Elements	No. of Filaments						
10.2.3	-	Yes	-	6	2 x 2	1*	-	-	154	39	20	16	15	85
10.2.5	-	Yes	-	-	-	-	8	100	48	12	40	13	198	211
10.3.1 (f_y = 120 ksi)	Yes	Yes	-	3	2 x 2	6	-	-	51	27	34	18	16	103
10.3.2 (no horizontal restraint)	Yes	-	-	4	8 point	6	-	-	104	60	27	74	146	357
10.3.2 (with horizontal restraint)	Yes	-	-	4	8 point	6	-	-	102	59	36	96	15	397
10.3.3	Yes	-	Yes	-	-	-	9	10	27	6	17	3	157	141
10.3.3	Yes	Yes	Yes	-	-	-	9	10	27	6	21	4	185	162
10.3.4 (L=200 in.)	Yes	Yes	-	-	-	-	8	100	48	12	27	10	153	163
10.4.1	Yes	-	-	6	2 x 2	6	6	100	148	81	45	218	371	1037
10.4.1	Yes	Yes	-	6	2 x 2	6	6	100	148	81	46	244	377	1142
10.4.2 (2 x 2 mesh)	-	Yes	-	4	2 x 2	6	16	NF	112	67	63	138	822	1056
10.4.2 (2 x 2 mesh)	Yes	-	Yes	4	2 x 2	6	16	NF	112	67	57	130	800	1007
10.4.2 (2 x 2 mesh)	Yes	Yes	Yes	4	2 x 2	6	16	NF	112	67	37	117	654	842
10.4.2 (4 x 4 mesh)	Yes	-	-	16	2 x 2	6	32	NF	384	111	58	508	5651	6471
10.4.2 (4 x 4 mesh)	Yes	Yes	-	16	2 x 2	6	32	NF	384	111	46	421	4344	5073
10.4.2 (4 x 4 mesh)	Yes	Yes	Yes	16	2 x 2	6	32	NF	384	111	40	395	3974	4670

Notes: (1) * Explicit integration is performed through the thickness.

(2) NF: 100 filaments in the edge beam and 10 filaments in the crown beam.

TABLE 10.1 SUMMARY OF IMPORTANT PARAMETERS AND THE COMPUTING EFFORT FOR SOME SELECTED EXAMPLES

As one can see from Table 10.1, the use of low speed storage for the elements' data and the stiffness matrix generally contribute to about 1/2 of the total CUS.

The cost per CUS when the job is run on lowest priority is about 0.0175¢. However, when normal priority is used, the cost would be 0.07¢/CU.

11. SUMMARY AND CONCLUSIONS

11.1 Summary

A numerical method of analysis including both geometric and material nonlinearities has been presented for the analysis of reinforced concrete shells with edge beams under short time and sustained loading. The response of a thin reinforced concrete shell can be traced through its elastic, inelastic and ultimate load ranges.

A finite element displacement formulation coupled with a time step integration solution is used. An iterative scheme based upon constant imposed displacement is used so that structures with local instabilities or strain softenings can also be analyzed.

A layered composite 9-node curved shell element with equivalent smeared steel layers is developed to represent the reinforced concrete shell. Material properties can vary throughout the thickness and across the surface of a shell element.

The edge beam is modelled as a composite 3D filamented reinforced concrete straight beam element with discrete reinforcement. The cross section of the beam is restricted to be rectangular. Material properties are assumed to be constant along the beam element, but they can vary across the cross section.

Material nonlinearities as a result of tensile cracking, tension stiffening between cracks, the nonlinear response of concrete in compression, and the yielding of the reinforcement are considered. The concrete model used is based upon nonlinear elasticity with a uniaxial and a biaxial stress states assumed for the beam and the shell elements, respectively. The steel reinforcement is assumed to be in a uniaxial stress state and is modelled as a bilinear material with strain hardening.

An effective torsional stiffness approach has been used to represent the nonlinear torsional behavior of the beam element.

An updated Lagrangian formulation has been used to take into account the nonlinear geometry effects due to the change in geometry of the structure. The formulation is based upon small strains and small incremental rigid body rotations.

An efficient procedure for the evaluation of creep strain based upon an integral formulation is incorporated. The creep strain increment at the current time step requires only the knowledge of the hidden state variables of the last time step. The key to the success of the creep model lies in the coefficients in the creep compliance function which can be readily determined from the available creep data. Creep under biaxial stress states is represented via the introduction of the creep Poisson's ratio.

Finally, a series of numerical examples analyzed by the computer program, based on the above principles, are presented and compared with the available theoretical and experimental results to demonstrate the applicability and the validity of the present method of analysis.

11.2 Conclusions

1. The present method of analysis has been shown to be capable of predicting the nonlinear response of reinforced concrete beams, plates and shells with edge beams under short time and long time loading fairly accurately.
2. Nonlinear geometry effects have been demonstrated to be significant as they tend to increase the ultimate load in a stiffening system and lower the ultimate load in a softening system.

3. The accurate modelling of the edge beam geometry and its boundary conditions have a decisive influence on the overall structural response.
4. Time dependent effects of creep and shrinkage are shown to be important for certain shell structures. Due to creep and shrinkage, significant stress redistribution occurs between different structural components. When coupled with the nonlinear geometry effects, this will tend to decrease the ultimate load further.
5. Design of shell structures should adequately consider the effects of nonlinear material and geometry, and the time dependent effects of creep and shrinkage. Special attention should be given to minimize the nonlinear geometry effects in a softening system.

11.3 Recommendations

1. A curved beam element compatible with the present shell element can be developed based upon the degeneration concept.
2. Prestressing can be incorporated into the beam element.
3. A multi-linear steel model is required in order to better represent the structural behavior near ultimate load when failure is initiated by yielding of the steel reinforcement.
4. More experimental tests are required on the long time behavior of reinforced concrete shells in order to verify the present analytical results.

REFERENCES

1. Ngo, D. and Scordelis, A. C., "Finite Element Analysis of Reinforced Concrete Beams," ACI Journal, V. 64, No. 3, March 1967.

2. Scordelis, A. C., "Finite Element Analysis of Reinforced Concrete Structures," Proceedings of the Specialty Conference on Finite Element Methods in Civil Engineering, Montreal, June 1972.

3. Scordelis, A.C., "General Report - Basic Problems," Proceedings, IASS Symposium on Nonlinear Behavior of Reinforced Concrete Structures, Darmstadt, West Germany, July 1978.

4. Scordelis, A.C., "Finite Element Modelling of Reinforced Concrete Structures," Seminar on the Finite Element Analysis of Reinforced Concrete Structures, University of Milan, June 1978.

5. Schnobrich, W. C., "Behavior of Reinforced Concrete Predicted by Finite Element Method," Proceedings of the Second National Symposium on Computerized Structural Analysis and Design, George Washington University, Washington, D.C., March 1976.

6. Wegner, R., "Finite Element Models for Reinforced Concrete," Preprint, Proceedings of the U.S.-Germany Symposium on Formulations and Computational Methods in Finite Element Analysis, Massachusetts Institute of Technology, Cambridge, August 1976.

7. Bell, J.C. and Elms, D., "Partially Cracked Finite Elements," Journal of the Structural Division, ASCE, V. 97, No. ST7, July 1971.

8. Lin, C. S., "Nonlinear Analysis of Reinforced Concrete Slabs and Shells," Ph.D. Dissertation, Division of Structural Engineering and Structural Mechanics, University of California, Berkeley, UC-SESM Report No. 73-7, April 1973.

9. Lin, C. S. and Scordelis, A. C., "Nonlinear Analysis of Reinforced Concrete Shells of General Form," Journal of the Structural Division, ASCE, V. 101, No. ST3, March 1975.

10. Hand, F. R., Pecknold, D. A., and Schnobrich, W. C., "Nonlinear Layered Analysis of Reinforced Concrete Plates and Shells," Journal of the Structural Division, ASCE, V. 99, No. ST7, July 1973.

11. Kabir, A. F., "Nonlinear Analysis of Reinforced Concrete Panels, Slabs and Shells for Time Dependent Effects," Ph.D. Dissertation, Division of Structural Engineering and Structural Mechanics, University of California, Berkeley, UC-SESM Report No. 76-6, December 1976.

12. Kabir, A. F. and Scordelis, A. C., "Analysis of RC Shells for Time Dependent Effects," Bulletin of the International Association for Shell and Spatial Structures, V. XXI, No. 69, April 1979.

13. Mueller, G., "Nonlinear Analysis of Reinforced Concrete Hyperbolic Paraboloid Shells," Division of Structural Engineering and Structural Mechanics, University of California, Berkeley, UC-SESM Report No. 77-6, October 1977.

14. Mueller, G., Kabir, A. F., and Scordelis, A. C., "Nonlinear Analysis of Reinforced Concrete Hyperbolic Paraboloid Shells," Proceedings, IASS Symposium on Nonlinear Behavior of Reinforced Concrete Spatial Structures, Darmstadt, West Germany, July 1978.

15. Arnesen, A., "Analysis of Reinforced Concrete Shells Considering Material and Geometric Nonlinearities," Report No. 79-1, Division of Structural Mechanics, University of Trondheim, Norway, July 1979.

16. Floegl, H., "Determination of Ultimate Strength of Thin Reinforced Concrete Shells with the Finite Element Method, Under the Consideration of Real Material Behavior and Geometric Nonlinearities," Ph.D. Dissertation, Institut für Baustatik und Festigkeitslehre de TU-Wien, Vienna, May 1981.

17. Mang, H. A. and Floegl, H., "Tension-Stiffening Concept for Reinforced Concrete Surface Structures," Final Report, "Advanced Mechanics of Reinforced Concrete," IABSE Colloquium, Delft, 1981.

18. Mang, H. A. and Floegl, H., "Analytical Prediction of Short-Term Behavior of Reinforced Concrete Panels, Slabs and Shells," Preprint, ASCE Convention, New York, May 1981.

19. Zienkiewicz, O. C., Taylor, R. L. and Too, J. M., "Reduced Integration Technique in General Analysis of Plates and Shells," International Journal for Numerical Methods in Engineering, V. 3, 1971.

20. Onate, E. and Zienkiewicz, O. C., "Some Problems in the Analysis of Thin Shells Using Isoparametric Shell Elements," Proceedings, IASS World Congress on Shell and Spatial Structures, Madrid, V. 2, 1979.

21. Bathe, K. J., Ramm, E. and Wilson, E. L., "Finite Element Formulations for Large Displacement and Large Strain Analysis," UC-SESM Report No. 73-14, Division of the Structural Engineering and Structural Mechanics, University of California, Berkeley, February 1974.

22. Belytschko, T. and Hsieh, B. J., "Nonlinear Transient Finite Element Analysis with Convected Coordinates," International Journal for Numerical Methods in Engineering, V. 7, 1973.

23. Murray, D. W. and Wilson, E. L., "Finite Element Large Deflection Analysis of Plates," Journal of the Engineering Mechanics Division, ASCE, V. 95, No. EM1, February 1969.

24. Aldstedt, E., "Nonlinear Analysis of Reinforced Concrete Frames," Report No. 75-1, Division of Structural Mechanics, University of Trondheim, Norway, March 1975.

25. Horrigmoe, G., "Finite Element Instability Analysis of Free Form Shells," Report No. 77-2, Division of Structural Mechanics, University of Trondheim, Norway, May 1977.

26. Van Greunen, J., "Nonlinear Geometric, Material and Time Dependent Analysis of Reinforced and Prestressed Concrete Slabs and Panels," Ph.D. Dissertation, Division of Structural Engineering and Structural Mechanics, University of California, Berkeley, UC-SESM Report No. 79-3, October 1979.

27. Malvern, L. E., "Introduction to the Mechanics of a Continuous Medium," Prentice-Hall, 1969.

28. Fung, Y. C., "Foundations of Solid Mechanics," Prentice-Hall, 1965.

29. Novozhilov, V. V., "Foundations of the Nonlinear Theory of Elasticity," Greylock Press, 1953.

30. Yaghmai, S., "Incremental Analysis of Large Deformations in Mechanics of Solids with Application to Axisymmetric Shells of Revolution," Ph.D. Dissertation, Division of Structural Engineering and Structural Mechanics, University of California, Berkeley, UC-SESM Report No. 68-17, December 1968.

31. Bathe, K. J. and Bolourchi, S., "Large Displacement Analysis of Three-Dimensional Beam Structures," International Journal for Numerical Methods in Engineering, V. 14, 1979.

32. Kanoknukulchai, W., "A Large-Deformation Formulation for Shell Analysis by the Finite Element Method," Ph.D. Dissertation, Division of Structural Engineering and Structural Mechanics, University of California, Berkeley, 1978.

33. Noll, W., "A Mathematical Theory of the Mechanical Behavior of Continuous Media," in Continuum Mechanics II - The Rational Mechanics of Materials, edited by Truesdell, C., Science Publishers, Inc., New York, 1965.

34. Krakeland, B., "Large Displacement Analysis of Shells Considering Elasto-Plastic and Elasto-Viscoplastic Materials, Report No. 77-6, Division of Structural Mechanics, University of Trondheim, Norway, December 1977.

35. Søreide, T. H., "Collapse Behavior of Stiffened Plates Using Alternative Finite Element Formulations," Report No. 77-3, Division of Structural Mechanics, University of Trondheim, Norway, June 1977.

36 Kupfer, H. B. and Gerstle, K. H., "Behavior of Concrete Under Biaxial Stresses," Journal of the Engineering Mechanics Division, ASCE, V. 99, No. EM4, August 1973.

37. Aoyama, H. and Noguchi, H., "Mechanical Properties of Steel and Concrete under Load Cycles Idealizing Seismic Actions - Studies on Bond between Concrete and Steel: (b) Concrete," AICAP-CEB Symposium, Rome, May 1979.

38. Argyris, J. H., Faust, G., Szimmat, J., Warnke, E. P. and Willam, K. J., "Recent Developments in the Finite Element Analysis of Prestressed Concrete Reactor Vessels," Nuclear Engineering and Design, V. 28, 1974.

39. Chen, W. F. and Saleeb, A. F., "Constitutive Equations for Engineering Materials - Volume 1: Elasticity and Modelling," John Wiley and Sons, 1982.

40. Chen, A.C.T. and Chen, W. F., "Constitutive Relations for Concrete," Journal of the Engineering Mechanics Division, ASCE, V. 101, No. EM4, August 1975.

41. Epstein, M., Rijub-Agha, K. and Murray, D. W., "A Two-Parameter Concrete Constitutive Law for Axisymmetric Shell Analysis," Proceedings, Symposium on Applications of Computer Methods in Engineering, University of Southern California, August 1977.

42. Murray, D. W., Chitnuyanondh, L., Rijub-Agha, K. Y. and Wong, C., "Concrete Plasticity Theory for Biaxial Stress Analysis," Journal of the Engineering Mechanics Division, ASCE, V. 105, No. EM6, December 1979.

43. Buyukozturk, O., "Nonlinear Analysis of Reinforced Concrete Structures," Computers and Structures, V. 7, 1977.

44. Cervenka, V. and Gerstle, K. H., "Inelastic Analysis of Reinforced Concrete Panels," IABSE Publications, V. 31-II, Zurich, 1971.

45. Valanis, K. C., "A Theory of Viscoplasticity without a Yield Surface," Archiwum Mechaniki Stossowanej, Warsaw, Vol. 23, 1971.

46. Bazant, Z. P., "Endochronic Inelasticity and Incremental Plasticity," International Journal of Solids and Structures, V. 4, 1978.

47. Bazant, Z. P. and Bhat, P. D., "Endochronic Theory of Inelasticity and Failure of Concrete," Journal of the Engineering Mechanics Division, ASCE, V. 102, No. EM4, August 1976.

48. ASCE Committee on Concrete and Masonry Structures, "State-of-the-Art Report on Finite Element Analysis of Reinforced Concrete," ASCE, 1982.

49. Liu, T. C., Nilson, A. H. and Slate, F. O., "Biaxial Stress-Strain Relations for Concrete," Journal of the Structural Division, ASCE, V. 98, No. ST5, May 1972.

50. Darwin, D. and Pecknold, D. A., "Nonlinear Biaxial Stress-Strain Law for Concrete," Journal of the Engineering Mechanics Division, ASCE, V. 103, No. EM2, April 1977.

51. Saenz, L. P., Discussion of "Equation for the Stress-Strain Curve of Concrete," by Desayi, P. and Krishnan, S., ACI Journal, V. 61, No. 9, September 1964.

52. Bashur, F. K. and Darwin, D., "Nonlinear Model for Reinforced Concrete Slabs," CRINC Report No. SL-76-03, University of Kansas Center for Research, Inc., Lawrence, Kansas, December 1976.

53. Elwi, A. A. and Murray, D. W., "A 3D Hypoelastic Concrete Constitutive Relationship," Journal of the Engineering Mechanics Division, ASCE, V. 105, No. EM4, August 1979.

54. Ottosen, N. S., "Constitutive Model for Short Time Loading of Concrete," Journal of the Engineering Mechanics Division, ASCE, V. 105, No. EM1, February 1979.

55. Sargin, M., "Stress-Strain Relationships for Concrete and the Analysis of Structural Concrete Sections," Study No. 4, Solid Mechanics Division, University of Waterloo, Waterloo, Ontario, Canada, 1971.

56. Kupfer, H. B. and Gerstle, K. H., "Behavior of Concrete under Biaxial Stresses," Journal of the Engineering Mechanics Division, ASCE, No. EM4, August 1973.

57. Murray, D. W., "Octahedral Based Incremental Stiffness Matrices," Journal of the Engineering Mechanics Division, ASCE, No. EM4, August 1979.

58. Cedolin, L., Crutzen, Y.R.J. and Poli, S. D., "Stress-Strain Relationship and Ultimate Strength of Concrete under Triaxial Loading Conditions," Journal of the Structural Engineering Mechanics Division," ASCE, No. EM3, June 1977.

59. Kotsovos, M. D. and Newman, J. B., "Generalized Stress-Strain Relations for Concrete," Journal of the Engineering Mechanics Division, ASCE, No. EM4, August 1978.

60. Ramstad, K. M., Taylor, M. A. and Herrmann, L. R., "Numerical Biaxial Characterization for Concrete," Journal of the Engineering Mechanics Division, ASCE, No. EM5, October 1974.

61. Noguchi, H., "Finite Element Nonlinear Analysis of Reinforced Concrete (Part 1: Stress-Strain Relationships for Concrete under Biaxial Stresses)," Transactions of AIJ, No. 252, February 1977.

62. Nelisson, L.J.M., "Biaxial Testing of Normal Concrete," Heron, V. 18, No. 1, 1972.

63. Rajagopal, K. R., "Nonlinear Analysis of Reinforced Concrete Beams, Beam-Columns and Slabs by Finite Elements," Ph.D. Dissertation, Iowa State University, Ames, Iowa, 1976.

64. ACI Committee 209, "Prediction of Creep, Shrinkage, and Temperature Effects in Concrete Structures," Paper SP 27-3, ACI Special Publications SP-27, April 1970.

65. Hognestad, E., "A Study of Combined Bending and Axial Load in Reinforced Concrete Members," Bulletin Series No. 399, Bulletin No. 1, Engineering Experiment Station, University of Illinois, 1951.

66. Karsan, I. D. and Jirsa, J. O., "Behavior of Concrete under Compressive Loadings," Journal of the Structural Division, ASCE, V. 95, No. ST12, December 1969.

67. Ngo, D., "A Network-Topological Approach to the Finite Element Analysis of Progressive Crack Growth in Concrete Members," Ph.D. Dissertation, Division of Structural Engineering and Structural Mechanics, University of California, Berkeley, UC-SESM Report No. 75-6, June 1975.

68. Scanlon, A., "Time Dependent Deflections of Reinforced Concrete Slabs," Ph.D. Dissertation, Department of Civil Engineering, University of Alberta, Edmonton, Canada, December 1971.

69. Gilbert, R. I. and Warner, R. F., "Tension Stiffening in Reinforced Concrete Slabs," Journal of the Structural Division, ASCE, V. 104, No. ST12, December 1978.

70. Argyris, J. H., Pister, K. S. and Willam, K. J., "Thermomechanical Creep of Aging Concrete - A Unified Approach," IABSE Publications, V. 36, 1976.

71. Selna, L. G., "Time Dependent Behavior of Reinforced Concrete Structures," Division of the Structural Engineering and Structural Mechanics, University of California, Berkeley, UC-SESM Report No. 67-19, 1967.

72. Zienkiewicz, O. C. and Watson, M., "Some Creep Effects in Stress Analysis with Particular Reference to Concrete Pressure Vessels," Nuclear Engineering and Design, No. 4, 1966.

73. Mukaddam, M. A. and Bresler, B., "Behavior of Concrete under Variable Temperature and Loading," ACI Special Publication SP-34, 1972.

74. Kang, Y. J., "Nonlinear Geometric, Material and Time Dependent Analysis of Reinforced and Prestressed Concrete Frames," Ph.D. Dissertation, Division of Structural Engineering and Structural

Mechanics, University of California, Berkeley, UC-SESM Report No. 77-1, January 1977.

75. Van Zyl, S. F., "Analysis of Curved Segmentally Erected Prestressed Concrete Box Girder Bridges," Ph.D. Dissertation, Division of Structural Engineering and Structural Mechanics, University of California, Berkeley, UC-SESM Report No. 78-2, January 1978.

76. Becker, J. and Bresler, B., "FIRE-RC, A Computer Program for the Fire Response of Structures - Reinforced Concrete Frames," Division of Structural Engineering and Structural Mechanics, University of California, Berkeley, Report No. UCB FRG 74-3, July 1974.

77. Roll, F., "Long-Time Creep-Recovery of Highly Stressed Concrete Cylinders," ACI Special Publication SP-9, March 1964.

78. Branson, D. E. and Christiason, M. L., "Time-Dependent Concrete Properties Related to Design - Strength and Elastic Properties, Creep and Shrinkage," ACI - Special Publication SP-27, 1971.

79. Branson, D. E., "Deformation of Concrete Structures," McGraw-Hill, 1977.

80. Browne, R., "Properties of Concrete in Reactor Vessels," Proceedings of Conference on Prestressed Concrete Pressure Vessels, Group C, Paper 13, London, 1967.

81. Willam, K., "Finite Element Analysis of Cellular Structures," Ph.D. Dissertation, Division of Structural Engineering and Structural Mechanics, University of California, Berkeley, December 1969.

82. Fonder, G. A. and Clough, R. W., "Explicit Addition of Rigid-Body Motions in Curved Finite Elements," AIAA Journal, V. 11, No. 3, 1973.

83. Cantin, G., "Rigid Body Motions in Curved Finite Elements," AIAA Journal, V. 8, No. 6, 1970.

84. Allman, D. J., "Some Fundamental Aspects of the Finite Element Analysis of Nonlinear Elastic Plate Bending," Proceedings, International Conference on Finite Elements in Nonlinear Mechanics, Geilo, Norway, V. 1, 1977.

85. Razzaque, A., "Program for Triangular Bending Element with Derivative Smoothing," International Journal for Numerical Methods in Engineering, V. 6, No. 3, 1973.

86. Clough, R. W. and Tocher, J. L., "Finite Element Stiffness Matrices for the Analysis of Plate Bending," Proceedings, Conference on Matrix Methods in Structural Mechanics, Wright-Patterson AFB, Ohio, 1965.

87. Felippa, C. A., "Refined Finite Element Analysis of Linear and Nonlinear Two-Dimensional Structures," Ph.D. Dissertation, Division of Structural Engineering and Structural Mechanics, University of California, Berkeley, 1966.

88. Carr, A. J., "A Refined Finite Element Analysis of Thin Shell Structures Including Dynamic Loadings," Ph.D. Dissertation, Division of Structural Engineering and Structural Mechanics, University of California, Berkeley, SESM Report No. 67-9, June 1967.

89. Olson, M. D. and Bearden, T. W., "A Simple Flat Triangular Shell Element Revisited," International Journal for Numerical Methods in Engineering, V. 14, No. 1, 1979.

90. Irons, B. M. and Razzaque, A., "Shape Function Formulations for Elements Other Than Displacement Models," Proceedings, Variational Methods in Engineering, Southhampton, 1972.

91. Johnson, C. P., "The Analysis of Thin Shells by a Finite Element Procedure," Ph.D. Dissertation, Division of Structural Engineering and Structural Mechanics, University of California, Berkeley, UC-SESM Report No. 67-22, September 1967.

92. Pian, T.H.H., "Derivation of Element Stiffness Matrices by Assumed Stress Distribution," AIAA Journal, V. 2, 1964.

93. Allman, D. J., "Triangular Finite Elements for Plate Bending with Constant and Linearly Varying Bending Moments," Proceedings, IUTAM Symposium on the High Speed Computing of Elastic Structures, University of Liege, 1970.

94. Hung, N. D., Detroux, P., Falla, P. and Fonder, G., "Implementation of the Duality in the Finite Element Analysis of Shells: A Mixed Mongrel Planar Shell Element," Proceedings, IASS World Congress on Shell and Spatial Structures, Madrid, V. 2, 1979.

95. Batoz, J. L., "Curved Finite Elements and Shell Theories with Particular Reference to the Buckling of a Circular Arch," International Journal for Numerical Methods in Engineering, V. 14, No. 5, 1979.

96. Thomas, G. R. and Gallagher, R. H., "A Triangular Element Based on Generalized Potential Energy Concepts," Chapter 9 of "Finite Elements for Thin Shells and Curved Members," Edited by Ashwell, D. G. and Gallagher, R. H., Wiley, 1976.

97. Dawe, D. J., "Some Higher Order Elements for Arches and Shells," Chapter 8 of "Finite Elements for Thin Shells and Curved Members," Edited by Ashwell, D. G. and Gallagher, R. H., Wiley, 1976.

98. Dhatt, D. G., "An Efficient Triangular Shell Element," AIAA Journal, V. 8, 1970.

99. Bonnes, G., "Curved Triangular Elements for the Analysis of Shells," Proceedings, Second Conference on Matrix Methods in Structural Mechanics, AFFDL-TR-68-150, Wright-Patterson AFB, Ohio, 1968.

100. Doherty, W. P., Wilson, E. L. and Taylor, R. L., "Stress Analysis of Axisymmetric Solids Utilizing Higher Order Quadrilateral Finite Elements," Report No. UC-SESM 69-3, Division of Structural Engineering and Structural Mechanics, University of California, Berkeley, 1969.

101. Wilson, E. L., Taylor, R. L., Doherty, W. P. and Ghaboussi, J., "Incompatible Displacement Models," International Symposium on Numerical and Computer Methods in Structural Mechanics," University of Illinois, Urbana, September 1971.

102. Dovey, H. H., "Extension of Three-Dimensional Analysis to Shell Structures Using the Finite Element Idealization," Ph.D. Dissertation, Division of Structural Engineering and Structural Mechanics, University of California, Berkeley, UC-SESM Report No. 74-2, January 1974.

103. Ahmad, S., Irons, B. M. and Zienkiewicz, O. C., "Analysis of Thick and Thin Shell Structures by Curved Finite Elements," International Journal for Numerical Methods in Engineering, V. 2, 1970.

104. Kanoknukulchai, W., "A Simple and Efficient Finite Element for General Shell Analysis," Report No. UC-SESM 78-1, Division of Structural Engineering and Structural Mechanics, University of California, Berkeley, January 1978.

105. Irons, B. M., "The Semiloof Shell Element," Chapter 11 of "Finite Elements for Thin Shells and Curved Members," Edited by Ashwell, D. G. and Gallagher, R. H., Wiley, 1976.

106. Talha, M. A., "A Theoretically Improved and Easily Implemented Version of the Ahmad Thick Shell Element," International Journal for Numerical Methods in Engineering, V. 14, No. 1, 1979.

107. Pawsey, S. F., "The Analysis of Moderately Thick to Thin Shells by the Finite Element Method," Ph.D. Dissertation, Division of Structural Engineering and Structural Mechanics, University of California, Berkeley, UC-SESM Report No. 70-12, August 1970.

108. Scordelis, A. C. and Lo, K. S., "Computer Analysis of Cylindrical Shells," ACI Journal, V. 61, 1964.

109. Zienkiewicz, O. C., "The Finite Element Method," Third Edition, McGraw-Hill, 1977.

110. Hibbitt, H. D., Marcal, P. V. and Rice, J. R., "A Finite Element Formulation for Problems of Large Strain and Large Displacement," International Journal of Solids and Structures, V. 6, 1970.

111. Chang, S. C., "An Integrated Finite Element Nonlinear Shell Analysis System with Interactive Computer Graphics," Ph.D. Dissertation, Department of Structural Engineering, Cornell University, New York, Report No. 81-4, February 1981.

112. Hughes, T.J.R. and Kanoknukulchai, W., "A Simple and Efficient Finite Element for Plate Bending," International Journal for Numerical Methods in Engineering, V. 11, 1977.

113. Hinton, E. and Bicanic, N., "A Comparison of Lagrangian and Serendipity Mindlin Plate Elements for Free Vibration Analysis," Computers and Structures, V. 10, 1979.

114. Hughes, T.J.R., Cohen, M. and Haroun, M., "Reduced and Selective Integration Techniques in the Finite Element Analysis of Plates," Nuclear Engineering and Design, V. 46, 1978.

115. Hughes, T.J.R. and Cohen, M., "The Heterosis Finite Element for Plate Bending," Computers and Structures, V. 9, 1978.

116. Sørensen, S. I., "Endochronic Theory in Nonlinear Finite Element Analysis of Reinforced Concrete," Report No. 78-1, Division of Structural Mechanics, University of Trondheim, Norway, March 1978.

117. Elwi, A. A., "Nonlinear Analysis of Reinforced Concrete," Ph.D. Dissertation, Department of Civil Engineering, University of Alberta, Edmonton, Alberta, 1980.

118. Schnobrich, W. C., "Analysis of Hipped Roof Hyperbolic Paraboloid Structures," Journal of the Structural Division, ASCE, V. 98, No. ST7, July 1972.

119. Jackson, A. T., "Finite Element Analysis of Compressive Membrane Action in Slabs," Ph.D. Dissertation, Department of Civil Engineering, University of Auckland, Auckland, New Zealand, Report No. 207, June 1979.

120. Timoshenko, S. P. and Goodier, J. N., "Theory of Elasticity," McGraw-Hill, 1970.

121. Lampert, P., "Post-Cracking Stiffness of Reinforced Concrete Beams in Torsion and Bending," ACI Special Publication No. SP-35, 1973.

122. Collins, M. P. and Lampert, P., "Redistribution of Moments at Cracking - The Key to Simpler Torsion Design," ACI Special Publication No. SP-35, 1973.

123. Dahlquist, G. and Gjörck, A., "Numerical Methods," translated by Anderson, N., Prentice-Hall, 1974.

124. Bergan, P., "Solution Techniques for Nonlinear Finite Element Problems," International Journal for Numerical Methods in Engineering, V. 12, 1978.

125. Argyris, J. H., "Continua and Discontinua," Proceedings, First Conference on Matrix Methods in Structural Mechanics, Wright-Patterson AFB, Ohio, 1965.

126. Whiteman, E. and Gaylord, E. H., "Analysis of Unbalanced Multistory Steel Rigid Frames," Proceedings of ASCE, May 1968.

127. Sharifi, P., "Nonlinear Analysis of Sandwich Structures," Ph.D. Dissertation, Division of Structural Engineering and Structural Mechanics, University of California, Berkeley, 1971.

128. Bergan, P., "Solution Algorithms for Nonlinear Structural Problems," Proceedings, International Conference on Engineering Applications of the Finite Element Method, Hovik, Norway, May 1979.

129. Powell, G. and Simons, J., "Improved Iteration Strategy for Nonlinear Structures," internal report, Division of Structural Engineering and Structural Mechanics, University of California, Berkeley, April 1980.

130. Frey, F., "L'analyse Statique Non Lineaire des Structures par la Methode des Elements Finis et Son Application a la Contruction Metallique," These de Doctorat, Lab. Mec. Mat. et Stat. Constr., Universite de Liege, 1978.

131. Batoz, J. L. and Dhatt, G., "Incremental Displacement Algorithms for Nonlinear Problems," International Journal for Numerical Methods in Engineering, V. 14, 1979.

132. Ramm, E., "Strategies for Tracing the Nonlinear Response Near Limit Points," Reprint from "Nonlinear Finite Element Analysis in Structural Mechanics," Proceedings of the Europe-U.S. Workshop, Ruhr-Universität Bochum, Germany, July 1980.

133. Crisfield, M. A., "A Fast Incremental/Iterative Solution Procedure that Handles Snap-Through," Proceedings, Computational Methods in Nonlinear Structural and Solid Mechanics, Washington, October 1980.

134. Riks, E., "An Incremental Approach to the Solution of Snapping and Buckling Problems," International Journal of Solids and Structures, V. 15, 1979.

135. Wempner, G. A., "Discrete Approximations Related to Nonlinear Theories of Solids," International Journal of Solids and Structures, V. 7, 1971.

136. Wilson, E. L., Bathe, K. J. and Doherty, W. P., "Direct Solution of Large Systems of Linear Equations," Computers and Structures, V. 4, 1974.

137. Wilson, E. L., "SOLID SAP - A Static Analysis Program for Three-Dimensional Solid Structures," UC-SESM Report No. 71-19, Department of Structural Engineering and Structural Mechanics, University of California, Berkeley, September 1971, revised December 1972.

138. Bathe, K. J., Wilson, E. L. and Peterson, F. E., "SAP IV - A Structural Analysis Program for Static and Dynamic Response of Linear Systems," EERC Report No. 73-11, College of Engineering, University of California, Berkeley, June 1973, revised April 1974.

139. Levy, S., "Bending of Rectangular Plates with Large Deflections," NACA Technical Note 846, 1942.

140. Schreyer, H. and Masur, E., "Buckling of Shallow Arches," Journal of the Engineering Mechanics Division, ASCE, V. 92, No. EM4, August 1966.

141. Leicester, R. H., "Finite Deformations of Shallow Shells," Journal of the Engineering Mechanics Division, ASCE, V. 94, No. EM6, December 1968.

142. Dhatt, G. S., "Instability of Thin Shells by the Finite Element Method," IASS Symposium for Folded Plates and Prismatic Structures, Vienna, 1970.

143. Jofriet, J. C. and McNiece, G. M., "Finite Element Analysis of Reinforced Concrete Slabs," Journal of the Structural Division, ASCE, V. 97, No. ST3, March 1971.

144. Hellesland, J. and Green, R., "Sustained and Cyclic Loading of Concrete Columns," Journal of the Structural Division, ASCE, No. ST4, April 1971.

145. Warner, R. F., "Long Reinforced Concrete Columns in Biaxial Bending," IABSE Publications, V. 29-I, 1969.

146. Bouma, A. L., Van Riel, A. C., Van Koten, H. and Beranek, W. J., "Investigations on Models of Eleven Cylindrical Shells Made of Reinforced and Prestressed Concrete," Symposium on Shell Research, Delft, 1961.

APPENDIX A - COMPUTER PROGRAM NASHL

University of California Department of Civil Engineering
November 1982 Faculty Investigator: A. C. Scordelis

COMPUTER PROGRAM FOR THE NONLINEAR ANALYSIS OF REINFORCED CONCRETE SHELLS WITH EDGE BEAMS

IDENTIFICATION:

NASHL - Nonlinear Analysis of Reinforced Concrete SHelLs with Edge Beams

Programmed by: E. C. Chan, University of California, Berkeley, 1982

PURPOSE:

The computer program has been developed to trace the quasi-static response of reinforced concrete shells of arbitrary shape and with edge beams under instantaneous and sustained loading. Nonlinear material and geometry, and the time dependent effects of creep and shrinkage are included. The shell element and the beam element can be used separately if desired. The types of analysis that can be performed by the computer program are:

1. Linear analysis
2. Linear bifurcation (buckling) analysis
3. Analysis with nonlinear material only
4. Analysis with nonlinear material and geometry

DESCRIPTION:

A finite element displacement formulation coupled with a time step integration solution is used to trace the quasi-static response of reinforced concrete shells with edge beams.

A layered composite 9-node curved shell element with smeared steel layers is used for the shell while a composite 3D filamented reinforced concrete beam element with discrete reinforcement is used for the edge beam.

Material nonlinearities as a result of tensile cracking, tension stiffening between cracks, the nonlinear response of concrete in compression, and the yielding of the reinforcement are considered. A concrete model based upon nonlinear elasticity is used. The steel is modelled as a bilinear material with strain hardening. The nonlinear torsional response of the beam element is represented by an effective torsional stiffness approach.

The effects of creep and shrinkage are also included. The model recognizes the time dependent variation of the concrete strength. For creep under biaxial stress states, a creep Poisson's ratio is introduced.

The program is coded in FORTRAN IV and has been tested on the CDC 7600 computer of the University of California, Berkeley. The blank common is dynamically dimensioned within the program so that the central memory can be utilized efficiently. The storage of the equations in block form allows the solution of a large structural problem.

RESTRICTIONS:

The size of the problem to be solved is only restricted by the available capacity of the computer. Additional restrictions will be given in the input instructions.

FORMAT OF INPUT DATA:

The input data is punched on cards in fixed format as specified. The cards must be in sequential order and consistent units must be used throughout the input.

An asterisk (*) appears before all steel reinforcement data in the input that follows - These cards must be omitted if no reinforcement is within the structure.

1. TITLE CARD (12A6)

Col. 1-72	HED	-	title of the problem to be printed with output

2. CONTROL CARD (11I5)

Col. 1-5	NUMNP	-	number of nodes
5-10	NELTYP	-	number of element types (max.= 3)
11-15	NTIME	-	number of time steps where analysis is required (max. = 30)
16-20	ICREEP	-	creep analysis indicator 0 = no analysis 1 = analysis required
21-25	ISHRINK	-	shrinkage analysis indicator 0 = no analysis 1 = analysis required
26-30	NORM	-	convergence norm code 0 = force norm 1 = displacement norm
31-35	KNORM	-	code for the norm data 0 = input fraction of absolute maximum component in the increment of external load vector in a step or the displacement increment in the first iteration within a step 1 = input the absolute values
36-40	KULT	-	ultimate (maximum) load analysis code 0 = not required 1 = required
41-45	ITNTYP	-	iteration type code 0 = constant stiffness iteration 1 = stiffness is reformed at the first iteration only 2 = stiffness is reformed at every iteration
46-50	KGCODE	-	geometric stiffness code 0 = not included 1 = included

Col. 51-55 IANAL - analysis type code

1 = linear analysis
2 = linear bifurcation analysis
3 = analysis with nonlinear material
4 = analysis with nonlinear material and geometry

Note:

2.1 Only proportional load will be considered in the linear bifurcation buckling analysis.

2.2 NTIME should be set equal to 1 for a linear analysis (IANAL=1) or a linear bifurcation buckling analysis (IANAL=2).

2.3 NTIME steps greater than 1, can also be used to increment NTIME load steps in a nonlinear monotonic increasing load analysis at a particular time. In this case, the DAYS(1) in the DAY CARD are all set to equal values and RMAX in paragraph 11.1 should be set to a large value.

2.4 A combination of a time dependent analysis and a monotonic increasing load analysis is possible where NTIME equals the sum of all the time steps and all the load steps.

2.5 KULT = 1 will terminate a nonlinear solution when the load-deflection curve passes its first zero slope (the stiffness matrix is nonpositive semi-definite). KULT = 0 permits load or displacement increments beyond this point.

3. BIFURCATION ANALYSIS CONTROL CARD (I5,2E10.3)

A blank card is required for analysis other than bifurcation analysis.

Col. 1-5 NITNV - maximum number of iterations allowed in inverse iteration

Col. 6-15 TOLV - convergence tolerance, expressed as $(\omega_j - \omega_{j-1})/\omega_j$, where ω_j is the smallest eigenvalue at the i^{th} iteration

16-25 PSHIFT - shifting in the eigenvalue when performing inverse iteration

Note:

3.1 The maximum number of iterations, NITNV, depends on a particular problem, the choice of PSHIFT and the convergence criterion. Usually, the solution should converge within 10 iterations.

3.2 The convergence tolerance, which gives the relative change in the smallest eigenvalue between two successive iterations, should be set to a small value, say 0.001.

3.3 PSHIFT may be set equal to an estimate of the magnitude of the smallest eigenvalue if it is known. This will speed up the convergence. However, if it is unknown, PSHIFT is generally set equal to zero.

3.4 PSHIFT can also be used to find the j^{th} eigenvalue when PSHIFT is set close to ω_j. Since ω_j has to be found by some other means, this option is generally not recommended.

4. OUTPUT CONTROL CARD (2I5)

Col. 1-5 KOUT - output indicator

0 = complete output is only required at the end of all iterations within each load or displacement step

1 = complete output is required for every iteration

6-10 KITER - output code for displacements and unbalanced forces

0 = output at the end of all iterations

1 = output for every iteration

5. CONVERGENCE NORM CARDS

Two cards are required. The values correspond to the type of norm specified in NORM and are input according to KNORM.

5.1 CONVERGENCE TOLERANCES (6E10.3)

Col.	1-10	TOLER(1)	- tolerance for force or displacement in global X-direction
	11-20	TOLER(2)	- tolerance for force or displacement in global Y-direction
	21-30	TOLER(3)	- tolerance for force or displacement in global Z-direction
	31-40	TOLER(4)	- tolerance for moment or rotation about global X-direction or shell surface tangent vector $\underset{\sim}{V}_1$
	41-50	TOLER(5)	- tolerance for moment or rotation about global Y-direction or shell surface tangent vector $\underset{\sim}{V}_2$
	51-60	TOLER(6)	- tolerance for moment or rotation about global Z-direction or shell surface normal vector $\underset{\sim}{V}_3$

Note:

5.1.1 Convergence is achieved if these tolerances are satisfied.

5.2 MAXIMUM ALLOWABLE VALUES (6E10.3)

Col.	1-10	VMAX(1)	- maximum force or displacement in global X-direction
	11-20	VMAX(2)	- maximum force or displacement in global Y-direction
	21-30	VMAX(3)	- maximum force or displacement in global Z-direction
	31-40	VMAX(4)	- maximum moment or rotation about global X-direction or shell surface tangent vector $\underset{\sim}{V}_1$
	41-50	VMAX(5)	- maximum moment or rotation about global Y-direction or shell surface tangent vector $\underset{\sim}{V}_2$

Col. 51-60 VMAX(6) - maximum moment or rotation about global Z-direction or shell surface normal vector $\underset{\sim}{V}_3$

Note:

5.2.1 The solution diverges and is stopped if any of the maximum allowable values is exceeded.

6. DAYS CARD (8F10.0)

Col. 1-80 DAYS(I) - days after casting at which time each analysis is required. Total number of entries equals NTIME+1.

Note:

6.1 Time dependent analysis will be skipped for the time step when two consecutive days (DAYS(I) and DAYS(I+1)) are set equal. This is used for incrementing load at a particular time.

7. TEMPERATURE CARD (8F10.0)

Col. 1-80 TEMPI(I) - ambient temperature in degrees at time DAYS(I). Total number of entries equals NTIME+1.

Note:

7.1 This is used to permit an analysis including temperature effects. These include the thermal induced strains due to change in temperature and the creep response at elevated temperature as governed by the temperature shift function $\phi(T)$, $T > T_o$, and T_o is the reference temperature (TEMPO in paragraph 9.2.3.1) for which the creep curve is given.

7.2 Analysis including temperature effects can only be performed when ICREEP and/or ISHRINK in paragraph 2 are/is set equal to 1.

8. NODAL POINT COORDINATE CARDS (7I5,3F10.0,I5,F10.0)

Col. 1-5	N	-	node number
6-10	ID(1,N)	-	code for translation in global X-direction
11-15	ID(2,N)	-	code for translation in global Y-direction
16-20	ID(3,N)	-	code for translation in global Z-direction
21-25	ID(4,N)	-	code for rotation about global X-direction or shell surface vector $\underset{\sim}{V}_1$
26-30	ID(5,N)	-	code for rotation about global Y-direction or shell surface vector $\underset{\sim}{V}_2$
31-35	ID(6,N)	-	code for rotation about global Z-direction or shell surface vector $\underset{\sim}{V}_3$

Boundary Condition Code:
- 0 - free to displace in the prescribed direction
- 1 - fixed against displacement in the prescribed direction
- >1 - slave node, input the master node number

36-45	X(N)	-	X-coordinate
46-55	Y(N)	-	Y-coordinate
56-65	Z(N)	-	Z-coordinate
66-70	KN	-	generation parameter
71-80	T(N)	-	shell thickness at node N, leave blank for node not belonging to a shell element

Note:

8.1 The nodes do not have to be in sequential order. However, the node with the largest number must be the last to be input, and all nodes which are not slaved must be numbered before the slave nodes.

8.2 The rotational degrees of freedom in the shell elements are defined with respect to the surface vectors $\underset{\sim}{V}_1$, $\underset{\sim}{V}_2$,

and $\underset{\sim}{V}_3$. The three vectors obtained following the procedure described in Chapter 6 form a right-hand system, where $\underset{\sim}{V}_1$ and $\underset{\sim}{V}_2$ are tangent to the shell surface and V_3 normal to it (Fig. A1). For the rotational degrees of freedom not belonging to a shell element, the global X,Y,Z coordinate system is used.

8.3 The slave node does not have any independent degrees of freedom and its displacements are completely described by the degrees of freedom in the global X,Y,Z coordinate of the master node.

8.4 The generation parameter KN appeared on the last card in a sequence and is used to generate the nodal point data of intermediate nodes. The node number in the generated node is incremented by KN such that $N_i = N_{i-1} + KN$. The nodal point coordinates are located at equal intervals. The boundary conditions for the generated nodes are set equal to that of the first node in the series. The generation will continue until N_i is equal to the last node number in the series.

8.5 When analyzing plates and shells using the shell elements, the inplane normal rotation about the $\underset{\sim}{V}_3$ vector should be constrained. However, this degree of freedom should remain free when a symmetry constraint is imposed by the use of boundary spring elements.

9. MATERIAL PROPERTIES CARDS

9.1 CONTROL CARD (3I5)

Col. 1-5 NUMCN - number of types of concrete material (max. = 4)

6-10 NUMST - number of types of steel material (max. = 6)

11-15 ITSF - code for tension stiffening in the concrete

0 = ignore tension stiffening
1 = use the default values (Fig. A3)
2 = input tension stiffening factors (Fig. A3)

9.2 CONCRETE PROPERTIES CARDS

A series of cards are repeated for NUMCN times.

9.2.1 CONCRETE PROPERTY INDICATORS (4I5,4F10.0)

Col. 1-5 I - concrete material type number

6-10 JMT(I) - concrete material data indicator

1 = input value
2 = use ACI formulae

11-15 JCR(I) - creep data indicator

1 = input value
2 = use ACI formulae

16-20 JSH(I) - shrinkage data indicator

1 = input data
2 = use ACI formulae

21-30 FC28(I) - compressive strength at 28 days after casting (psi when ACI formulae used above)

31-40 CNU(I) - Poisson's ratio

41-50 RHO(I) - weight per unit volume (pcf when ACI formulae used above)

51-60 CTEMP(I) - coefficient of thermal expansion (default = $5.5 \times 10^{-6}/°F$)

9.2.2 ELASTIC MATERIAL PROPERTIES (5F10.0)

Omit if JMT(I) = 2, otherwise input the concrete properties in absolute values at time = DAYS(1).

Col. 1-10	EC(I)	-	uniaxial modulus of elasticity, E_o
11-20	FCC(I)	-	uniaxial compressive strength, f'_c
21-30	FTC(I)	-	uniaxial tensile strength, f'_t
31-40	CSC(I)	-	crack shear constant, α
41-50	USC(I)	-	uniaxial ultimate strain in compression, ε_{cu}

Note:

9.2.2.1 The parameters E_o, f'_c, f'_t and ε_{cu} are used to define the shape of the uniaxial stress-strain curve as shown in Fig. A2. For a linear material, f'_c and f'_t are input as large values while ε_{cu} is arbitrarily set to $\gamma \cdot f'_c/E_o$, $\gamma \geq 2.0$.

9.2.3 CREEP DATA CARDS

Omit if JCR(I) = 2, otherwise the creep coefficients $a_i(\tau)$ and λ_i obtained from experimental data by using the procedure described in Chapter 4 are to be input.

9.2.3.1 CONTROL PARAMETERS (2I5,F10.0)

Col. 1-5	NAGE(I)	-	number of ages at which the creep curves are provided (max. = 15)
6-10	NSER(I)	-	number of terms in the creep compliance series (max. = 3)
11-20	TEMPO(I)	-	reference temperature T_o for creep curves (default = 68°F)

9.2.3.2 CONCRETE AGES (8F10.0)

Col. 1-80 SAGE(I,J) - ages at which creep curves are provided (use as many cards as required)

9.2.3.3 AGE SCALE FACTORS, $a_i(\tau)$ (3E15.6)

Col. 1-45 ACI(I,M,N) - age scale factor $a_i(\tau)$ for the creep compliance function (input row-wise for $a_i(\tau)$ at each age τ for every λ_i, a total of M×N = NAGE(I) × NSER(I) for each concrete material I)

9.2.3.4 CREEP EXPONENTIAL FACTORS, λ_i (3F10.0)

Col. 1-30 W1(I,J) - creep exponent factors (J=1,NSER(I))

9.2.3.5 TEMPERATURE SHIFT COEFFICIENTS, $\phi(T)$ (4F10.0)

Col. 1-40 W2(I,J) - coefficients c_i in the polynomial approximation of the temperature shift function $\phi(T)$, in which $\phi(T) = c_0 + c_1 r + c_2 r^2 + c_3 r^3$, $r = T/T_0$ and T is the ambient temperature described in paragraph 7

9.2.4 SHRINKAGE DATA CARDS (3E15.8)

Omit if JSH(I) = 2.

Col. 1-45 TEPSS(I,J) - total shrinkage strains at days J (J=1,NTIME+1) when analysis is needed (use as many cards as required)

9.2.5 CONCRETE MIX PARAMETERS (3F10.0)

Col. 1-10 SLUMP(I) - slump of concrete in inches (2.7 in. for standard condition)

11-20 SIZE(I) - minimum size or thickness of members in inches (6.0 in. for standard condition)

21-30 RH(I) - percentage relative ambient humidity (40.0 for standard condition)

*9.3 TENSION STIFFENING FACTOR CARDS

Omit if ITSF = 0 or 1, otherwise 2 cards are required. This set of tension stiffening factors is assumed to be valid for all types of concrete and steel.

9.3.1 STRAIN RATIO, $\varepsilon_s/\varepsilon_t$ (6E10.3)

Col. 1-60 EP(I) - multiples of concrete tensile cracking strain ε_t at which the tension stiffening factor changes

9.3.2 TENSION STIFFENING FACTOR (6E10.3)

Col. 1-60 TSF(I) - tension stiffening factors in the steel for each ratio of $\varepsilon_s/\varepsilon_t$

Note:

9.3.1 The modified stress-strain relationship for the steel is shown in Fig. A3 together with the default tension stiffening factors.

*9.4 STEEL MATERIAL PROPERTY CARD (I5,5E10.3)

This card is to be repeated for NUMST times. No card is required for NUMST = 0.

Col. 1-5	N	-	steel material type number
6-15	ES(N)	-	initial modulus, E_s
16-25	FYS(N)	-	yield stress, f_y
26-30	ESTAR(N)	-	strain hardening modulus, E_{sh}
31-40	ESU(N)	-	ultimate strain at failure, ε_{su}
41-50	STEMP(N)	-	coefficient of thermal expansion (default = 6.5×10^{-6}/°F)

Note:

9.4.1 A typical stress-strain curve for steel is shown in Fig. A4.

10. ELEMENT GROUP CARDS

A series of cards is required for each element type in the structure. The element group need not be in sequential order, and the input format will be described later.

11. LOAD CARDS

This series of cards is to be repeated for NTIME times. The load vector thus formed is the reference load for each time step.

11.1 ITERATION CONTROL CARD (9I5,2F10.0,I5)

For linear or linear bifurcation analysis, use one blank card.

Col.	1-5	N	- joint number with imposed displacement
	6-10	IX(1)	- constraint code for displacement in global X-direction
	11-15	IX(2)	- constraint code for displacement in global Y-direction
	16-20	IX(3)	- constraint code for displacement in global Z-direction
	21-25	IX(4)	- constraint code for rotation about global X-direction or surface vector $\underset{\sim}{V}_1$
	26-30	IX(5)	- constraint code for rotation about global Y-direction or surface vector $\underset{\sim}{V}_2$
	31-35	IX(6)	- constraint code for rotation about global Z-direction (rotation about $\underset{\sim}{V}_3$ vector must not be constrained)
Constraint Code		IX(I):	0 = free 1 = constrained
	36-40	NITER	- maximum number of iterations in a step
	41-45	NLJ	- number of loaded nodes
	46-55	RMAX	- maximum displacement increment allowed to be imposed in a displacement step (the direction of RMAX has to be known)

Col. 56-65 PFMAX - maximum external load increment that can be imposed on the structure in a displacement step (must be a +ve value)

66-70 NLSTEP - maximum number of displacement steps allowed in a time step

Note:

11.1.1 There should only be a single degree of freedom constrained within the structure for which imposed displacement increments will be applied.

11.1.2 In each displacement step, the constrained degree of freedom will be increased by RMAX. The corresponding increase in the external load must not exceed PFMAX. Otherwise the iteration will be carried out for constant external load increment equal to PFMAX rather than the imposed displacement.

11.1.3 The solution will proceed to the next time step at the end of NLSTEP displacement increments or when PFMAX is reached.

11.1.4 Iteration with constant external load may be achieved by inputting the desired load increment equal to PFMAX and setting RMAX to a large value. For monotonic increasing load, DAYS(I) and DAYS(I+1) are set equal to each other.

11.1.5 Time dependent analysis with no increase in the external load within a time step requires the input of NITER only. PFMAX must be set to zero.

11.2 CONCENTRATED NODAL LOAD CARDS (I5,6F10.0)

Omit if NLJ = 0, otherwise one card must be provided for every loaded node. Sequential ordering is not essential.

Col.	1-5	N	- node number
	6-15	RB(1)	- concentrated load in global X-direction
	16-25	RB(2)	- concentrated load in global Y-direction
	26-35	RB(3)	- concentrated load in global Z-direction
	36-45	RB(4)	- concentrated moment about global X-direction or surface vector $\underset{\sim}{V}_1$
	46-55	RB(5)	- concentrated moment about global Y-direction or surface vector $\underset{\sim}{V}_2$
	56-65	RB(6)	- concentrated moment about global Z-direction (must be zero for moment about the surface vector $\underset{\sim}{V}_3$)

11.3 ELEMENT DISTRIBUTED LOAD MULTIPLIER CARD (5F10.0,I5)

One blank card is required if there are no distributed loads. The distributed loads as specified in the element cards are added to the joint loads to obtain total reference external load on the structure.

Col.	1-10	FM(1)	- multiplier for pressure in global X-direction
	11-20	FM(2)	- multiplier for pressure in global Y-direction
	21-30	FM(3)	- multiplier for pressure in global Z-direction
	31-40	FM(4)	- multiplier for the gravity load (+ve for load acting in the -ve global Z-direction)
	41-50	FM(5)	- multiplier for the normal pressure (used only by the shell element)

Col. 51-55 ICNSERV - code for loading type

0 = conservative
1 = nonconservative

10. ELEMENT GROUP CARDS

A. TYPE 1 - REINFORCED CONCRETE SHELL ELEMENT

A.1 CONTROL CARD (3I5)

Col. 1-5	MTYPE	-	element type identifier, MTYPE=1
6-10	NUMSHL	-	number of shell elements
11-15	NTSL	-	number of steel reinforcing patterns (max. = 10)

Note:

A.1.1 For shell element without reinforcement, NTSL must be input as zero.

A.2 INTEGRATION SCHEME CARD (I5,F10.0)

Col. 1-5	NINT	-	number of integration points across the shell surface
6-15	W(2)	-	integration parameter

Note:

A.2.1 Three options are provided,

(1) 2 x 2 Gaussian quadrature (used when 24*NUMSHL $\geq$ available DOF or whenever possible)

NINT = 4, W(2) = 0.0

(2) 3 x 3 Gaussian quadrature (generally not recommended)

NINT = 9, W(2) need not be input

(3) 8-point rule (used if 2 x 2 Gaussian quadrature fails)

NINT = 8, $0.0 \leq W(2) \leq 40/49$

W(2) = 40/49 for W(2) input as 3.0

W(2) = 0.0001 is recommended

*A.3 REINFORCEMENT ARRANGEMENT CARDS

This series of cards is to be repeated for NTSL times.

A.3.1 CONTROL CARD (2I5)

Col. 1-5 L - type of reinforcement pattern

6-10 NSLAY(L) - number of smeared steel layers in type L

A.3.2 REINFORCEMENT LAYOUT CARD (3I5,3F10.0,I5)

One card is required for each reinforcing layer. See Fig. A5.

Col. 1-5 J - layer number

6-10 MTN(J) - steel material type

11-15 IDC(J) - reinforcing direction code
0 = reinforced in both orthogonal directions $\underset{\sim}{A}$ and $\underset{\sim}{B}$
1 = reinforced in $\underset{\sim}{A}$ direction only
2 = reinforced in $\underset{\sim}{B}$ direction only

16-25 ZS(L,J) - coordinate of the reinforcing layer measured from mid-depth (+ve in the z' direction)

26-35 PS(L,J) - smeared thickness of the reinforcing layer

36-45 ALPH(L,J) - angle in degrees in the global XY plane measured from X axis, which defines the reinforcing direction $\underset{\sim}{A}$ (set equal to 0.0 when both directions $\underset{\sim}{A}$ and $\underset{\sim}{B}$ coincide with local $\tilde{x}'$ and $\tilde{y}'$, and set equal to 180.0 when the projection of $\underset{\sim}{A}$ on the XY plane makes 0.0 degree with the X axis

46-50 NLCI(J) - integration station closest to the reinforcement layer (Fig. A5)

Note:

A.3.2.1 The reinforcing direction $\underset{\sim}{A}$ is defined by the angle ALPH(L,J) (Angle θ in Fig. A5) so that $\underset{\sim}{A}$ is tangent to the shell surface in the plane defined by vectors $\underset{\sim}{Z}$ and $\underset{\sim}{C}$, in which $\underset{\sim}{Z}$ is parallel to the global Z axis

and $\underset{\sim}{C}$ lies in the global XY plane. $\underset{\sim}{B}$ is tangent to the shell surface and is normal to $\underset{\sim}{A}$.

A.3.2.2 The local Cartesian axes x', y', and z' at a point are defined so that x' is parallel to the isoparametric ξ line, z' is normal to the shell surface, and y' is normal to both x' and z' (Fig. A5).

A.3.2.3 integration stations are increased in the direction of -ve z' local axis (Fig. A5).

A4. ELEMENT CARDS

Two cards are required for each shell element.

A.4.1 ELEMENT ARRANGEMENT CARD (13I5,F10.0)

Col.			
1-5	NE	-	element number
6-10	IX(1)	-	node N1
11-15	IX(2)	-	node N2
16-20	IX(3)	-	node N3
21-25	IX(4)	-	node N4
26-30	IX(5)	-	node N5
31-35	IX(6)	-	node N6
36-40	IX(7)	-	node N7
41-45	IX(8)	-	node N8
46-50	IX(9)	-	node N9
51-55	MCT(NE)	-	concrete material type
56-60	NCL(NE)	-	number of equal concrete layers, must be an even number (max. = 6)
61-65	ISC(NE)	-	code for the reinforcement 0 = no reinforcement 1 = reinforcement exists
66-70	ANGLO(NE)	-	angle in degrees in the global XY plane defining the direction

of desired output stresses (Fig. A5) (< 0.0 if stresses are output in the local x', y' and z' coordinate system)

Note:

A.4.1.1 The ordering of nodes, N1 to N9, (Fig. A5), must be strictly adhered to following a counter-clockwise direction.

A.4.1.2 In curved shells, the interpretation of the stress directions may be difficult, a prescribed direction may be used if desired. The stress output directions A and B are characterized by the angle ANGLO(NE) (Angle θ in Fig. A5) in the global XY plane.

A.4.1.3 The line joining nodes N9 and N8 gives the approximate x' direction.

A.4.2 ELEMENT DISTRIBUTED LOAD CARD (5F10.0)

Col.	1-10	ELD(1)	- pressure (force per unit area) in global X-direction on YZ plane (+ve in the X-direction)
	11-20	ELD(2)	- pressure (force per unit area) in global Y-direction on XZ plane (+ve in the Y-direction)
	21-30	ELD(3)	- pressure (force per unit area) in global Z-direction on XY plane (+ve in the Z-direction)
	31-40	ELD(4)	- weight density of the shell
	41-50	ELD(5)	- pressure normal to the shell surface (+ve in the z' direction)

*A5. REINFORCEMENT DISTRIBUTION CARDS (9I5)

The type of reinforcement pattern at each of the integration points over the shell surface has to be input for every shell element.

The series of cards are ordered sequentially from the first element to the last element.

Col. 1-45 NSTYP(J) - reinforcement pattern type at integration point J (J = 1, NINT)

Note:

A.5.1 NSTYP(J) = 0 when no reinforcement exists at an integration point J.

A.5.2 The location of the integration points are shown in Fig. A6. However, the exact location need not be known in general. Note that their locations are dependent on the numbering of nodes N1 to N9.

B. TYPE 2 - BOUNDARY SPRING ELEMENT

B.1 CONTROL CARD (2I5)

Col. 1-5 MTYPE - element type identifier, MTYPE = 2

6-10 NUMBD - number of boundary spring elements

B.2 ELEMENT CARD (8I5,E10.3)

One card is required for each element unless automatic data generation is used.

Col. 1-5 IBJ(1) - node NP at which element is placed

6-10 IBJ(2) - node I
11-15 IBJ(3) - node J
16-20 IBJ(4) - node K
21-25 IBJ(5) - node L

} nodes defining the direction of boundary spring element (Fig. A7)

26-30 KD - code for translational spring
0 = does not exist
1 = exists

31-35 KR - code for rotational spring
0 = does not exist
1 = global rotational degrees of freedom defined in the global X,Y,Z coordinates (Fig. A1)
2 = global rotational degrees of freedom defined in the surface coordinate system of the shell element (Fig. A1)

36-40 KN - data generation parameter

41-50 SPS - spring stiffness (set to 10^{10} when left blank) for both translational and rotational springs

Note:

B.2.1 The direction, $\hat{\underset{\sim}{N}}$, of the boundary spring element can be defined either by node I or by the four nodes I, J, K, and L.

B.2.2 When only node I is used, nodes J, K, and L are left blank.

B.2.3 Nodes I, J, K and L need not be unique but they cannot be colinear. The cross product $\hat{\underset{\sim}{a}} \times \hat{\underset{\sim}{b}}$ defines the direction, $\hat{\underset{\sim}{N}}$, of the boundary spring (Fig. A7).

B.2.4 The boundary elements are used to impose irregular boundary conditions. The degrees of freedom at the node where the spring is placed should be free to displace or rotate.

B.2.5 The boundary spring can have both translational and rotational stiffnesses equal to SPS.

B.2.6 The generation parameter, KN, appearing on the last card of a series will generate boundary spring placing at node $NP_i = NP_{i-1} + KN$ with stiffness and direction identical to the first element in the series until NP_i equals the last node in the generated series.

B.2.7 The use of rotational boundary spring elements to impose rotational restraint in a shell will avoid the difficulties encountered in the definition of the surface vectors $\underset{\sim}{V}_1$, $\underset{\sim}{V}_2$ and $\underset{\sim}{V}_3$.

C. TYPE 3 - REINFORCED 3D CONCRETE BEAM ELEMENT

C.1 CONTROL CARD (2I5)

Col. 1-5	MTYPE	-	element type identifier, MTYPE = 3
6-10	NUMBM	-	number of beam elements

C.2 BEAM CROSS SECTION CARDS

C.2.1 CONTROL CARD (I5)

Col. 1-5	NSECT	-	number of types of beam cross section (max.=10)

C.2.2 BEAM CROSS SECTIONAL GEOMETRY CARD (5I5,5F10.0)

Col. 1-5	N	-	section number
6-10	MC(N)	-	type of concrete material
11-15	NFY(N)	-	number of filament layers in the local y' direction (Fig. A8) (max.=10)
16-20	NFZ(N)	-	number of filament layers in the local z' direction (Fig. A8) (max.=10)
21-25	NSS(N)	-	number of longitudinal steel reinforcement bars (Fig. A8) (max.=16)
26-35	B	-	dimension in the y' direction (Fig. A8)
36-45	H	-	dimension in the z' direction (Fig. A8)
46-55	TSF(N)	-	scaling factor for the basic tension stiffening factors input earlier in paragraph 9.3
56-65	EY(N)	-	location of c.g.c. of the beam uncracked concrete section relative to the reference axis (Fig. A9) in the direction of local y axis

66-75 EZ(N) - location of c.g.c. of the beam uncracked concrete section relative to the reference axis (Fig. A9) in the direction of local z axis

Note:

C.2.2.1 The x', y' and z' axes located at the c.g.c. of the beam uncracked concrete section have the same orientation as the beam local x, y, and z axes (Fig. A9).

*C.2.3 LONGITUDINAL STEEL REINFORCEMENT CARD (2I5,3F10.0,2I5)

Omit if NSS(N) = 0, otherwise repeat for NSS(N) times.

Col. 1-5 M - steel reinforcement M

6-10 MSS(M,N) - steel material type

11-20 SAS(M,N) - area of steel reinforcement (Fig. A8)

21-30 SSY(M,N) - y' coordinate of the steel reinforcement (Fig. A8)

31-40 SSZ(M,N) - z' coordinate of the steel reinforcement (Fig. A8)

41-45 NLCI(M,N,1)- concrete layer in the y' direction closest to the reinforcement

46-50 NLCI(M,N,2)- concrete layer in the z' direction closest to the reinforcement

Note:

C.2.3.1 The layer numbers are increased in the directions of both y' and z' axes. The two integers, K and L in Fig. A8, thus represent the location of a concrete filament.

*C.2.4 TORSIONAL REINFORCEMENT CARD (I5,6F10.0)

Omit if NSS(N) = 0, otherwise one card is required for each type of cross section.

Col. 1-5	MSTYPE	-	steel material type
6-15	AST	-	total top steel area
16-25	ASB	-	total bottom steel area
26-35	ASH	-	area of each hoop reinforcing bar
36-45	YO	-	core dimension in y' direction
46-55	ZO	-	core dimension in z' direction
56-65	S	-	spacing of hoop reinforcement

C.3 ELEMENT DATA CARDS

Two cards are required for each beam element.

C.3.1 BEAM LAYOUT CARD (5I5)

Col. 1-5	N	-	beam element number
6-10	IX(1)	-	node I
11-15	IX(2)	-	node J
16-20	KNODE	-	node K
21-25	ISECT	-	beam section type

Note:

C.3.1.1 The local beam axes x, y, and z in Fig. A9 are defined such that x lies on the line joining nodes I and J. z axis is normal to the plane containing nodes I, J, and K. y axis is normal to both x and z, and forms a right-hand system of coordinates.

C.3.1.2 The node K is chosen arbitrarily but the plane containing nodes I, J, and K must be parallel to one of the

principal planes of the uncracked concrete beam cross section.

C.3.2 ELEMENT DISTRIBUTED LOAD CARD (4F10.0)

Col.	1-10	ELD(1)	- pressure load (force per unit length) in global X direction acting in the Xx plane (+ve in the X direction)
	11-20	ELD(2)	- pressure load (force per unit length) in global Y direction acting in the Yx plane (+ve in the Y direction)
	21-30	ELD(3)	- pressure load (force per unit length) in global Z direction acting in the Zx plane (+ve in the Z direction)
	31-40	ELD(3)	- weight per unit length of the beam

DESCRIPTION OF OUTPUT

The complete input together with the generated data are output with appropriate labels for error checking.

The output for the results at the end of a load or displacement step for KOUT=0, or at the end of each iteration for KOUT=1 consists of:

(1) Total external nodal loads in the global coordinate system.

(2) Unbalanced nodal loads in the global coordinate system.

(3) Total nodal displacements in the global coordinate system.

(4) When a time dependent analysis is performed, the time dependent load is also output.

(5) The output for each of the element groups is:

5.1 Shell Element

At each of the first 4 integration points (Fig. A6), the following are output for each integration station through the thickness (Fig. A5):

(i) stresses in the concrete in the local x,y,z coordinate or in the prescribed stress directions

(ii) concrete states in the principal stress directions

(iii) principal stresses in the concrete and their directions relative to the local x axis

(iv) stresses and states of the steel in the reinforcing directions

(v) integrated force and moment resultants at a section in the prescribed directions

The positive directions for the stresses and the stress resultants are shown in Fig. A10. Tensile stresses are +ve.

5.2 3D Beam Element

(i) stresses and states for each concrete and steel filament as well as the torsional states

(ii) member end forces

(iii) integrated force and moment resultants at the mid-length of the beam element

The +ve directions for the member end forces are shown in Fig. A9.

5.3 Boundary Spring Element

(i) the extensional and the rotational spring forces

The +ve directions are shown in Fig. A7.

Note:

1. For linear analysis, only (1), (3) and (5) will be output.
2. For linear bifurcation buckling analysis, the buckling load factor, ω, and the buckled shape as well as (1), (3) and (5) associated with the reference external load will be output.

The corresponding values at the bifurcation load can be obtained by scaling the output (1), (3) and (5) by ω.

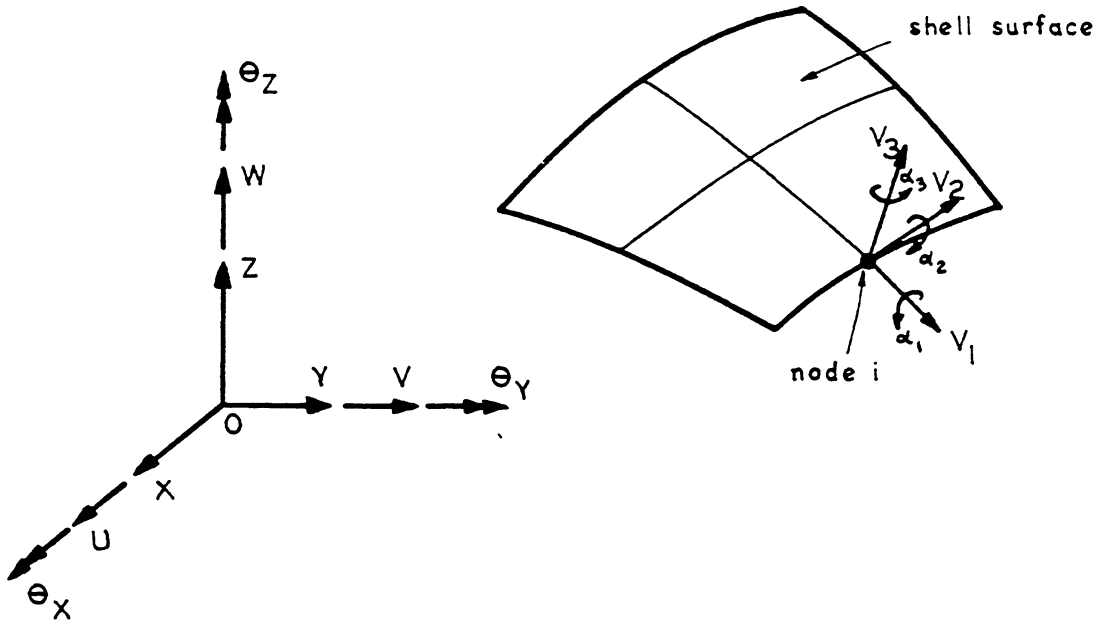

FIG. A1 GLOBAL AND SURFACE COORDINATE SYSTEMS

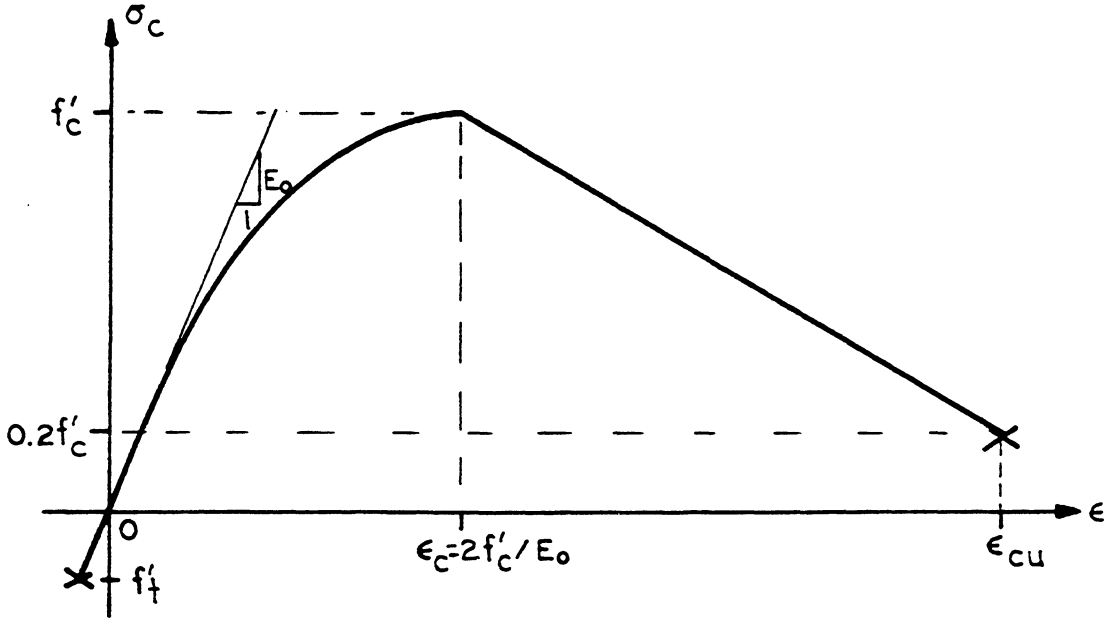

FIG. A2 TYPICAL CONCRETE UNIAXIAL STRESS-STRAIN CURVE

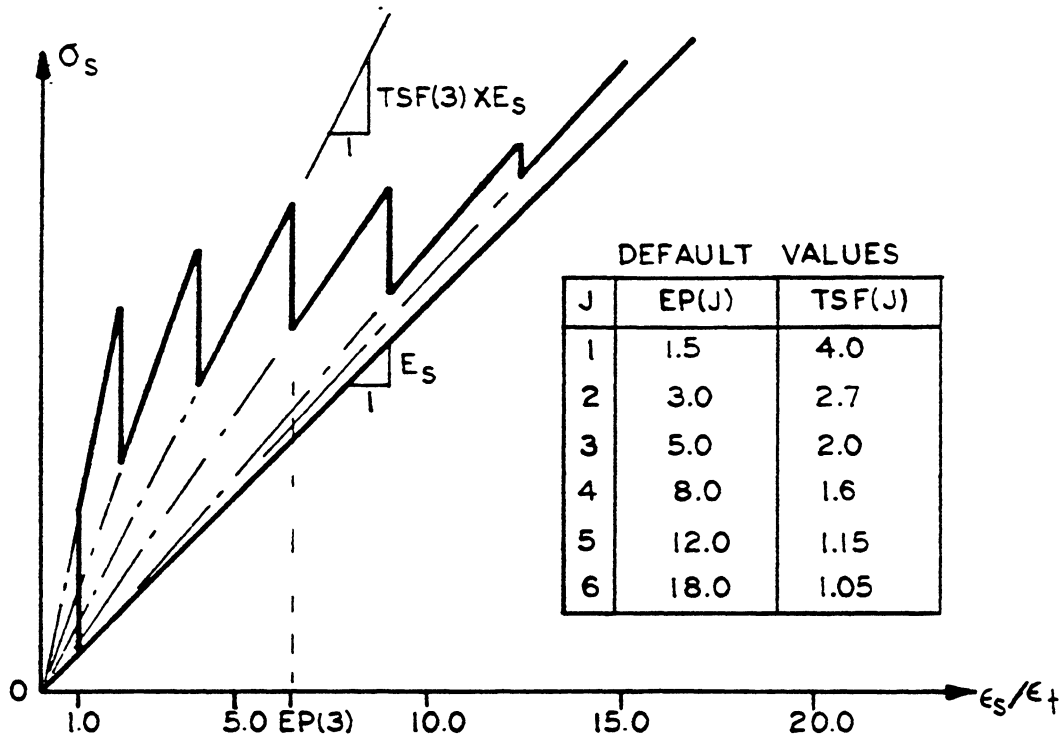

DEFAULT VALUES

J	EP(J)	TSF(J)
1	1.5	4.0
2	3.0	2.7
3	5.0	2.0
4	8.0	1.6
5	12.0	1.15
6	18.0	1.05

FIG. A3 TYPICAL MODIFIED STRESS-STRAIN DIAGRAM FOR STEEL INCLUDING THE TENSION STIFFENING EFFECT IN THE CONCRETE

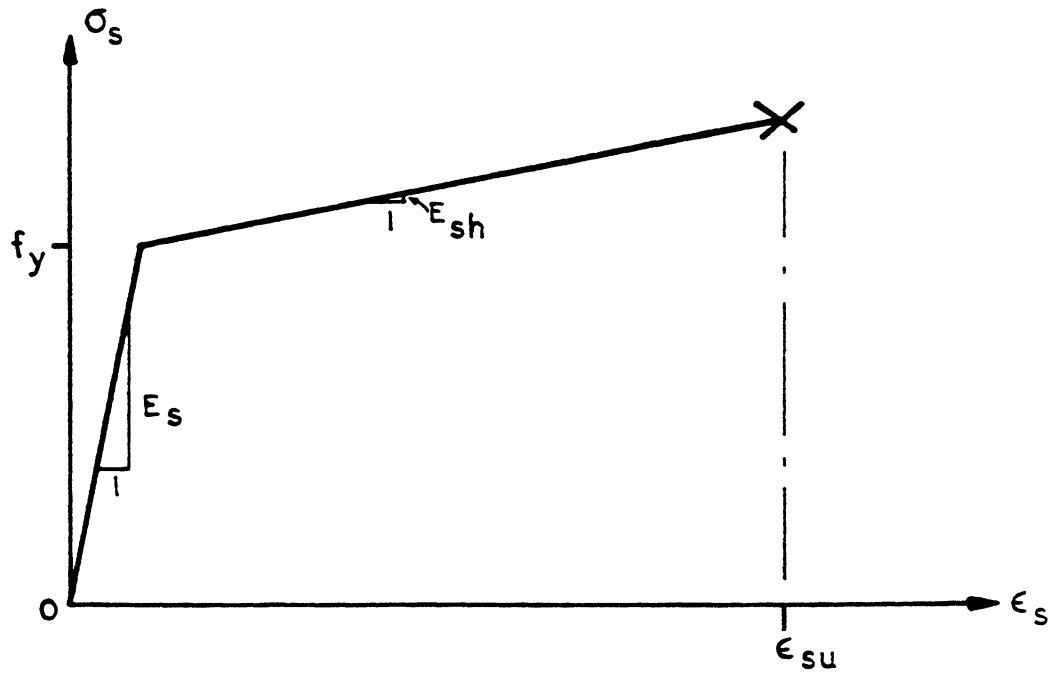

FIG. A4 TYPICAL STRESS-STRAIN CURVE FOR STEEL

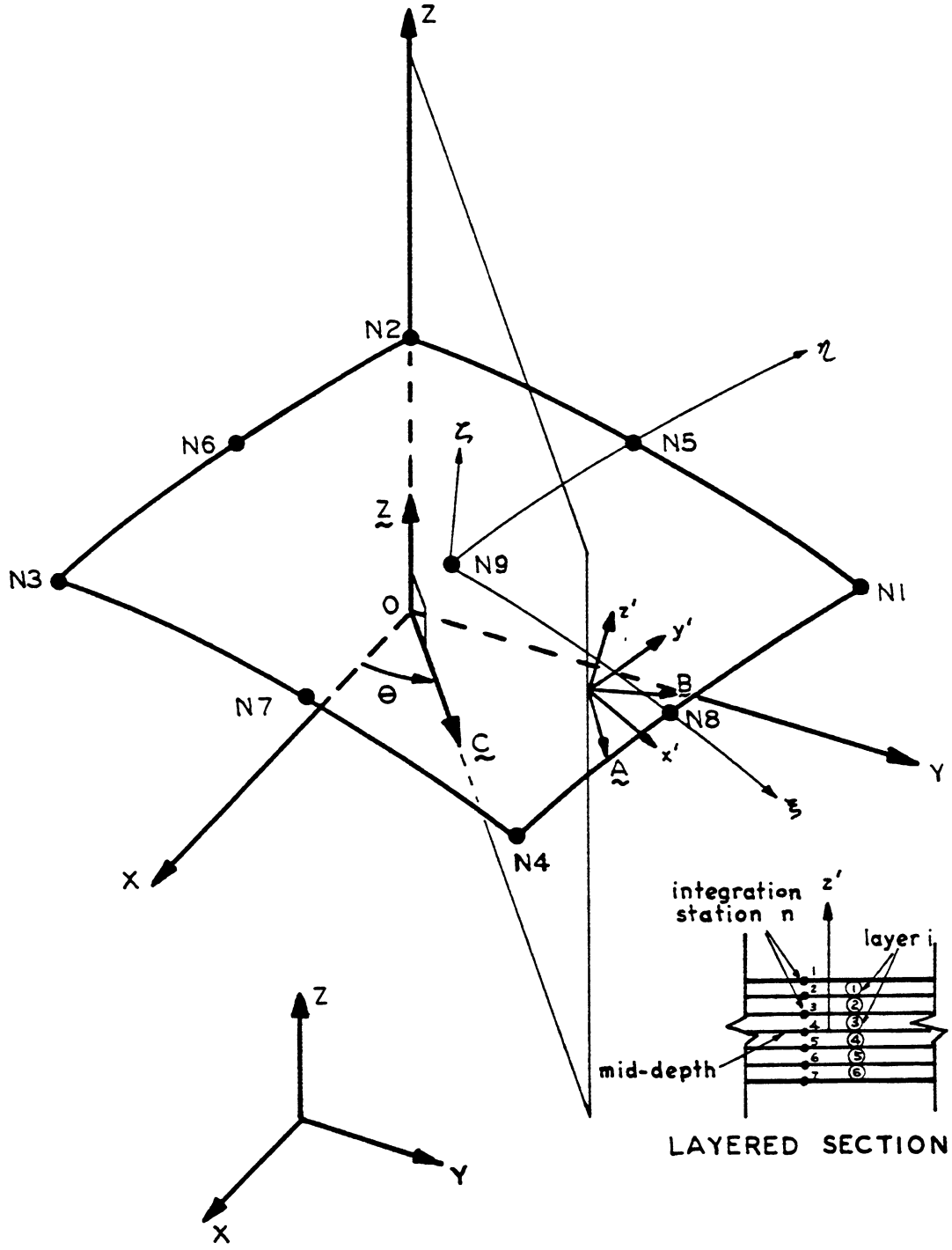

FIG. A5 GEOMETRY AND COORDINATE SYSTEMS OF SHELL ELEMENT AND DIRECTIONS OF STEEL REINFORCEMENT AND STRESS OUTPUT

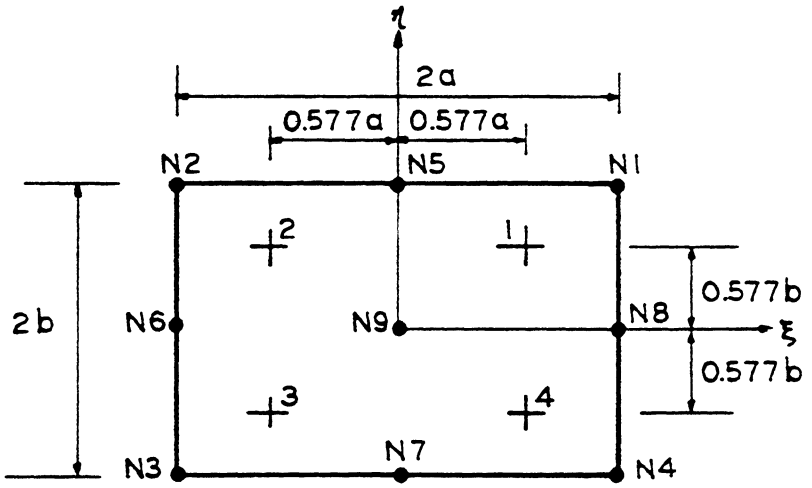

2X2 GAUSSIAN RULE

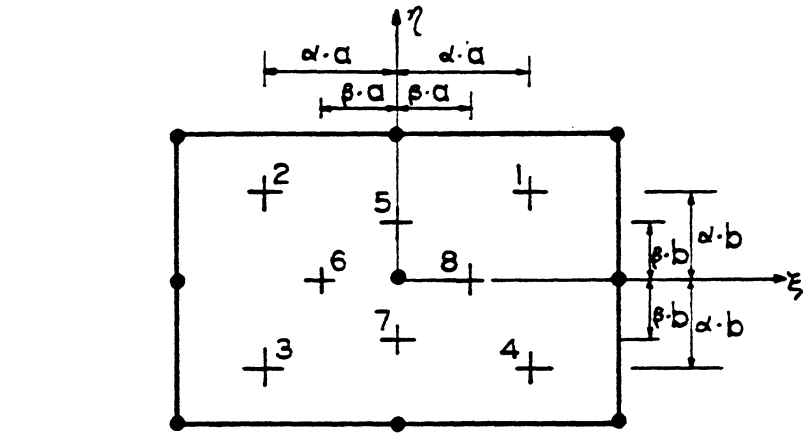

$W_\beta = W(2)$

$W_\alpha = 1 - W_\beta$

$\alpha = 1/(9W_\alpha)^{1/4}$

$\beta = \dfrac{(2/3 - 2W_\alpha\alpha^2)^{1/2}}{W_\beta^{\frac{1}{2}}}$

8 POINT RULE

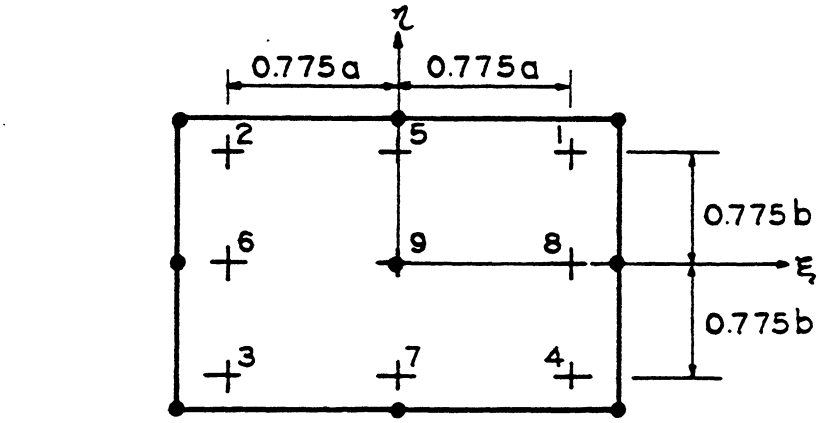

3X3 GAUSSIAN RULE

FIG. A6 LOCATION OF INTEGRATION POINTS FOR DIFFERENT INTEGRATION SCHEMES

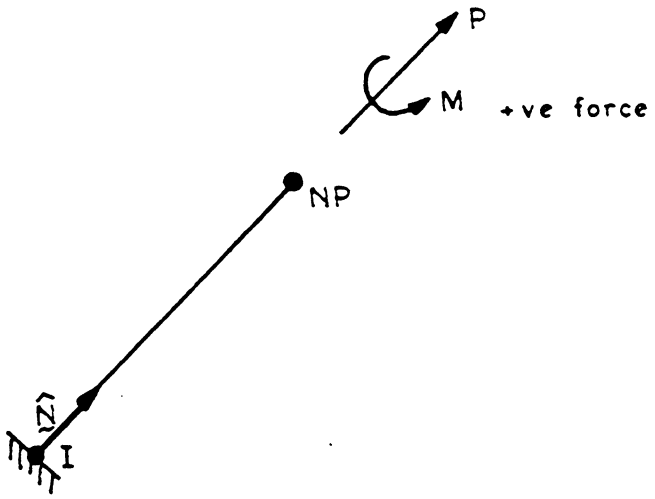

(a) SPRING DIRECTION DEFINED BY NODE I

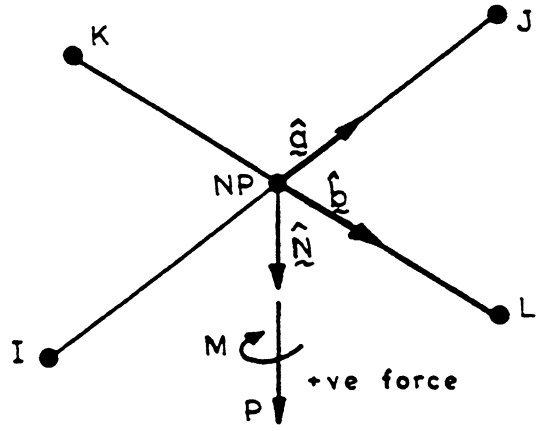

(b) SPRING DIRECTION DEFINED BY NODES I, J, K AND L

FIG. A7 BOUNDARY SPRING ELEMENT SHOWING +ve DIRECTION OF SPRING FORCES

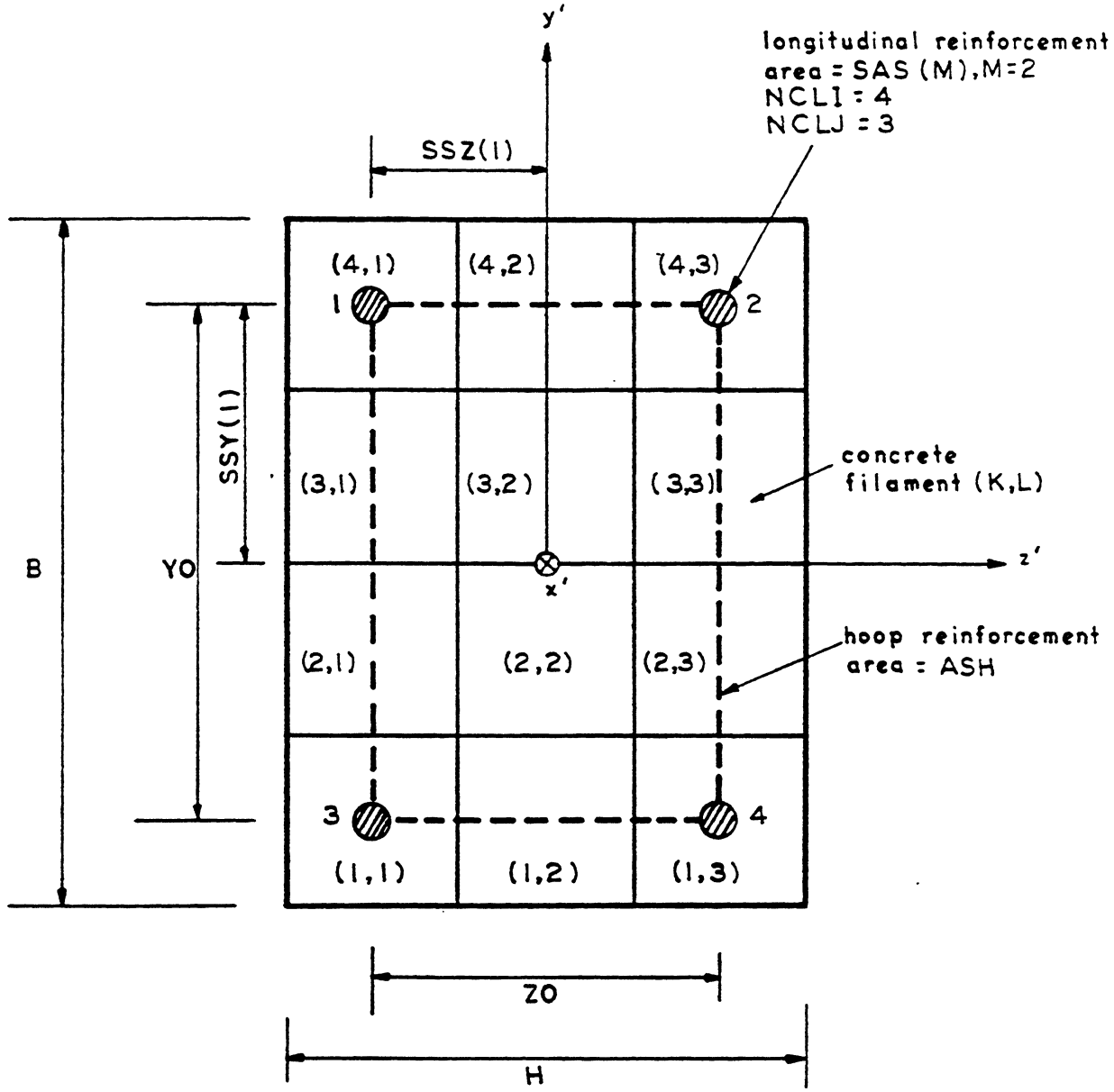

NFY = 4 AST = SAS(1) + SAS(2) K = layer number in y' direction

NFZ = 3 ASB = SAS(3) + SAS(4) L = layer number in z' direction

NSS = 4

FIG. A8 TYPICAL BEAM CROSS SECTION

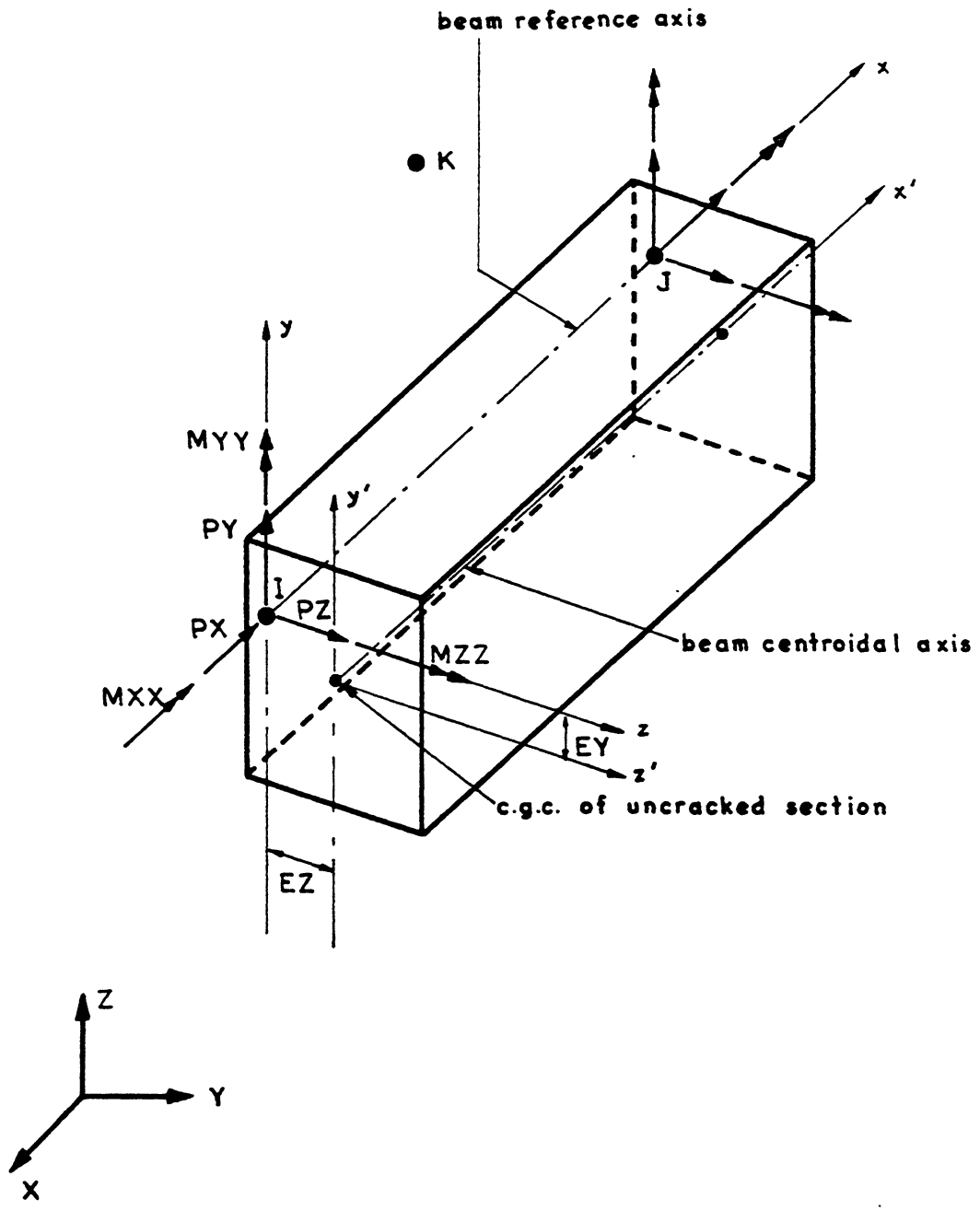

FIG. A9 COORDINATE SYSTEM, GEOMETRY AND +ve DIRECTION OF INTERNAL FORCES FOR A BEAM ELEMENT

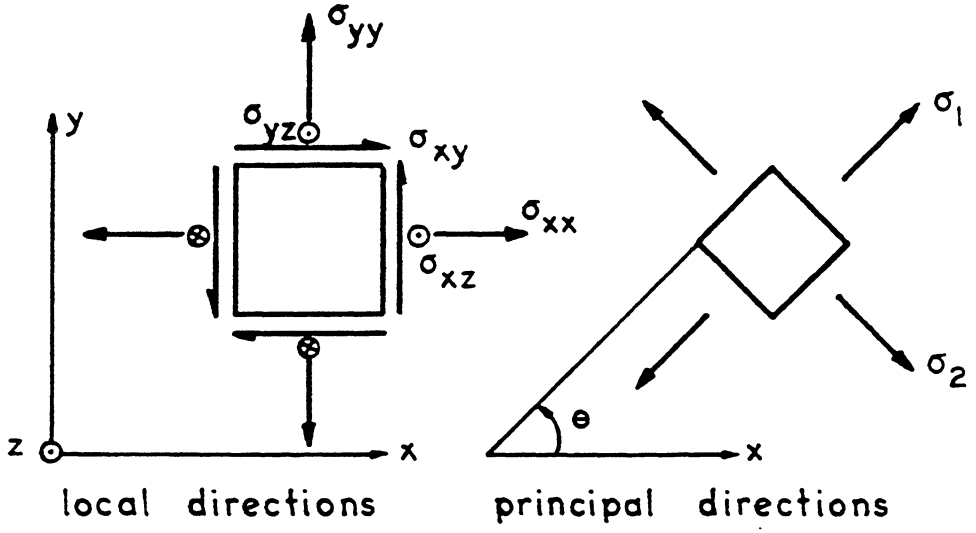

(a) POSITIVE DIRECTION FOR STRESSES

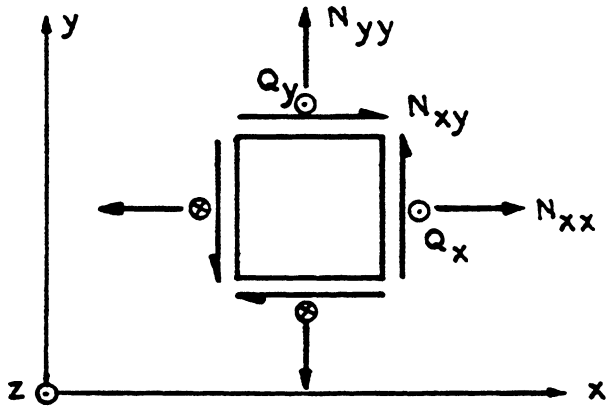

(b) POSITIVE DIRECTION FOR FORCE RESULTANTS

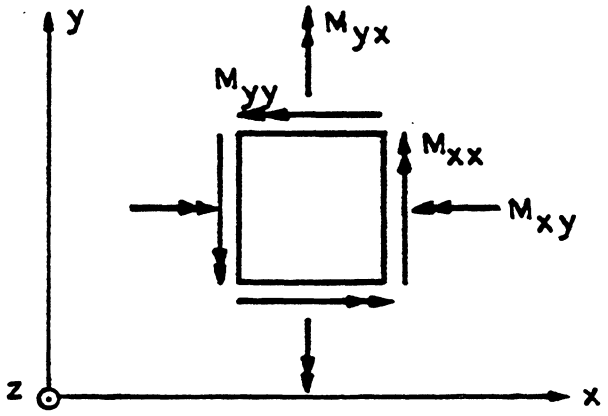

$M_{xy} = M_{yx}$

(c) POSITIVE DIRECTION FOR MOMENT RESULTANTS

FIG. A10 POSITIVE DIRECTION FOR STRESSES AND STRESS RESULTANTS FOR A SHELL ELEMENT